2017

Development and calibration of discrete element method inputs to mechanical responses of granular materials

Zamir Imtiyaz Syed
Iowa State University

Recommended Citation
Syed, Zamir Imtiyaz, "Development and calibration of discrete element method inputs to mechanical responses of granular materials" (2017). *Graduate Theses and Dissertations*. 16226.
https://lib.dr.iastate.edu/etd/16226

Development and calibration of discrete element method inputs to mechanical responses of granular materials

by

Zamir Syed

A dissertation submitted to the graduate faculty

in partial fulfillment of the requirements for the degree of

DOCTOR OF PHILOSOPHY

Major: Civil Engineering (Geotechnical Engineering)

Program of Study Committee:
JeramyAshlock, Co-major Professor
Mehari Tekeste, Co-major Professor
Vernon Schaeffer
Bora Cetin
Shankar Subramaniam

Iowa State University

Ames, Iowa

2017

DEDICATION

For

my daughter, Inaya,

who emerged into this world as the final words of this dissertation were typed.

TABLE OF CONTENTS

LIST OF TABLES

LIST OF FIGURES

NOMENCLATURE

q = shear stress;

p’= effective stress;

m = mass of DEM particle;

$F_{resultant}$ = resultant force on particle;

$\ddot{x}$ = acceleration of particle;

$M_{resultant}$ = resultant moment on particle;

I = mass moment of inertia of particle;

$\ddot{\theta}$ = angular acceleration of particle;

b = stress ratio;

S_r = degree of saturation;

β =damping coefficient;

R_i=Radius of i’th particle;

G_i = shear modulus of i’th particle;

ν_i = Poisson’s ratio of i’th particle;

k_n = normal contact stiffness;

k_t = tangential contact stiffness;

R_e = effective contact radius;

G_{eff} = effective shear modulus at contact;

v_n = Poisson’s ratio of n’th particle;

v_e = effective Poisson’s ratio at contact;

δ_t = tangential overlap;

μ_s = sliding friction coefficient;

F_c = normal contact force;

$v_{rel,tan}$ = relative tangential velocity between two particles at point of contact;

ω_1 = angular velocity of particle 1;

ω_2 = angular velocity of particle 2;

R_{eff} = effective radius of two particles in contact, where $\frac{1}{R_{eff}} = \frac{1}{R_1} + \frac{1}{R_2}$;

R_1, R_2 = radii of particle 1 and 2 respectively;

F_c = normal force acting between particles in contact;

μ_R = rolling friction coefficient;

$T_{EPSD,t+\Delta t}$ = torque contribution in next DEM calculation cycle;

$T_{r,t}$ = torque contribution in previous DEM calculation cycle;

k_r = radial particle stiffness;

k_t = tangential particle stiffness;

$\Delta\theta_r$ = incremental relative rotation between particles;

E_{eff} = effective Young's modulus at contact;

a = cohesion energy density;

e = coefficient of restitution;

$F_{\text{normal contact damping}}$ = force due to normal contact damping;

γ_n normal contact damping coefficient;

γ_t tangential contact damping coefficient;

Δt_{crit} Rayleigh wave propagation time;

R_{min} = minimum particle radius;

d = particle diameter;

ρ = particle density;

x_0,y_0,z_0 = parent particle coordinates;

x_1,y_1,z_1 = neighbor particle coordinates;

$\overrightarrow{PN}$ = vector between the parent and neighbor particles;

$\overrightarrow{IC}$ = vector between point I and the new particle center, C;

A_s = aggregate separation;

{a b c} = coordinates of point I;

{u v w} = components of the unit vector $\overrightarrow{IC}$;

θ = angle of rotation in radians;

F_{n_min} = minimum contact force;

c = damping coefficient;

v = particle velocity;

P_0 = confining pressure;

ζ = damping ratio;

$F_{cohesion}$ = the interparticle force due to cohesion;

$Acont$ = the projected interparticle area;

C = a cohesion coefficient;

$D_{effective}$ is the effective diameter between two interacting particles;

σ_d = deviatoric stress;

σ_1 = first principle stress;

σ_3 = third principle stress;

q_{cone} = cone index;

F_{cone} = cone penetrometer shaft reaction force;

D_{cone}=diameter of the ASABE standard cone (D_{cone} for 30 degree cone = 12.53 mm);

ω_1 = angular velocity of particle 1;

ω_2 = angular velocity of particle 2;

N = normal force acting between particles in contact;

μ_R = rolling friction coefficient;

$T_{r,t}$ = torque contribution in previous DEM calculation cycle;

k_r = radial particle stiffness;

$\Delta\theta_r$ = incremental relative rotation between particles;

F_s = force due to sliding friction;

M_R = moment due to rolling friction;

$V(t)$ = velocity of particle;

$\omega(t)$ = angular velocity of particle;

$\frac{d}{dt}E_{in}$ = instantaneous power transferred to the system;

$\frac{d}{dt}E_{kinetic}$= rate of change of particle kinetic energy;

$\frac{d}{dt}E_{friction}$= rate of energy dissipation through friction;

$\frac{d}{dt}E_{viscous}$= rate of energy dissipation from viscous effects;

v_s = sliding velocity (tangential velocity);

$E_{friction\text{-}simple}$ = $E_{friction}$ with combined sliding and rolling terms;

μ_{eff} = effective fiction coefficient that combines sliding and rolling friction coefficients.

φ_p = interparticle friction angle

φ = internal angle of friction

e_0 = initial void ratio

SF = solid fraction

σ_{d_cs} = critical state strength

P_0 = confining pressure

α = dilatancy

e_{min} = minimum void ratio

e_{max} = maximum void ratio

D_r = relative density

B = tool diameter

e_c = eccentricity from contact to centroid

M_a = applied moment in single particle analysis

M_R = maximum rolling resistance

ACKNOWLEDGMENTS

I want to first and foremost thank my co-major professors, Mehari Tekeste and Jeramy Ashlock, whose continuous support and guidance made my dissertation completion possible. I am extremely grateful for their patience, motivation, enthusiasm, support, and immense knowledge. I also wish to thank the other members of my past and present, dissertation committee: Drs. David White, Fouad Fanous, Shankar Subramaniam, Max Morris, Bora Cetin, and Vernon Schaefer for their advice and helpful recommendations throughout this process. I would like to thank my graduate student colleagues Junxing Chen, Mohammad Mousavirad, and Matthew Schramm for their advice, recommendations and support. I would also like to extend my deepest gratitude to Hans Kelpe, Engineering Manager at Vermeer Corporation for mentoring me and challenging me to be a better engineer. Finally, I would like to thank my family for their continuous support and encouragement in my personal and professional experiences.

ABSTRACT

Simulation of soil excavation is difficult. Tools which manipulate soil are difficult to evaluate in a virtual environment prior to prototype or manufacture. Soil behaves as a discontinuous material in normal excavation activities. Therefore, numerical methods which naturally model discontinuous media, such as the Discrete Element Method (DEM), can be used to perform simulations of soil excavation. However, DEM input parameters must be calibrated to accurately model the mechanical behavior of soil. The goal of this research was to develop intelligent methodologies to calibrate DEM input parameters to reproduce the mechanical responses of soil and other granular materials subject to traditional laboratory tests, such as triaxial and direct shear tests. A mechanistic understanding of the interaction between sliding and rolling friction was developed and correlated with the critical state strength of drained granular media. In addition, the fundamental soil mechanics concept of relative density was successfully applied to the DEM calibration methodology to predict peak granular strength and dilatancy. Sensitivity analyses of DEM input parameters were used to enhance the characterization of mechanical behavior of DEM specimens. A calibration algorithm was developed to quickly and mechanistically relate DEM input parameters to laboratory measured mechanical behavior of soils. The algorithm eliminates unnecessary iterations during the DEM parameter calibration by enforcing a sophisticated understanding of the mechanisms of granular shear strength. The outcomes of this research greatly simplify the calibration of DEM parameters of soil for use in industrial excavation problems.

CHAPTER 1. INTRODUCTION AND BACKGROUND

This chapter describes the industry problem in which the research is rooted as well as the technical hurdles that must be overcome in order to provide meaningful contributions to the fields of soil mechanics and machine-soil interaction. The overall goals, objectives, and significance of the research to excavation equipment industry will be described. The organization of the dissertation will also be forecasted.

Literature will be reviewed in the numerical methods in geomechanics, theoretical background of Discrete Element Method (DEM), DEM simulations of laboratory tests, DEM input parameters calibration, and simulation of machine-soil interaction. To broaden the understanding of granular materials, literature on agricultural grain flow was also reviewed.

Industry Problem

The author has worked in the specialty excavation industry for 10 years, which includes the design, analysis, and manufacture of trenchers, plows, blades, and horizontal directional drilling equipment.

Modeling soil cutting in directional drilling applications using the Finite Element Method (FEM) has been the traditional approach in the excavation industry. There are many existing studies of soil cutting simulations using FEM; however, their solution accuracy compared to physical testing varies significantly with respect to tool geometry, soil type, and tool dynamics (Abo-Elnor et al., 2003; Kushwaha and Shen, 1995; Mouazen and Nemenyi, 1999; Rosa and Wulfsohn, 2002; Tekeste et al., 2009). Indeed, the author found it difficult to reconcile the continuum assumptions of FEM with the discontinuous nature of granular soil in modeling the horizontal directional drilling. Ultimately, an alternate tool was selected, the Discrete Element Method (DEM), to simulate tool-soil interaction which did not have similar limiting assumptions of FEM which was developed based on continuum mechanics. The drawback of using DEM has been calibration of granular material DEM input parameters. Thus, this research is focused on developing robust calibration methodologies for DEM input parameters based on the mechanical outcomes of common laboratory tests, such as the triaxial and direct shear tests.

Impact on industry

The impact of robust DEM input calibration to mechanical outcomes of simple physical tests is threefold:

1) Navigation, or trajectory planning, of an underground directional drill string can be made possible just by understanding and robustly modeling the soil.
2) Tools that manipulate granular material can be optimized on many fronts (performance, structure, cost).
3) Time and resources can be conserved by simulating complex excavation tasks before breaking ground, which could help engineers select the right tool for the job.
4) With a robust and mechanistic DEM calibration approach, it is possible to attain a better understanding of granular mechanics at the micro and phenomenological scales.

Technical Problem

This research addresses the technical problem that underlies the industrial need for a simulation software to reliably predict navigation of an underground directional drill head by resolving cutting, pushing, and draft forces. The problem of forecasting the navigation of a horizontal drill string into soil is unresolved because constitutive soil models as a discontinuous medium are not yet fully robust and practically useful in the engineering work flow.

Others have attempted to simulate soil drilling using FEM (Xianguo and Bo, 2002; Jianhua and Wang, 2005) and DEM (Xie et al., 2013; Chung and Ooi, 2006); however, the hurdle the previous studies had encountered was a lack of robust model for the simulation of soil subjected to large and discontinuous shear strains. While acute empirical calibrations and validations of constitutive soil models have been performed, they were only valid over the empirically tested range, thereby reducing the robustness of predictions.

Goal of the Research

The overall goal of this research is to create robust simulations of tool-soil and tool-grain interaction that can help make important decisions in fast-paced development cycles in specialty excavation and agricultural equipment industries. There is a need for data-driven decision making in industry, but unresolved technical challenges limit engineers' ability to generate data. As with all mechanistic modeling technology, simulation data can fill in the gaps in empirical knowledge and help make proper determination of technological direction. The overarching industrial goal of this research in modeling and simulation is to improve the product development cycle from design, analysis, and testing, to customer experience. There is immense demand on engineers to reduce the number of design iterations and limit the number of physical prototypes. Simulation technology helps engineers make the right decisions early in the design stage to prevent unnecessary prototype and testing iterations. Stress analysis and durability simulations have significantly improved product quality across automotive, aerospace, excavation, and agricultural industries. Similarly, soil and granular simulation will bring exciting improvements to soil cutting and grain manipulation systems.

Objectives

In this study, DEM simulation development, laboratory test simulation, DEM calibration, and model validation represent the four research objectives, which are addressed through the following tasks:

1. DEM particle model and simulation development which comprises (a) development or selection of interparticle interactions (DEM contact laws); (b) soil DEM particle definition; and (c) automated implementation of DEM particle assembly generation and boundary conditions for triaxial test calibration. Based on literature relevant to soils, interparticle interactions were selected. Using particle generation algorithms and calibration experiments, boundary conditions were developed using the LIGGGHTS (2015) DEM open software platform.
2. Development of DEM simulations of standard laboratory tests including triaxial and direct shear tests. The bulk mechanical stress and strain responses will be integrated into the DEM calibration methodologies.

3. DEM calibration methodology. The development of a DEM calibration methodology, which is a closed loop workflow and systematically able to generate calibrated DEM parameters to mechanical outcomes of standard laboratory tests.
4. DEM validation using simple tests. The final objective for this research is to provide application test cases to validate the DEM calibration methodology. DEM models will be compared to physical experiments to assess the DEM predicted mechanical behaviors for simple tests of soil-tool and grain-equipment interaction problems. As with any modeling technique, it is important to find the limits of real-world accuracy along with ranges of robust predictive ability.

Significance of the Research

Mechanistic calibration of DEM models is currently limited because of the technical complexity of DEM parameter interactions. Indeed, researchers have proposed new interparticle interactions, but the confounding nature of existing DEM parameter interactions has not been resolved. For instance, even straightforward Coulombic friction between particles is poorly understood in the DEM literature in the presence of confounding rolling motion. Similarly, the effects of interparticle cohesion are overstated when the effects of initial configurations of DEM assemblies are not controlled for. Robust micromechanical modeling methods which do not isolate interaction terms are scarce. This research aims to show that robust DEM calibration can only be achieved when micromechanical models can be reconciled with phenomenological granular behavior.

Industry is slow to adopt state-of-the-art modeling techniques for a variety of reasons. In the author’s experience, the difficulty in obtaining useful data from new models is great and requires significant time and resource investment in learning, developing, and calibrating models to serve a particular business use. A significant benefit of this research is that the calibration portion of the DEM learning curve will be reduced to a simple, closed-loop recipe. Engineers will be able to focus on developing a product rather than calibrating and validating material models. Another benefit of this research to industry is a shorter product development cycle. Engineers are required to make consequential decisions early in a product development cycle – often with limited information. Pre-calibrated DEM models can provide engineers with important simulation data enabling enhanced data driven decision making early in the design stages of a product.

What follows is an example of possible industrial use of properly calibrated DEM models from the author's personal experience. During his time at Vermeer Corporation, he was tasked with predicting the trajectory of an underground directional drill head being pushed through soil. Due to the large deformation and soil shearing behavior observed in physical experiments, he chose DEM as an appropriate method to model the soil. However, after many attempts, calibration of the DEM model became the bottleneck. He started research studies to resolve the DEM calibration problem. Indeed, if a robust DEM calibration method for soils were available in 2011, the author's department at Vermeer Corporation would have greatly benefitted.

Organization of the Document

Following this introductory section, the remainder of this chapter will review previous literature and background information for the study. Following the current chapter, this dissertation is organized into 4 additional chapters. Chapter 2 describes laboratory tests and virtual DEM simulation methods. Chapter 3 describes the micromechanical interaction between sliding and rolling friction. Chapter 4 presents the results and analyses for early, foundational work in DEM calibration, which includes statistical analysis on large dataset from virtual triaxial tests. Chapter 5 discusses validation studies which were used to examine where and when the calibration methodology can be used. The final chapter discusses conclusions from development and validation phases of the research and offers suggestions for future research. The list of works cited follows the conclusions.

Literature Review

This research aims to calibrate discrete element simulation parameters against physical triaxial, oedometer, and direct shear test behaviors with known boundary conditions. Therefore, literature describing discrete element modeling of standardized tests will be reviewed. Previous attempts at empirical and theoretical calibration of DEM models will also be described in the context of granular soil behavior. The validation phase of this research involves physical experiments. Therefore, literature linking models to hopper discharge, blade mixing, and cone penetrometer testing will also be discussed.

Numerical Methods in Geomechanics

The finite element method (FEM) and the discrete element method (DEM) are two numerical methods that can be applied to geomechanics. This section discusses each method then compares the two and discusses whether DEM can model soil behavior.

Finite element method

The finite element method (FEM) has been used to solve geomechanical problems. FEM requires continuous constitutive laws to define stiffness behavior. Calibration of constitutive models has been done on a large scale by Duncan et al. (1980). Stress-strain relationships were well defined by hyperbolic functions. Coefficients for the hyperbolic functions were fitted to physical triaxial test data using a least squares algorithm. FEM inherently limits the utility of the hyperbolic constitutive models calibrated in Duncan et al. (1980). Duncan et al. (1980) suggested that when elemental stresses exceed the allowable stresses, the elements are considered to be failed. If a significant number of elements fail, then the accuracy of the system suffered. Therefore, the hyperbolic models from Duncan et al. (1980) were best used at small to moderate strains (i.e., less than 2% strain). Additional constitutive modeling schemes have been shown to fit stress strain curves of geomaterials. Active adaptation of constitutive laws was shown to fit experimental data from triaxial tests very well using genetic algorithms (Rokonuzzaman and Sakai, 2010).

Although FEM is a very powerful tool, it has some limitations. It is very difficult to model stress softening behavior in implicit time stepping schemes. In explicit time stepping schemes, softening can be modeled, but computation time and mesh sensitivity increase significantly. Algorithms to increase the stability of larger time steps, such as fractional step algorithms, have been shown to effectively work around these limitations (Li et al., 2003). In addition, modeling large strains often required frequent remeshing due to loss of elemental aspect ratio and other symptoms of excessive mesh distortion (Vavourakis et al., 2013). Li et al. (2003) and Vavourakis et al. (2013) showed that some of the limitations in FEM were practical and can be worked around. A more theoretical limitation has to do with the fundamental assumption that the material being modeled by FEM is a continuum. That is, the elemental deformation between nodes can be modeled by a continuous displacement function that approximates the solution of the partial differential equations of continuum mechanics (Logan, 2002). This assumption excludes discontinuous media, such as soils at large shear strains. These limitations do not prohibit the usage of FEM for geomechanical problems, but these limitations invite the framework of numerical methods with more flexible fundamental assumptions.

Discrete element method

The discrete element method (DEM) has been used to address some of the FEM limitations. DEM was adapted for granular materials by Cundall and Strack (1979) from molecular dynamics methods that were proposed by Alder and Wainwright (1957). The use of DEM as a viable numerical method for solving soil mechanics problems began relatively recently. Some work in the 1990s (Carrillo et al., 1996) sparked great interest in adapting DEM to geomechanics problems. O’Sullivan’s (2011) comprehensive review of the literature provided a detailed analysis of the use of DEM adapted for geomechanics problems since 1998. O’Sullivan (2011) showed that the general DEM literature began to explode after 1996. She also reported that in 2009, more than half of all geomechanics-related DEM papers used 2D DEM. 3D DEM consisting of 10000+ particles was nonexistent before 2002.

The calculation scheme of DEM is shown in Figure 1. After initial and boundary conditions are defined, contact forces and resultant forces are calculated on each particle. The equation of motion for each particle is integrated over an explicit time step and particle coordinates are updated. Contact forces are recalculated and the cycle repeats itself until the simulation is over.

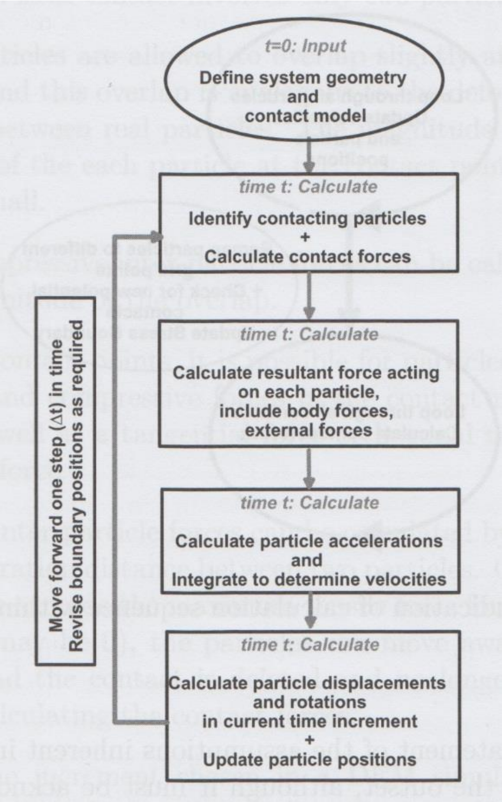

Figure 1. Flow chart of DEM calculations. Source: Particulate Discrete Element Modeling (O'Sullivan, 2011)

The equations of motion for each particle are shown in equations 1.1 and 1.2,

$$F_{resultant} = m\ddot{x} \tag{1.1}$$

$$M_{resultant} = I\ddot{\theta} \tag{1.2}$$

where:

$F_{resultant}$ = resultant force on particle;

m = mass of particle;

$\ddot{x}$ = acceleration of particle;

$M_{resultant}$ = resultant moment on particle;

I = mass moment of inertia of particle; and

$\ddot{\theta}$ = angular acceleration of particle.

DEM has been implemented in two styles: block DEM and particulate DEM. Both styles use a similar calculation scheme to what is shown in Figure 1. Block DEM codes simulate large linear elastic blocks participating in contact dynamics. The block codes are used to simulate the dynamics of large physically polygonal geometries (Lanaro, 1997). Particulate DEM uses small geometries with elastic or elastoplastic deformation laws, most of which are Hookean or Hertzian closed form solutions (LIGGGHTS, 2015). Some DEM codes use rigid spheres with coefficients of restitution to determine resultant velocities from the impact of two rigid spheres (Zhu et al., 2007). The rigid sphere approach is best suited to loose granular flow, while soft sphere approaches model dense systems better (Delaney et al., 2007). The open source LIGGGHTS software uses the soft sphere approach (LIGGGHTS 2015).

Zhang and Thornton (2005) demonstrated that properly calibrated DEM can produce virtually identical results to those produced by commercial FEM codes within the elastic range.

DEM as a model for soil behavior

The literature shows that individual soil response characteristics can be reasonably simulated using DEM (O’Sullivan, 2011). The initial portion of the stress-strain curve of a triaxial test, the psuedo-elastic modulus, has been reasonably reproduced by simulation (Thorton and Zhang, 2005). Very simple DEM simulations of Cassagrande's shear test have been used to calibrate particle interactions to reproduce physical results (Richefeu et al., 2005). Critical state behavior has been modeled with DEM as well, with an implication that void ratio had a strong non-linear association with confining stress (Zhang and Thorton, 2005). Dilatancy was not well simulated using current DEM practices (Taibi et al., 2005). Failure as predicted by ellipsoidal DEM was very similar to that predicted by the theoretical Lade model (Ng, 2004). Cemented soils have also been simulated in the literature (Xu et al., 2011).

Studies have also ventured to model granular materials using application/field behavior instead of traditional lab tests. For instance, Coetzee and Els (2009) calibrated DEM input parameters using blade interactions with granular materials. Pile resistance in soil was qualitatively studied by Wang et al. (2012), and soil response due to excitation by a bulldozer blade has been studied as well (Tsuji et al., 2012). The interesting thing about these studies is that the global soil behavior of interest was qualitatively reproduced without a standardized method of calibrating DEM inputs.

Boundary conditions

A number of studies utilizes typical periodic boundaries in unsuccessful attempts to model axisymmetry when simulating triaxial tests (Zhang and Thornton, 2005; Roux, 2005; Sitharam et al., 2005). These boundary conditions were non-physical. Better models have been developed for quarter axisymmetric simulations (Cui and O'Sullivan, 2005). Similarly, several papers reported 2D simulations to qualitatively assess parameter sensitivities and correlations (Calvetti and Nova, 2005; Kruyt and Rothenburg, 2005; Vu-Quoc et al., 2001). Lu and Frost (2010) concluded that 3D triaxial simulations were, overall, better than 2D simulations when to simulating triaxial behavior. Regarding the modelization of the latex membrane that house the soil sample in a triaxial test, stress controlled boundaries have been developed (Cui et al., 2007) and have been shown to provide significantly different peak and post peak soil behavior than servo-controlled walls (Cheung and O'Sullivan, 2008). Cheung and O’Sullivan (2008) also showed that the local responses varied with respect to boundary condition type, specifically the location of shear banding and central bulging of triaxial test specimens.

There is a divergence in the literature on the topic of servo controlled versus flexible membrane boundary conditions. One frequently cited paper, Utili and Nova (2008), used the servo-controlled membrane approach to simulate confining stress. Despite the work by Cheung and O’Sullivan (2008) that showed the non-physicality of rigid servo-controlled membranes, many subsequent papers still used the servo-controlled approach (e.g., Gong et al., 2011; Kozicki et al., 2012; Sayeed et al., 2012; Salot et al., 2009). Another type of membrane boundary is that which is seen in the simulation of undrained triaxial tests. Undrained triaxial tests have been simulated under constant volume conditions (Gong et al., 2011). The membrane formulations were servo-controlled, but algorithms that monitor the volume of the sample enforced constant volume conditions.

DEM particle properties and interactions

Particle friction had a strong effect on behavior exhibited by samples subject to triaxial compression (Calvetti and Nova, 2005). Interestingly enough, Kruyt and Rothenburg (2005) demonstrated that granular assemblies offer resistance even when particle friction and cohesion were nonexistent and suggested that some internal kinematic constraints provide granular assemblies some stiffness. Liu et al. (2005) showed the effects of interparticle friction in simulated shear box tests. Zhao et al. (2011) showed that the variations observed in Liu et al. (2005) occur in triaxial test simulations as well. Figure 2 showed the effects of varying sliding friction coefficient on the mechanical response of samples subject to triaxial compression.

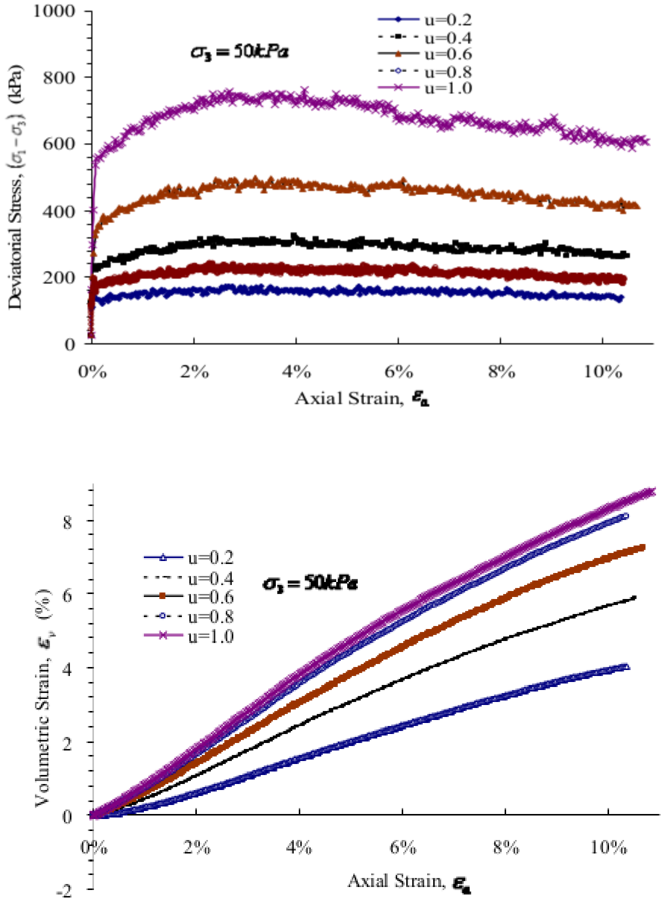

Figure 2. Triaxial test response, stress-strain response (above) and volume change response (below) (Zhao, Shao and Ji, 2011)

Limits to friction angle of a specimen have been shown in simulations where particles were free to rotate. Preventing rotation altogether resulted in over-constrained particles, and lead to higher than expected internal friction angle (Calvetti and Nova, 2005). Huang et al. (2013) quantified the increase in internal friction angle by incrementally increasing the rolling friction coefficient per particle. Figure 3 shows the effect of rolling friction coefficient on internal friction angle.

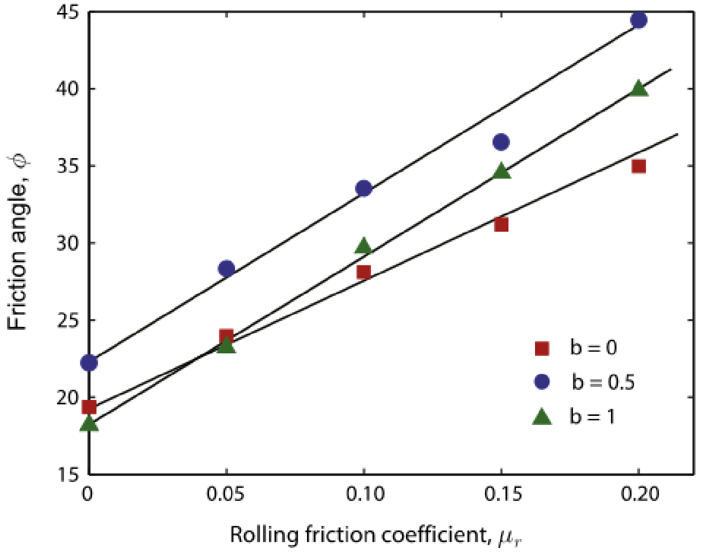

Figure 3. Effect of rolling friction on internal friction angle. Where b=stress ratio, b=0 is traditional triaxial compression, b=1 is triaxial extension (Huang et al., 2013)

There are a few particle cohesion models available. The model implemented in the LIGGGHTS DEM software, JKR cohesion, estimates the contact area between spherical particles and applies a bond proportional to a user-prescribed bond energy density (LIGGGHTS manual, 2015). Others prescribed cohesion on the basis of theoretical, Laplace style water bridging between particles (Soulie et al., 2006). Delenne et al. (2005) developed formulations for the breakage of cohesive bonds that account for combined loads. Scholtes et al. (2009) showed the macro-scale effects of Laplace style cohesion in triaxial test simulations. All of the formulations in the literature make the assumption that a DEM particle was not representative of a collection of smaller particles. This makes the models less than ideal for soil mechanics applications where a DEM particle is never used to model a single soil particle. Figure 4 shows the relationship of cohesion with peak strength and critical state strength, as well as the effects on volume change behavior. It is interesting to note that the effect of cohesion on the volume change response was small compared to the effect on the stress response.

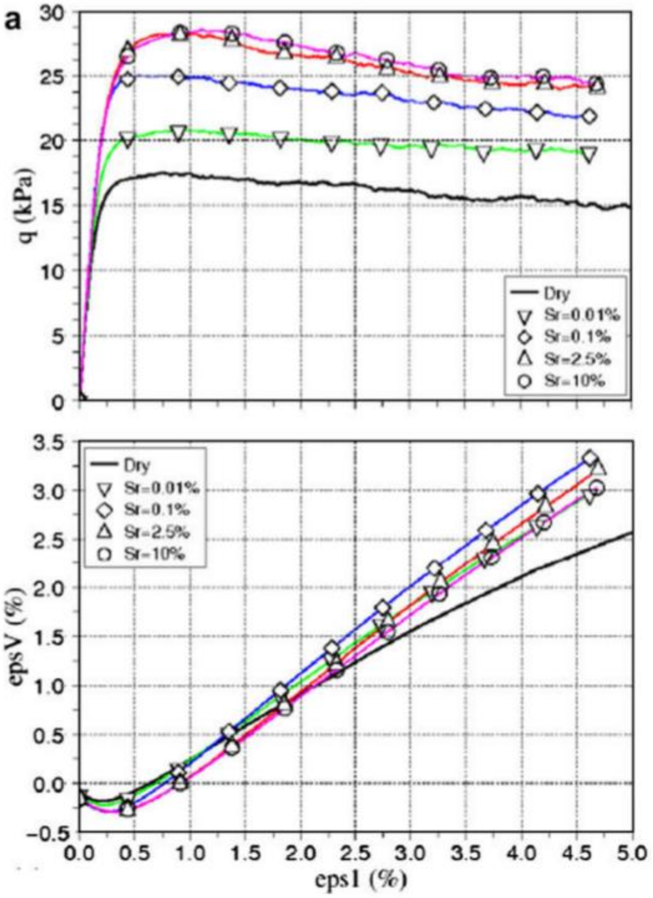

Figure 4. Triaxial test simulations while varying interparticle cohesion Sr = degree of saturation of sample, as saturation increases, cohesion does as well (Scholtes et al., 2009)

Developing accurate pore pressure models historically involved the coupling of DEM code with fluid dynamics code. Excess pore pressure causing dilatancy has been simulated by adjusting porosity on a per volume basis (Takahara et al., 2005).

Some researchers have explored using aspherical particles in DEM simulations of soils. O'Sullivan and Bray (2001) found that ellipsoidal and cluster type particles were adequate for capturing the shape characteristic values of real sands. O'Sullivan and Bray (2001) also showed that aspherical particles offer higher stress ratios than spherical particles when subject to plane strain compression tests. In addition, particle angularity was correlated with rotation when subject to biaxial compression and that spherical particles rotate significantly more than aspherical particles. Rotation differences were insignificant between aspherical particle shapes (Nouguier-Lehon and Frossard,. 2005). These studies suggest that that any aspherical particle formulation can be used without significant negative consequence. Lu and Frost (2010) showed that aspherical particles under triaxial compression can reasonably model volume change at rather high strain levels (14%) but not necessarily at low strains. Lu and Frost (2010) also show that up to 50% higher coordination numbers were achieved when using aspherical particles over spherical particles. According to Lee et al. (2011), polyhedral particles were able to model the complex behavior of sand even better than traditional spherical, ellipsoidal, and clump logic DEM. This is very interesting indeed, but the computation cost of the polyhedral particles has been reported to be very high. A very thorough assessment of particle shape by Kozicki et al. (2012) showed the various achievable stress-strain and volume change responses. Figure 5 shows the effects of particle shape on mechanical response to triaxial compression.

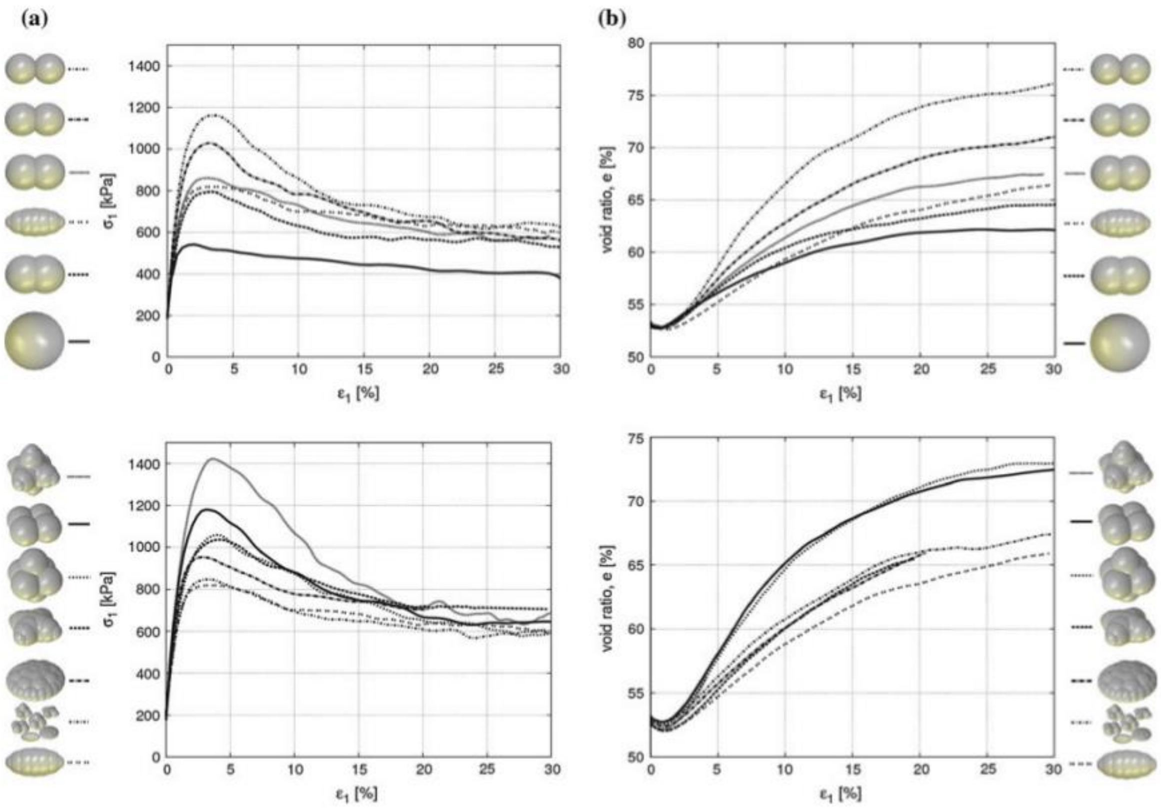

Figure 5. Effect of varying particle shapes on the mechanical response of samples subject to triaxial compression (Kozicki et al., 2012)

The effects of particle size and particle size distribution have also been studied in numerical triaxial tests. Though the study used a non-stress controlled flexible membrane, Andrade and Avila (2012) showed that triaxial stress-strain response as well the evolution of void ratio differed between three ranges of simulated particle size. It is important to note that real soils cannot be modeled by pure spheres of a single size because crystallization occured at high packing densities (O'Sullivan, 2002; O'Sullivan et al., 2004). A crystallized structure resulted in shear planes forming along predictable lattice boundaries. Polydisperse particles and angular particles prevented crystallization, and thereby prevented lattice boundary shear plane formation.

Varying normal contact stiffness was found to significantly alter triaxial test response behavior (Zhao et al., 2011). Figure 6 shows how deviatoric stresses change as a response to varying particle stiffness in a virtual sample that is subjected to triaxial compression.

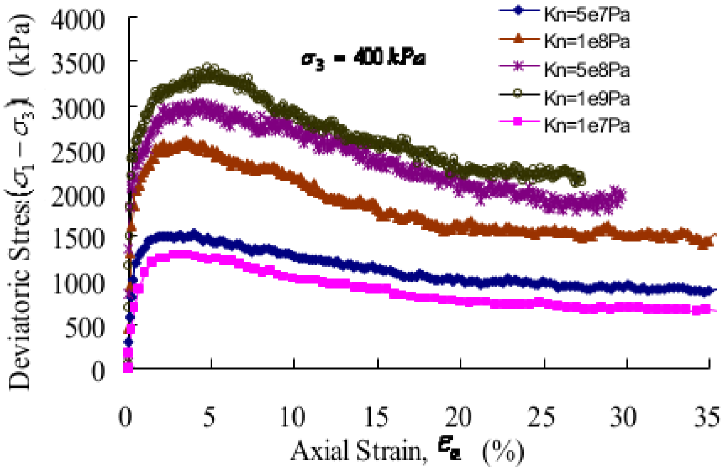

Figure 6. Effect of varying particle stiffness on mechanical response of sample subject to triaxial compression (Zhao et al., 2011)

Ng (2006) outlined the sensitivities of generally understudied parameters such as shear modulus of particles, density, damping, and simulation time step. Ng (2006) reported that density and time step (so long as explicit stability was satisfied) did not have significant effect on triaxial behavior. On the other hand, damping and particle shear modulus were shown to modify triaxial behavior considerably. Damping had a very significant effect on 3D triaxial test simulations. Figure 7 shows increasing damping generally increases the magnitude of stress response of a sample, while preferentially affecting the volume change response at high axial strains.

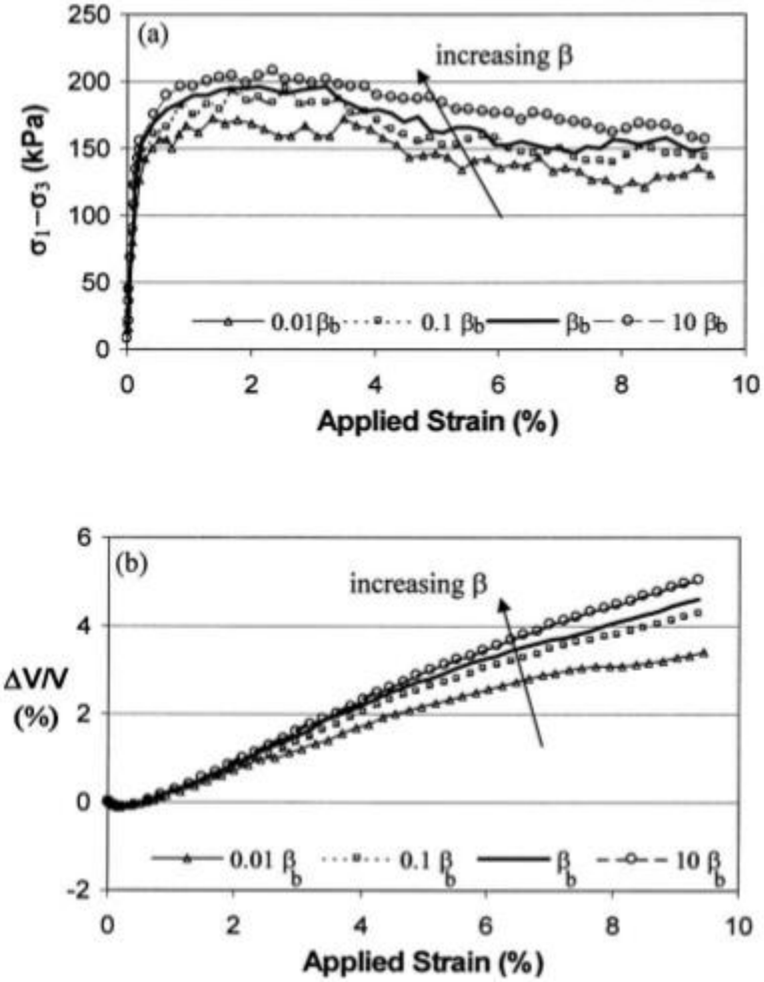

Figure 7. Varying damping while measuring mechanical response of triaxial test simulations. β=damping ratio (Ng, 2006)

Initial conditions

The initial solid fraction of a sample has large effects on triaxial response behavior. Specifically, the peak deviatoric stress and dilatancy are increased by lowering initial void ratio (Guo and Zhao, 2013). Asymptotic deviatoric stress at large strains are unaffected within the range of void ratios from 0.539 to 0.645 (Guo and Zhao, 2013). Figure 8 shows the dependence of mechanical response on initial solid fraction.

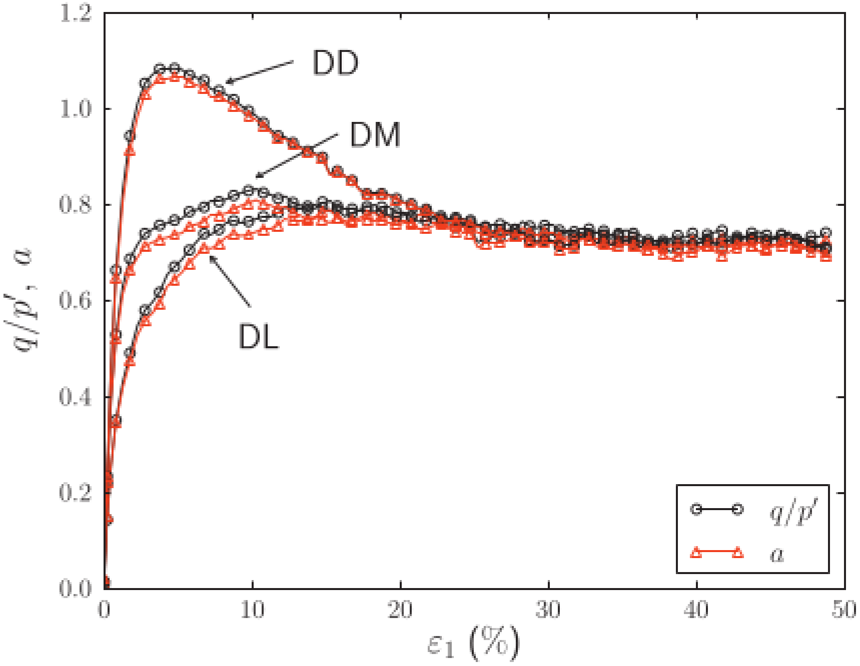

Figure 8. Stress-strain response of drained triaxial test samples. DD=very dense, DM=medium dense, DL = loose (Guo and Zhao, 2013)

The result in Figure 8 was meaningful because it suggested that proper calibration of DEM inputs to geomechanical behavior required that initial solid fraction be controlled. Indeed, the geometry and loading of the particles have an effect on the void space in a specimen. Shamsi and Mirghasemi (2012) demonstrated that void space was associated with particle angularity and confining pressure but did not define minimum or maximum initial void ratios or porosities as functions of either one. Sayeed et al. (2012) allowed samples to consolidate under different confining pressures until they reached a target porosity. The interesting thing here is that the target porosity was controlled by manipulating interparticle friction during consolidation. Where Shamsi and Mirghasemi (2012) treated initial void ratio as a dependent variable, Sayeed et al. (2012) show that initial void ratio can be manipulated as an independent variable. Figure 9 shows the effects of varying confining pressure and constant porosity on the stress-strain response of simulated triaxial test samples.

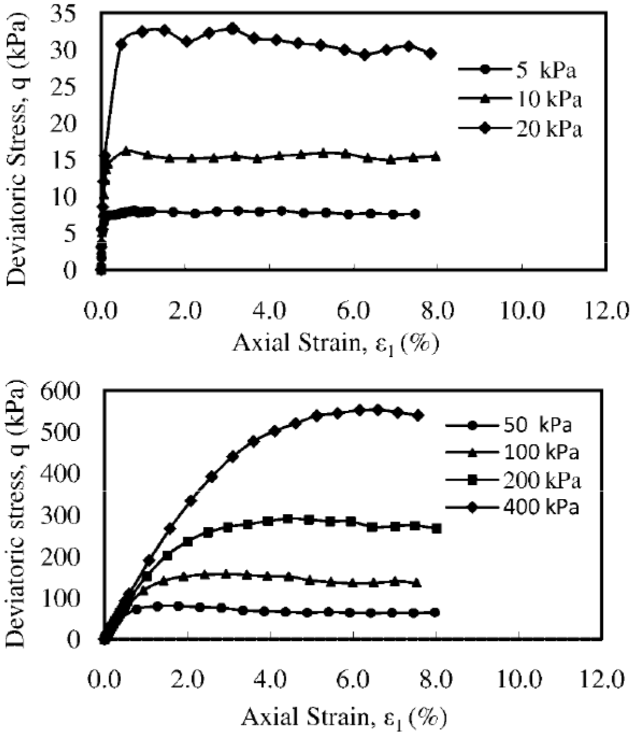

Figure 9. Effect of confining pressure on triaxial test response behavior (Sayeed et al., 2012)

Salot et al. (2009) present a comprehensive analysis of possible initial states that a virtual triaxial test sample can have. Physical limits of initial void ratio were quantified then used to calibrate a DEM model to a physical triaxial test. Salot et al. (2009) showed that calibration was improved significantly by including initial void ratio as an independent variable.

Localization

DEM simulations have qualitatively reproduced common localization phenomena such as shear banding and particle crushing. Although outside the scope of my current research, it is important to touch on localization because it demonstrates a modeling capability that is fundamentally different from constitutive models in continuum mechanics. While shear banding has been modeled using continuum methods, such as FEM (Vardoulakis, 1989), it was highly dependent on local mesh structure. Indeed, the sensitivity of mesh local mesh refinement was highlighted in Vavourakis et al. (2013) who showed that solution accuracy was highly dependent on the method of adaptive remeshing over large strains. On the other hand, because DEM simulations are calibrated at the particle interaction level, localization occurs during the natural course of shearing and compression. Bardet and Proubet (1991) showed 2D shear banding in biaxial shear test simulations. Oda and Kazama (1998) related shear banding to phenomenological dilatancy. The mechanisms of deformation in shear banding were presented by Iwashita and Oda (2000) using DEM with added rolling resistance. Iwashita and Oda (2000) reported void formation and large particle rotations along shear band boundaries. The results of Iwashita and Oda show that DEM was particularly capable of robust modeling of localization without explicit intention of capturing such phenomena.

Cheng et al. (2003) and Bolton et al. (2008) showed mechanisms of particle crushing at high confining pressures in 2D confined compression. Cheng et al. further described phenomenological plasticity (2004) and development of critical state (2005) in the context of grain crushing. Cheng et al's work shows that particle-level understanding of stress capacity can be mechanistically used to predict grain crushing.

Calibration of DEM simulation data with geomechanical laboratory tests

Utili and Nova (2008) developed particle interaction tables from empirical calibration of biaxial tests that negate the need for a user to calibrate DEM inputs at all. However, some undesirable elements of that study, such as particle-rotation inhibition, pure spherical particle usage, and the 2D nature of the simulations, prevent the calibration from being complete. Despite that, Utili and Nova (2008) assembled a weathering cliff analysis that shows that even under plane-strain conditions, which the literature has shown to decrease accuracy, soil flow can be modeled with qualitative agreement to physical experiments. Mechanical outcomes of triaxial tests were calibrated by Zhang et al. (2011), Medina-Cetina and Khoa (2009) use a rigorous probabilistic method to calibrate DEM inputs using sensitivity information with very small standard error, though only results matching the stress-strain responses to experimental data are reported. Belheine et al. (2009) show rigorous calibration of a DEM model with data from triaxial tests on sand. The calibration took place over three confining pressures and included volume change data. Salot et al. (2009) improved upon existing calibration by controlling initial state of dense particle assemblies independently of confining pressure. The open loop method that Salot et al. (2009) prescribed used traditional soil mechanics concepts, such as relative density, to decompose a simulated mechanical soil response to reduce the number of variables that needed to be calibrated. Finally, machine learning methods, although gaining in popularity, have been applied to DEM calibration on a limited basis. Neural networks have been used to develop relationships between soil angle of repose and DEM parameters (Benvenuti, 2016), but require extensive simulation data to establish a viable calibration model.

Cone Penetrometer Simulations

DEM simulation of cone penetrometer testing is not well described in current literature. Instead, other similar simulations of physical testing were drawn from. Plate sinkage, wedge sinkage, and cone penetration testing (CPT) will also be reviewed because the simulation of penetration and sinkage testing involves similar mechanics.

Asaf et al. (2007) simulated wedge sinkage and performed energy analysis that showed that friction energy is the dominant sources of resistance to deformation. Calibration was performed using two different wedge angles because non-unique solutions were found when minimizing error with a single wedge. Between 20 and 30 iterations were required to minimize the objective function presented by Asaf et al. (2007).

Ucgul et al. (2014) used angle of repose tests to calibrate a soil model for cone and disk penetration simulation. Interestingly enough, it appeared the hysteretic contact models exhibited better correlation than Hertz-Mindlin to physical test results. The authors did not show how they calibrated the plastic deformation in the hysteresis contact model.

Table 1 is a summary of important geometric parameters described in various papers which simulated penetration tests. One important parameter is the ratio of the tool size to the average particle size (B/d_{50}). Jiang et al. (2006) suggested that 13 particles should always be in contact with a tool face in order to get a steady state cone resistance. A future research objective is to define the minimum B/d_{50} as a scale-invariant measure of DEM solution quality. Physical cone penetrometer experiments have defined the container radius at which boundary conditions do not affect the magnitude of steady state cone resistance, Bolton (1993) showed that cone resistance was insensitive to container radius larger than 40x the tool radius.

Table 1. Summary of cone penetration simulations in literature

Study	Type	Particle Density (kg/m^3)	Particle Size	Initial State	Normal Stiffness	V_{cone} (m/s)	B/d_{50} [b]
Alvaro and Ooi 2016	30 deg ASABE	2600	5mm +/-10%	Porosity = 0.53 pre-cons	Hookean Hysteretic, 100/500-2500 kN/m	0.03	-
Arroyo et al 2011	CPT	-	26.5mm Cu [a] =1.31	$0.75<D_r<0.97$	Hookean, 300MN/m	0.10	2.7
Falagush et al 2015	CPT	2650	1-2mm	Porosity 0.37-0.42	Hookean, 500 KN/m	-	18
Jiang et al 2014	CPT	2600	7.6mm C_u=1.3	2D Void Ratio = 0.27	Hookean,75MN/m	1	21

[a] C_u = coefficient of uniformity

[b] B/d50 = ratio of tool diameter to mean particle diameter.

All of the studies in Table 1 used the Hookean model for contact stiffness even though some studies show that Hookean particle models cannot reproduce certain dynamic soil behavior (Wensrich and Stratton, 2011). Alternative penetration simulations were presented by Jiang et al. (2014) which showed that inclined penetration angles change cone resistance as a function of overburden pressure. As an interesting extension, Jiang et al. (2015) shows the effects of altering gravity on cone resistance. Velocity dependence of cone resistance was described by Tran et al. (2016) who showed that a non-dimensional inertial number was significantly correlated with a transition from quasi-static shear and compression to dense granular flow.

Soil-Blade Interaction

Chen at al. (2013) showed how varying DEM input parameters affected blade resistance in DEM simulation of soil-sweeping. In fact, soil–sweep characteristics were used to calibrate the DEM parameters. While the work in Chen et al. (2013) was interesting, the lack of overburden pressure in the calibration limited its extension to real excavation applications. Tamas et al. (2013) presented an alternative approach to Chen et al. (2013) by calibrating the DEM input parameters using direct shear tests and using the soil-sweep simulation as a validation tool. Soil sweep simulations have also been used to optimize blade geometry with respect to tillage forces (Ucgul et al., 2015). A notable feature of Ucgul et al's (2015) work was that angle of repose and cone penetrometer tests were used to calibrate DEM parameters while the soil sweep was used as a validation tool.

Blade *mixing* in cylindrical chamber has also been simulated (Chandratilleke et al., 2012) in the context of powder processing; however, the results were within-simulation comparisons of blade geometry. Regardless, blade mixing was interesting because it was possible to apply overburden pressure by filling the blade mixing chamber well beyond the height of the blade which blade-sweep experiments and simulations do not account for. Blade mixing simulations have also been used to analyze massflow rate of granular assemblies through periodic slices (Sarkar and Wassgren, 2012), which can be extended to grain processing simulations.

Grain flow in hopper

Lawton and Marchant (1980) performed direct shear tests on grain products and found that the height from which the direct shear box was filled has a significant effect on strength of the granular assemblies. The take away from Lawton and Marchant's result was that the bulk density of a single species and moisture content of grain can change with respect to specimen preparation method and has an effect on mechanical strength. To affirm the validity of using direct shear tests to estimate grain strength, Molenda and Horabik (2004) showed that internal friction angle from direct shear tests correlate with triaxial test results for dense wheat assemblies over a large range of moisture content. Therefore, there is reasonable evidence to suggest that direct shear testing of seeds and grains is a valuable tool for DEM calibration. Molenda and Horabik shared direct shear test data on many seeds and grains with varying levels of moisture (Table 2).

Table 2. Mechanical properties of various seeds and grains over a range of moisture content (Source: Molenda and Horabik, 2004)

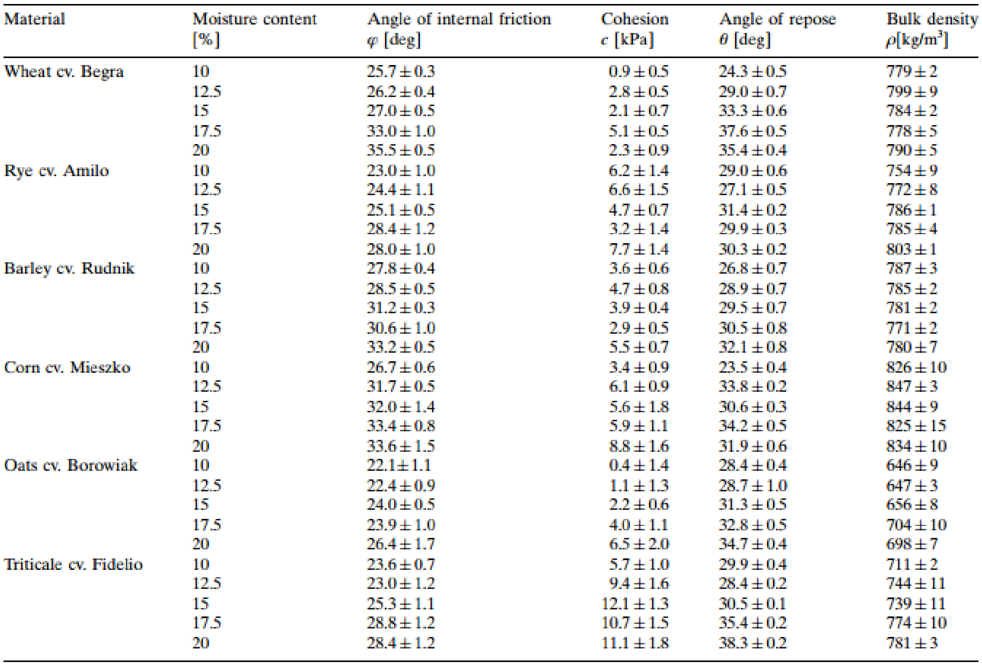

Material	Moisture content [%]	Angle of internal friction φ [deg]	Cohesion c [kPa]	Angle of repose θ [deg]	Bulk density ρ[kg/m^3]
Wheat cv. Begra	10	25.7 ± 0.3	0.9 ± 0.5	24.3 ± 0.5	779 ± 2
	12.5	26.2 ± 0.4	2.8 ± 0.5	29.0 ± 0.7	799 ± 9
	15	27.0 ± 0.5	2.1 ± 0.7	33.3 ± 0.6	784 ± 2
	17.5	33.0 ± 1.0	5.1 ± 0.5	37.6 ± 0.5	778 ± 5
	20	35.5 ± 0.5	2.3 ± 0.9	35.4 ± 0.4	790 ± 5
Rye cv. Amilo	10	23.0 ± 1.0	6.2 ± 1.4	29.0 ± 0.6	754 ± 9
	12.5	24.4 ± 1.1	6.6 ± 1.5	27.1 ± 0.5	772 ± 8
	15	25.1 ± 0.5	4.7 ± 0.7	31.4 ± 0.2	786 ± 1
	17.5	28.4 ± 1.2	3.2 ± 1.4	29.9 ± 0.3	785 ± 4
	20	28.0 ± 1.0	7.7 ± 1.4	30.3 ± 0.2	803 ± 1
Barley cv. Rudnik	10	27.8 ± 0.4	3.6 ± 0.6	26.8 ± 0.7	787 ± 3
	12.5	28.5 ± 0.5	4.7 ± 0.8	28.9 ± 0.7	785 ± 2
	15	31.2 ± 0.3	3.9 ± 0.4	29.5 ± 0.7	781 ± 2
	17.5	30.6 ± 1.0	2.9 ± 0.5	30.5 ± 0.8	771 ± 2
	20	33.2 ± 0.5	5.5 ± 0.7	32.1 ± 0.8	780 ± 7
Corn cv. Mieszko	10	26.7 ± 0.6	3.4 ± 0.9	23.5 ± 0.4	826 ± 10
	12.5	31.7 ± 0.5	6.1 ± 0.9	33.8 ± 0.2	847 ± 3
	15	32.0 ± 1.4	5.6 ± 1.8	30.6 ± 0.3	844 ± 9
	17.5	33.4 ± 0.8	5.9 ± 1.1	34.2 ± 0.5	825 ± 15
	20	33.6 ± 1.5	8.8 ± 1.6	31.9 ± 0.6	834 ± 10
Oats cv. Borowiak	10	22.1± 1.1	0.4 ± 1.4	28.4 ± 0.4	646 ± 9
	12.5	22.4 ± 0.9	1.1 ± 1.3	28.7 ± 1.0	647 ± 3
	15	24.0 ± 0.5	2.2 ± 0.6	31.3 ± 0.5	656 ± 8
	17.5	23.9 ± 1.0	4.0 ± 1.1	32.8 ± 0.5	704 ± 10
	20	26.4 ± 1.7	6.5 ± 2.0	34.7 ± 0.4	698 ± 7
Triticale cv. Fidelio	10	23.6 ± 0.7	5.7 ± 1.0	29.9 ± 0.4	711 ± 2
	12.5	23.0 ± 1.2	9.4 ± 1.6	28.4 ± 0.2	744 ± 11
	15	25.3 ± 1.1	12.1 ± 1.3	30.5 ± 0.1	739 ± 11
	17.5	28.8 ± 1.2	10.7 ± 1.5	35.4 ± 0.2	774 ± 10
	20	28.4 ± 1.2	11.1 ± 1.8	38.3 ± 0.2	781 ± 3

Coetzee (2009) modeled corn grains in DEM using true-scale practices. The shape and aspect ratio of corn grains were approximated in DEM using clumps, or clusters, of particles. Experimental direct shear tests showed that dry corn has an internal friction angle of approximately 23 degrees. Coetzee also showed that under typical specimen preparation methods, there was no significant difference between peak and critical state internal friction angles. Two dimensional direct shear simulations were used to calibrate the sliding coefficient of friction. Coetzee went further to define particle stiffness using confined compression tests, but found the hysteretic features of compression were not possible to reproduce using their DEM methodology.

CHAPTER 2. METHODS

The work described in this section focuses on setting up a triaxial test in the DEM environment. Existing methods are reviewed for generating dense particle samples and develop a new particle generation algorithm. To control the stress state of a specimen, a stress-controlled membrane was developed. Results from a parameter study on the stability of the stress-controlled membrane are shown. The results of some small studies to examine the effects of viscous damping on sample stability are also presented. Next, a walk through is described of initial state development of a virtual triaxial test specimen beginning with dissipating energy at initialization to dynamically and statically equilibrating a sample. The discussion on initial state is completed by presenting a cap adjustment method by which sample becomes isotropically stressed. The calculations associated with post processing are shared which describe source code modifications for the LIGGGHTS software. Physical testing is also described for validation of DEM calibration in the context of grain hopper discharge, blade mixing, and cone penetrometer testing.

DEM Contact Laws

Discrete element method (DEM) is a numerical technique where particle interactions are modeled using equations of motion and contact laws for force and overlap relationships. Cundall and Strack (1979) developed DEM to simulate the behavior of granular materials. Equations of motion for each particle are shown in equations 2.1 and 2.2. The resultant force on a particle, $F_{resultant}$, is calculated in equation 2.1

$$F_{resultant} = m\ddot{x} \tag{2.1}$$

where

m = particle mass and

$\ddot{x}$ = particle acceleration.

The resultant moment on a particle, $M_{resultant}$, is calculated by equation 2.2

$$M_{resultant} = I\ddot{\theta} \tag{2.2}$$

where

I = mass moment of particle inertia and

$\ddot{\theta}$ = angular particle acceleration.

$F_{resultant}$ and $M_{resultant}$ account for body forces, force fields, and interparticle interactions. DEM codes, such as the open-source LIGGGHTS (2015), use idealized elastic spheres to model contacts between particles that interact with each other according to Hookean or Hertzian contact laws. In addition, forces that depend on contact such as micro-scale cohesion, restitution (damping), sliding friction, and rolling friction, can also act on particles. This section details the forces that arise from various forms of particle interaction.

Contact stiffness

The simplified Hertzian contact formulation (as used in Chen and Hung, 1991) is the relationship between contact force and normal approach between two spheres and is shown in equation 2.3.

$$F_n = k_n\delta_n \tag{2.3}$$

The stiffness, k_n, is a function of normal displacement and elasticity parameters.

$$k_n = \frac{2G_{eff}\sqrt{2R_e}}{3(1-\nu_e)}\delta_n;$$

$$R_e = \frac{2R_1R_2}{R_1+R_2};$$

$$G_{eff} = \frac{2(2-\nu_1)(1+\nu_1)}{E_1} + \frac{2(2-\nu_2)(1+\nu_2)}{E_2};$$

$$\nu_e = \frac{1}{2}(\nu_1 + \nu_2);$$

R_i=Radius of i'th particle;

G_i = shear modulus of i'th particle; and

ν_i = Poisson's ratio of i'th particle.

Each DEM particle also has tangential contact stiffness (Mindlin, 1949) which creates a tangential contact force which is opposite the direction of the tangential overlap, δ_t. The tangential contact forces are calculated by equation 2.4.

$$F_t = k_t\delta_t \qquad 2.4$$

$$k_t = 8G_{eff}\sqrt{R_{eff}\delta_t} \qquad 2.5$$

DEM simulations often used the simplified Hertzian contact stiffness formulation over linear contact stiffness formulation because certain wave propagation behavior in dense granular material has been qualitatively correlated (Wensrich and Stratton, 2011).

Friction

When contact between DEM particles is established, contact-dependent interparticle forces, such as friction forces, can be activated. Force due to sliding friction between two particles exhibiting relative tangential motion is calculated by equation 2.6

$$F_s \leq \mu_s F_c \, sign(v_{\mathrm{rel,tan}}) for \; v_{\mathrm{rel,tan}} \neq 0 \tag{2.6}$$

where

μ_s = sliding friction coefficient,

F_c = normal contact force, and

$v_{\mathrm{rel,tan}}$ = relative tangential velocity between two particles at point of contact.

Per the usual convention, the orientation of the direction vector of $F_{sliding}$ is opposite the tangential relative velocity vector. In addition to sliding friction, rolling friction is present as a contact-dependent force. Rolling friction is a particle’s resistance to relative rolling motion between particles as a function of normal contact forces (F_c) and shear stiffness. Two rolling friction models are built into LIGGGHTS: the Constant Directional Torque (CDT) model and the Elasto-Plastic Spring Dashpot (EPSD) model. The CDT model adds torque to a particle by equations 2.7, 2.8, and 2.9.

$$T_{CDT} = \frac{\mu_R F_c \omega_{shear} R_{eff}}{|\omega_{shear}|} \tag{2.7}$$

$$\omega_r = \omega_1 - \omega_2 \tag{2.8}$$

$$\omega_{\mathrm{shear}} = proj_{shear\ contact\ plane}(\omega_r) \tag{2.9}$$

where

ω_1 = angular velocity of particle 1,

ω_2 = angular velocity of particle 2,

R_{eff} = effective radius of two particles in contact, where $\frac{1}{R_{eff}} = \frac{1}{R_1} + \frac{1}{R_2}$,

R_1, R_2 = radii of particle 1 and 2 respectively,

F_c = normal force acting between particles in contact, and

μ_R = rolling friction coefficient.

The rotational resistance in the CDT model can exceed the moment required to fully mobilize a particle and therefore, it can create an oscillatory equilibrium state. On the other hand, rotational resistance in the EPSD model was bounded by full mobilization torque. The torque contribution from the EPSD model is described in equations 2.10-2.14. Note that since equation 2.9 limits resistance torque, the rolling resistance behavior was perfectly plastic above full mobilization torque.

$$T_{EPSD,t+\Delta t} = T_{r,t} + \Delta T_r \tag{2.10}$$

$$|T_{r,t+\Delta t}| \leq T_{r-max} \tag{2.11}$$

$$T_{r-max} = \mu_r R_{eff} F_c \tag{2.12}$$

$$\Delta T_r = -k_r \Delta\theta_r \tag{2.13}$$

$$k_r = k_t R_{eff}^2 \tag{2.14}$$

where

$T_{EPSD,t+\Delta t}$ = torque contribution in next DEM calculation cycle,

$T_{r,t}$ = torque contribution in previous DEM calculation cycle,

k_r = radial particle stiffness,

k_t = tangential particle stiffness, and

$\Delta\theta_r$ = incremental relative rotation between particles.

The CDT and EPSD rolling friction models have been compared by Ai et al. (2011) who reported that the EPSD model is superior to the CDT model in terms of achieving low-kinetic energy steady state conditions for pseudo-static DEM analyses.

Cohesion

Cohesion or adhesion models introduce an attractive force between particles that is often proportional to particle size, contact overlap, contact area, and contact pressure. Cohesion models are frequently constructed using the mathematical underpinning of liquid bridge formation between two particles. Many liquid bridging models have been described in literature (Mason and Clark, 1965; Hotta et al., 1974; Rabinovich, 2005; Washino et al., 2013) and have been implemented in DEM code (Washino et al., 2013; Nguyen et al., 2014). The influence of various liquid bridging adhesion models have been quantified and compared in dense assemblies (Souli et al., 2006), flow conditions (Tsunazawa et al., 2016) and fluidized beds (Gu et al., 2016).

The JKR model was ubiquitous in commercial and open source DEM software, though it has numerous limitations. The attractive force in the JKR model was calculated by equation 2.15.

$$F_{JKR} = \frac{4E_{eff}}{3R_{eff}}a^3 - \sqrt{16\pi E_{eff}a^3} \qquad 2.15$$

where $\frac{1}{E_{eff}} = \frac{1-\nu_1^2}{E_1} + \frac{1-\nu_2^2}{E_2}$;

$\frac{1}{R_{eff}} = \frac{1}{R_1} + \frac{1}{R_2}$;

ν_n = poisons ratio of the n'th particle;

a = cohesion energy density.

F_{JKR} only acts to bring particles closer together; it can never be a repulsive force. The JKR cohesion model is an effective modeling technique for elastic particles with large surface energy. In Chapter 4, the JKR model was shown to be phenomenologically poor when performing mesoscale modeling of soils.

The projected-area cohesion model was developed to resolve the shortcomings of the JKR model. The Mohr-Coulomb failure intercept, on which traditional soil mechanics characterizes cohesion, is a continuum concept. The projected area cohesion model attempted to pass the continuum assumption down to the particle level by considering a cubic envelope which enclosed each spherical DEM particle. Thus, for simple cubic lattice packing in monodisperse assemblies with average coordination number of 6, void space outside the project cubes was reduced to zero. The area of the faces of each cube was proportional to the attractive force by the cohesion coefficient. The continuum assumption was supported in cases where coordination number = 6. However, in the case of very tightly packed DEM assemblies with low stiffness, the total attractive forces will likely exhibit significant increases as void ratio decreases.

Contact damping

Energy can be lost when DEM particles collide with one another. Contact damping is a modeling technique which estimated viscous losses during collisions. The ratio of kinetic energy before vs. after a collision is called the coefficient of restitution, *e*. The normal and tangential components of contact losses are calculated separately. The normal component of contact damping force is calculated by equations 2.16-2.21.

$$F_{\text{normal contact damping}} = -\gamma_n v_{\text{n-ij}} \tag{2.16}$$

$$\gamma_n = -2\sqrt{\frac{5}{6}}\,\beta\sqrt{S_n m_{eff}} \geq 0 \tag{2.17}$$

$$S_n = 2\,E_{eff}\sqrt{R_{eff}\delta_n} \tag{2.18}$$

$$\beta = \frac{\ln(e)}{\sqrt{\ln^2(e)+\pi^2}} \tag{2.19}$$

$$\frac{1}{E_{eff}} = \frac{1-\nu_1^2}{E_1} + \frac{1-\nu_2^2}{E_2} \tag{2.20}$$

$$\frac{1}{m_{eff}} = \frac{1}{m_1} + \frac{1}{m_2} \tag{2.21}$$

The tangential contact damping forces are calculated by equations 2.22-2.24.

$$F_{\text{tangential contact damping}} = -\gamma_t v_{\text{t-ij}} \tag{2.22}$$

$$\gamma_t = -2\sqrt{\frac{5}{6}}\,\beta\sqrt{S_t m_{eff}} \geq 0 \tag{2.23}$$

$$S_t = 2\,G_{eff}\sqrt{R_{eff}\delta_n} \tag{2.24}$$

Contact damping forces act in the direction opposite to the relative velocity between particles in contact.

Timestep

DEM codes, such as LIGGGHTS, use explicit central difference algorithms to update the positions and velocities of particles over small timesteps. The explicit algorithms are stable only if error is bounded and system energy is conserved. The stability of a simulation is highly dependent on the magnitude of the timestep. Theoretical minimum timesteps have been developed for a variety of particle contact formulation types. These minimum timesteps are called *critical timesteps.* For elastic spheres using the Hertzian contact formulation, the critical timestep was established by Sheng et al. (2004), see equation 2.25.

$$\Delta t_{crit} = \frac{\pi R_{min}}{\alpha_e}\sqrt{\rho/G} \tag{2.25}$$

Where R_{min} = minimum particle radius

ρ = particle density

G = shear modulus

and α_e is given by the roots of equation 2.26

$$(2-\alpha_e^2)^4 = 16(1-\alpha_e)\left[1-\frac{1-2\nu}{2(1-\nu)}\ \alpha_e^2\right] \tag{2.26}$$

An approximation of α_e is given in equation 2.27.

$$\alpha_e = 0.1631\nu + 0.876605 \tag{2.27}$$

By equation 2.25, particle size, density, and stiffness all affect the magnitude of the critical timestep.

Another limitation on the maximum timestep is the time necessary to detect particle's neighbors during DEM simulation. It is desired that a particle only directly affect its immediate neighbors over a single timestep. It is also desired that excessive interparticle overlap be avoided in any single timestep. The LIGGGHTS 3.0 manual (2015) indicated that each particle had a zone of neighbor detection around it. This zone was called the *skin*. By default, the skin was 1 mm thick. Therefore, it was desired that particle motion be limited by the thickness of the skin. As an example, in a triaxial test simulation, particle displacements were greatest at large strains (i.e. during constant volume expansion after critical state has been reached). If the simulated lid were compressing the triaxial test sample at 0.010 m/s, it could be assumed that some particles were moving at a rate of just under 0.015 m/s (due to constant volume expansion). This resulted in a maximum timestep of 0.067 seconds. Indeed, this was a very large timestep when compared to the Hertz elastc sphere timestep establish by Sheng et al. (2004).

Thornton and Antony (2000) presented a strategy for increasing the timestep of the DEM simulation under quasi-static conditions. The strategy was to increase particle density until the minimum contact timestep and the Rayleigh wave timestep were the same. Thornton and Antony (2000) reported that density scaled up by a factor of 10^{12} had negligible effects on the results of a quasi-static direct shear test. Particle density was shown to have small effects on triaxial test results using ellipsoidal particles as well (Ng, 2006), though density was only scaled up by a factor of 100. It should be noted that neither Ng (2006) nor Thornton and Antony (2000) had active body forces in their simulations. It was necessary that gravity was turned off in order to keep the effects of density negligible. O'Sullivan (2011) indicated that the use of density-scaling should be approached with caution and that its validity was questionable. For this reason, new density scaling test were performed to find out how much to increase density by before results become significantly affected. The details of a density scaling study are found in Chapter 5.

Development of DEM Simulations

The technical details of DEM simulations used to model geomechanical behavior have been documented in the literature. Studies have investigated boundary conditions, initial conditions, particle interactions, sample composition, and environmental conditions.

Boundary conditions

A number of studies utilized typical periodic boundaries in unsuccessful attempts to model axisymmetry when simulating triaxial tests (Powrie et al., 2005; Roux, 2005; Sitharam et al., 2005). These boundary conditions were non-physical. Better models were developed for quarter axisymmetric simulations (Cui and O'Sullivan, 2005). Similarly, several papers reported 2D simulations to qualitatively assess parameter sensitivities and correlations (Calvetti and Nova, 2005; Kruyt and Rothenburg, 2005; Vu-Quoc et al., 2001). Lu and Frost (2010) concluded that 3D triaxial simulations were, overall, better than 2D simulations when to simulating triaxial behavior. Regarding the modelization of the latex membrane that house the soil sample in a triaxial test, stress controlled boundaries were developed (Cui et al., 2007) and have been shown to provide significantly different peak and post peak soil behavior than servo-controlled walls (Cheung and O'Sullivan, 2008). Cheung and O’Sullivan (2008) also showed that the local responses vary with respect to boundary condition type, specifically the location of shear banding and central bulging of triaxial test specimens.

There was a divergence in the literature on the topic of servo controlled versus flexible membrane boundary conditions. One frequently cited paper, Utili and Nova (2008), used the servo-controlled membrane approach to simulate confining stress. Despite the work by Cheung and O’Sullivan (2008) that showed the non-physicality of rigid servo-controlled membranes, many subsequent papers still used the servo-controlled approach (e.g., Gong et al., 2011; Kozicki et al., 2012; Sayeed et al., 2014; Salot et al., 2009). Another type of membrane boundary is that which is seen in the simulation of undrained triaxial tests. Undrained triaxial tests have been simulated under constant volume conditions (Gong et al., 2012). The membrane formulations are servo-controlled, but algorithms that monitor the volume of the sample enforced constant volume conditions.

Sample generation

Sullivan (2011b) reported that two methods for generating samples, dynamic pluviation and algorithmically generated samples, were capable of modeling response behaviors of granular geomaterials. Pluviation methods had the advantage of requiring very little supervision. Samples were pluviated into a container under the acceleration of gravity until they reached a dense state. There were two drawbacks of this method. First, the final size of the pluviated sample was unknown. Therefore, without a priori knowledge of the sample density and size, several attempts to pluviate a sample was required. The second drawback was that pluviation required several DEM calculation cycles, which added significant computation time to the analysis. O’Sullivan (2011b) mentioned that preparing a sample by dynamic methods took at least as long as it took to simulate a triaxial test. Because Bernhardt and O’Sullivan (2012) and Ng (2004) reasoned that pluviation is the simpler option, pluviation of particles to build samples was attempted. The pluviation attempts were successful, but they took too long to produce dense, high quality samples. Pluviation was relegated to serve as a backup plan and work on algorithmic generation of samples began.

Algorithmic, or constructional, sample generation has been seen in the literature in many forms (Jiang et al., 2003; Scheibel, 1983; Ferellec, 2008). In 3D, however, it was limited to just a few methods. Ferrez (2001) showed a particle insertion method where dense virtual samples were achieved by randomly attempting to insert non-contacting particles, the largest ones first, followed by successively smaller particles, until a sample was dense enough for geomechanical simulation. Another method was the triangulation approach used by Cui and O’Sullivan (2003) where a volume is converted to a tetrahedral mesh. The vertices and edges of each tetrahedral element served as boundary conditions for the insertion of spherical particles. These two methods were good, but both insert non-contacting particles that had to be scaled up by radial expansion to achieve proper initial stress states. The 2D advancing front method developed by Feng et al. (2003) was an algorithm where a seed particle was cloned along random vectors from the seed particle's centroid. Critics of the advancing front method showed that excessive void space was usually present at the boundaries of a sample (Bagi, 2005). Bagi (2005) proposed a method that populated the boundaries with non-random particles and works inward which generally solved the problem in 2D.

Feng et al. (2003) and Bagi (2005) have only implemented their methods in 2D. Preliminary work in sample generation included developing a theoretical 3D extension of work presented by Feng et al. (2003), extending the Feng et al. method further to include aspherical particles, and implementing it in efficient code. The following sections present my preliminary work that contributed to sample generation.

There are three distinct steps in the constructional algorithm. The first is establishing the desired initial parameters such as particle properties, prescribed particle overlap (based on mean stress), boundary conditions, desired coordination numbers, and sample angularity. The second step, construction, involves inserting particles with the goal of satisfying the desired coordination numbers and aspherical requirements. The geometrical scheme behind the construction step is defined in the section on constructional theory. The third step is a quality control step. Coordination numbers of particles are tracked during particle insertion. If a coordination number falls far short of the desired coordination number, a flag is thrown and the offending particle and neighbors are deleted and re-generated.

It was observed that samples could be generated at certain coordination numbers, but when samples are equilibrated, the applied mean stress will determine the true coordination number at the beginning of a triaxial test simulation. Sayeed et al. (2012) documented the effect of mean stress on average coordination number and invited the reader to notice how initial coordination numbers increase with increasing confining pressures. As a result, very high coordination numbers were not a goal during sample generation. The important point was to bring a sample to equilibrium under the correct confining pressure *and* with clearly defined coordination numbers.

Constructional algorithm

A constructional algorithm was developed to address the limitations of Bagi (2005) and Feng et al (2003). The constructional algorithm operates by taking advantage of closed form analytical geometry. Trigonometric relations, vector operations, and rotation matrices constitute the bulk of the manipulations. A step-by-step particle generation attempt is outlined in this section. The steps for particle generation follow.

1. Detect neighbor particles around the seed, or parent, particle. A random neighboring particle is selected to serve as the neighbor. The separation distance, d, between the parent and the neighbor is calculated in equation 2.28.

$$d = (x_0 - x_1)^2 + (y_0 - y_1)^2 + (z_0 - z_1)^2 \qquad 2.28$$

where x_0,y_0,z_0 = parent particle coordinates;

x_1,y_1,z_1 = neighbor particle coordinates; and

d = distance between particles.

2. Construct the vector between the parent and neighbor particles. Dividing by the magnitude of the vector gives us the unit vector between particles. This unit vector is called PN.

$$\overrightarrow{PN} = \frac{(x_0 - x_1)}{d}\hat{\imath} + \frac{(y_0 - y_1)}{d}\hat{k} + \frac{(z_0 - z_1)}{d}\hat{k} \qquad 2.29$$

3. Calculate the distance of new particle from parent in the direction of PN based on aspherical parameter (or lack thereof). Call this point I. If the new particle is not part of an aspherical aggregate, the magnitude of travel on the PN vector from P is shown in equation 2.30.

$$addition_{onPN} = d/2 \qquad 2.30$$

4. Calculate the magnitude of the vector between point I and the new particle center, C. Even though it does not exist yet, the orientation of the new particle does not need to be known *a priori*.

$$\left\|\overrightarrow{IC}\right\| = \sqrt{D_e^2 - d^2} \qquad 2.31$$

If the new particle is part of an aspherical aggregate, the aggregate separation, A_s, of the particle will need to be calculated. As in the spherical case, the magnitude of the vector between I and C needs to be known (equation 2.32).

$$\left\|\overrightarrow{\mathrm{IC}}\right\| = \mathrm{A_s}\sin(\alpha) \tag{2.32}$$

where

$$\alpha = \arcsin(D_e \sin\left(\frac{\gamma}{d}\right)) \tag{2.33}$$

and

$$\gamma = \arccos(\frac{d^2 - A_s^2 - D_e^2}{-2A_sD_e}) \tag{2.34}$$

The magnitude of travel on the PN vector can be calculated for aspherical aggregates using equation 2.35.

$$addition_{onPN} = \sqrt{A_s^2 - \left\|\overrightarrow{IC}\right\|^2} \tag{2.35}$$

5. Point I, which lies on the vector between P and N, now has the coordinates shown in equation 2.36.

   $$I = X_0 + (\overrightarrow{PU})(addition_{onPN}) \tag{2.36}$$

   where X_0 is an array which contains the coordinates of point P.

6. Use point I to generate a vector orthogonal to PN at a random orientation. Since orthogonality is established when the dot product of two vector equals zero, it is possible to algebraically deduce the orthogonal vector orientation. The unit vector PN is known, and a new unit vector, IC, needs to be orthogonal to PN. If two components of IC are randomly generated, the third can be deduced from equations 2.37 and 2.38,

   $$\overrightarrow{PN} \cdot \overrightarrow{IC} = 0 \tag{2.37}$$

   $$\overrightarrow{IC} = (random * \hat{\imath}) + (random * \hat{\jmath}) + z\hat{\jmath} \tag{2.38}$$

   where ‘random’ is a unique random number between -1 and 1, and z is unknown. Each instance of ‘random’ is a different random number. The third component, *z*, in equation 3.38 can be algebraically solved.

7. $\overrightarrow{IC}$ is not yet a unit vector. Each component of $\overrightarrow{IC}$ needs to be divided by the magnitude of $\overrightarrow{IC}$, which was calculated in equation 2.31 or 2.32 depending on aspherocity.

8. This new unit vector is used with the magnitude of $\overrightarrow{IC}$ to establish coordinates for point C.

$$C = I + \overrightarrow{IC} * \left\|\overrightarrow{IC}\right\| \qquad 2.39$$

When point C is generated, a sphere the size of a new particle is projected.

This sphere is checked for interference against neighbor particles. If there is no interference, it is necessary to revisit equation 2.39 to generate a new random vector. This counter-intuitive step exists because positive interference ensures that an initial coordination number of 3 is achieved. The next step clocks the orientation of the random vector until interference is no more. To reiterate, the calculation is working backwards from a condition of interference to marginal contact of neighboring particles. The particle travel steps of the clocking procedure are equal to half of the allowable overlap between to particles. This way, a successfully generated particle will always be in favorable contact with 3 other particles, the parent, the neighbor, and another near field random neighbor. It has been found that the random vectors that project spheres into non-interfering spaces work to generate particles most of the time (5 out of 6 times), but when there is very little void space left around a parent, (i.e., only space enough for one particle to squeeze in) the random generation of vectors nearly always discovers interference, thereby failing to create an optimally dense packing.

9. Perform the clocking operation by dotting the random vector $\overrightarrow{IC}$ against the rotation vector, R, which is shown in equation 2.40.

$$R = \begin{bmatrix} \big(a(v^2+w^2) - u(bv+cw-ux-vy-wz)\big)(1-\cos(\theta) + x\cos(\theta) + (-cv+bw-wy+vz)\sin(\theta)) \\ \big(b(u^2+w^2) - v(au+cw-ux-vy-wz)\big)(1-\cos(\theta) + y\cos(\theta) + (cu-aw+wy-uz)\sin(\theta)) \\ \big(c(u^2+v^2) - w(au+bv-ux-vy-wz)\big)(1-\cos(\theta) + z\cos(\theta) + (-bu+av-vx+uy)\sin(\theta)) \end{bmatrix} \qquad 2.40$$

where {a b c} = coordinates of point I.

{u v w} = components of the unit vector $\overrightarrow{IC}$.

θ = angle of rotation in radians.

Iterating step nine until the interference between the sphere C and its neighbors is below the allowable particle overlap creates three contacting neighbors, each with a coordination number of two.

Successive loops through the entire algorithm will create new particles with at least two contacts. The speed and quality of the algorithm is highly dependent on the magnitude of allowable particle overlap. Recall from step 9, above, that the rotation matrix is applied to the vector $\overrightarrow{IC}$ in increments which are equal to half the allowable particle overlap. As the allowable particle overlap increases, achievable coordination numbers also increase. In addition, the number of rotation operations is reduced, thereby increasing the speed of the algorithm. Excessive particle overlap can result in a fast algorithm that produces unrealistic coordination numbers (7-8+) while very low particle overlap can result in a slow algorithm that produces very low coordination numbers (~4). The Hertzian solution to the normal approach of two particles in contact can serve as a basis for determining allowable particle overlap.

Particle overlap

A sample of particles subject to confining pressure will exhibit some appreciable local deformation at their contact interfaces. It is important to capture the magnitude of this deformation so that neighbor particles may be initialized with slight overlaps. Intentional overlaps give algorithms a lot of freedom to achieve desired coordination numbers. In addition, after particle generation is complete and the confined sample is brought to equilibrium using DEM calculation cycles, these cycles can be kept to a minimum if initial overlap is correctly predicted. Individual particle overlaps are difficult to prescribe before a sample is generated because, since each particle ends up with its own coordination number and since particles cannot all lie on high stiffness contact chains, confining stresses may act significantly on some particles while leaving others unaffected (or less affected). While individual magnitudes of overlap on particles are difficult to predict, it is possible to calculate an average particle overlap. An average particle overlap allows us to generate the proper number of particles in a container without the need for shrinking the container or expanding the radii of the particles to make up for the inevitable particle overlap that occurs during the application of confining stresses. When bringing the sample to equilibrium is the only bit of sample preparation that a DEM code is required to do, this reduces simulation time.

A uniform average effect of confining pressure on overlap was calculated. Using the simplified Hertzian contact formulation (as used in Chen and Hung, 1991), the relationship between contact force and normal approach between two spheres is shown in equations 2.41.

$$F_n = k_n \delta_n \tag{2.41}$$

Where the stiffness, k_n, is a function of normal displacement and elasticity parameters.

$$k_n = \frac{2G_e\sqrt{2R_e}}{3(1-\nu_e)}\delta_n;$$

$$R_e = \frac{2R_aR_b}{R_a+R_b};$$

$$G_e = \frac{1}{2}(G_a + G_b);$$

$$\nu_e = \frac{1}{2}(\nu_a + \nu_b);$$

R_i=Radius of i’th particle;

G_i = shear modulus of i’th particle; and

ν_i = Poisson’s ratio of i’th particle.

Indeed, the simplified non-linear Hertzian model was used because the DEM code of choice, LIGGGHTS, also used it. The contact force, F_n, was known in order to effectively use equation 2.41. This process involved the following assumptions.

- Confining stresses created a homogeneous isotropic stress field inside the sample. Of course, this was not true, but this assumption did not interfere with the goal of populating a container with the correct number particles.
- The magnitude of force acting between particles was known.

This was where particle generation became difficult. From experience in simulating confining pressures acting on cylindrical samples, strong and weak force chains have been seen developing without any hint of predictability. Therefore, the magnitude of the contact force per particle varied wildly. Researchers (Cundall, 1987; Masson and Martinez, 2001; Cui and Sullivan, 2006; Kuhn, 1999; Zhang et al., 2008; Tordesillas and Muthuswamy, 2009) reported that weak and strong force chains develop in random, dense packings. Stronger force chains contained particles which exhibited greater inter-particle overlap than those belonging to weaker force chains. Predicting these force chains ahead of simulation time was difficult. Therefore, predicting overlap was mostly futile. This did not derail sample generation, it just compromised the elegance of the process. One thing that was known was that the minimum contact force per particle occured on the outer cylindrical layer of a triaxial test sample. The minimum contact force was known simply from the definition of stress and the magnitude of confining stress (equation 2.42).

$$F_{n\_min} = P_0 d^2 \tag{2.42}$$

where d = particle diameter

As it stands, the minimum contact force did us little good in predicting an appropriate particle overlap for generating a sample. Overlap was even considered because it was necessary to get the correct number of monodisperse particles (and aspherical aggregates) into a sample so that sample equilibration did not need to be iterated to find a reasonable sample that met geometric and density requirements. Increasing the overlap parameter was seen to increase the speed of the particle generation algorithm as well because coordination number minimums were satisfied more quickly and the void search algorithms had to work less to find vacancies for potential new neighbors. Therefore, some brute-force tactics were undertaken to prescribe an appropriate overlap. Several parameter studies were run to determine the necessary overlap to match ASTM's geometric standards for triaxial test samples. Overlap was specified, samples were generated, then samples were equilibrated, and the resulting radii of the equilibrated samples were compared to the ideal sample sizes specified in ASTM standards.

Coding strategies

There are a few mentions in the literature about how complex and challenging a 3D extension of the advancing front method (Feng et al., 2003) was to implement (Benhardt et al., 2012; O'Sullivan, 2011a). It is true that the complexity was seemingly overwhelming, but an effective coding strategy helped to logically organize large amounts of data without interfering with the flow of the algorithm. The algorithm was written in object oriented Python. Object orientation was a very powerful programming philosophy that immensely helps programmers organize and enrich data. Object orientation reduced complexity by allowing a programmer to create attributes for existing data without creating additional data structures to hold the attributes. This reduced the complexity of the code considerably.

The algorithm employed two classes, a particle class and a sample class. The particle class instantiated an object which was a physical particle that had no offending interferences with other particles and had at least three contacting neighbors. A master list of particles that is created in a main subroutine consisted of a list of particle class objects.

The sample class kept track of the physical location of each particle object. The entire sample was divided into neighborhoods based on geometrical bounds. Particles in a particular neighborhood constituted a neighborhood list. The sample class object maintained these lists. Neighborhood information was also stored within particle class objects as well. However, the neighborhood stored by the particle objects was a perceived neighborhood, which means that if a particle were to lie on or near the boundary between two neighborhoods, the particle perceived itself as part of both neighborhoods.

The neighborhood scheme may seem to be excessive organization, but for 3D samples, it was the only way that samples were generated in reasonable time periods. The most computationally expensive part of generating particles was checking particles for interference. If there was no intelligent method for picking likely neighbors to check interference against, then an algorithm must have checked interference against all particles in the sample. In 2D, this posed very few problems. However, in 3D, when more than 3,000 particles were in the coarsest triaxial test sample and more than 50,000 in the finest sample, checking against this many particles for each generation attempt simply took too long. Without the neighborhood scheme, a triaxial test sample of 18,000 particles took over 20 hours to generate on a 2 GHz Opteron processor. On the other hand, when a list of likely neighbors was only 20 particles long, interference checking was very quick. Increasing the speed of interference checking allowed engineers to initiate extra generation attempts that had low chances of producing denser particle arrangements; a failed generation attempt was no longer excessively costly. The neighborhood scheme reduced the time to produce an 18,000 particle sample from 20 hours to less than one hour on a 2 GHz Opteron processor.

The general flow of the algorithm was as follows:

1. Seed particle and first neighbor was generated. Information was added to neighborhood lists.
2. First particle in list was identified, probabilistic determination of aspherocity.
3. Attempted to generate as many non-interfering neighbors which contact 3+ particles
4. Added a new particle to appropriate neighborhood lists.
5. Checked if new particles were near a boundary, if yes, flagged them for later treatment.
6. Identified next particle in list and return to step 3.

Close scrutiny of these steps revealed that the particle list grew with every new particle added and was self-limiting because when no more void volume was available to support new neighbors, the particle list stopped growing and the algorithm exhausted itself.

The algorithm developed in the section on constructional theory was implemented such that complex volumes were populated with particles. By meshing volumes with tetrahedral elements that had edge lengths equal to particle diameter, complex geometry were represented by a point cloud of nodes. Taking concepts from Shewchuk (1996) and Devillers (2002), an algorithm was developed to determine whether or not a generated particle was inside a point cloud. Therefore, complex boundaries were approximated with precision that varied with particle size.

Stress controlled membrane development

Boundary conditions to properly model a stress controlled flexible membrane were coded into a LIGGGHTS script. The specific type of boundary selected was a pressure boundary rather than a servo-controlled displacement based boundary. The reasons for this were numerous, but the most important reason was that internal particle displacements in servo-controlled boundaries was seen to be very different than in pressure controlled boundaries (Cheung and O’Sullivan, 2008). In particular, particle rotations, and thus internal shear forces manifested differently. The pressure boundary was implemented in the LIGGGHTS input script itself. LIGGGHTS had a built-in servo-controlled membrane, but not a pure pressure membrane, so the membrane had to be algorithmically formulated and coded before the project could move forward.

The pressure membrane consisted of a loop within the input script. The loop was outlined as follows:

1. Detected the longitudinal length of the cylindrical sample.
2. Divided the sample in to ten disks of equal thickness along the longitudinal length of the sample.
3. For each disk:
    A. Detected the radius at which the outer most particle lie (R_{outer})
    B. Detected all particles that lie outside of a ring of radius R_{outer} - particle diameter.
    C. Found the average radius at which the particles (from 3b) lie
    D. Calculated a projected area based on the average radius of the particles (from 3b) and the thickness of the disk (from 2).
    E. Calculated the total force radial force to be applied to the particles from 3b based on prescribed confining pressure and the area calculated from 3d.
    F. Calculated the force per particle to be applied to the particles from 3b based on the number of particles detected in 3b.

The membrane loop was useful within the input script of LIGGGHTS because it allowed additional calculations that were useful in post processing, such as on-the-fly volume, stress, and strain calculations.

Frequency of confinement pressure updates

It was necessary to update confining pressures periodically because particles subject to confining pressure had the freedom to move deeper into the sample past the outer cylindrical boundary layer. It was desired that the pressure update interval be kept at a minimum to save computation time.

A small study was run to check the effects of membrane update intervals. The results determined what reasonable confining pressure update intervals were. Table 3 shows the design of the study, as well as the results. This study used 3 mm frictionless particles and stability was assessed at the initial confinement stages of equilibration. The sample was subject to a confining pressure of 200 kPa.

Table 3. Confining pressure update interval study

timestep [s]	# of steps	Update Interval	Stable?
2.00E-08	1.00E+04	2.00E-04	Stable
2.00E-08	2.00E+04	4.00E-04	Stable
2.00E-08	5.00E+04	1.00E-03	Stable
2.00E-08	1.00E+05	2.00E-03	Stable
2.00E-08	2.00E+05	4.00E-03	Unstable
2.00E-08	5.00E+05	1.00E-02	Unstable

The results from Table 3 indicated that the largest stable update interval is $2x10^{-3}$ s. It was possible that this interval could have been larger if the resolution of the study was finer, but $2x10^{-3}$ s was adequate to model confinement without dragging the simulation down with excessive computation time.

Damping studies

There were three considerations for selecting damping coefficients (and damping ratios) in a triaxial test simulation. The triaxial test must have been stable, the effects of damping on the mechanical response must have been negligible, and the mechanical response must have been smooth over the entire range of axial compression. These three criterion formed the limits of the useable range of damping coefficients.

The lower limit of damping was a result of the condition of stability. The critical value of damping coefficient varied with particle size, particle friction, and other particle properties which dissipate energy, however, only particle size was really significant. For 3 mm diameter frictionless particles, the critical minimum value for damping coefficient was found to be 0.12 N-s/m. Similarly, for 2 mm diameter frictionless particles, the critical minimum value for stability was found to be 0.08 N-s/m.

The criterion of negligibility was less straightforward. Since the damping coefficient had a linear relationship with velocity in its contribution to total damping forces, the velocity of sample compression was taken into consideration. The damping ratio, defined in equation 2.43, considered velocity dependent damping forces in relation to total forces due to confinement.

$$\zeta = \frac{cv}{P_0 d^2} \qquad 2.43$$

Where c = damping coefficient [N-s/m];
v = particle velocity [m/s];
P_0 = confining pressure [Pa]; and
d = particle diameter.

Equation 3.44 describes the criterion of negligibility for triaxial test simulations.

$$\zeta < 0.01 \qquad 2.44$$

The condition described in equation 19 was a conservative criterion of negligibility. It was possible that a larger damping ratio could lead to negligible damping effects, but the preliminary parameter study to define acceptable damping had a coarse resolution. If a higher damping ratio was needed for some reason, additional parameter studies would have to be performed to verify that damping effects were negligible.

The need for additional damping was dictated by the desired smoothness of mechanical response. While the strain-strain response of the triaxial test sample was usually smooth, the volume change response was subject to sudden fluctuations if damping was inadequate. These large fluctuations usually occurred after strain exceeded 2% or 3% and correlated to large reorganizations of particles in the sample. The particle reorganization was visually observable and was usually associated with significant particle rotations.

A small study was performed to assess the effects of damping coefficient and damping ratio on the mechanical response of a sample subject to triaxial compression. The purpose of this study was to establish an appropriate damping ratio that would cause negligible changes to the stress strain-response of a sample, yet maintain smooth volume change curves at large strains. Maintaining smooth volume change response was a problem, even if the triaxial compression test was numerically stable. Figure 10 shows the volumetric strain response for a stable sample with inappropriate damping.

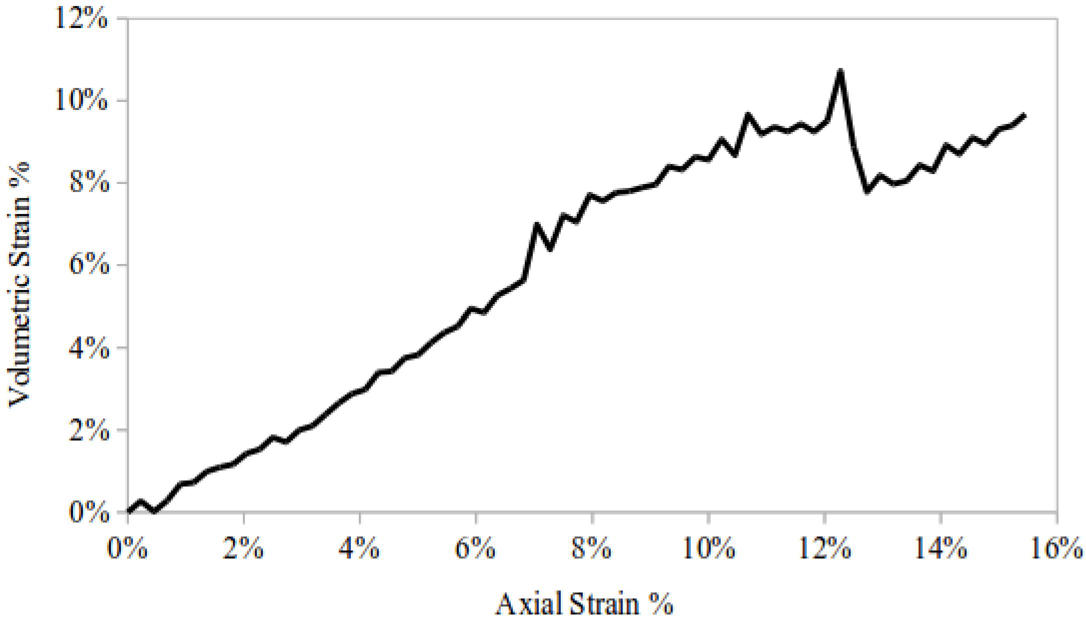

Figure 10: Non-smooth volumetric strain response of a sample subject to triaxial compression

In Figure 10, the volumetric strain curve experiences a jump at around 12% strain. This was not a behavior that was seen in physical triaxial tests, therefore, work was needed to eliminate such anomalies.

Three triaxial tests were performed. Each of the triaxial tests began with identical initial states. The particles were 3 mm in diameter. 30% of the particles were aspherical aggregates with an aspect ratio of 1.5. Interparticle sliding friction was set at 0.3; rolling friction was set at 0.5. Cohesion was set at 50 Pa. Damping coefficients and damping ratios were varied over the ranges described in Table 4.

Table 4: Variation of damping over three triaxial test simulations

Trial #	Damping Coefficient [N-s/m]	Damping Ratio
1	0.18	0.001
2	0.36	0.002
3	3.6	0.01

The mechanical responses of the triaxial tests are presented in Figure 11 and Figure 12. The stress-strain response is shown in Figure 11 and the volumetric strain response is shown in Figure 12.

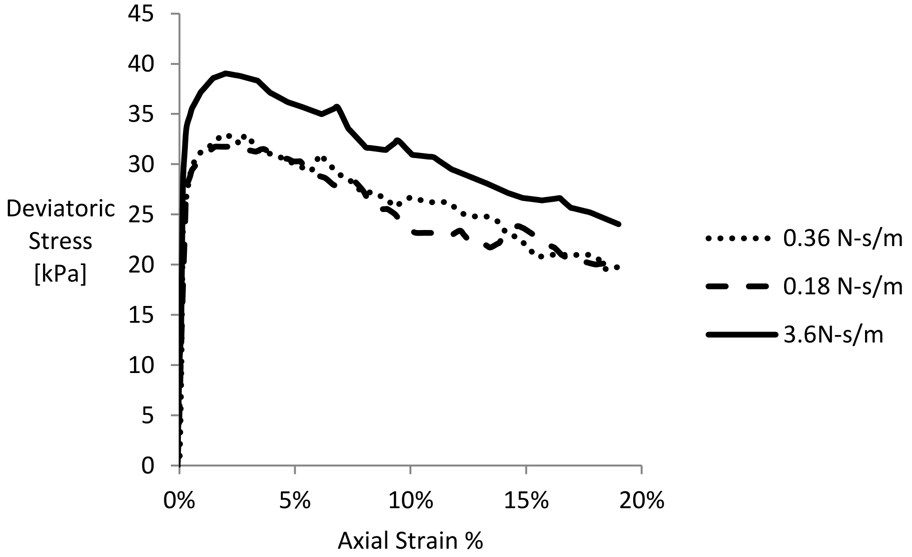

Figure 11: Stress-strain response of three triaxial tests

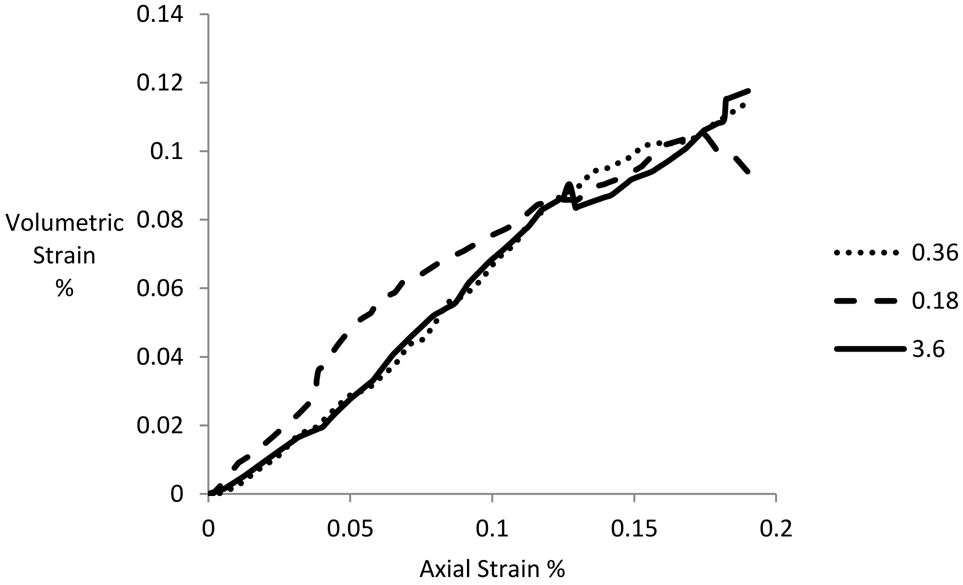

Figure 12: Volumetric strain response of three triaxial tests

From Figure 11, the stress response of the high damping condition (damping coefficient = 3.6 N-s/m) was significantly higher than the lower damping conditions. This was in agreement with the literature (Ng, 2006). The stress responses of the two low damping conditions were nearly the same.

The volume change results in Figure 12 showed interesting results. All three volumetric strain curves were in reasonably good agreement with each other. These results were different than the results obtained in Ng (2006). The disparity in results was likely due to differences in boundary formulations (Ng, 2006) used rigid boundaries that moved as deviator strain is applied). It was evident that the condition with damping set at 0.36 N-m/s produced smooth strain curves. The lower damping condition (0.18 N-s/m) produced a curve with a jump at strain=4%. The high damping condition produced a curve which is smooth until ~13% strain. A small dip occurred at 13%, which was then recovered by small jump at ~18%.

Varying damping coefficient significantly affected the stress response of the triaxial test samples, but not the volumetric response. The most interesting result in this study was that varying the damping coefficient from 0.18 N-m/s to 0.36 N-s/m did not significantly affect the stress response. This was significant because the 0.36 N-s/m condition produced a smooth volume change curve while the 0.18 N-s/m condition did not. This meant that increasing the damping coefficient from 0.18 N-s/m to 0.36 N-s/m increased the smoothness of the volume strain curve without significantly affecting the global mechanical response of the sample.

From the preliminary studies, damping ratio significantly affected the stress-strain response of a specimen, while absolute damping coefficient had a significant effect on stability and smoothness of volume change.

Initial state and equilibration

The initial state of a triaxial test sample was just as important in virtual environments as it was in physical environments. Just as in physical tests, samples were carefully prepared and then subjected to confining pressure for significant amounts of time in order to achieve equilibrium. Virtual tests underwent similar equilibration periods.

The steps involved in setting up a virtual triaxial test follow; significant steps in the process (marked with a *) are discussed in more detail.

1. Defined the radius and height of the cylinder of the triaxial test specimen.
2. Generated particles inside container volume.
    a. Several simulation variables were set during the generation process.
        i. Particle size
    b. Particle density
    c. Particle angularity parameters
    d. Percent of sample that is aspherical
    e. Aspect ratio of aspherical particles
    f. Particle overlap
        i. This should be set so that enough particles can be generated in the container volume.
        ii. Dependent on particle Young's modulus.
3. Began dissipative equilibration. Using container boundaries as simulation boundary conditions, allowed the sample to equilibrate for a short period of time (0.32 physical seconds).*
    a. Damping coefficient during this time was very high (250 N-s/m)
    b. Anchored the specimen at the end of the dissipative equilibration step.*
4. Began dynamic equilibration. Remove circumferential boundary and apply confining pressure and vibratory excitation. Run DEM calculations for a short time to increase coordination number and reduce sample volume.*
    a. Damping was still very high (250 N-s/m).
    b. Particle coefficient of friction was very low (0.01).
5. Gradually reduced damping until damping coefficient satisfied criteria of negligibility.
    a. Negligibility criteria: $F_{damping} / F_{contact} = 10^{-2}$.
    b. Ran DEM calculations until total vibratory excitation time equaled 0.2 seconds of physical time.

6. Began static equilibration. Turned off vibratory excitation. Reduced damping to optimum value.*
    a. Confining pressure was still active.
    b. Ran DEM calculations for an additional 0.2 physical seconds.
7. Adjusted cap height to zero out the deviator stress.*
    a. Established acceptable limits, $\sigma_d = 0.05P_0$.
    b. Cap adjustment did not incur more than 0.1% axial strain.
    c. Sample did not incur a single cycle of strain hysteresis.
    d. This was only performed if necessary (majority of samples have no need for this).
8. Checked sample average coordination number and volume.
    a. If inadequate, discarded sample and start over.
9. Adjusted particle properties to reflect desired triaxial test values.
    a. Adjusted parameters:
        i. Sliding friction
        ii. Rolling friction
        iii. Viscous damping
        iv. Restitution
        v. Cohesion
10. Initiated triaxial compression by displacing the upper cap.

Dissipative equilibration

All of the energy poured into constructing proper initial specimens would have been for naught if sample equilibration was not standardized. There was surprisingly little literature that addresses equilibration. When initializing particles with overlap, there was high potential energy in the initial system. Care was taken to gradually dissipate the high potential energy while maintaining the shape and volume of the specimen. A method to dissipate potential energy that was computationally inexpensive was developed.

Because the sample was most volatile at the beginning of equilibration, the first step was to prevent large volume change while dissipating potential energy. The outer layer of the sample was detected and was fixed in space while DEM cycles ensue. Significant damping was applied during this phase to prevent particle inertia from excessively altering the contact state of the particles. The fixed particles formed a shell around the remaining particles so that the global geometry of the sample did not change. The shell can be seen in Figure 13. The blue particles were frozen and the red ones were free to reorient themselves to minimize potential energy.

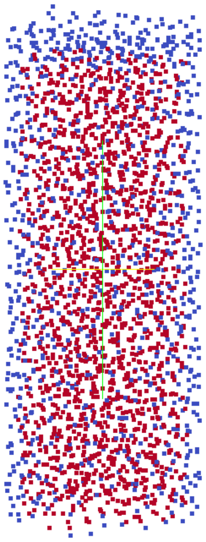

Figure 13: Triaxial test sample, blue particles are fixed, red particles are free

Alternatively, a rigid container was inserted around the sample. Both approaches worked equally well under most conditions. However, if particle overlap was very high and the force per particle generated at the initialization of the sample exceeded that which is required to compress a particle greater than a distance of [1 x particle radius], then particles escaped the sample using the rigid container method. The rigid container method was more computationally efficient, so it was employed as long as Young's modulus was high (greater than 10^8 Pa) and confining pressure is moderate (1.1 MPa or less).

Regardless of the method, kinetic energy increased rapidly at the beginning of this process. As particles found new minima, kinetic energy gradually tapered down until the system comes to rest. The next step of equilibration was to remove the constraints from the outer layer of particles. At this point, considerable energy was removed from the system, but significant damping was still required to maintain the geometry and volume of the sample. As the constraints were removed from the outer particles, they were replaced by confining pressures. The confining pressures were applied as a step input (no ramping). This produced a transient response to the confining pressure. The high damping served to quell any particle oscillations and inertial effects that the step input of confining pressure produced.

Anchor the Specimen

From earlier discussions, the instability of the sample was established as a continuous threat to the successful DEM simulation of a triaxial test. A boundary condition was proposed that could potentially anchor the triaxial test sample while still allowing free deformation and shear band formation. From the literature, it was seen that boundary conditions alter the triaxial test response significantly. For instance, membrane formulations (servo-controlled vs. pressure boundaries) have been shown to influence the locality of shear band development (Cheung and O'Sullivan, 2008). For this reason, the selection of an anchoring boundary condition was insightful such that sample deformation behavior was not impeded or distorted. It was proposed that the top and bottom caps had very high friction which would prevent the sample from exhibiting radial movement. The sample did not *need* to be anchored, but it was possible to use smaller damping coefficients if the anchor was present. Smaller damping was desired because larger cap velocities could be used while maintaining a constant damping ratio, and thereby decreasing the simulation time.

Commonly, other 3D triaxial test simulations in DEM used axi-symmetrical or similar boundary conditions which help stabilize models. In other cases, some studies simulated significant friction on the top and bottom boundaries of the simulation to enhance stability. Indeed, these methods enhanced stability, but the symmetric boundary conditions had unique setbacks. The axi-symmetric boundary conditions required non-physical assumptions of soil movement in a triaxial test such as limited radial shear banding. In addition, the axi-symmetric boundaries guided material flow. For this reason, axisymmetry was not used. The frictional caps were much more reasonable.

Dynamic equilibration

The triaxial test sample preparation process involved three regimes of equilibration, dissipative, dynamic, and static regimes. The dynamic regime had the sole purpose of increasing the average coordination number of the sample.

The dynamic regime of equilibration involved vibrating a seed particle in a confined sample while altering viscous damping to achieve acceptable coordination numbers. The damping was initially set high at 250 N-s/m (same as in the dissipative regime). Subsequent DEM calculations were ran to begin raising the coordination number while further dissipating energy. When the sample found a minimum volume at a particular damping level, particle damping was lowered. At low damping, confining pressure slowly squeezed the sample into a slightly more slender cylinder. The total number of particles in the sample determined the limits of the squeezing. Eventually, after several DEM cycles, the sample found a new minimum. Keep in mind, at this point, the damping was not yet at a desired simulation value. It was lower than its initial value (250 N-s/m), but higher than its eventual simulation value (~0.5 N-m/s). When the new minimum potential was achieved, the sample compression began. Very soon after the compression of the sample began and the transient response of the sample to the step velocity change of the compression cap was attenuated, the damping was lowered to the desired simulation value. Bringing the sample to equilibrium not only requires the sample was brought to a minimum potential energy state, but also to minimize kinetic energy in the presence of constant cap velocity. Choosing an arbitrary kinetic energy to end equilibration on was not ideal. It was observed that kinetic energy was very low, then spiked during sudden shifts in contact arrangement between particles. It was better to monitor the volume of the sample during equilibration. As the sample volume approached an asymptote, average coordination number did as well. Thus, when volume change, dV/dt, approached zero, a maximum coordination number was achieved. The maximum coordination numbers varied based on confining pressure, damping coefficient, Young's modulus, etc, and they did not exactly coincide with the coordination numbers produced by the particle generation algorithm (due to the assumptions that the overlap calculation had to make).

Initiating sample compression with particle damping at higher than simulation values is worth discussing here. The literature indicated that damping had a significant effect on triaxial response behavior of a sample (Ng, 2006), particularly on the peak force and large strains portions of the stress-strain curve. However, it was seen from Ng's (2006) results that at very small strains, the effect of varying damping was negligible. From preliminary studies, it was found that the sample was very unstable at the instant of the velocity stepped onto the cap. It was necessary that damping be temporarily held at a slightly higher value until the transient inertial effects of stepping the cap velocity were attenuated. If the desired simulation damping was moderate (damping/contact ratio = .001), then the necessity of holding higher damping during equilibriation was questionable. However, at near zero damping, the sample was unstable.

An example of sample equilibration is shown in Figure 14. The sample was subject to confining pressures of 200 kPa and a viscous damping coefficient of 0.18 (which corresponded to a damping ratio of 0.001).

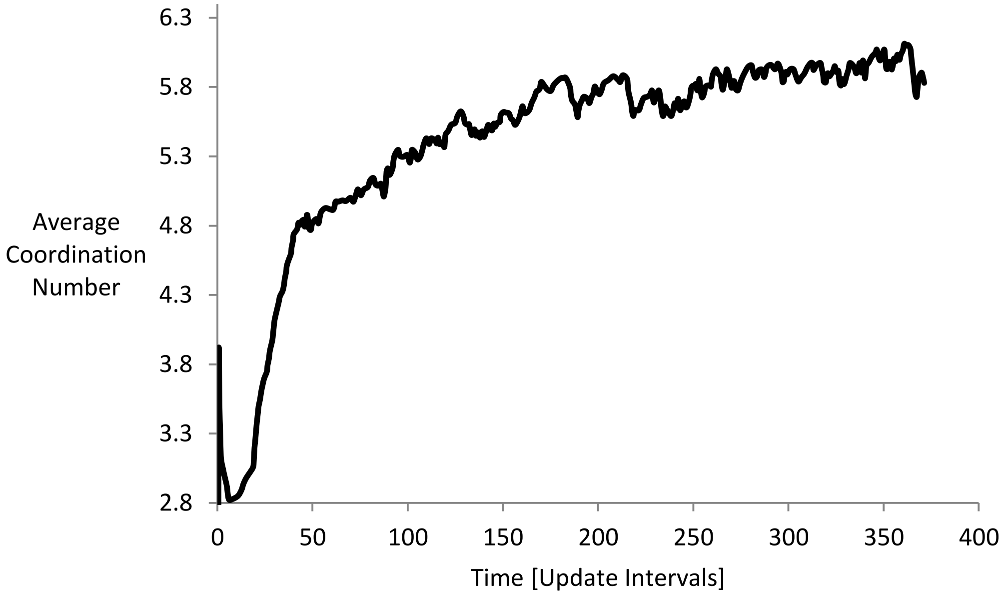

Figure 14: Quasi-static Equilibration

From Figure 14, adequately large coordination number and therefore dense samples were formed on small time scales (less than 1 seconds). However, 1 second of physical time took a very long time to simulate in an explicit DEM calculation.

The main drawback to the method described above was that it took a very long time to simulate equilibration. After the initially dense packing relaxed, it spent a long time re-densifying. Additional methods were proposed to bring the sample to an equilibrated dense packing (coordination number > 6) more quickly.

A method was proposed to use kinetic energy imparted into the sample by vibrations to accelerate the reorganization of particles into denser states. The proposed method involved vibration of a single particle that lies on or near the longitudinal axis of the triaxial test sample. The particle was preferably located at sample mid-height, at the centroid of the sample. The location of the vibrating particle is shown in Figure 15.

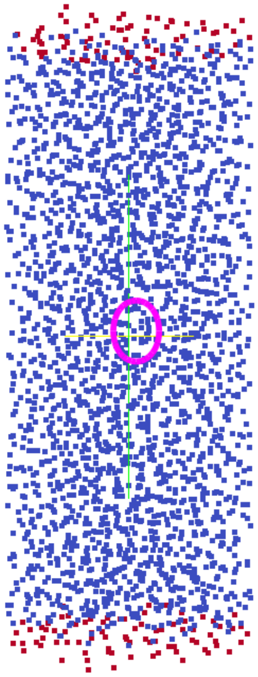

Figure 15: The magenta circle approximates the location of the excited particle

Vibrating a single particle imparted kinetic energy into the sample that could potentially hasten particle rearrangement. Indeed, elastic and geometric particle properties determined the efficacy of vibrational input frequencies. Some parameter studies were in order to determine which frequencies excited particles such that they achieved higher coordination numbers.

The first parameter study looked at mid-range frequency excitation. Kinetic energy was not held constant for these tests. Instead, vibrational amplitude was held constant at

10% of particle diameter in each of the three translational degrees of freedom. Each degree of freedom was excited in-phase. The particle and simulation properties are shown below.

- Particle diameter = 3mm
- Young's modulus = 29×10^9 Pa
- Viscous damping coefficient = 0.4 N-s/m
- Cohesion = 50 Pa
- Rolling friction coefficient = 0.5
- Sliding friction coefficient = 0.05
- Coefficient of restitution = 0.01
- Confining pressure = 200 kPa

Frequencies between 20 Hz and 70 Hz were examined. The first run of simulations of the samples used 5 Hz increments between samples (test 1: 20 Hz, test 2: 25 Hz, test 3: 30 Hz, etc). A second run of simulations were ran to refine areas that were found to be interesting with an increment in frequency of 0.25 Hz. The results are shown in Figure 16. Note that an update interval step was 100 000 time steps, with each time step being 2×10^{-8} seconds; therefore each update interval step was 0.002 seconds of real time. That means 100 steps was 0.2 seconds of real time.

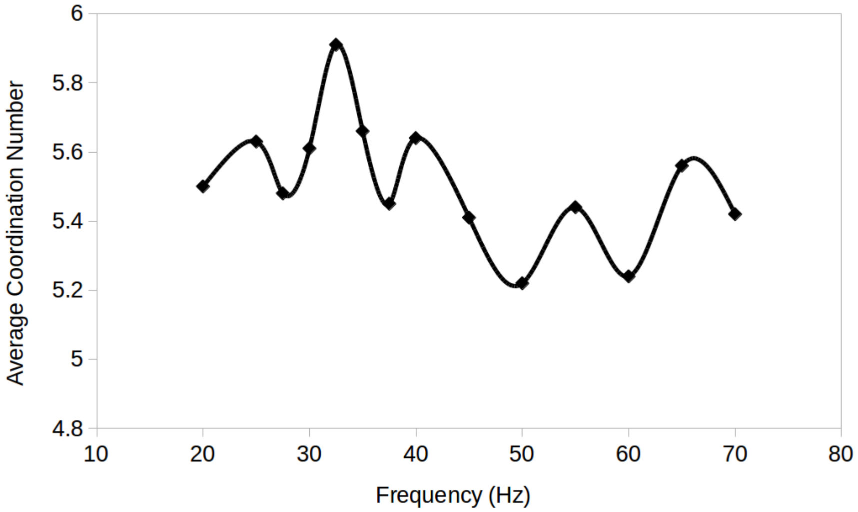

Figure 16: Coordination number as a function of vibrational frequency

It was found that at mid-range frequencies, the optimal excitation frequency was 32.5 Hz. An additional sample was simulated to compare against the quasi-static method presented in Figure 14. This sample was excited at 35 Hz with an amplitude of 0.1D, or 0.3mm. The average coordination number as a function of time is shown in Figure 17.

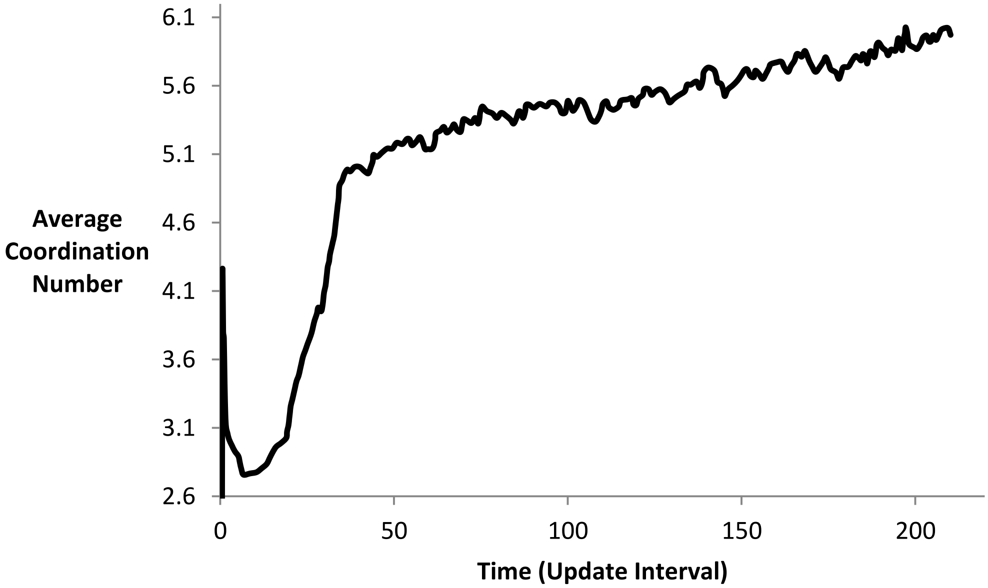

Figure 17: Coordination number evolution in a vibrating sample (freq =35 Hz, amplitude = 0.1D). The sample is subject to 200 kPa of confining pressure and viscous damping of 0.18 N-s/m. The particles in the sample have a Young's modulus of 29 GPa and a coefficient of friction = 0.05

From Figure 17, coordination number in the vibrating condition rose rapidly when compared to the quasi-static case in Figure 14. The time savings of vibrating the sample (at 35 Hz) to dense equilibrium was nearly double.

Low frequencies were checked, though not as thoroughly as the mid-range frequencies. Low frequencies were checked with variable amplitudes and directions of excitation. A small study was designed. The study design is shown in Table 5.

Table 5: Low frequency equilibration, table of excitations

Frequency [Hz]	Amplitude [m]	Direction
10	1D	X,Y,Z
10	1D	Z
2.5	3D	Z
2.5	4D	Z

Note: D = particle diameter in DEM simulation in Table 5.

The particle and simulation properties are as follows.

- Young's modulus = 29 GPa
- Friction = 0.05
- Viscous damping coefficient = 0.18 N-s/m
- Cohesion = 50 Pa
- Rolling friction coefficient = 0.5
- Sliding friction coefficient = 0.05
- Coefficient of restitution = 0.01
- Confining pressure = 200 kPa

The excitation was introduced into the sample the same way as before, by exciting a single particle near the centroid of the sample. The results of this study were intriguing in that coordination number would vary considerably throughout the course of a single excitation cycle. Figure 18 shows the results of the first 200 update intervals.

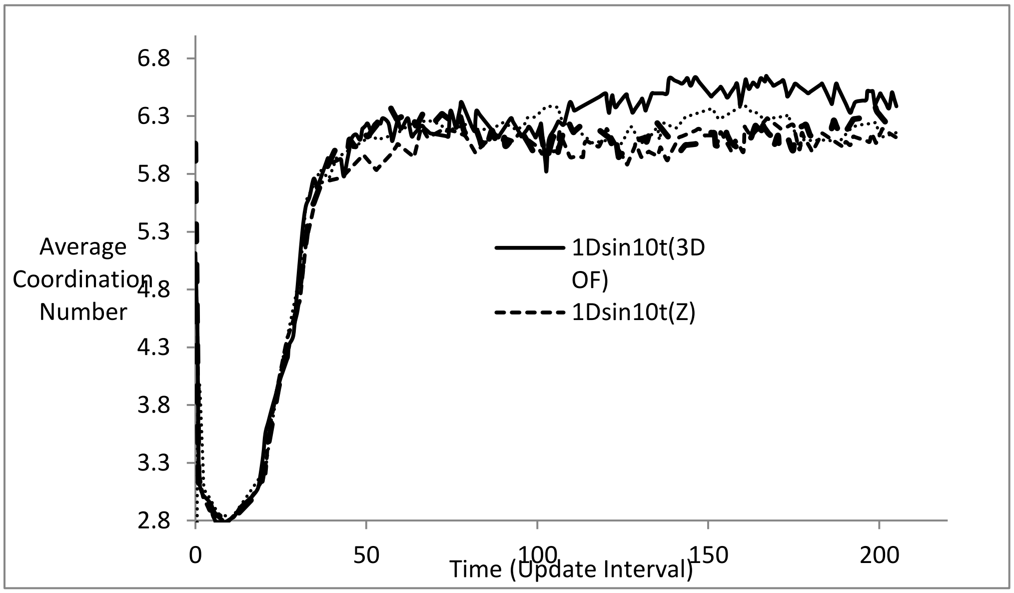

Figure 18: Low frequency equilibration, coordination number as a function of time

From Figure 18, the increase in coordination number as a function of time was rapid until a coordination number of 6.25 was achieved. After that point, all of the samples loosened a little bit before they reached a final coordination number. Only the 10 Hz test with excitation in X, Y, and Z surpassed a coordination number of 6.5. The speed at which high coordination numbers were achieved was, indeed, noteworthy. A dense sample was achieved in less than 150 update intervals (0.3 seconds).

High frequencies were also checked. Another small study was designed to query the response of the sample to high frequency vibrations. The study varies frequency and amplitude as shown in Table 6.

Table 6: Frequency and amplitude variation for high frequency excitation study

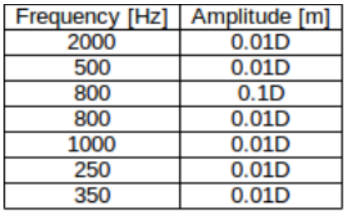

Frequency [Hz]	Amplitude [m]
2000	0.01D
500	0.01D
800	0.1D
800	0.01D
1000	0.01D
250	0.01D
350	0.01D

Note: In Table 6, ‘D’ is synonymous with particle diameter.

The excitation was introduced into the sample the same way as before, by exciting a single particle near the centroid of the sample. The particle and simulation properties were as follows:

- Young's modulus = 29 GPa
- Diameter = 0.003 m = 3 mm
- Viscous damping coefficient = 0.18 N-s/m
- Cohesion = 50 Pa
- Rolling friction coefficient = 0.5
- Sliding friction coefficient = 0.01
- Coefficient of restitution = 0.01
- Confining pressure = 200 kPa

Selected sample coordination numbers from this study are presented in Figure 19.

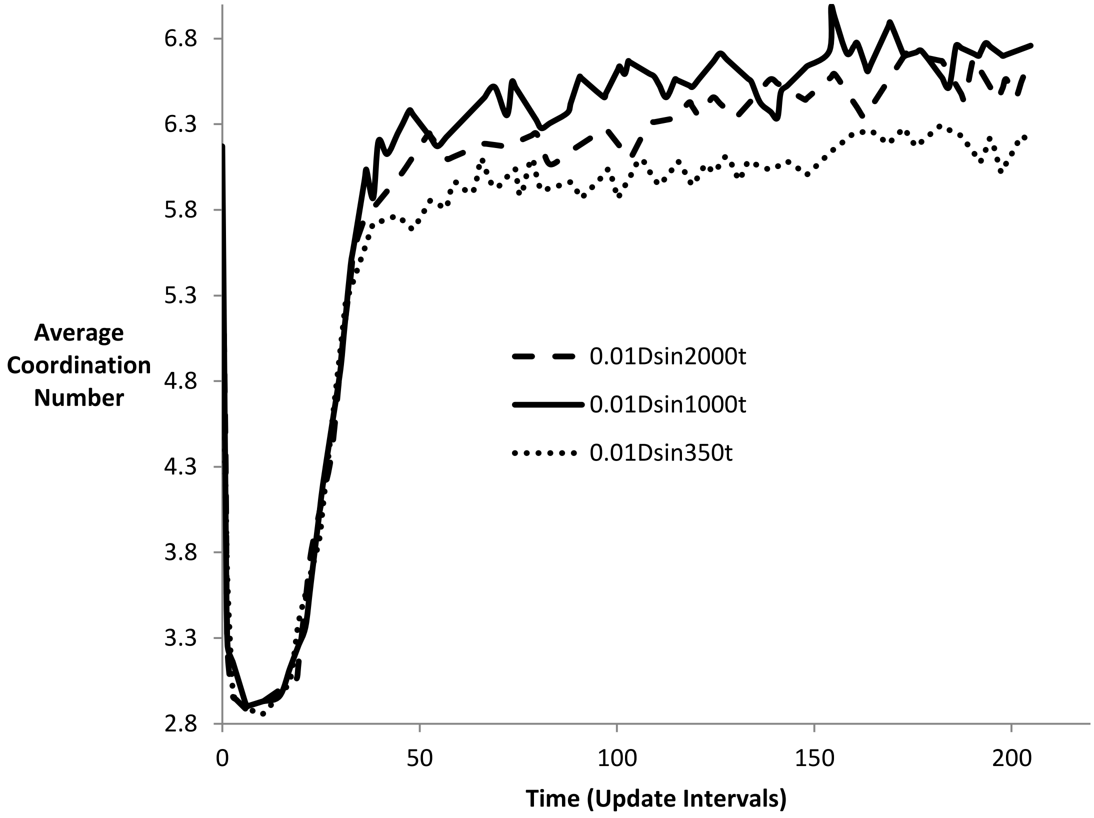

Figure 19: High frequency equilibration, coordination numbers with respect to time

From Figure 19, the sample was brought to adequate coordination numbers rather quickly for the high amplitude 800 Hz test, and the 1000 Hz and 2000 Hz tests as well. The remaining tests showed slow increases in average coordination number by comparison.

Now that a broad range of excitation frequencies were tested for increasing coordination number during equilibration, a quick comparison across frequency regimes was in order. Two tests from the low frequency regime were chosen, as was one test from the middle frequency range, and one test from the high frequency range. One quasi-static equilibration run was also included. The particle and simulation environment properties were identical across all tests except for the excitation parameters. The results of the cross-regime study are shown in Figure 20. Only the first 100 update intervals are shown (0.2 sec).

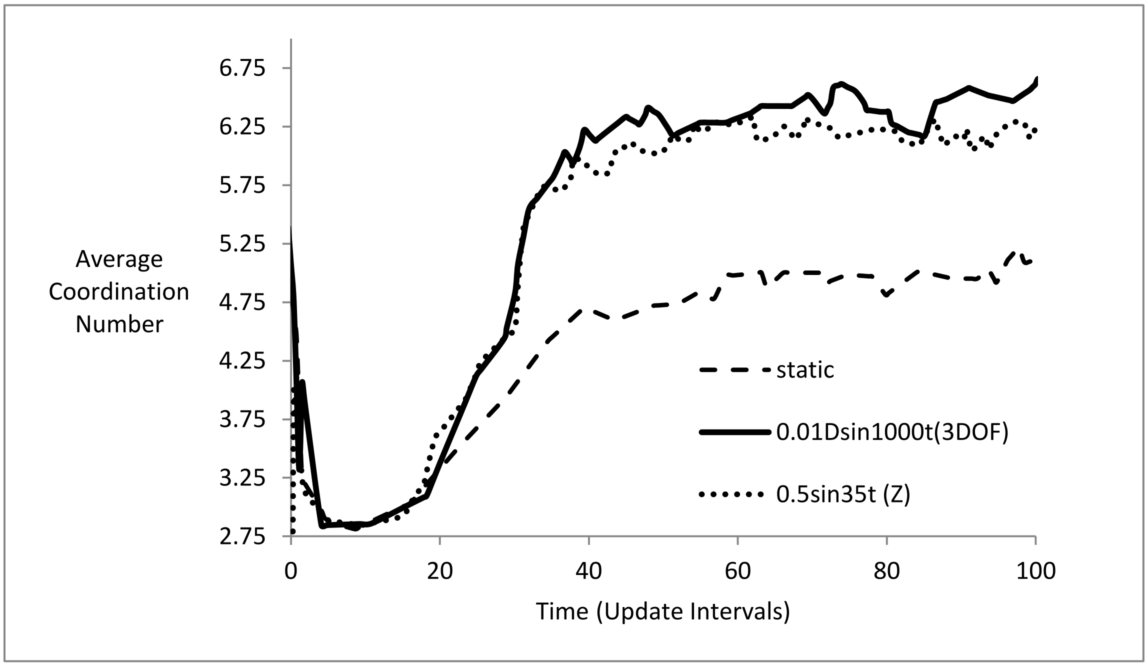

Figure 20: Cross regime study, coordination number vs. time

The static test exhibited the slowest progress toward a dense equilibrated sample. The dynamically excited samples showed very similar behavior to each other until update interval 80, at which point the high frequency excitation sample carried higher coordination numbers than the rest of the dynamic tests. The fastest equilibration occurred when the sample was subjected to an X,Y,Z excitation at 1000 Hz and an amplitude of 0.01 x particle diameter.

It is worthwhile to compare the contact uniformity of statically and dynamically equilibrated samples, which was possible by comparing the standard deviation of the average coordination number at the end of equilibration (Oda et al., 1982). This was analogous to Kuhn's (2003) parameter, valance, which described the probability of a particle to have a particular coordination number. A smaller standard deviation generally indicated more uniform contact force networks. Lower standard deviation from average coordination number moved us closer to an ideal sample. Table 7 compared means and standard deviations of coordination number in samples prepared from static and dynamic equilibration methods.

Table 7: Comparing average coordination number and standard deviation between statically and dynamically equilibrated samples.

End of Equilibriation			
Static		Dynamic, 0.01Dsin(t x 1000hz)	
Ave Coordination Number	Standard deviation	Ave Coordination Number	Standard deviation
6.16	4.74	6.78	5.01

The dynamically equilibrated sample had a slightly higher standard deviation (5.7% higher). At the same time, the coordination number achieved by the dynamically equilibrated sample was also significantly higher (10% higher). By the standards of the majority of published literature, the dynamically equilibrated sample was of higher quality because of the higher coordination number, but the magnitude of detriment to the sample quality by raising the standard deviation was unknown.

Indeed, the variation of sample response with respect to Young's modulus needed consideration. A second study measuring the effects of reducing Young's modulus by an order of magnitude was performed. The study used the same particle and environmental parameters as the previous frequency response study (whose results are shown in Figure 19). The best test runs from each excitation regime were chosen. These tests were re-ran with identical simulation parameters with the exception a reduced Young's modulus. Table 8 shows the study design.

Table 8: Study design and results

			Coordination Number	
Regime	Excitation	Damping [N-s/m]	E = 29x10^9 Pa	E = 29x10^8 Pa
Low Freq	3Dsin(tx2.5t)	0.18	6.09	6.72
Mid Freq	0.1Dsin(tx32.5Hz)	0.4	5.26	5.44
High Freq	0.01Dsin(tx1000Hz)	0.18	6.65	6.88
Static	-	0.18	5.21	5.72

Figure 21 shows these results in graphical format.

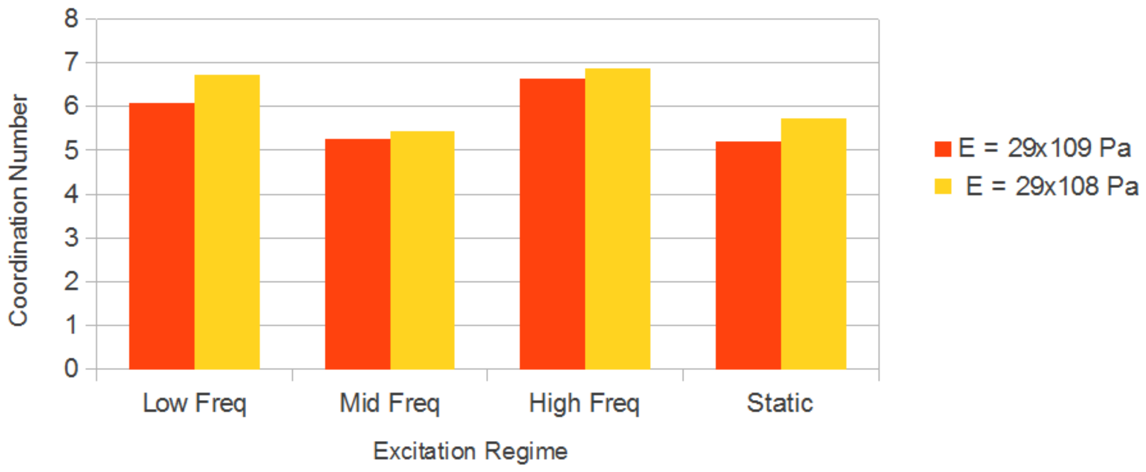

Figure 21: Equilibrated sample coordination number amongst particles of varying stiffness compared across four excitation regimes

As in Figure 21, coordination number generally increased when particle Young's modulus was reduced. This was an important find because it indicated coordination number was not as pertinent in samples with particles of lower stiffness. The upper limit of particle stiffness (Young’s modulus = 290 GPa) still needed to be tested to verify that adequate coordination numbers were achieved in reasonable spans of equilibration time.

In conclusion, the high frequency seed excitation resulted in reliably high coordination numbers in reasonably short simulation times during the dynamic equilibration regime of the virtual triaxial test sample preparation.

Static equilibration

Of the three equilibration regimes, the static regime's purpose was to reduce the volume of the virtual triaxial test sample until it reached a true minimum. Sample volume was addressed in the dynamic equilibration section, but that section focused much more heavily on coordination numbers. The conversation about coordination numbers focused on achieving average sample coordination numbers in the mid-6's or higher. The conversation about specimen volume was much less specific and needed to be addressed further.

It was mentioned that specimen volume will asymptotically approach a steady state value during equilibration. When the volume reaches steady state, it was deemed to be *equilibrated*. This steady state value was not known ahead of time and was a function of Young's modulus, confining pressure, friction, particle size, and sample size. The time it takes to get to steady state volume was also unknown. It was seen that damping significantly affected the time it took for a sample to reach steady state. When visually looking at the evolution of volume during equilibration, it was easy to erroneously conclude that a sample had been successfully equilibrated. For example, the volume evolution shown in Figure 22 was incomplete, though it seemed to have reached a minimum. This sample was dynamically equilibrated at 1000Hz with an amplitude of 0.01D, where D = particle diameter.

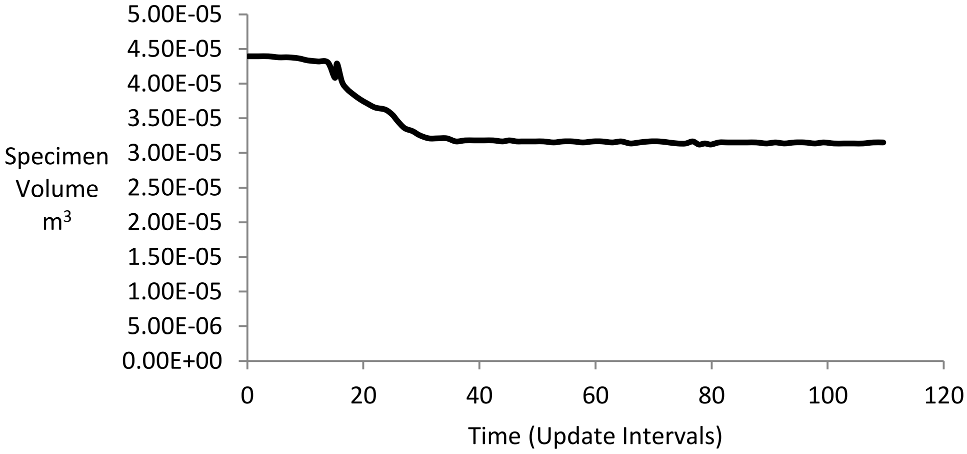

Figure 22: Sample volume evolution subject to confining pressure. End volume = 3.15×10^{-5} m^3

The slope of the volume with respect to time at the 110th update interval was very small (in the absolute sense) at -1.26x10^{-7} m^3/step. The coordination number at this point was 6.63. From a cursory perspective, it looked like the sample was sufficiently close to steady state, but when the volumetric strain during a triaxial compression test was observed, its appearance was unexpected and discontinuous. The volumetric strain of this sample subject to triaxial compression is shown in Figure 23.

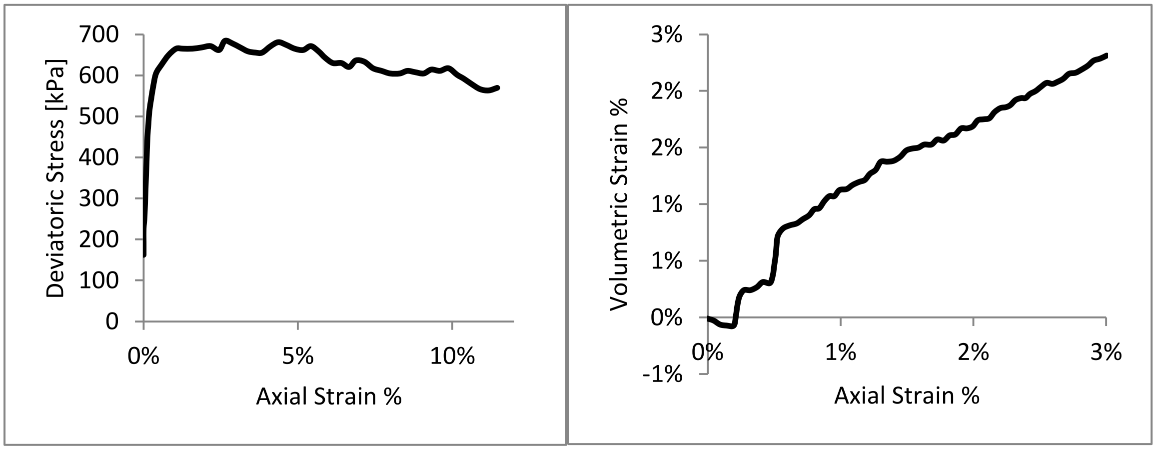

Figure 23: (a.) - left: Stress-strain response during triaxial compression, (b.) - right: Evolution of volumetric strain during triaxial compression. Small strain data is shown. Note that the X-axes of the two figures are not the same

If only checking the stress-strain response of the sample, Figure 23a, qualitative success could be declared, but indeed, the sample was not successful. By all accounts, the volumetric strain response of the sample was of poor quality. The rapid changes in volume indicate rapid reorganization of particles, more or less a collapse, that was verified visually by animating the simulation. Rigorous quality criteria needed to be developed to systematically produce specimens that re-created the behavior of geomaterials.

Strategies needed to be developed to get sample volume as close as possible to a true physical steady state value. A statically equilibrated sample of 3393, 3 mm diameter, particles was seen to achieve a volume of 2.95x10^{-5} m^3 when subjected to confining pressure of 200 kPa. This was lower than the minimum volume observed in Figure 22.

To gain further insight into what the cause of the excessive volume was, some additional results were considered. Two additional samples were equilibrated, one with low frequency vibrations, one with high frequency vibration. The vibratory excitation in the samples was turned off after reaching 0.4 seconds of physical time. The confining pressure, however, was left active and the sample was left to equilibrate for an additional 0.2 seconds under these quasi-static conditions. Figure 24 and Figure 25 show the evolution of sample volume over time. Both of these samples were subject to a viscous damping coefficient of 0.18 N-s/m.

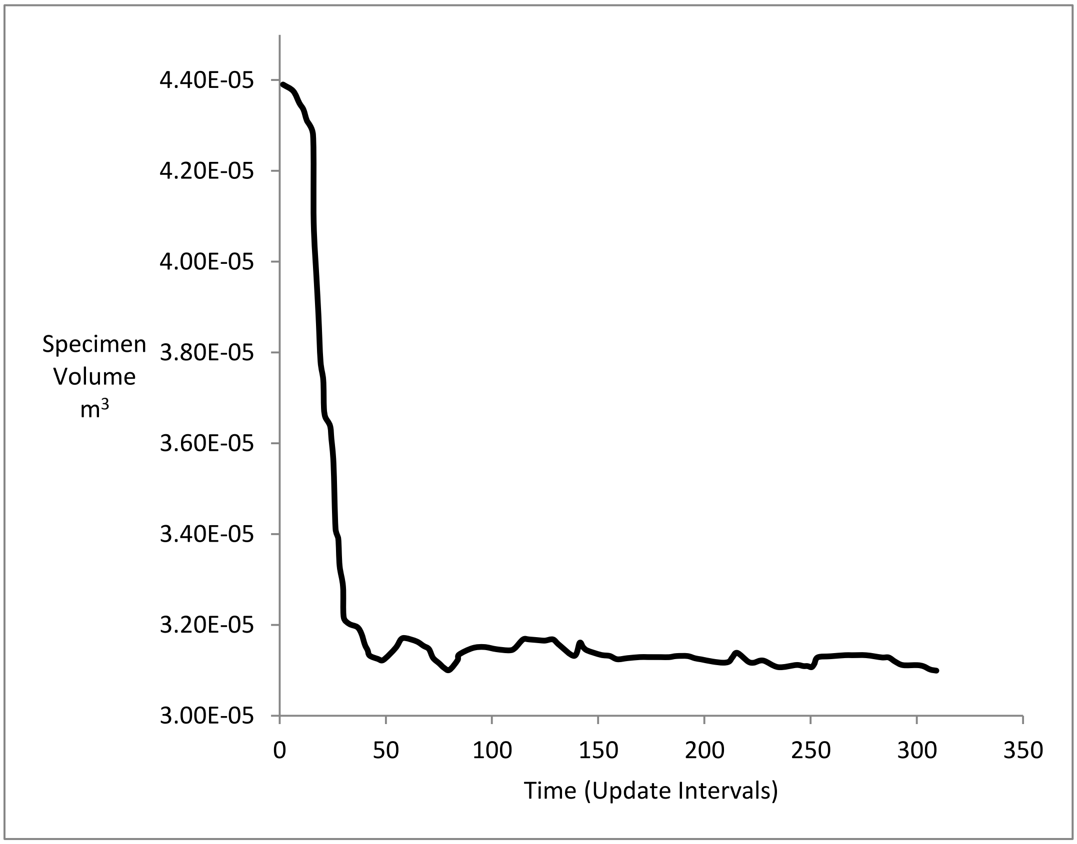

Figure 24: A sample equilibrated dynamically at high frequency for 200 steps, then statically for 100 steps. End volume=3.11x10^{-5} m^{3}

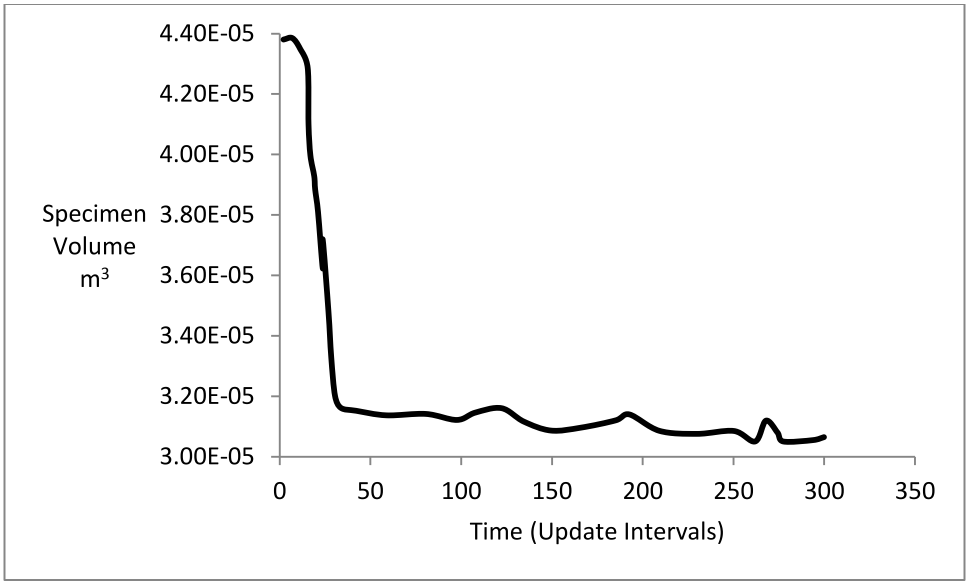

Figure 25: A sample equilibrated dynamically at low frequency for 200 steps, then statically for 100 steps. End volume = 3.06×10^{-5} m^3

The two figures, Figure 24 and Figure 25, show that during the dynamic portion of equilibration, the true minimum volume was not achieved. Further volume reduction occurred in the static regime after step 200. The figures also showed that high frequency equilibration yielded a larger sample than low frequency equilibration, though it would be inappropriate to draw conclusions from this observation. It was inferred from this data that pure static equilibration resulted in the lowest sample volume. This was seen to be true in recent simulations. Unfortunately, pure static equilibration was too computationally expensive, and worse yet, the resulting coordination numbers were not reliably high. Something interesting about the data was that the sample in the low frequency condition responded better to static confining forces than the sample in the high frequency condition, even after the dynamic excitation had been turned off (after 0.2 seconds).

It was hypothesized that damping played a significant role in the densification of a virtual triaxial test sample. Results from a small pilot study confirmed this hypothesis. The next step was to quantitatively asses the influence of damping on sample volume at the end of the equilibration window.

A small study was designed to help gain some valuable insight into the process. Six equilibration simulations were performed. During the first 0.2 seconds of equilibration, a seed near the centroid of the sample was vibrated at 1000 Hz with an amplitude of 0.03 mm in the 3 translational degrees of freedom (high frequency excitation). The sample was also subject to a confining pressure of 200 kPa. During the latter 0.2 seconds of equilibration, the vibration was turned off leaving the confining pressure to quasi-statically compress the sample. This study was very similar to the sample seen in Figure 24. The goal of the study was to find the threshold of damping during the quasi-static equilibration regime that allowed the sample to compress down close to its true steady state volume while maintaining stability. It was expected that at some lower limit of damping, the kinetic energy was not reduced enough to compress the sample at all, and that this lower limit occured well above the required damping to maintain a stable sample.

The simulation parameters used for the study were the following:

- Particle diameter = 3mm
- Young's modulus = 29×10^9 Pa
- Viscous damping coefficient = 0.4 N-s/m
- Cohesion = 50 Pa
- Rolling friction coefficient = 0.5
- Sliding friction coefficient = 0.01
- Coefficient of restitution = 0.01
- Confining pressure = 200 kPa

The viscous damping coefficient was varied from 0.08 N-s/m to 0.18 N-s/m during the static portion only. The dynamic portion of each test maintained 0.18 N-s/m of viscous damping. Figure 26, Figure 27, and Figure 28 show the results of these tests.

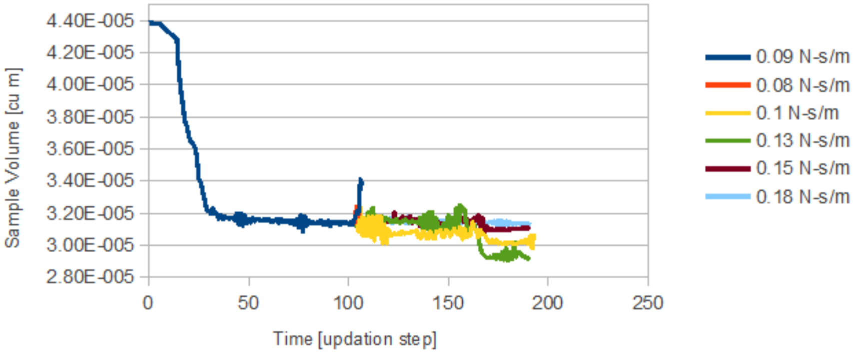

Figure 26: Volume evolution with respect to time in dynamic and static regimes

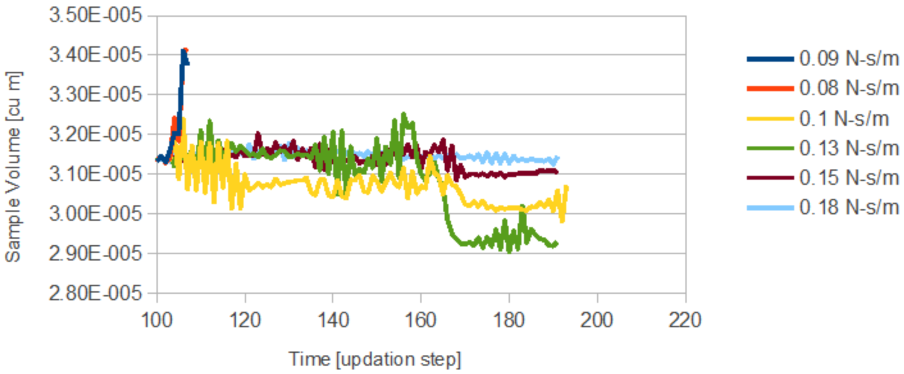

Figure 27: Volume evolution in static regime only

From Figure 26 and Figure 27, varying damping during the static regime significantly affected the final volume of the sample. At very low damping (0.09 N-s/m and below), the sample became unstable. On the high end of damping (0.15 N-s/m and higher), the volume did not come very close to a true minimum. The volume is best minimized by the test run in which damping coefficient was set to 0.13 N-s/m. It is noted from Figure 28 that there is a true optimal damping coefficient that will minimize volume.

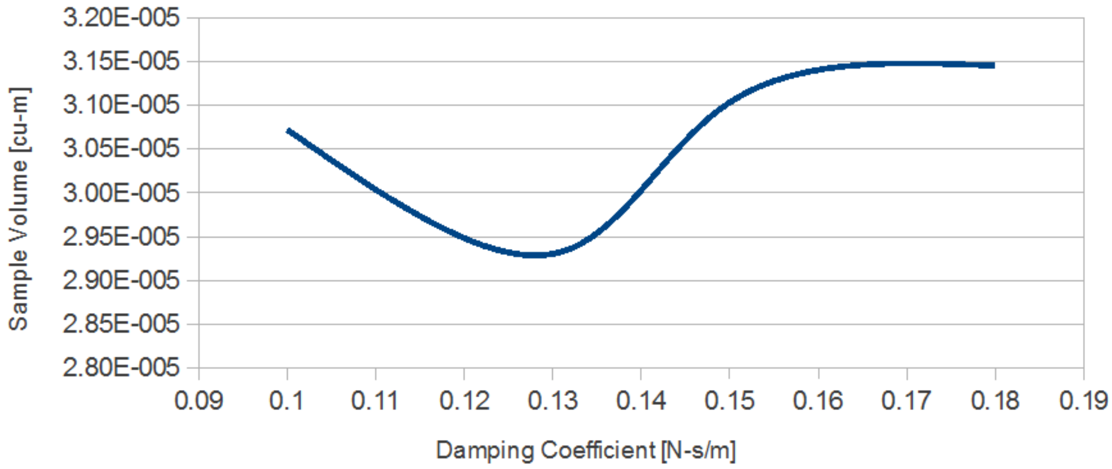

Figure 28: Sample volume as a function of damping at 0.4 seconds of equilibration

Since our optimal volume was achieved using a damping of 0.13 N-s/m, average coordination number should be checked in this sample to make sure that the static regime had not reduced it. Figure 29 shows the evolution of the coordination number with respect to time of the sample that was assigned a damping coefficient of 0.13 N-s/m.

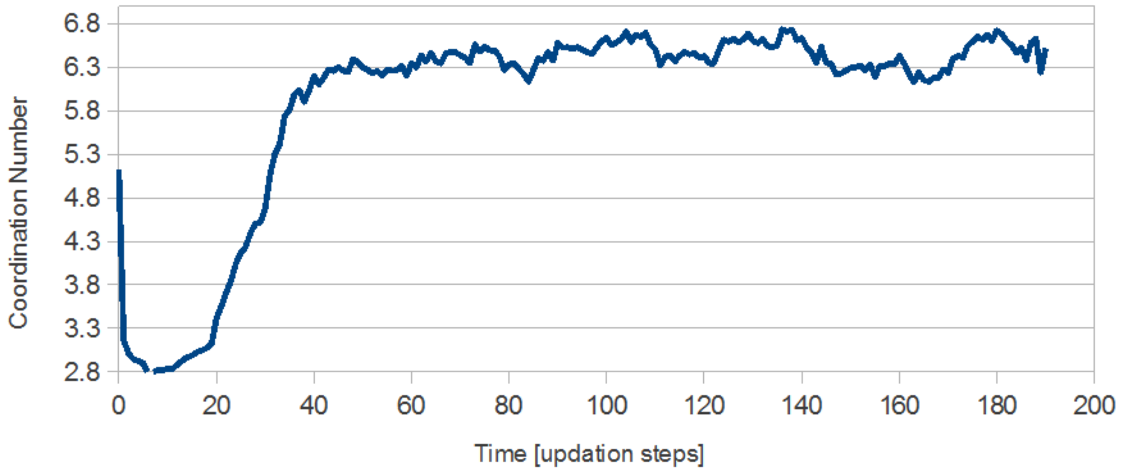

Figure 29: Coordination number evolution, damping = 0.13 N-s/m

Several additional equilibration simulations were run with stiffer and softer particles. Figure 30 shows the results of studies that vary particle stiffness. Optimal damping coefficient changed slightly, but the sample behavior was very sensitive to these very small changes, so it was necessary document them.

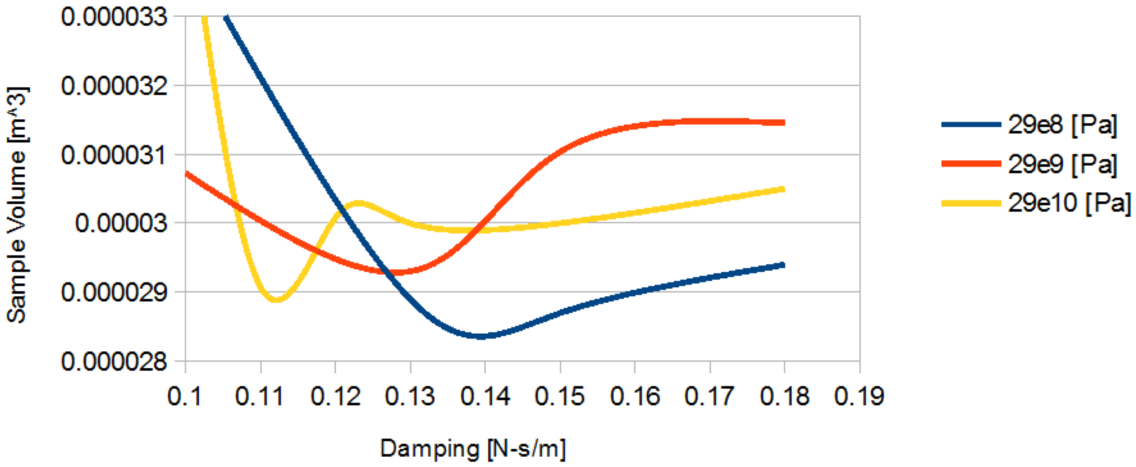

Figure 30: Sample volume as a function of damping at 0.4 seconds of equilibration of various particle Young's moduli

Figure 30 shows the optimal damping coefficients for various particle Young's moduli for use during the static regime of equilibration. It was suspected that the curve for Young's modulus = $29\text{x}10^9$ Pa could use some additional refinement because the minimum should have occurred at a magnitude that falls between the minimums of the other two curves.

Post processing methods

There were several methods available in the literature for processing stresses within a sample. These methods fell into two classes, particle methods and boundary methods (O'Sullivan, 2011b). Both classes of methods calculated sample stresses adequately for stiff particles (Young's modulus > 10^9 Pa), but only the boundary methods worked well for softer particles. As seen in Bagi (1999), the Gauss integral theorem related boundary forces to stresses by way of volume. This method was directly implemented in the LIGGGHTS input script. A description of the implementation is outlined here.

1. Detected the height of the sample.
2. Divided the sample into ten layers of equal thickness.
3. Detected the average radius of each layer.
4. Calculated the cross sectional area for each layer assuming that the layer is roughly cylindrical.

5. Calculated the average cross sectional area, A_{ave}, of all layers.
6. Summed forces on the one of the caps (in our case, the upper cap), F_A.
7. Calculated the average axial stress, σ_A, from F_A and A_{ave}.

Axial stresses were calculated every time confining pressures were updated (discussed in the physical triaxial test and oedometer sections).

Cap adjustments

At the end of equilibration of a virtual triaxial test sample, the deviator stress was usually non-zero. Just as in a physical triaxial test, the upper cap needed to be adjusted until the deviator stress was sufficiently close to zero (ASTM, 2007a). Indeed, the magnitude of axial strain incurred during the cap adjustment process was minimal. An upper limit of ± 0.1% axial strain adjustment had been set. When the required adjustment was greater than ± 0.1% of strain, then the sample was deemed poor and was discarded.

Several triaxial tests were simulated without any cap adjustment. From the results of these tests, it was possible that the global elastic modulus of the sample could be approximated at small strains. A plot of the stress-strain response of a simulated triaxial test is shown in Figure 31.

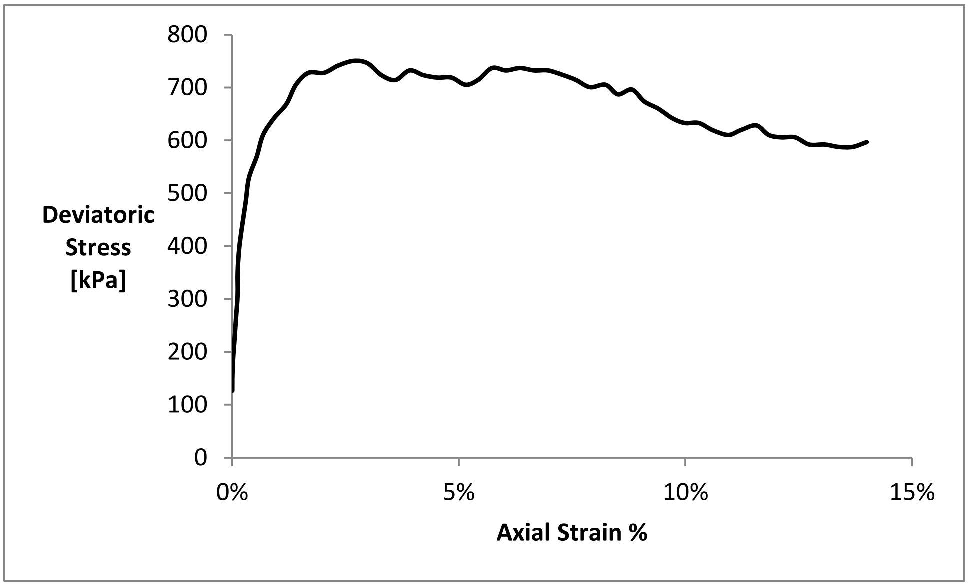

Figure 31. Stress-strain response of triaxial test sample

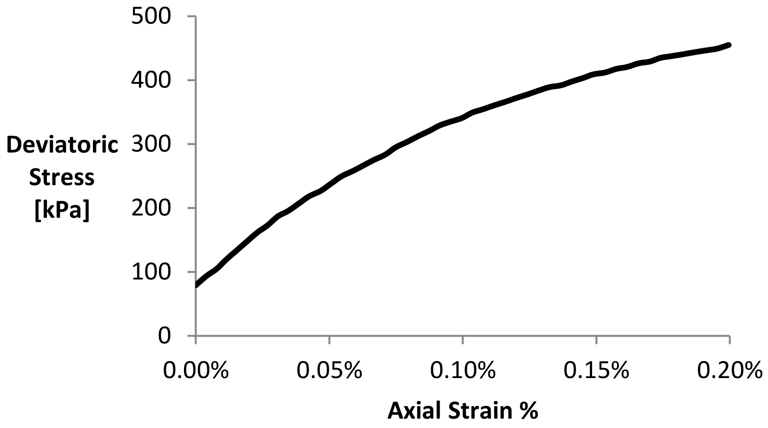

Figure 32. Stress-strain response of a triaxial test sample at very small strains

The sample in Figure 31 consisted of particles of diameter = 3 mm and Young's Modulus = $29x10^9$ Pa. The approximate elastic modulus of the sample near zero strain was $3.56x10^8$ Pa. Linearizing the stress-strain relationship at very small strains allowed for linearly extrapolating the required strain adjustment that would yield zero deviator stress. In the case of the sample in Figure 31, the required axial strain adjustment was -0.0222%, which was well below the limit of 0.1%. Of course, linear extrapolation of the slope to zero deviator stress resulted in a slight overestimation of the magnitude of cap adjustment. Therefore, the adjustment was made in small steps, 1/10th of the estimated adjustment, and the deviator stress was checked after each small adjustment. This allowed for stopping the adjustment before any significant overshoot occurred. Significant overshoot was undesirable because backtracking the cap would cause the sample to undergo hysteresis, which has been shown to cause irreversible particle reorientation even at very small stains (O'Sullivan et al., 2008).

After the adjustment was made, the deviator stress should be sufficiently close to zero. In Jiang et al. (2003), a criterion was used such that the first principle stress in the sample was less than 5% away from the magnitude of confining pressure. The same criterion was used here. Since the simulation program output was standardized to deviator stress, an equivalent criterion for deviator stress was constructed. The deviator stress should be less than 2.5% of the confining pressure. As an example, a sample subject to 200 kPa of confining pressure would be allowed to have a maximum initial deviator stress of 5 kPa. Additional adjustments were required if the initial adjustment did not satisfy the deviator stress criteria. After the deviator stress was brought sufficiently close to zero, the adjusted axial strain was set to zero.

It should be noted that cap adjustments were very rarely needed. It was found that if interparticle friction was low (coefficient of friction ~ 0.01) during equilibration, and the number of particles in the sample was sufficiently high (8000+), then the resulting first deviatoric stress in the sample (as measured by the cap reaction) was close to zero. In other words, the sample approached an isotropic stress state as equilibration progressed.

Physical variation

Although DEM is a deterministic method, the triaxial test specimens generated for each simulation were random. Referring back to the section entitled 'Algorithmic construction,' equation 3.38 calculated the direction of a vector using random numbers. The vector was used to place neighbor particles around a parent particle. The random numbers were generated using an established method, the Mersenne twister, which used the CPU clock of a computer to establish a seed or a basis for calculating a random number in a uniform distribution (Matsumoto and Nishimura, 1998).

Physical triaxial tests have physical sample variation as well, but they also have measurement error. Measurement error was eliminated due to the nature of deterministic virtual measurements, therefore it was enough to simply quantify the physical variation in random samples with respect to critical points on resulting stress-strain and volumetric strain curves. A study was performed to quantify the physical variation in mechanical responses of virtual specimens as a function of total number of particles in a sample.

LIGGGHTS source code modifications

Two modifications were made to the default LIGGGHTS installation. The first modification was a change in the C++ source code that calculates cohesion. Even though the current project used a Hertzian contact scheme, the cohesion calculations were inherited from Hookean calculation files. In the source (src) folder of the installation, the file "pair_gran_hooke_history.cpp" contains the relevant calculations that needed to be changed. The variable, *Acont*, was declared on line 122 and was defined in the conditional branches of the following lines. *Acont* was the area over which the cohesion acts. Equation 2.45 shows how cohesive force was constructed within the LIGGGHTS program.

$$F_{cohesion} = C \times Acont \tag{2.45}$$

where $F_{cohesion}$ = the interparticle force due to cohesion;

$Acont$ = the projected interparticle area; and

C = a cohesion coefficient which was defined as “cohesion energy density.” The physical meaning of C varied with respect to the construction of $Acont$.

The geomechanical definition of cohesion was also a continuum definition. The projected cohesive area accounted for the void space around a particle (sphere). Therefore, the projected area was represented by equation 2.46.

$$Acont = (D_{effective})^2 \tag{2.46}$$

where $D_{effective}$ was the effective diameter between two interacting particles; see equation 2.47.

$$D_{effective} = 2\left(\frac{1}{D_i} + \frac{1}{D_j}\right)^{-1} \tag{2.47}$$

where D_i and D_j were diameters of two interacting particles.

After updating the cohesion area definition, a compile flag needed to be set to enable aspherical aggregates (molecule package). While in a terminal, the compile flag was set by navigating to the “liggghts_path/src” directory and issuing a “make molecule-yes” command, then a “make clean-all” command. Then the source code was compiled normally and the updated cohesion definition and the aspherical aggregate capability were enabled.

Physical Laboratory Tests

To address the objective of this study, hopper and direct shear tests were conducted at the Advanced Soil Dynamics Laboratory at the Department of Agriculture and Biosystems Engineering at Iowa State University (Ames, IA). Direct shear, oedometer, and triaxial tests were performed at the Department of Civil Engineering, Graduate Laboratories at the University of Michigan (Ann Arbor, MI). Finally, blade mixing and cone penetrometer tests were performed in the Singularity Solutions Laboratory (Ann Arbor, MI). A brief description of each type of laboratory test is described here.

Triaxial Test

The triaxial compression test was first performed by Karman (1911) to study brittle rock mechanics. The test has since been adapted to study many natural and granular materials including soils (Bishop and Henkel, 1957), gravel, agricultural products, and collections of manufactured particles.

A generic schematic of a triaxial test setup is shown in Figure 33.

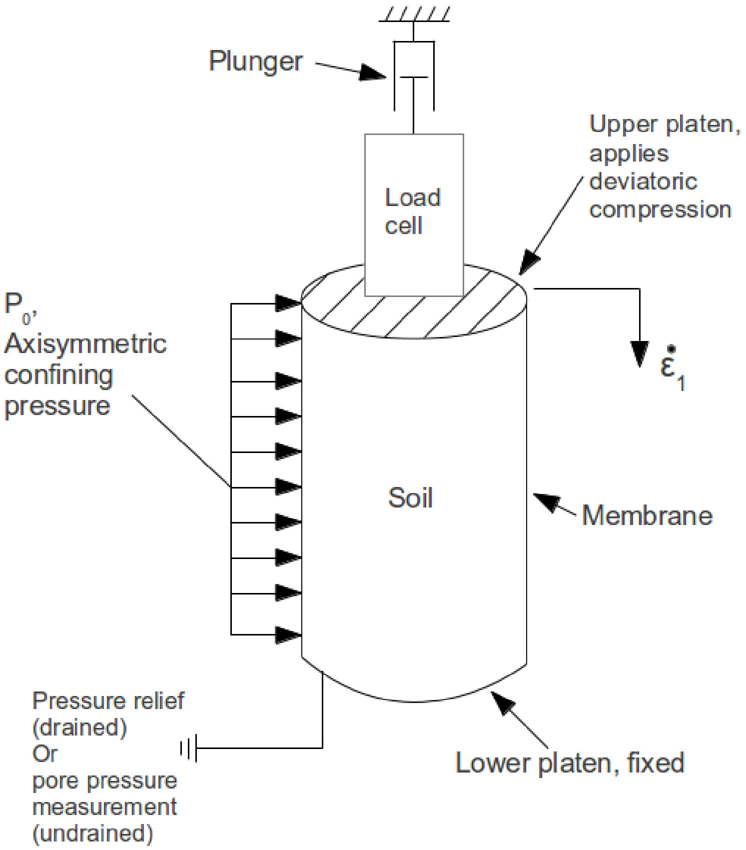

Figure 33. Triaxial test schematic

Three methods were used for conducting triaxial tests on soils, ASTM D2850 for unconsolidated undrained (UU) soils; ASTM D4757 for consolidated undrained (CU) soils; and ASTM D7181 for consolidated drained (CD) soils. These three types of triaxial tests existed to accommodate soil composition, consolidation, and the resulting application of the soil strength data collected from the tests. Fine grained soils generally experienced undrained loading (CU, UU) while coarse grained soil experience drained conditions (CD). Similarly, fast rates of loading that did not allow pore pressure to dissipate support undrained loading conditions (CU, UU), even in coarse grained materials, while slow rates of loading often supported drained conditions (CD). Soil consolidation generally referred to the volume reduction of the triaxial test sample right before the onset of triaxial compression. When the sample was in a triaxial cell and was subjected to confining pressures, some consolidation of the sample occurred, meaning, the volume was reduced. When the volume reached a steady state minimum, the sample had reached the end of consolidation and was termed consolidated. If the triaxial compression began before the sample was fully consolidated, the sample was called under-consolidated.

Axial stresses and strains were measured during a triaxial compression test. The expected qualitative stress-strain and volumetric strain responses are shown in Figure 34 for drained and undrained conditions.

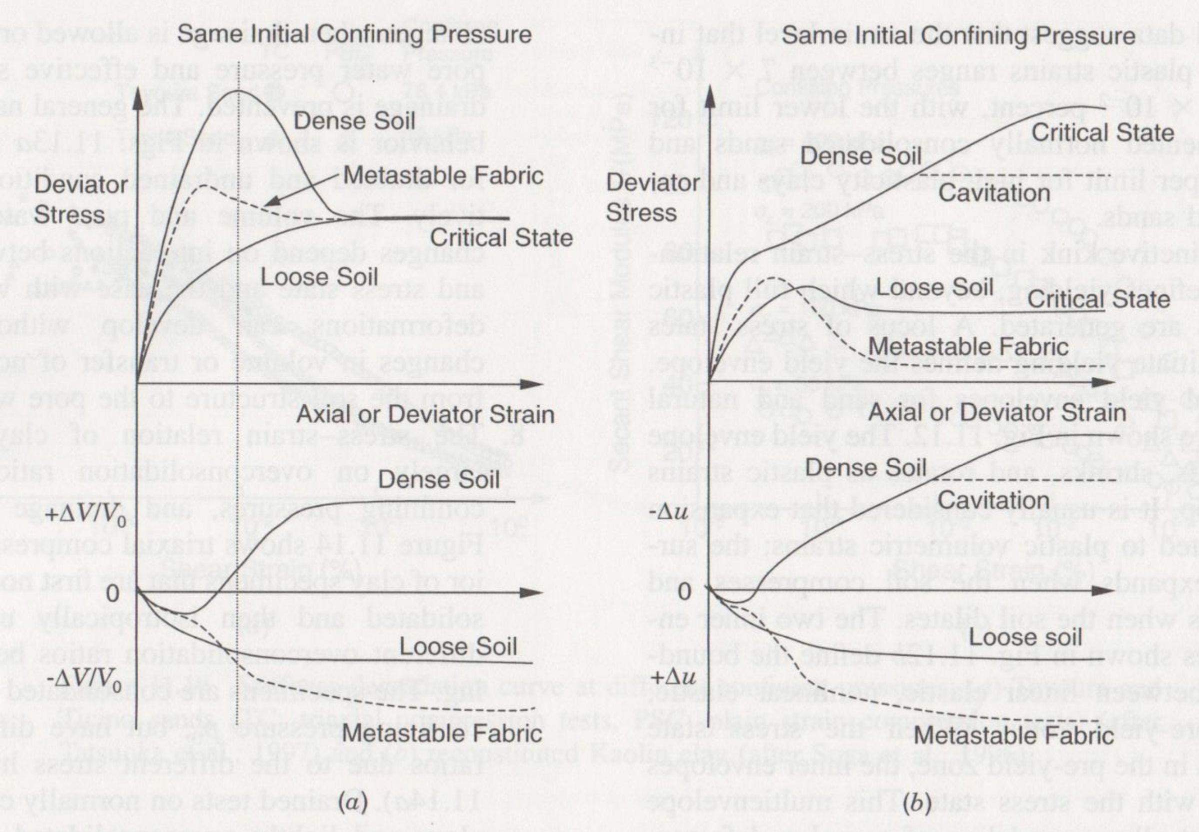

Figure 34. Generic triaxial test response data for (a) drained conditions, (b) undrained conditions (Mitchell, 2005)

Important points on the stress strain response are shown in Figure 35.

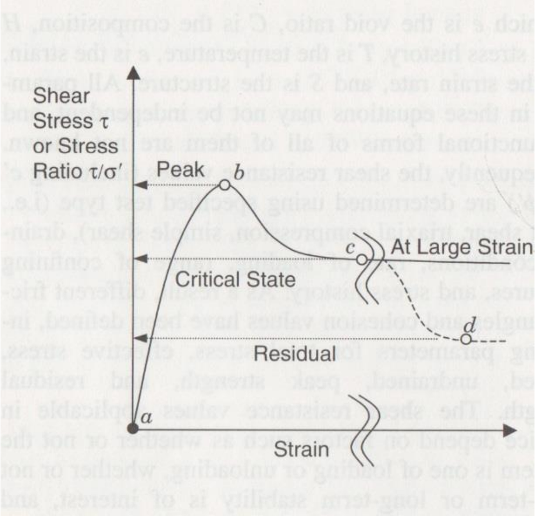

Figure 35. Important points on the stress strain response of a triaxial test specimen (Mitchell 2005)

In Figure 35, point *a* was important because the effective elastic modulus of the sample was calculated here. Point *b* was where the peak strength of the sample was observed. Point *c* was the critical state of the sample where the sample compression occurred under unchanging axial stresses and constant volume. Figure 35 also shows the critical state strength which is observed at much larger strains than point *c*.

It is interesting to note that the stress-strain response to triaxial compression was traditionally plotted using the first principle deviatoric stress on the Y-axis and axial strain on the X-axis (see Figure 34). The deviatoric stress was a stress state that was written in matrix form. The first principle deviatoric stress is shown in equation 2.48.

$$\sigma_d = \frac{(\sigma_1 - \sigma_3)}{2} \tag{2.48}$$

where σ_1 and σ_3 are the first and third principle stresses, and σ_d is the first principle deviatoric stress. The deviatoric stress state was an important concept in failure theories because it was the stress state that contributes to shape change (Collins, 2003).

Oedometer Test

The oedometer test is a confined compaction test. Soil specimen were extruded into hollow cylindrical space with low aspect ratio (i.e., a short, squat, cylinder) so that its initial geometry resembled a disk. The specimen was confined on the top and bottom by porous media so that moisture drained from the specimen. The specimen was then incrementally compressed. Each increment of compression entailed a period of time in which the specimen's volume reached steady state. It may take several minutes to several days for the specimen to properly drain and achieve a steady state volume under a given compressive load. The specimen may undergo one or several unload/reload cycles to further provide insight into the compaction behavior of a specimen. Figure 36 shows a schematic of the oedometer test apparatus.

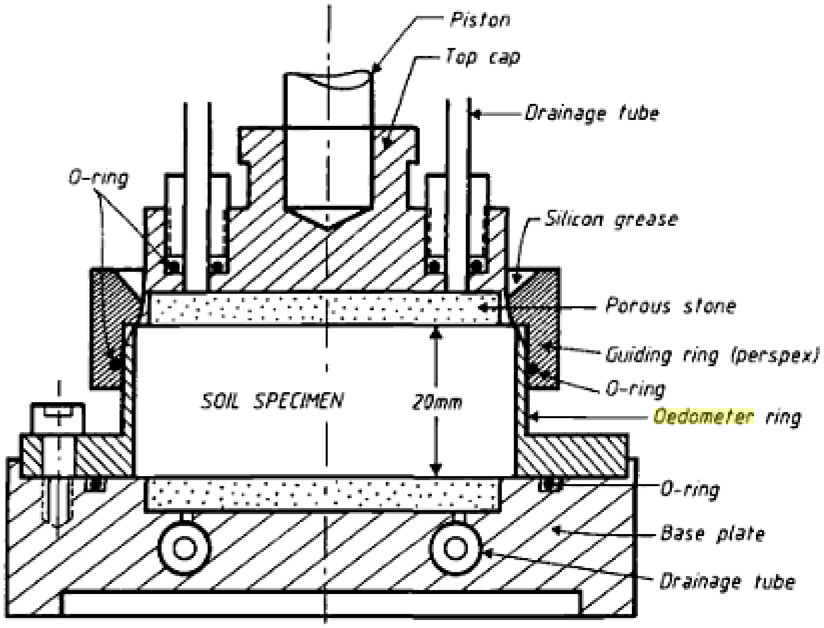

Figure 36. Oedometer test apparatus (Sandbaekken et al., 1986)

The compressive force that was applied to the sample was a known quantity. Therefore, calculating the average axial stresses in the specimen was the same as in the triaxial test. Calculating the third principal stress (or the radial stresses) required that a strain gauge be placed on the outside of the oedometer ring (see Figure 36) to measure hoop strains. Hoop strains may be converted to radial soil stresses by pressure vessel equations. Raw data gathered from a single increment of loading in an oedometer test is shown in Figure 37.

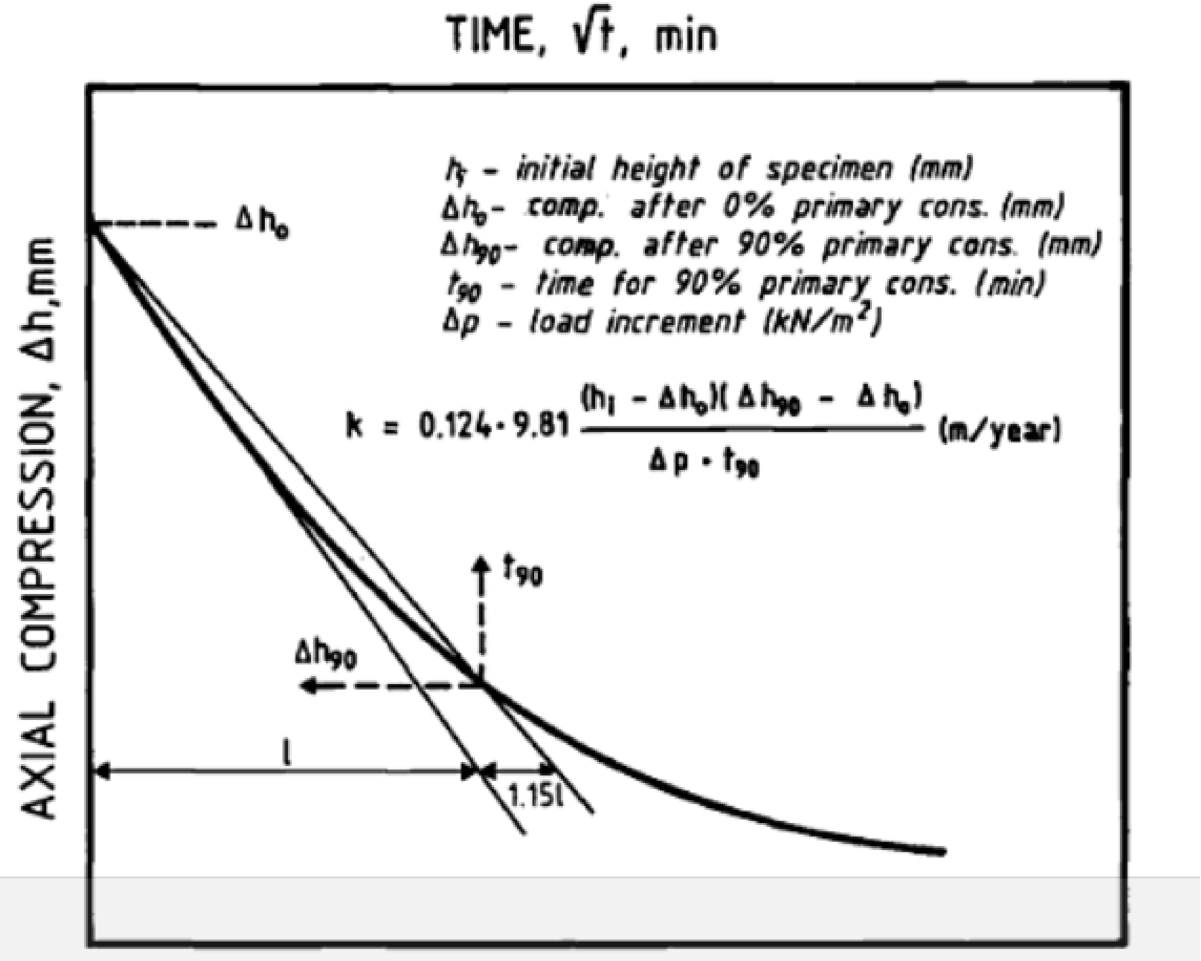

Figure 37. Coefficient of permeability is calculated from the axial compression versus time data raw data (Sandbaekken et al., 1986)

The raw data was treated to provide more insight into the compaction behavior of soil. As seen in Figure 37, permeability constants were extracted from the data. Mean pressure was plotted against void ratio or volumetric strain to find the oedometer modulus. Also, the unloading cycles revealed the preconsolidation pressure in the specimen.

Direct Shear Test

Direct shear tests, as described in ASTM D3080, were used to characterize mechanical properties of granular materials. The direct shear test was a drained laboratory test where a granular specimen was loaded into a circular or square shaped chamber and sheared under a known normal force along a specified shear plane. Porous platens were placed above and below the specimen to enable drainage during shearing. Figure 38 shows a cut-away side view of the direct shear apparatus (DSA).

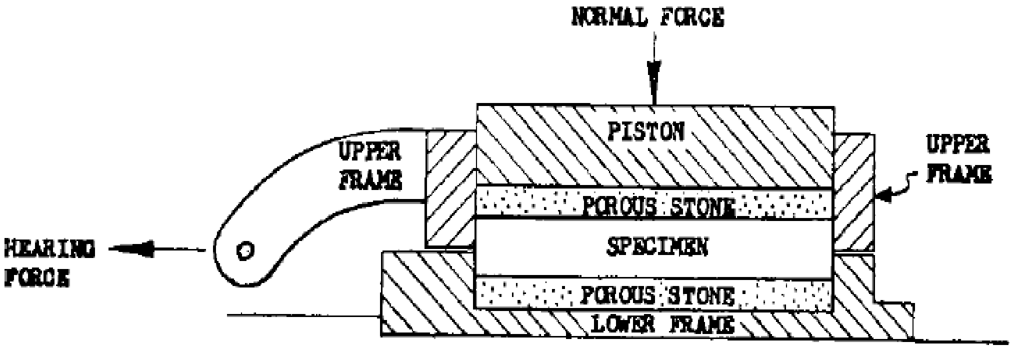

Figure 38. Direct shear box diagram, cross sectional view (Source: ASTM, D3080)

Undisturbed and reconstituted specimens were used in the DSA. Undisturbed specimens were gathered from sampling tube methods (ASTM, D1587). Alternatively, reconstituted samples were tamped to the desired bulk density according to ASTM D3080, section 7.5.2. In the case of moist specimens, the test was run for a minimum of 50x the 50% consolidation time so that only a drained response was captured.

Shear box displacement and vertical piston displacement was captured and stored continuously during the test. A calibrated and capable load cell was used to measure the resistance of the granular material to shearing. There were two significant output data sets from the direct shear test. The first was a displacement vs. shear stress curve which described the strength of the granular material and from which it was possible to describe the Mohr-Coulomb failure envelope. The second was a height change vs. displacement curve which described the volume change behavior during shearing.

The direct shear test was a quick and easy way to characterize soils; however, the accuracy of the test was impeded by the imposition of a shear plane. Therefore, the measured shear strength did not necessarily occur on the weakest failure plane. Despite its limitations, it was an effective calibration tool because a virtual direct shear test will exhibit the same forced shear plane. Therefore, the error in physical and virtual direct shear tests was consistent.

Hopper Discharge Test

A grain hopper was developed and built by Research Assistant, Mohammad Mousaviraad at the Soil Dynamics Laboratory at Iowa State University. The hopper was used to collect data on granular material flow and was used as a validation tool for DEM calibration. The hopper footprint was a square with side length=27cm. The hopper walls were made of transparent Lexan polypropylene sheet. The hopper bucket was 50 cm in height. Three chute configurations were available, 0 degree, 30 degree, and 60 degree. A load cell was placed under a collection bucket under the discharge chute of the hopper to measure massflow rate. In addition, a string potentiometer coupled ball was used to continuously measure the height of the center of the granular surface. The hopper discharge test was used to measure the mechanical flow characteristics of corn grains. Figure 39 shows the hopper in the 60 degree chute configuration, filled with corn grains before a discharge test. The grey ball at the top of the corn grain assembly was the string potentiometer coupled ball.

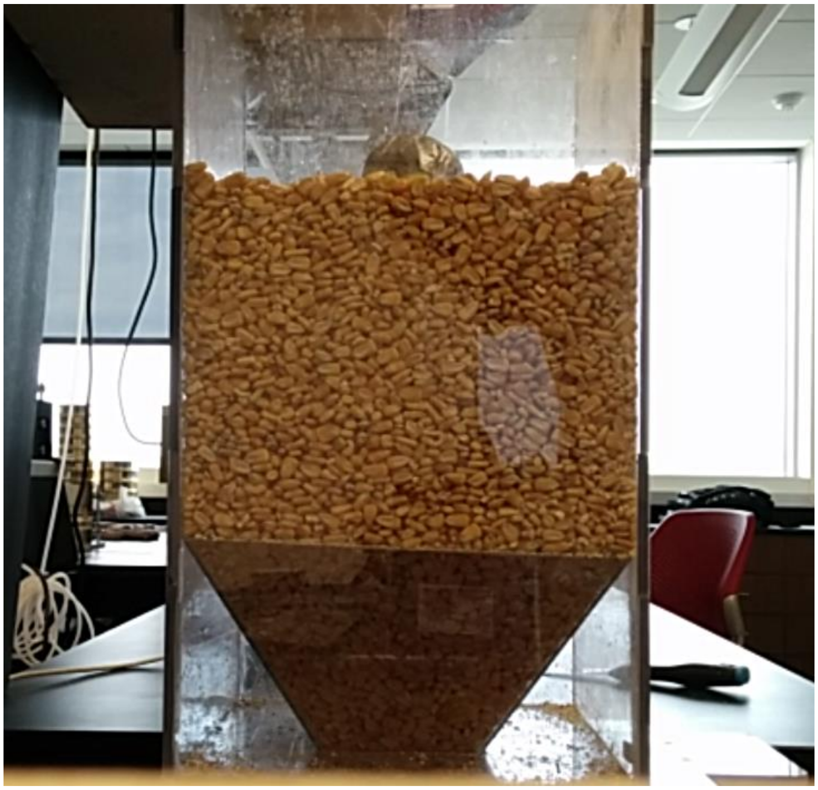

Figure 39. Hopper filled with corn grains before discharge test

Corn grains were gently poured into the hopper in the loosest state possible until the desired fill height was achieved. Then, the data acquisition system was activated and the hopper-stop plate was quickly pulled to initiate grain flow. The mass leaving the hopper and the top surface center displacement was continuously measured. The test concluded when the hopper was empty.

Blade Mixing Test

A blade mixing apparatus was developed to validate DEM calibration models. A torsional load cell was fabricated by outfitting a hollow, square (side length=20 mm), aluminum shaft with four strain gages in a full Wheatstone bridge configuration (Figure 40). It was calibrated by applying a known moment load to the shaft and measuring voltage drop across the Wheatstone bridge circuit. Voltage drop was amplified using an Avia HX711 instrumentation amplifier.

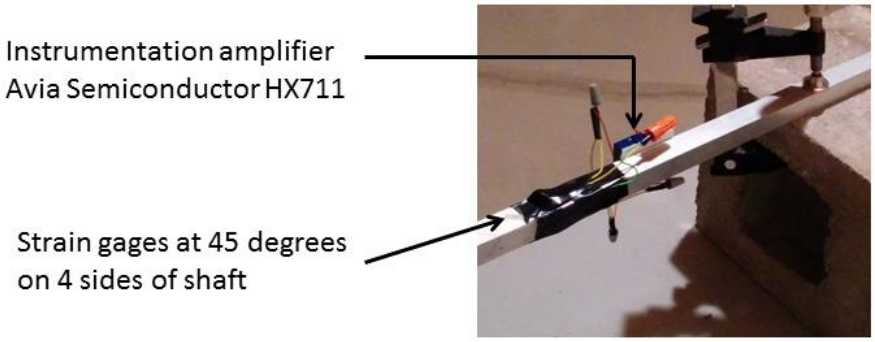

Figure 40. Full Wheatstone bridge torque cell mounted on shaft

A string potentiometer was pulley-coupled to the aluminum shaft to measure angular position. A rectangular (100 mm x 23 mm) steel mixing blade was also bolted to the shaft. The shaft-blade assembly was lowered into a low density polyethylene (LDPE) bucket while a bearing constrained all movement except cylindrical rotation. The LDPE bucket was reinforced with wooden 2x4's to prevent excessive base deformation during operation.

The bucket was filled with granular material and lightly tamped and leveled (Figure 41) to a desired height and bulk density. The bulk density of the media in the mixing bucket was measured and recorded.

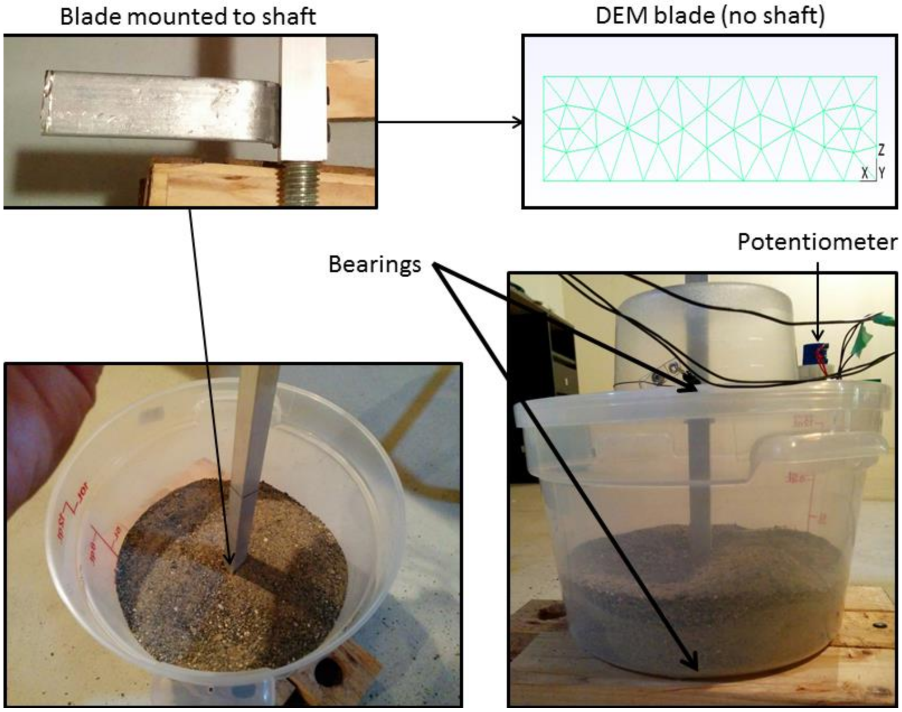

Figure 41. Blade mixing apparatus

Each material testing trial undergoes a consistent procedure. After the granular media is leveled and the data acquisition equipment is active, the blade shaft is manually rotated to sweep the blade through the granular material. Shaft torque and blade angle was measured continuously with respect to time at 10 Hz. Data was acquired via an Arduino Uno microcontroller and saved as comma separated value file on a computer in real time. After the data trace was secured, the blade was removed and the granular specimen was mixed or re-pluviated to establish virgin conditions.

Cone Penetrometer Test

The construction of the soil cone penetrometer was described in ASABE S313.3 (2006). It was typically a slender shaft affixed to a 30 or 60 degree steel cone which penetrated soil either *in-situ* or in lab conditions. The cone was manually plunged into a soil surface at a constant rate. The resistance exhibited by the soil was measured by a load cell which lay in series with the shaft. The depth of penetration was monitored by an ultrasonic range sensor. It was often necessary to place a plate at the surface of the soil to accurately and consistently measure penetration depth because ultrasonic sensors over uneven terrains created noisy depth profiles.

The inner diameter of the PVC pipe section was 10.3 cm. The ratio of container diameter to ASABE cone diameter was 8.2. The PVC pipe section had an adhesively bonded ruler affixed to its inner diameter to determine fill height. The weight scale on which the soil and pipe was weighed was zeroed with only the pipe section present to determine the weight and bulk density of the soil.

ASABE EP542 (2006) defines the standard method for reporting cone penetrometer resistance using a metric called the cone index, also referred to as cone resistance or penetration resistance. The cone index was calculated in equation 2.49. A typical cone penetration resistance or cone index curve was shown in Figure 42.

$$q = \frac{4F_{cone}}{\pi D_{cone}} \tag{2.49}$$

Where q=cone index;

F_{cone} = reaction force;

D_{cone}=diameter of the ASABE cone (D_{cone} for 30 degree cone = 12.53 mm).

In uniform soils, penetration resistance typically reached a steady state limit, q_{lim}. Undrained shear strength was shown to correlate with q_{lim} (Schmertmann, 1975).

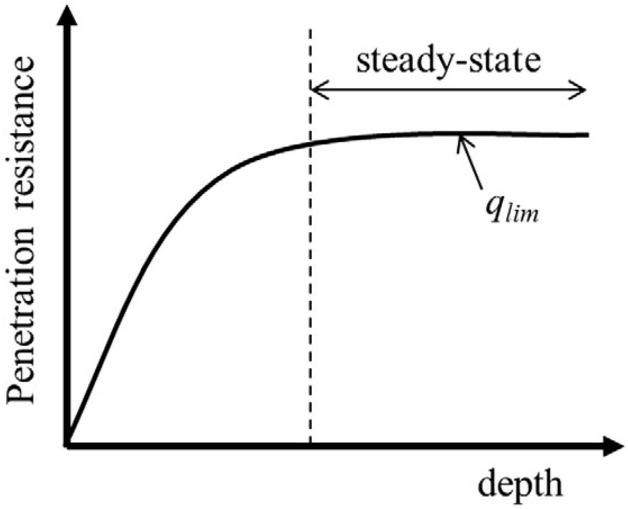

Figure 42. Typical cone penetration resistance or cone index (Source: Alvaro and Ooi, 2016)

Cone penetrometer tests were used in a lab setting to characterize Michigan 2NS Sand (2NS) and Norfolk Sandy Loam (NSL). Cone penetrometer tests underwent consistent procedures. The initially dry soil samples were reconstituted to the desired moisture and bulk density and added to the PVC pipe section. The data acquisition system was activated and the cone of the cone penetrometer device was brought to the top of the soil assembly. Care was taken to ensure that the cone penetrometer was close to vertical and that the ultrasonic senor had a clean flat surface to reflect off of in order to capture accurate depth measurements. The cone was manually lowered into the soil using as little force as possible (to avoid dynamic effects). The cone was lowered until the bottom of the container was reached. The data acquisition system was disconnected and data was secured. The specimen was then removed and re-pluviated into the container for subsequent testing.

CHAPTER 3. A COUPLED SLIDING AND ROLLING FRICTION MODEL FOR DEM CALIBRATION

Abstract

The accuracy of dense Discrete Element Method (DEM) simulations is sensitive to initial density, contact orientation, and interparticle interaction parameters (i.e., contact stiffness, friction, cohesion, particle size and shape, restitution). Although studies have characterized the effects of individual particle interaction parameters on mechanical responses of loaded granular material, research combining parameters for calibration is scarce. Robust calibration methodology combining sliding and rolling friction coefficients was developed and validated to predict critical state soil strength of initially dense DEM particle assemblies.

Introduction

Triaxial test simulations have been used effectively to calibrate discrete element methods (DEM) parameters to mechanical responses of granular materials using open-loop and probabilistic methods (e.g., Zhang et al., 2011; Wang and Tonon, 2010; Medina-Cetina and Khoa, 2011; Belheine et al., 2009; Salot et al., 2009). However, closed-loop and single-iteration calibrations of DEM parameters to bulk mechanical behavior is challenging because many interparticle interactions are coupled such that they attenuate or intensify each other’s effects on mechanical outcomes. One such coupling is the complex interaction of sliding and rolling friction. It has been shown that sliding friction coefficient is positively associated with bulk friction characteristics (Liu et al., 2005; Widulinski et al., 2009; Zhao et al., 2011). Similarly, Huang et al. (2013) showed that rolling friction coefficient significantly affected the bulk internal friction angle of dense granular assemblies. Rolling friction was of particular interest because it simplifies particle shape modeling (Wensrich and Katterfeld, 2012). Free particle rotation interlocked particles have been described in the context of shear band development (Iwashita and Oda, 1998) and strength (Utili and Nova, 2008). To show the moderating effects of rolling friction, Widuliński et al. (2009) compared the effects of varying the sliding friction coefficient in two rolling friction conditions. These studies provided insight into the complexity of interaction between sliding friction and rolling friction, but limited information has been reported. Modeling physically accurate shearing behavior in soils required robust shape approximation which is computationally impractical for real-world systems. Rotationally-free DEM codes with shape approximation cannot develop expected shear capacity without moment to resist rotation. Indeed, rolling friction models were introduced in DEM code to bridge this gap. However, the complexity of kinetic shear resistance has increased with the addition of the rolling friction coefficient. To ease calibration, a semi-empirical combined friction model was proposed based on single particle behavior. This combined friction model strongly correlated with critical state mechanical strength from triaxial and direct shear test simulations making it an ideal base for calibration.

DEM applications in terramechanics

DEM was used to simulate natural geomechanical phenomena (Utili and Nova, 2008) and soil-tool interaction problems (Obermayr et al., 2013; Shmulevich, 2010; and Chen et al., 2013). When particles in a DEM environment were used to model granular geomaterials, particle interaction parameters were generally tuned within the context of standardized lab tests (uniaxial, triaxial, oedometer, and Cassagrande's shear test). The selection of the lab test varied with respect to the physical phenomena, failure plane orientation, and strain rate that are being simulated. For instance, virtual uniaxial test simulations were used to calibrate DEM parameters to unconfined strength (Yoon, 2007). For simulating dynamic processes, stress wave velocities were the target of calibration (Holt et al., 2005). Triaxial test simulations were commonly used as a calibration tool for simulation of slow, pseudo-static, in-situ soil manipulation (Ting et al., 1989). However, Salazar et al. (2015) demonstrated that even mechanical responses from simple box shear tests were difficult to calibrate against.

Background

Discrete Element Method

Discrete element method (DEM) is numerical technique where particle interactions are modeled using equations of motion and contact laws. Cundall and Strack (1979) developed DEM from to simulate the behavior of granular materials. Equations of motion for each particle are shown in equations 3.1 and 3.2. The resultant force on a particle, $F_{resultant}$, is calculated in equation 3.1

$$F_{resultant} = m\ddot{x} \tag{3.1}$$

where

m = particle mass and

$\ddot{x}$ = particle acceleration.

The resultant moment on a particle, $M_{resultant}$, is calculated by equation 3.2

$$M_{resultant} = I\ddot{\theta} \tag{3.2}$$

where

I = mass moment of particle inertia and

$\ddot{\theta}$ = angular particle acceleration.

$F_{resultant}$ and $M_{resultant}$ account for body forces, force fields, and interparticle interactions. DEM codes, such as the open-source LIGGGHTS, use idealized elastic spheres to model contacts between particles that interact with each other according to Hookean or Hertzian contact laws. In addition, forces that depend on contact (e.g., micro-scale cohesion, restitution (damping), sliding friction, and rolling friction) can also act on particles. Hertzian contact is simplified in DEM code for efficient calculation, as in equation 3.3.

$$F_n = k_n \delta_n \tag{3.3}$$

where $k_n = \frac{4}{3}E^*\sqrt{R^*\delta_n}$;

$\frac{1}{E^*} = \frac{1-\nu_1^2}{E_1} + \frac{1-\nu_2^2}{E_2}$;

$\frac{1}{R^*} = \frac{1}{R_1} + \frac{1}{R_2}$;

k_n = normal stiffness;

δ_n = normal overlap;

E_1,E_2 = Young's modulus of 1st and 2nd particle respectively;

ν_1,ν_2 = Poisson's ratio of 1st and 2nd particle respectively;

R_1,R_2 = Radius of 1st and 2nd particle respectively.

When contact is established, contact-dependent interparticle forces, such as friction, can be activated. Force due to sliding friction between two particles exhibiting relative tangential motion is calculated by equation 3.4

$$F_{sliding} = \mu_s N \tag{3.4}$$

where

μ_s = sliding friction coefficient, and

N = normal contact force.

Per the usual convention, the orientation of the direction vector of $F_{sliding}$ is opposite the tangential relative velocity vector. In addition to sliding friction, rolling friction is present as a contact-dependent force. Rolling friction is a particle's resistance to relative rolling motion between particles as a function of normal contact forces (N) and shear stiffness. Two rolling friction models are built into LIGGGHTS: the Constant Directional Torque (CDT) model and the Elasto-Plastic Spring Dashpot (EPSD) model. The CDT model adds torque to a particle by equations 3.5, 3.6, and 3.7 (LIGGGHTS Manual 2015).

$$T_{CDT} = \frac{\mu_R N \omega_{shear}}{|\omega_{shear}| R_{eff}} \tag{3.5}$$

$$\omega_r = \omega_1 - \omega_2 \tag{3.6}$$

$$\omega_{\text{shear}} = proj_{shear\ contact\ plane}(\omega_r) \tag{3.7}$$

where

ω_1 = angular velocity of particle 1,

ω_2 = angular velocity of particle 2,

R_{eff} = effective radius of two particles in contact,

N = normal force acting between particles in contact, and

μ_R = rolling friction coefficient.

The rotational resistance in the CDT model can exceed the moment required to fully mobilize a particle and therefore, it can create an oscillatory equilibrium state. On the other hand, rotational resistance in the EPSD model is bounded by full mobilization torque. The torque contribution from the EPSD model is described in equations 3.8-3.12. Note that since equation 3.9 limits resistance torque, the rolling resistance behavior is perfectly plastic above full mobilization torque.

$$T_{EPSD,t+\Delta t} = T_{r,t} + \Delta T_r \tag{3.8}$$

$$|T_{r,t+\Delta t}| \leq T_{r-max} \tag{3.9}$$

$$T_{r-max} = \mu_r R_{eff} N \tag{3.10}$$

$$\Delta T_r = -k_r \Delta\theta_r \tag{3.11}$$

$$k_r = k_t R_{eff}^2 \tag{3.12}$$

where

$T_{EPSD,t+\Delta t}$ = torque contribution in next DEM calculation cycle,

$T_{r,t}$ = torque contribution in previous DEM calculation cycle,

k_r = radial particle stiffness,

k_t = tangential particle stiffness, and

$\Delta\theta_r$ = incremental relative rotation between particles.

Ai et al. (2011) reported that the EPSD model is superior to the CDT model in terms of achieving low-kinetic energy steady state conditions for pseudo-static DEM analyses.

Methods

Single particle model

A single particle model was developed to study the combined effects of sliding and rolling friction at the micro-scale. A rigid sphere was placed on a surface while two forces acted on it (Figure 43). The particle exhibited motion only resisted by inertia, sliding friction, and rolling friction. A free body diagram of the single particle model is shown in Figure 44.

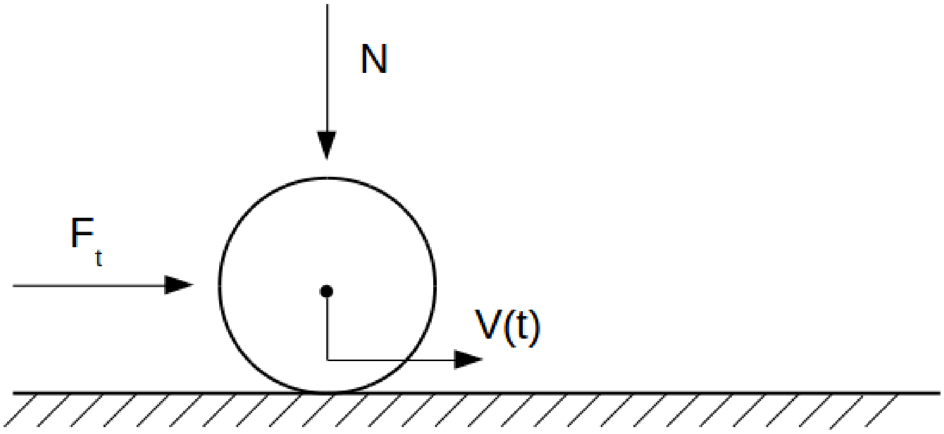

Figure 43. Single particle model of rigid sphere on plane.

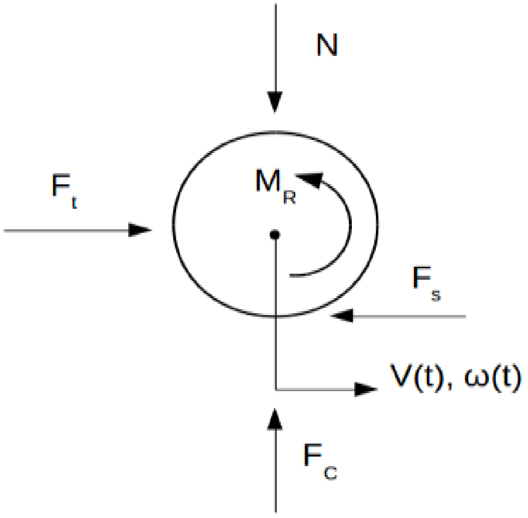

Figure 44. Free body diagram of single particle model.

Where F_t = arbitrary force oriented parallel with surface that the particle is resting on,

N = arbitrary force acting perpendicular to the surface that the particle is resting on,

F_c = contact force,

F_s = force due to sliding friction,

M_R = moment due to rolling friction,

$V(t)$ = velocity of particle, and

$\omega(t)$ = angular velocity of particle.

The energy balance of the single particle system provided a fundamental coupling of resistance to rotational and translational motion against a rigid plane (equation 3.13).

$$\frac{d}{dt}E_{in} = \frac{d}{dt}E_{kinetic} + \frac{d}{dt}E_{friction} + \frac{d}{dt}E_{viscous} \qquad (3.13)$$

where $\frac{d}{dt}E_{in}$ = instantaneous power transferred to the system;

$\frac{d}{dt}E_{kinetic}$= rate of change of particle kinetic energy;

$\frac{d}{dt}E_{friction}$= rate of energy dissipation through friction;

and $\frac{d}{dt}E_{viscous}$= rate of energy dissipation from viscous effects.

To simplify analysis, a rigid sphere was considered. Therefore, elastic and plastic strain energy was *not* included in equation 3.13. In addition, the rigid sphere was non-cohesive. Equation 3.14 describes the friction term of the energy balance equation.

$$\frac{d}{dt}E_{friction} = \mu_s N\, v_s + \mu_R N\, r\, \omega \qquad (3.14)$$

where v_s = sliding velocity (tangential velocity);

and r = particle radius.

In order to reduce sliding and rolling friction coefficients into a single effective friction term, the rate of dissipation needed to be truncated so that it was only dependent on linear velocity and normal contact force (equation 3.15).

$$\frac{d}{dt}E_{friction-simple} = \mu_{eff} N\, V \qquad (3.15)$$

where $E_{friction\text{-}simple}$ = $E_{friction}$ with combined sliding and rolling terms;

and μ_{eff} = effective fiction coefficient that combines sliding and rolling friction coefficients.

To proceed, a single particle model with null rolling friction coefficient, μ_R=0, was considered, relationships between linear and angular velocity needed to be established. By the definition of rolling friction coefficient in the EPSD model, boundary conditions for the ratio of angular velocity to linear velocity for a rigid body were limited by equation 3.16.

$$0 \leq \frac{\omega r}{V} \leq 1 \tag{3.16}$$

A rolling Hertzian sphere's resistance to motion was dependent on the magnitude of the normal force present. In fact, it was found that the ratio of shearing forces to normal forces affects the upper bound of $\frac{\omega r}{V}$ (Figure 45). Numerical simulations of a rolling sphere on a flat plane reveal that, in the absence of μ_R, the sliding friction coefficient affected $\frac{\omega r}{V}$ up to a ceiling.

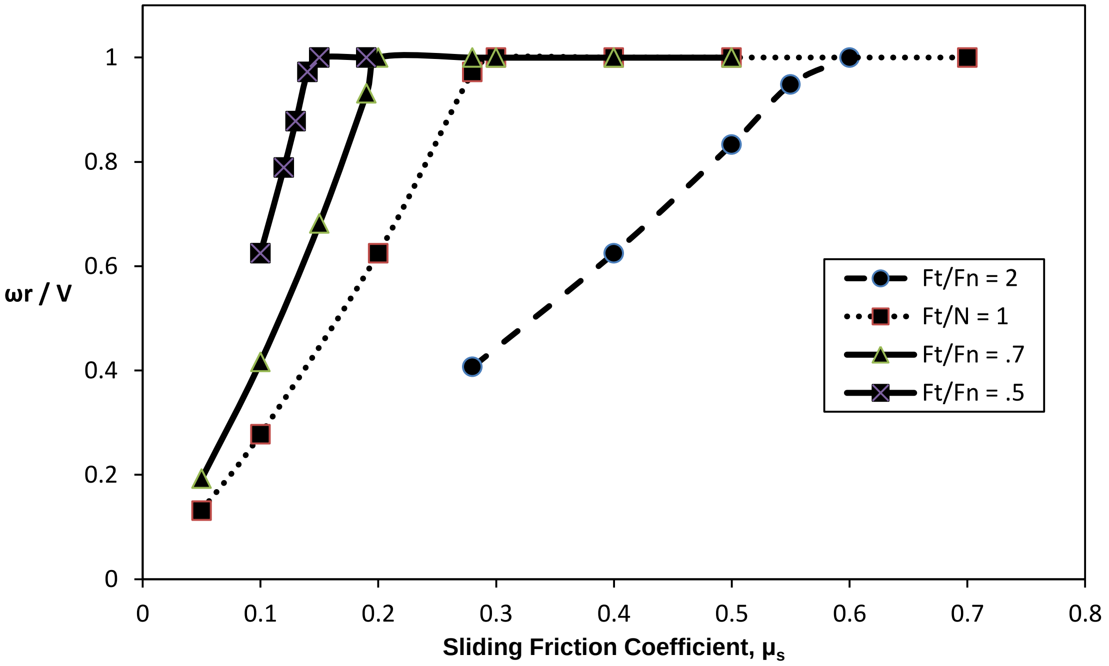

Figure 45. Relationship between tangential and linear velocity for various force ratios with respect to sliding friction coefficient

The limiting friction for each force ratio, F_t/F_n, is plotted in Figure 46.

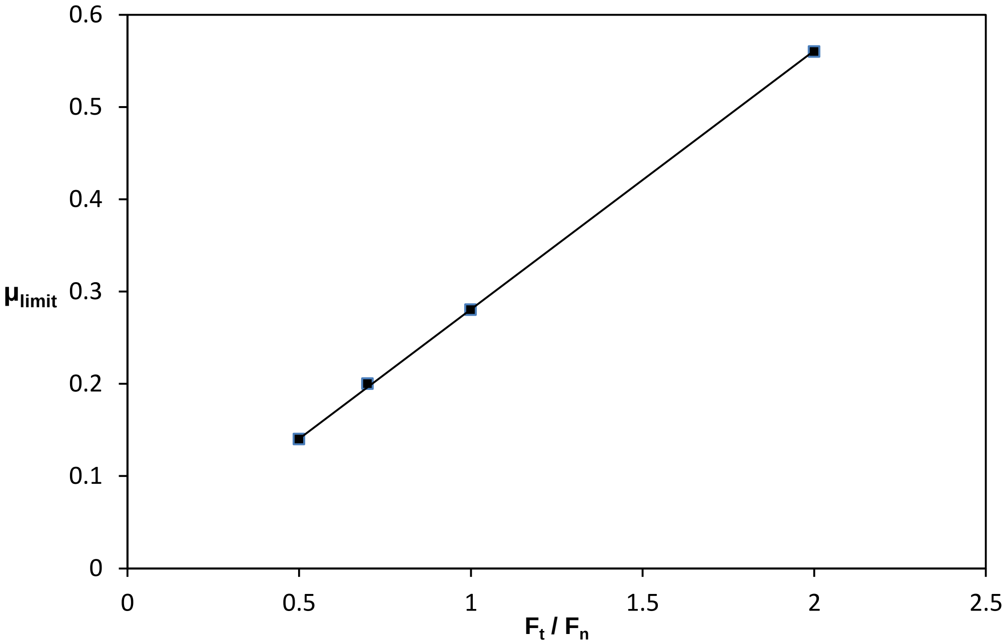

Figure 46. Limiting friction coefficient with respect to force ratio

The limiting coefficient of sliding friction was a linear function of F_t/F_n which was approximated as $\mu_{limit} \sim 0.28(\frac{F_t}{F_n})$. Since $\frac{\omega r}{V}$ was not affected by sliding friction coefficients above the limiting friction, any sliding friction coefficients that exceed the limiting friction were superfluous. Therefore, the minimum effective coefficient of friction was defined by the condition statement in equation 3.17 and 3.18. Observations by Suhr and Six (2016) of contact force dependent coefficient of friction confirm the results in Figure 46.

$$if\ \frac{\omega r}{V} \geq 1, then\ \mu_{\min} = \mu_{limit} \tag{3.17}$$

$$else\ \mu_{\min} = \frac{\omega r}{V} \mu_{limit} \tag{3.18}$$

The extreme case of $\mu_R = 0$ was reduced to a boundary condtion. The other extreme case of $\mu_R \geq \mu_s$ was trivial. The relationship between $\frac{\omega r}{V}$ and μ_{eff} were now effectively described. Adding rolling friction coefficient back into the system, angular velocity was linearly related to total moment, and rolling resistance moment was linearly related to rolling friction coefficient. Therefore the function for $\frac{\omega r}{V}$ was nearly linear with respect to rolling friction coefficient (equation 3.19).

$$\frac{\omega r}{V} = \left(1 - \frac{\mu_R}{\mu_s'}\right) \tag{3.19}$$

where $\mu_s' = \frac{\omega r}{V}\mu_{min} + \mu_s\left(1 - \frac{\omega r}{V}\right)$

By including equation 3.18 into energy dissipation rate (equation 3.13), and substituting μ_s' for μ_s to respect the limits established by μ_{min}, the new frictional dissipation rate equation was written as equation 3.20.

$$\frac{d}{dt}E_{friction} = \mu_s' NV + \mu_R \frac{\omega r}{V} NV \tag{3.20}$$

Factoring out N and V resulted in equation 3.21.

$$\frac{d}{dt}E_{friction} = \left[\mu_s' + \mu_R \frac{\omega r}{V}\right] N\, V \tag{3.21}$$

The effective coefficient of friction was capped by μ_s, therefore the contribution of the μ_R is linearly adjusted to μ_R' (equation 3.22).

$$\mu_R' = \mu_R\left(1 - \frac{\mu_s'}{\mu_s}\right) \tag{3.22}$$

The linear adjustment of μ_R was an approximation that yields good results for calibration purposes. The reduced frictional dissipation rate equation (3.15) provided a template to extract an effective friction coefficient (equations 3.23 and 3.24).

$$\text{If } \mu_R > \mu_{min}\text{, then } \mu_{eff} = \mu_s' + \mu_R' \frac{\omega r}{V} \tag{3.23}$$

$$\text{else } \mu_{eff} = \mu_s' \tag{3.24}$$

The equation for effective friction coefficient was only valid for rolling friction coefficients that were smaller than the sliding friction coefficient. In the case where rolling friction coefficient exceeded sliding friction coefficient, the effective friction coefficient was capped by sliding friction. In addition, the minimum effective friction coefficient was zero. Therefore, a complete solution for effective friction coefficient of Hertzian sphere on a plane is presented in equations 3.25-3.27.

$$\text{If } \mu_R \geq \mu_s\text{, then } \mu_{eff} = \mu_s; \tag{3.25}$$

$$\text{Else if } \mu_R < \mu_s \text{ and } \mu_R > \mu_{min} \text{ then } \mu_{eff} = \mu_s' + \mu_R' \frac{\omega r}{V}; \tag{3.26}$$

$$\text{Else } \mu_{eff} = \mu_s' \tag{3.27}$$

Where $\frac{\omega r}{V}$ is described in Figure 45.

To verify the model for effective friction coefficient, the single particle model was simulated 81 times in LIGGGHTS and only the sliding and rolling friction coefficients were uniformly varied between 0 and 1 per a 9^2 factorial design. A Hertzian contact model was used and the Young's modulus and Poisson's ratio of the sphere and wall were $1.0\text{x}10^9$ Pa and 0.3, respectively. Cohesion and damping were excluded from the simulations. The current set of simulations was run with shear history activated. However, in preliminary studies, it was found that shear history did not affect the results at all. In addition, tangential contact components were very insensitive to changes. Steady state particle acceleration was captured and stored. The equation of motion combining sliding and rolling friction was used to assess effective friction (equation 3.28).

$$F_t - F_F = m\frac{dv(t)}{dt} \tag{3.28}$$

where $F_F = \mu_{eff} N$.

Substituting the acceleration obtained from the single particle numerical model and solving for μ_{eff} produced the raw data shown in Figure 47. The approximation for μ_{eff} was shown as the translucent surface. The residual error between the numerical model and the approximation was shown as a color map projected below the data. Points were plotted with respect to normalized rolling friction (μ_R/μ_s) because the EPSD rolling friction model was insensitive to μ_R greater than μ_s.

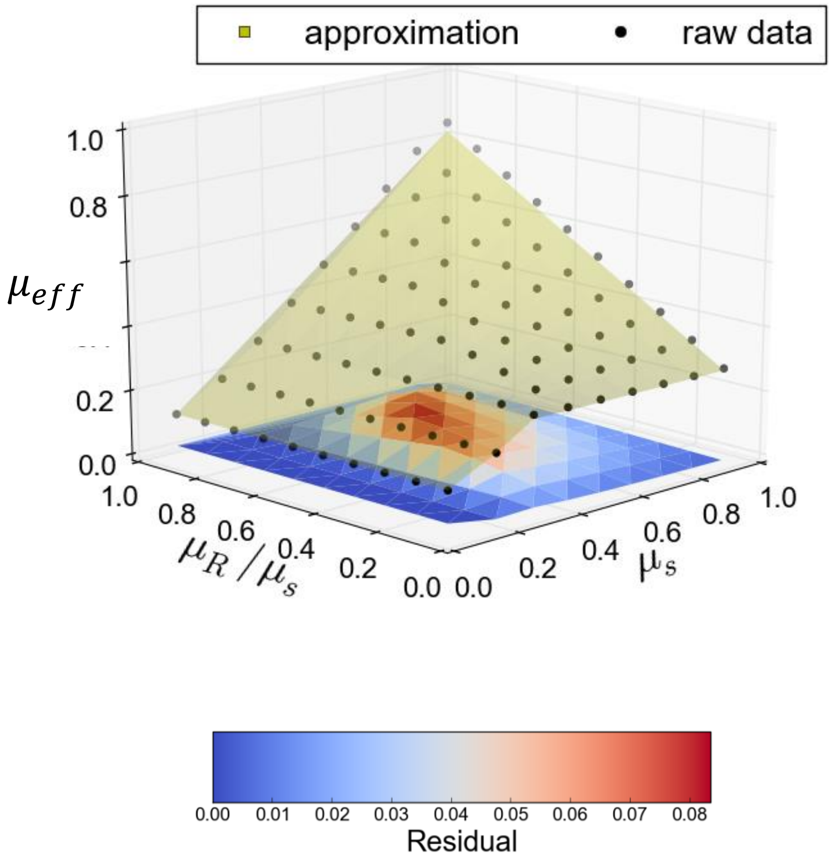

Figure 47. Effective friction coefficient, approximation compared to numerical simulation for F_t/F_n =1.

The residual error in Figure 47 was likely due to the linearization of rolling friction effects which are non-linear with respect to normal force, Young's modulus, and viscoelastic constants (Karapetyan, 2010). However, for the purposes of calibration, the error was small and did not detract from the utility of this approximation. Large error may occur when the particle Young's modulus is low, such that there becomes a significant different between the particle radius and the effective contact radius. This error should be quantified in future work.

The DEM model used to simulate the results in Figure 47 was tested for sensitivity to tangential contact stiffness and damping. The variation in effective friction was found to be much smaller than the residuals calculated in Figure 47. Therefore, tangential stiffness and damping were left activated for all subsequent simulations.

Figure 47 verified the utility of μ_{eff} for a single particle rolling on a plane. For calibration purposes, the relationship between μ_{eff} and bulk friction angle needs to be tested. It was hypothesized that μ_{eff} is proportional to bulk friction angle for dense granular assemblies. Equations 3.25-3.27 provided the framework for the scale-invariant interparticle friction angle. As such, it was also hypothesized that the relationship between interparticle friction angle and critical state friction angle was scale-invariant.

Triaxial tests

The influence of effective friction needed to be quantified on the macro-scale, especially with respect to global strength and volume change characteristics of dense granular assemblies.

Eleven triaxial test simulations were ran with different combinations of sliding and rolling friction coefficients. All triaxial tests were created as cylindrical specimens with varying numbers of DEM particles (all exceeding 10,000) shown in Figure 48a. An approach similar to the one described by Wang and Tonon (2010) was used to write a custom operator for LIGGGHTS to model confining pressure for membrane-wrapped cylindrical specimens. The confining pressure in the triaxial test simulations was varied, and the specimens were equilibrated under the confining pressure until void ratio and reaction forces at the caps approached steady state. The caps were adjusted slightly (less than 0.01% strain) to produce an isotropic stress state in the specimen. After numerical inspection that the specimen was in equilibrium at an isotropic stress state, it was deviatorically compressed until axial strain reached 35%, as shown in Figure 48.

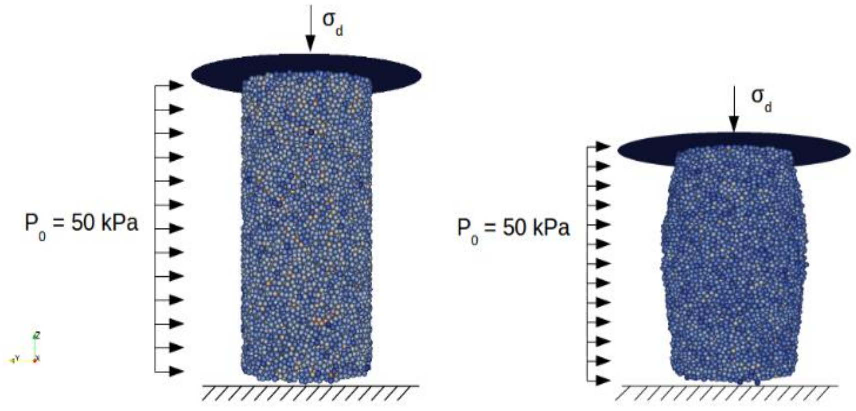

(a) (b)

Figure 48. Triaxial test specimen, a) before triaxial compression, and b) after triaxial compression.

Direct shear tests

Ten direct shear tests were also modeled in DEM with each test exceeding 10000 particles. The virtual shear box was a 3D rectangular prism with a square base (100 mm x 100 mm) and a height of 50 mm. The lid of the shear box acted as a rigid body and exerted normal force on the particle assembly within the box. Both sliding and rolling friction coefficients between the particles and the box wall were kept at 0.9. Particles were initialized in random positions in the shear box at a target solid fraction. The large potential energy in the system due to particle overlap was dissipated over 100k DEM calculation cycles. Upon reaching equilibrium, the top half of the shear box was advanced at a rate of 0.1 mm/s until the total displacement reached 12 mm. Reaction forces from the upper half of the shear box was monitored. The bulk friction angle from virtual direct shear tests is reported by the ratio of shear to normal force acting on the box. A particle assembly in the shear box is shown in Figure 49.

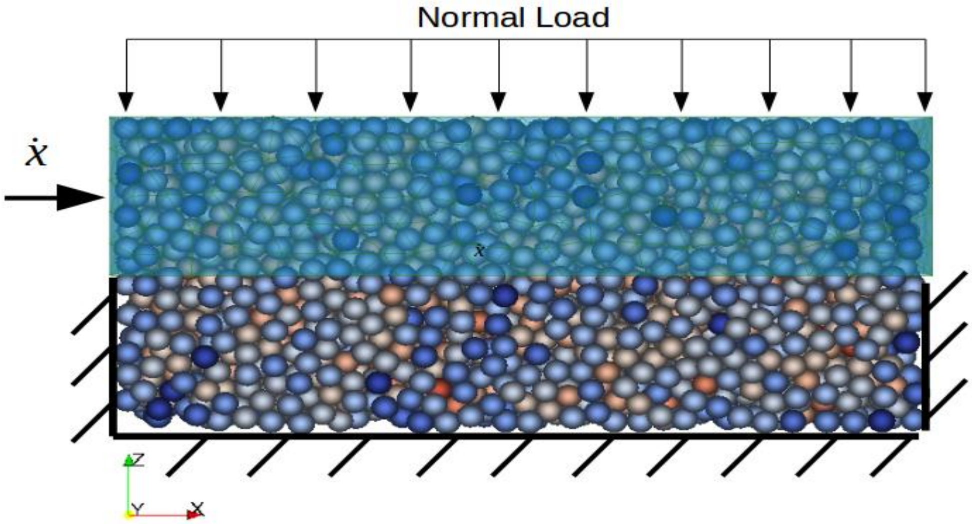

Figure 49. Boundary conditions of virtual direct shear test

Particle size distribution

O'Sullivan et al advised that monodisperse spheres cannot model real soils because crystallization occurred at high packing densities (2002) and O'Sullivan cautioned that monodisperse spheres could not form a realistic number of contacts per particle so the moment imparted on particles was not physically accurate (2011). However, in the presence of rolling friction, the moment imparted on a virtual particle was independent of particle size distribution and shape. Mono and polydisperse specimens were created to assess differences in mechanical response. The poly disperse specimens were created using a Gaussian distribution of particle centered on a mean radius. The mean radius and standard deviation of particles are reported for each specimen.

Results

The triaxial test simulations were run until axial strain reached 25%. Volumetric strain and deviator stress (equation 3.29) were calculated and plotted for each simulation.

$$\sigma_d = \frac{\sigma_1 - \sigma_3}{2} \tag{3.29}$$

In the triaxial/biaxial test case, third principle stress is equal to confining pressure (σ_3=P_0). As described in equation 30, first principle stresses, σ_1, were obtained by dividing the triaxial test specimen into ten layers ($n=10$) along the z-axis (see Figure 48). The reaction at the cap of the triaxial test apparatus (R) was then divided by surface area at the interface between each layer (A_i). Then, deviator stresses from each layer were averaged over the entire specimen.

$$\sigma_1 = \frac{1}{n}\sum_{i=1}^{n}\frac{R}{A_i} \tag{3.30}$$

Monodisperse vs. Polydisperse

A common observation in numerical simulations of mono and poly-disperse specimens was that the critical state strength of granular assemblies was independent of variance in particle size distribution as long as the mean particle size remains constant. That is, a monodisperse specimen with particle radius = 1.5 mm exhibits a similar critical state strength as a polydisperse specimen with a Gaussian size distribution and mean radius = 1.5 mm. Figure 50 shows the virtual stress-strain and volume change response of mono and poly-disperse specimens with identical microscale friction characteristics. Initial void ratio was iterated to match complete mechanical responses between mono- and polydisperse specimens. Yan and Dong (2011) reported identical observations in cubic triaxial tests of polydisperse sphere. Details of the DEM simulation parameters were summarized in Table 9. Noting this observation, subsequent triaxial tests were performed using both monodisperse and polydisperse specimens.

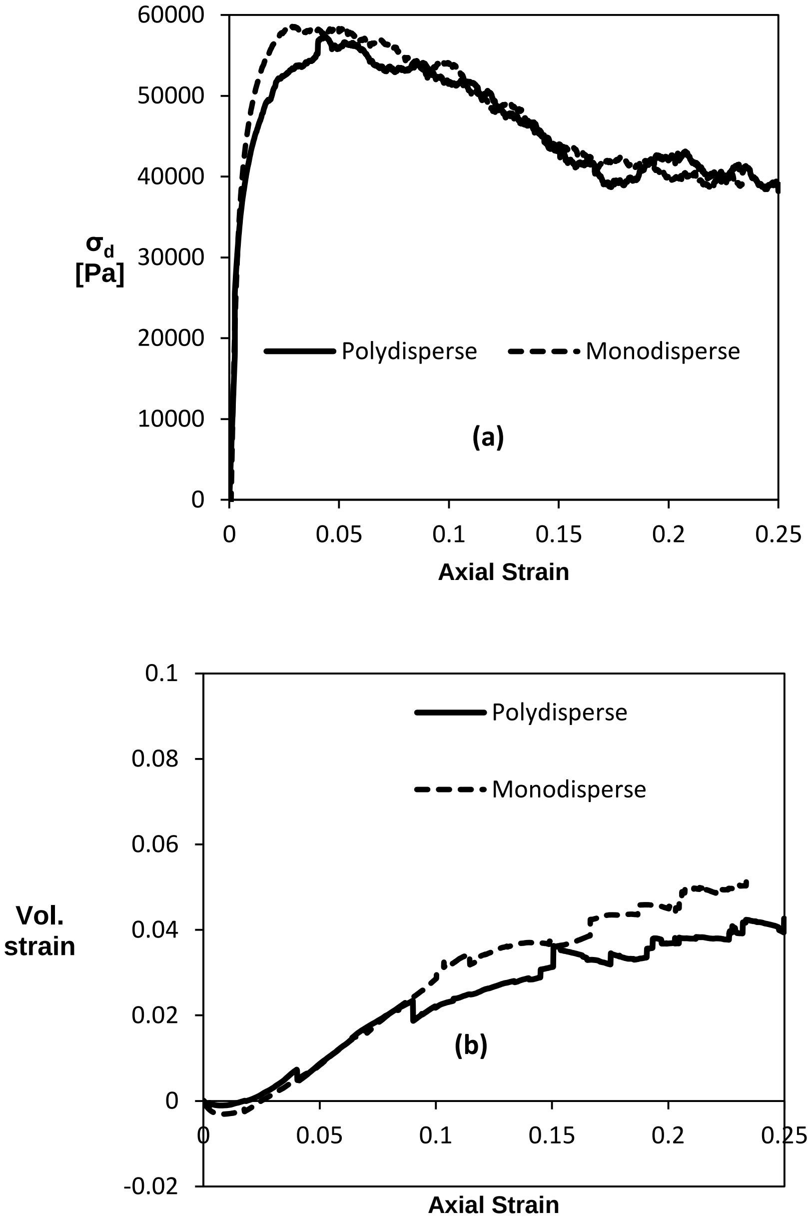

Figure 50. Stress-strain (a) and volume change (b) response from triaxial tests with mono and poly-disperse specimens

Table 9. DEM parameters for comparison of mono and polydisperse triaxial test specimens

	Specimen	
DEM Parameter	Monodisperse	Polydisperse
Input Parameters		
Particle radius, r	1.5mm	mean=1.5mm, SD=0.03mm
Contact model	Hertz	
Youngs modulus, E	2.9×10^6 kPa	
Poisson's ratio, ν	0.3	
Sliding friction coef, μ_s	0.5	
Rolling friction model	EPSD2	
Rolling friction coef, μ_R	0.2	
Confining pressure, P_0	50 kPa	
Initial void ratio, e_0	0.7390	0.7770
Number of particles	29468	26775

Effective friction coefficient

Additional mono and polydisperse triaxial test simulations were performed with DEM characteristics identical to the parameters shown in Table 9, except particle size, sliding friction, rolling friction, and confining pressure. The DEM parameters used in the simulations are shown in Table 10. Additional triaxial test simulation data from Yan and Dong (2011), Huang et al. (2014), Thornton (2000), Kozicki (2012), and Gong et al. (2012) is included to provide additional corroboration for the interparticle-to-bulk friction relationship defined by combining sliding and rolling effects. It is interesting to note that the mentioned authors used various contact formulations and particle size distributions. The relationships described the effective friction coefficient are independent of particle size and contact style.

Table 10. DEM parameters and specimen properties of triaxial test simulations

Trial	Mono-poly disperse	E [kPa]	P_0 [kPa]	Mean particle radius [m]	Std dev of particle radius [m]	μ_s	μ_R
1	mono	2.9x10^{6}	50	0.0017	0	0.5	0.2
2	poly	2.9x10^{6}	50	0.0017	0.0002	0.4	0.2
3	mono	2.9x10^{6}	70	0.0012	0	0.4	0.2
4	poly	2.9x10^{6}	100	0.0013	0.0002	0.4	0.1
5	mono	2.9x10^{6}	120	0.002	0	0.2	0.2
6	poly	4.0x10^{6}	30	0.002	0.0003	0.3	0.1
7	mono	5.0x10^{6}	120	0.0012	0	0.35	0.25
8	mono	4.0x10^{6}	120	0.0016	0	0.5	0.5
9	poly	4.0x10^{6}	30	0.001	0.0002	0.3	0.2
10	mono	2.9x10^{6}	400	0.005	0	0.6	0.32
11	mono	2.9x10^{6}	400	0.005	0	0.6	0.5

The virtual triaxial test results were analyzed to find the critical state strength of the material. To determine the critical state strength, volume change was monitored and deviator stress was recorded when dilatancy angle approached zero. The bulk friction angle at critical state was determined by constructing Mohr's circle for each trial.

The calculation of μ_{eff} required the force ratio, F_t/F_n, to be known. In the case of granular assemblies, F_t/F_n was calculated from the bulk friction angle, φ (equation 3.31).

$$\frac{F_t}{F_n} = \tan(\varphi) \tag{3.31}$$

Equation 3.30 was necessary for all $\mu_R < \mu_{min}$.

The interparticle friction angle, φ_p, was calculated by equation 3.32.

$$\varphi_p = \tan^{-1}(\mu_{eff}) \tag{3.32}$$

Figure 51 shows the relationship between interparticle friction angle and bulk friction angle at critical state from the simulated parameter sets in Table 10.

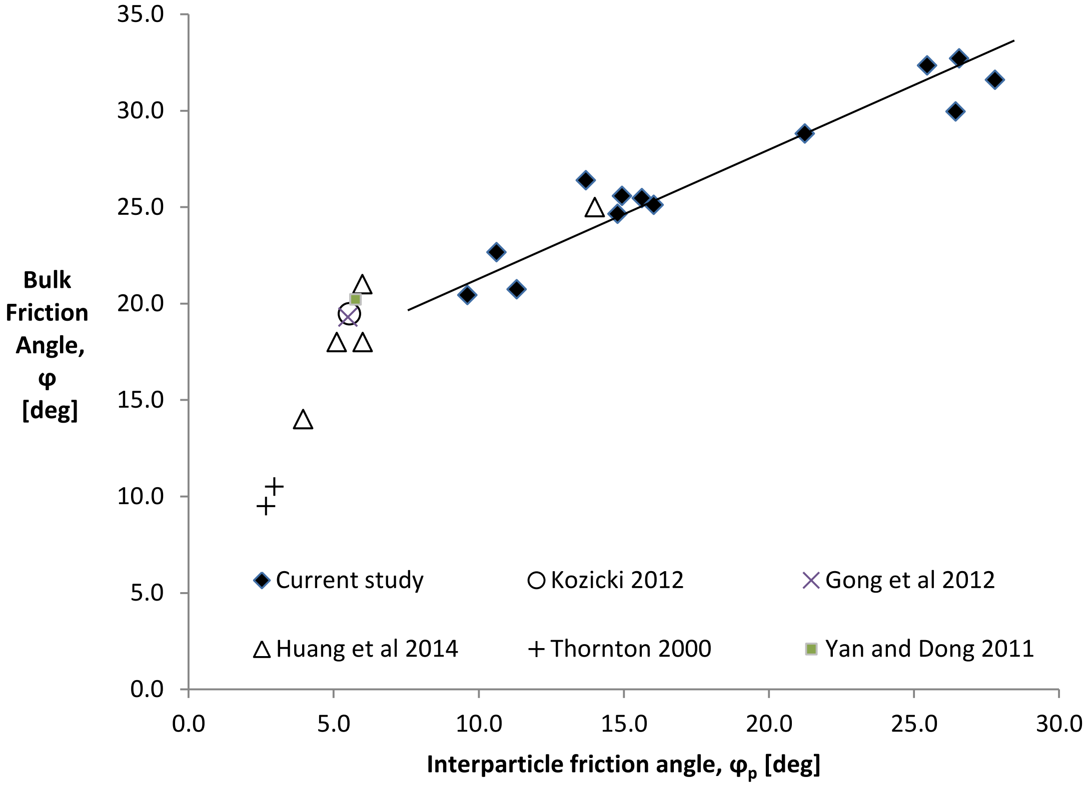

Figure 51. Relationship between effective interparticle friction angle and bulk critical state friction angle from virtual triaxial test simulations (Note: this not a simple reproduction of data, rather it follows the methods to calculate φ_p defined in section 0).

The linear portion of the bulk friction angle curve was empirically related to the interparticle friction angle by the linear regression equation (3.32), where R^2=.93, RSS=1.29.

$$\varphi = 0.682\varphi_p + 14.7 \tag{3.33}$$

The external virtual triaxial test simulation data found in Figure 51 was generally simulated using spheres with either free or fixed rotation in the absence of a rolling friction model. In the case of free rotation, μ_R was taken as zero. For instance, Thornton (2000) reported that bulk friction angle did not necessarily increase as interparticle sliding friction increased. However, our analysis showed that increasing sliding friction alone did not increase the effective interparticle friction angle, φ_p and therefore, all of

Thornton's data was concentrated below $\varphi_p=5^o$. In the case of fixed rotation, $\mu_R=\mu_s$ was assumed. However, $\mu_R=\mu_s$ was not always a valid assumption because the effective friction paradigm only considered moment imparted on a particle from friction effects, therefore, fixed rotation often produced stronger particle assemblies when compared to equivalent $\mu_R=\mu_s$ systems. For instance, Huang et al. (2014) reported fixed rotation triaxial test simulation with $\varphi_p = 27^o$ and $\varphi = 49^o$, which deviated significantly from the prediction of equation 3.32. However, equation 3.32 performed well for the strength ranges of real sands, powders, and other natural granular materials.

Bulk friction angle of granular material varied with respect to the testing method. Therefore, virtual direct shear tests were also used to investigate the relationship between effective interparticle friction angle, φ_p, and critical state bulk friction angle, φ (Figure 52).

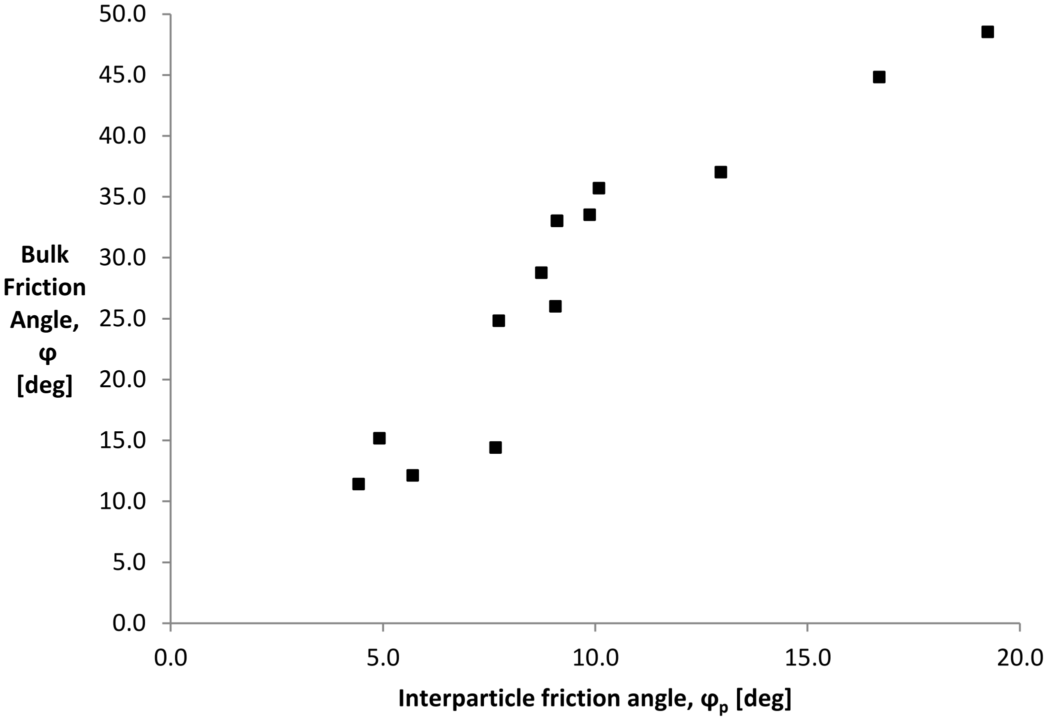

Figure 52. Bulk friction angle with respect to interparticle friction angle from direct shear tests

The direct shear data reported in Figure 52 was qualitatively similar to triaxial test data. There was a notable quantitative difference in that virtual direct shear tests reported higher bulk friction angles than virtual triaxial tests for equivalent granular materials.

Discussion

Two hypotheses were tested using the framework established in equations 3.25-3.27.
1) Effective friction coefficient, μ_{eff}, was uniquely proportional to the bulk friction angle: The results in Figure 51 showed a clear relationship between interparticle friction (as determined by μ_{eff}) and bulk friction angle.
2) Effective friction coefficient provided a scale-invariant calibration parameter. Table 10 showed that, though various particle sizes and size distributions were used to generate triaxial and direct shear test specimens, the resulting interparticle friction angle scaled uniquely with bulk friction angle. Future work will address implementing μ_{eff} in scaling laws for dense granular dynamics.

Calibration

The empirical relationship from Figure 51 was leveraged to calibrate a DEM simulation to physical test results. This study considered the triaxial test data on Toyura sand reported by Fukushima and Tatsuoka (1984). The calibration table is presented in Table 11.

Table 11. Calibration procedure for Toyura sand

	Parameter	Value	Reference
Physical triaxial test data	P_0 [kPa]	400	Fukushima and Tatsuoka (1984)
	Stress ratio, b	3.3	
	Bulk friction angle, ϕ [deg]	32.2^{o}	
Calibration	Desired ϕ_p	25.5^{o}	Eqn 3.33, figure 9
	desired μ_{eff}	0.476	Equation 3.32
	F_t/F_n	0.630	Equation 3.31
Possible DEM parameter set	R_{mean}	1.6mm	Scale-invariant
	μ_s	0.476	equation 3.25
	μ_R	0.476	equation 3.25

The DEM parameter sets from calibration were not unique solutions for critical state strength. Some additional material characterization produced initial guesses for either μ_s or μ_R, however, if none was available, $\mu_R=\mu_s$ was used. Figure 53 shows the stress strain response of a virtual triaxial test with the calibrated parameter set.

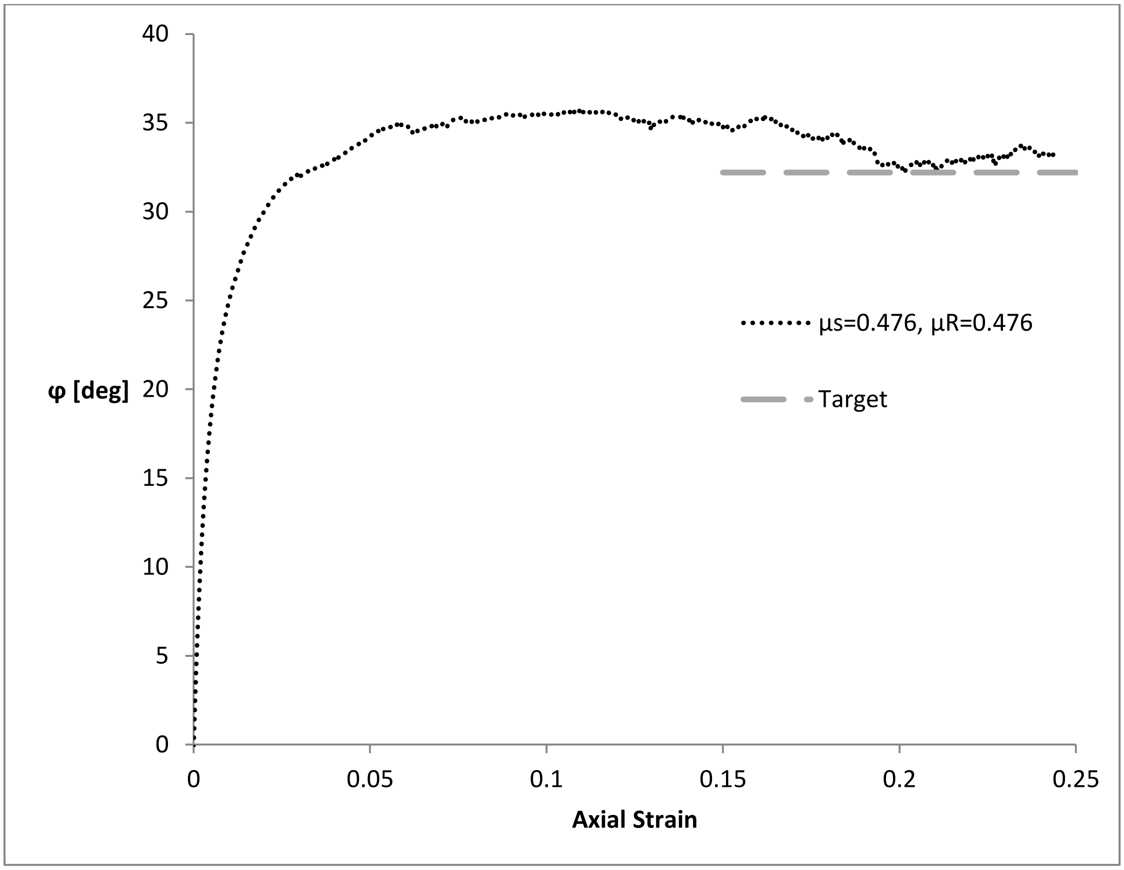

Figure 53. Stress-strain response of virtual triaxial tests with calibration parameters

If relative density of a physical specimen was available, more rigorous calibration, especially of volume change, was performed by appending the relative density method proposed by Salot et al. (2009). Minimum and maximum virtual packing densities were unique to particle size, distribution, and stiffness. Therefore, the scale invariance of calibration in Table 11 did not apply. This study also considered direct shear test response from Lings and Deitz (2004) of Leighton Buzzard sand at 90% relative density. Table 12 shows the relevant bulk mechanical characteristics of Leighton Buzzard sand and the accompanying calibration set. Figure 54 and Figure 55 show the stress-displacement and volume change response of the virtual direct shear tests that correspond to the calibrated parameter set from Table 12.

Table 12. Direct shear calibration table including relative density effects

	Parameter	Value	Reference
Physical direct shear test data	Crit state friction angle, ϕ [deg]	31^o	Lings and Deitz (2004)
	Desired Peak friction angle [deg]	48^o	Lings and Deitz (2004)
	Relative density, D_r [%]	90%	Lings and Deitz (2004)
	Height change [mm]	1.5mm	Lings and Deitz (2004)
Calibration	Desired ϕ_p	$\sim 9^o$	Figure 10
	desired μ_{eff}	0.17	Equation 3.32
	F_t/F_n	0.50	Equation 3.31
Possible DEM parameter set	R_{mean}	1.5mm	
	μ_s	0.2	equation 3.25
	μ_R	0.1	equation 3.25
	Young's Modulus [Pa]	$1\text{x}10^9$ Pa	
	Initial void ratio	0.72	Salot et al. (2009)

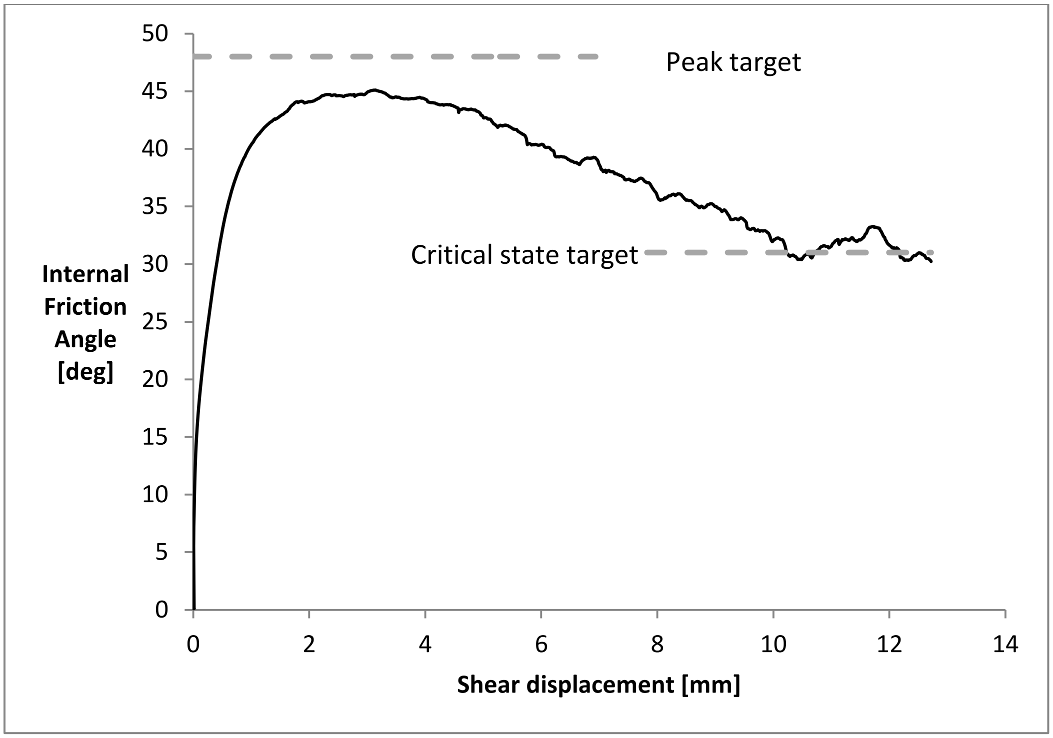

Figure 54. Direct shear calibration of internal friction angle

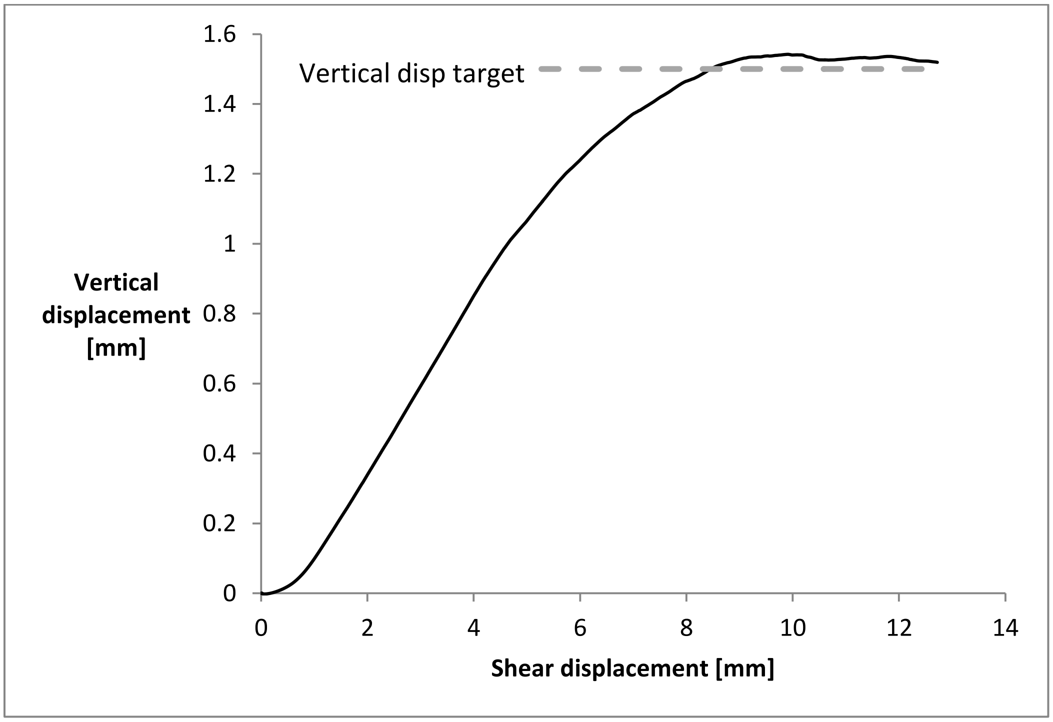

Figure 55. Direct shear calibration of volume change (vertical displacement)

Some error in the peak strength and vertical displacement targets were observed. Note that in the current study, Salot at al’s (2009) relative density method scaled nearly linearly with peak strength in the majority of the range of relative density. However, at very high and very low initial void ratios, the packing density deviated from the assumed linearity. The monodisperse specimen from Figure 50 and Table 9 was iterated over many different initial void ratios. The relationship between initial void ratio and peak strength is shown in Figure 56.

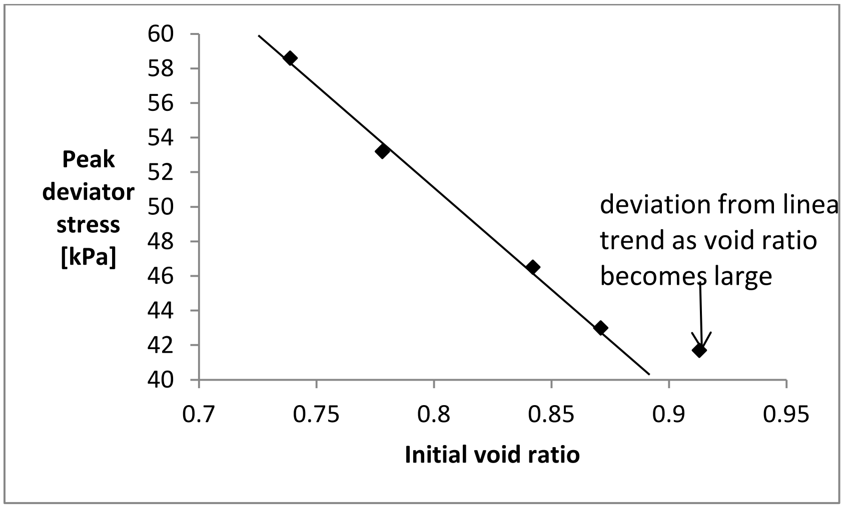

Figure 56. Peak strength vs. initial void ratio

Conclusion

Effective friction coefficient (μ_{eff}) of a granular material varied linearly with critical state strength of dense granular assemblies and was used to calibrate DEM particle interaction parameters to mechanical responses of triaxial tests. A linear statistical model that related μ_{eff} to bulk friction angle was used to calibrate DEM simulations.

This study demonstrated the value of using μ_{eff} as a low-error friction term that improved the accuracy of statistical calibrations of DEM parameters to physical phenomena. However, more work is needed to determine analytical and empirical expressions for relative initial density in DEM specimens (e.g., Salot et al. 2009), specimen angularity, and dynamic parameters to further refine the accuracy of calibration. In addition, work that narrows the physical ranges of μ_R would push the predictive capacity of DEM simulation.

CHAPTER 4. DEVELOPMENT OF DEM CALIBRATION

Introduction

DEM inputs needed to be understood micro-mechanically *and* phenomenologically before thoughtful calibration could take place. Large data sets were generated and explored to provide a foundation understanding of univariate relationships between micromechanical inputs to mechanical responses of dense granular material subject to shearing. In addition, dimensional analysis was used to combine multiple DEM input variables to study interactions. Alternate micro-mechanical formulations for interparticle DEM interactions were also considered when traditional, popular, or otherwise built-in formulations were not adequate.

A statistical approach was used for analyzing data in the exploratory phase of DEM calibration development. Analytical and semi-empirical approaches for sliding rolling friction were discussed in Chapter 3.

DEM

For the subsequent statistical analyses, results from many DEM simulations were parsed and analyzed. DEM simulations used the familiar Hertz-Mindlin contact law described in the Methods chapter. The rolling friction was modeled using the EPSD model built into LIGGGHTS. Additionally, particle shape and cohesion were modeled using techniques that will be described here.

Particle shape was modeled using multi-spheres or *clump logic*. Aspherical particles can be created by bonding spherical particles together. Pill shaped particles were used in the current study. Kozicki et al. (2012) reported that as the aspect ratio of pill shaped clumps increases, the strength and dilatancy also increase. Figure 5 from chapter 2 shows what the clumps look like and their influence on mechanical behavior.

The EPSD rolling friction model was applied to each particle whether or not clump logic was used to influence particle shape. DEM specimens were contrasted using a mix of clumps and single spheres. The parameter, *%Aspherical*, indicates what percentage of the specimen was made of pill shaped clumps. The *aspect ratio* parameter was a ratio of the major and minor dimensions of the pill.

The cohesion formulation used in the current study was projected-area cohesion. A small study assessing the effects of projected area cohesion coefficient on mechanical behavior of virtual triaxial test specimens is presented later in this chapter. Refer to equations 5.4 and 5.5 for the calculation of attractive forces between particles.

Finally, the structural state of a DEM assembly was often described by *void ratio*, *porosity*, or *solid fraction*. Solid fraction and void ratio will be used interchangeably with the reminder to the reader that void ratio and solid fraction are related by equation 4.1.

$$void\ ratio = \frac{1}{SolidFraction} - 1. \qquad 4.1$$

Statistical Method

An exploratory experimental design was devised to relate DEM inputs to mechanical responses of drained triaxial tests.

Design of experiment

An experiment was designed to assess the statistical relationships between DEM input parameters and mechanical responses of virtual triaxial tests. A fractional factorial design of experiment was generated with the following assumptions:

DEM input parameters

Sliding friction coefficient: 3-level variable (0.1, 0.55, 0.9), assumed non-linear

Rolling friction coefficient: 2 level variable (0.1, 0.5), assumed linear

Young's modulus: 3-level variable (29x10^7, 29x10^8,29x10^9 Pa), assumed logarithmic scale

Projected-area cohesion coefficient: 2-level variable (0, 35kPa), assumed linear

Percentage of specimen aspherical: 2-level variable (10, 30%), assumed linear

Aspect ratio of aspherical particles: 2-level variable (1.5, 2.0), assumed linear

Test parameters

Initial solid fraction: 3 level variable (0, 50, 100%), assume non-linear

Confining stress: 3-level variable (2x10^5, 6x10^5, 10x10^5 Pa), assumed non-linear

A full factorial design of eight independent, 2-and-3 levels variables required 1024 experimental runs; too many to complete in a timely manner. A fractional factorial model was used to cut down on the number of virtual triaxial test runs. The total number of test runs was limited to 150. The experimental design was generated using the R software (2013) and is shown in Table 13.

Table 13. Mixed Level Fractional Factorial Experimental Design

Trial	Cohesion (2) Pa	Confining Pressure (3) Pa	Young's Modulus (3) Pa	Rolling Friction Coefficient (2)	Sliding Friction Coefficient (3)	Relative Density (3)	Aspect Ratio (2)	% Aspherical (2)
1	0	600000	2.9E+09	0.1	0.1	0	1.5	0.1
2	35000	600000	2.9E+09	0.1	0.1	0	1.5	0.1
3	35000	600000	2.9E+10	0.1	0.1	0	1.5	0.1
4	0	1000000	2.9E+10	0.1	0.1	0	1.5	0.1
5	35000	1000000	2.9E+10	0.1	0.1	0	1.5	0.1
6	0	600000	2.9E+09	0.5	0.1	0	1.5	0.1
7	35000	600000	2.9E+09	0.5	0.1	0	1.5	0.1
8	35000	600000	2.9E+10	0.5	0.1	0	1.5	0.1
9	0	1000000	2.9E+10	0.5	0.1	0	1.5	0.1
10	35000	200000	2.9E+08	0.1	0.55	0	1.5	0.1
11	35000	600000	2.9E+08	0.1	0.55	0	1.5	0.1
12	0	1000000	2.9E+08	0.1	0.55	0	1.5	0.1
13	0	200000	2.9E+09	0.1	0.55	0	1.5	0.1
14	35000	200000	2.9E+10	0.1	0.55	0	1.5	0.1
15	0	600000	2.9E+10	0.1	0.55	0	1.5	0.1
16	0	600000	2.9E+08	0.5	0.55	0	1.5	0.1
17	35000	1000000	2.9E+08	0.5	0.55	0	1.5	0.1
18	0	200000	2.9E+09	0.5	0.55	0	1.5	0.1
19	35000	200000	2.9E+09	0.5	0.55	0	1.5	0.1
20	0	600000	2.9E+09	0.5	0.55	0	1.5	0.1
21	35000	1000000	2.9E+09	0.5	0.55	0	1.5	0.1
22	35000	200000	2.9E+10	0.5	0.55	0	1.5	0.1
23	0	600000	2.9E+10	0.5	0.55	0	1.5	0.1
24	35000	600000	2.9E+08	0.1	0.9	0	1.5	0.1
25	35000	1000000	2.9E+08	0.1	0.9	0	1.5	0.1
26	0	200000	2.9E+09	0.1	0.9	0	1.5	0.1
27	35000	200000	2.9E+09	0.1	0.9	0	1.5	0.1
28	0	1000000	2.9E+09	0.1	0.9	0	1.5	0.1
29	0	200000	2.9E+10	0.1	0.9	0	1.5	0.1
30	35000	200000	2.9E+10	0.1	0.9	0	1.5	0.1
31	0	600000	2.9E+08	0.5	0.9	0	1.5	0.1
32	35000	600000	2.9E+08	0.5	0.9	0	1.5	0.1
33	35000	1000000	2.9E+08	0.5	0.9	0	1.5	0.1
34	0	200000	2.9E+09	0.5	0.9	0	1.5	0.1
35	35000	200000	2.9E+09	0.5	0.9	0	1.5	0.1
36	0	600000	2.9E+09	0.5	0.9	0	1.5	0.1
37	0	1000000	2.9E+09	0.5	0.9	0	1.5	0.1
38	35000	200000	2.9E+10	0.5	0.9	0	1.5	0.1
39	35000	200000	2.9E+08	0.1	0.1	0	1.5	0.3
40	35000	600000	2.9E+09	0.1	0.1	0	1.5	0.3
41	35000	1000000	2.9E+09	0.1	0.1	0	1.5	0.3
42	35000	600000	2.9E+10	0.1	0.1	0	1.5	0.3
43	35000	600000	2.9E+08	0.1	0.55	0	1.5	0.3
44	35000	600000	2.9E+09	0.1	0.55	0	1.5	0.3
45	0	1000000	2.9E+09	0.1	0.55	0	1.5	0.3
46	35000	1000000	2.9E+09	0.1	0.55	0	1.5	0.3
47	0	600000	2.9E+10	0.1	0.55	0	1.5	0.3
48	35000	600000	2.9E+10	0.1	0.55	0	1.5	0.3
49	0	1000000	2.9E+09	0.5	0.55	0	1.5	0.3
50	35000	600000	2.9E+10	0.5	0.55	0	1.5	0.3
51	35000	200000	2.9E+08	0.1	0.9	0	1.5	0.3
52	0	600000	2.9E+09	0.1	0.9	0	1.5	0.3
53	0	1000000	2.9E+09	0.1	0.9	0	1.5	0.3
54	35000	1000000	2.9E+09	0.1	0.9	0	1.5	0.3
55	0	600000	2.9E+10	0.1	0.9	0	1.5	0.3
56	0	1000000	2.9E+10	0.1	0.9	0	1.5	0.3
57	35000	600000	2.9E+08	0.5	0.9	0	1.5	0.3
58	35000	1000000	2.9E+08	0.5	0.9	0	1.5	0.3
59	35000	200000	2.9E+09	0.5	0.9	0	1.5	0.3
60	0	600000	2.9E+09	0.5	0.9	0	1.5	0.3
61	35000	1000000	2.9E+09	0.5	0.9	0	1.5	0.3
62	35000	600000	2.9E+10	0.5	0.9	0	1.5	0.3
63	35000	600000	2.9E+09	0.1	0.1	0	2	0.1
64	35000	600000	2.9E+10	0.1	0.1	0	2	0.1
65	35000	600000	2.9E+10	0.5	0.1	0	2	0.1
66	35000	200000	2.9E+09	0.1	0.55	0	2	0.1
67	35000	1000000	2.9E+10	0.5	0.55	0	2	0.1
68	35000	1000000	2.9E+08	0.1	0.9	0	2	0.1
69	35000	200000	2.9E+10	0.1	0.9	0	2	0.1
70	0	1000000	2.9E+10	0.5	0.9	0	2	0.1
71	35000	1000000	2.9E+10	0.1	0.1	0	2	0.3
72	0	200000	2.9E+08	0.5	0.1	0	2	0.3
73	0	1000000	2.9E+08	0.1	0.55	0	2	0.3

Table 13 continued

Trial	Cohesion (2) Pa	Confining Pressure (3) Pa	Young's Modulus (3) Pa	Rolling Friction Coefficient (2)	Sliding Friction Coefficient (3)	Relative Density (3)	Aspect Ratio (2)	% Aspherical (2)
74	0	600000	2.9E+10	0.1	0.55	0	2	0.3
75	35000	600000	2.9E+10	0.5	0.9	0	2	0.3
76	35000	1000000	2.9E+10	0.5	0.9	0	2	0.3
77	35000	600000	2.9E+08	0.1	0.1	0.5	1.5	0.1
78	35000	200000	2.9E+10	0.1	0.1	0.5	1.5	0.1
79	0	600000	2.9E+09	0.5	0.55	0.5	1.5	0.1
80	35000	1000000	2.9E+09	0.5	0.55	0.5	1.5	0.1
81	35000	200000	2.9E+08	0.1	0.9	0.5	1.5	0.1
82	35000	1000000	2.9E+10	0.5	0.9	0.5	1.5	0.1
83	35000	200000	2.9E+08	0.1	0.55	0.5	1.5	0.3
84	0	200000	2.9E+10	0.1	0.55	0.5	1.5	0.3
85	35000	600000	2.9E+08	0.5	0.55	0.5	1.5	0.3
86	0	600000	2.9E+10	0.5	0.55	0.5	1.5	0.3
87	0	200000	2.9E+10	0.1	0.9	0.5	1.5	0.3
88	35000	600000	2.9E+08	0.5	0.9	0.5	1.5	0.3
89	0	1000000	2.9E+10	0.5	0.9	0.5	1.5	0.3
90	35000	600000	2.9E+10	0.5	0.1	0.5	2	0.1
91	0	1000000	2.9E+08	0.1	0.55	0.5	2	0.1
92	0	200000	2.9E+09	0.1	0.55	0.5	2	0.1
93	0	200000	2.9E+10	0.1	0.55	0.5	2	0.1
94	35000	200000	2.9E+10	0.1	0.55	0.5	2	0.1
95	35000	600000	2.9E+08	0.5	0.55	0.5	2	0.1
96	0	200000	2.9E+10	0.1	0.9	0.5	2	0.1
97	0	600000	2.9E+09	0.5	0.9	0.5	2	0.1
98	0	600000	2.9E+09	0.1	0.1	0.5	2	0.3
99	35000	600000	2.9E+09	0.1	0.1	0.5	2	0.3
100	35000	1000000	2.9E+09	0.1	0.1	0.5	2	0.3
101	35000	600000	2.9E+08	0.1	0.9	0.5	2	0.3
102	0	200000	2.9E+09	0.1	0.9	0.5	2	0.3
103	35000	200000	2.9E+09	0.1	0.9	0.5	2	0.3
104	0	600000	2.9E+09	0.1	0.9	0.5	2	0.3
105	0	1000000	2.9E+09	0.1	0.9	0.5	2	0.3
106	0	600000	2.9E+08	0.1	0.1	1	1.5	0.1
107	35000	1000000	2.9E+08	0.1	0.1	1	1.5	0.1
108	35000	200000	2.9E+09	0.1	0.1	1	1.5	0.1
109	0	200000	2.9E+10	0.1	0.1	1	1.5	0.1
110	0	200000	2.9E+08	0.1	0.55	1	1.5	0.1
111	35000	200000	2.9E+08	0.1	0.55	1	1.5	0.1
112	0	200000	2.9E+09	0.5	0.55	1	1.5	0.1
113	0	200000	2.9E+10	0.5	0.55	1	1.5	0.1
114	35000	200000	2.9E+08	0.1	0.9	1	1.5	0.1
115	0	600000	2.9E+08	0.1	0.9	1	1.5	0.1
116	35000	600000	2.9E+09	0.5	0.9	1	1.5	0.1
117	35000	1000000	2.9E+09	0.5	0.1	1	1.5	0.3
118	35000	1000000	2.9E+10	0.5	0.1	1	1.5	0.3
119	35000	200000	2.9E+08	0.1	0.55	1	1.5	0.3
120	0	1000000	2.9E+08	0.1	0.55	1	1.5	0.3
121	0	200000	2.9E+10	0.1	0.55	1	1.5	0.3
122	35000	200000	2.9E+10	0.5	0.55	1	1.5	0.3
123	0	600000	2.9E+08	0.1	0.9	1	1.5	0.3
124	0	200000	2.9E+09	0.1	0.9	1	1.5	0.3
125	35000	600000	2.9E+08	0.5	0.9	1	1.5	0.3
126	35000	1000000	2.9E+08	0.5	0.9	1	1.5	0.3
127	0	1000000	2.9E+10	0.5	0.9	1	1.5	0.3
128	35000	600000	2.9E+08	0.1	0.1	1	2	0.1
129	0	1000000	2.9E+09	0.1	0.1	1	2	0.1
130	35000	600000	2.9E+09	0.5	0.1	1	2	0.1
131	0	600000	2.9E+10	0.5	0.1	1	2	0.1
132	35000	1000000	2.9E+10	0.5	0.1	1	2	0.1
133	0	1000000	2.9E+08	0.1	0.55	1	2	0.1
134	0	1000000	2.9E+09	0.1	0.55	1	2	0.1
135	0	600000	2.9E+08	0.5	0.55	1	2	0.1
136	35000	600000	2.9E+08	0.5	0.55	1	2	0.1
137	35000	200000	2.9E+08	0.1	0.9	1	2	0.1
138	0	200000	2.9E+09	0.1	0.9	1	2	0.1
139	35000	200000	2.9E+09	0.1	0.9	1	2	0.1
140	0	600000	2.9E+09	0.5	0.9	1	2	0.1
141	35000	200000	2.9E+10	0.5	0.9	1	2	0.1
142	35000	1000000	2.9E+09	0.1	0.1	1	2	0.3
143	0	600000	2.9E+10	0.1	0.1	1	2	0.3
144	0	1000000	2.9E+10	0.1	0.1	1	2	0.3
145	35000	200000	2.9E+10	0.1	0.55	1	2	0.3
146	35000	1000000	2.9E+09	0.5	0.55	1	2	0.3
147	0	600000	2.9E+10	0.5	0.55	1	2	0.3
148	35000	1000000	2.9E+08	0.1	0.9	1	2	0.3
149	35000	200000	2.9E+09	0.1	0.9	1	2	0.3
150	0	600000	2.9E+09	0.5	0.9	1	2	0.3

All variables that were assigned two levels had been studied in the literature and shown to have linear relationship with at least peak strength or critical state strength of associated triaxial test responses. Other variables that were chosen to be three level variables did not have conclusive information to assume linearity. For instance, Thornton (2000) showed an unclear relationship between sliding friction and critical state strength; therefore, sliding friction was assigned three levels.

Initial solid fraction

Repeatability

The large dataset allowed the study of univariate effects of initial solid fraction on mechanical responses of triaxial tests. The generation of initial states was not deterministic. However, the calculations cycles of DEM simulations *were* deterministic. Therefore, a quick test of the reliability of the initial states was performed to verify the initial state algorithm. The constant input parameters of the simulations were as follows:

Contact Formulation: Hertz-Mindlin
Young's Modulus = $29\text{x}10^4$ kPa
Particle diameter = 3 mm
Confining pressure = 200 kPa
Sliding friction = 0.3
Rolling friction = 0.3
% Aspherical = 28-29%
Aspect ratio of aspheres = 1.5
Cohesion = 50 Pa
Viscous damping coefficient = 1 N-s/m

Repeatability of triaxial tests was assessed at solid fraction of 1.50 and is shown in Figure 57.

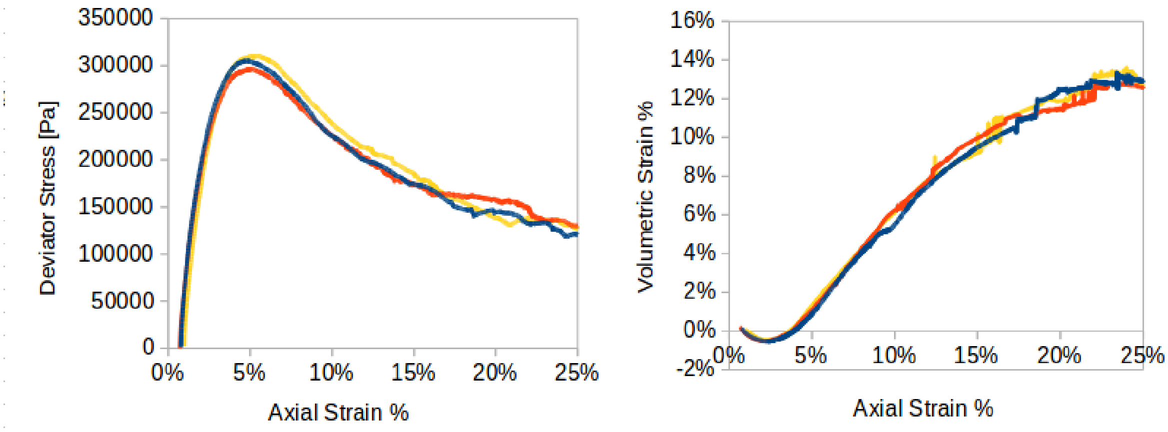

Figure 57. Repeatability of triaxial tests at initial solid fraction=1.50.

The stress-strain and volume change responses of the three DEM triaxial specimens are very close, but not identical. Variation in the experimental results can be attributed to variation in initial state.

Initial solid fraction analysis

Initial solid fraction was a 2-level variable in the experimental design. A study was designed to assess the linearity of solid fraction with respect to various mechanical responses of a virtual soil sample subject to triaxial compression. Only over-consolidated samples were considered. The effects of initial solid fraction were assessed on five outcomes of the mechanical response of a triaxial test (peak stress, strain at peak stress, minimum volumetric strain, dilatancy angle, and maximum volumetric strain). Figure 58 shows a clear positive association between peak strength and initial solid fraction.

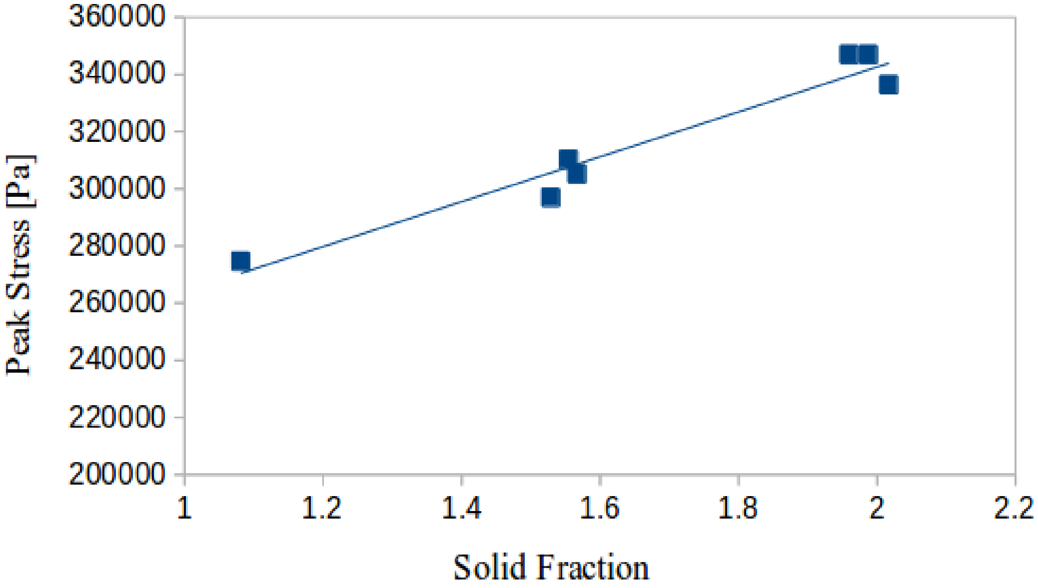

Figure 58. Correlating peak strength with initial solid fraction

Conversely, the association between strain-at-peak-strength and initial solid fraction was negative (Figure 59). The result in Figure 59 was expected because in physical testing, the strain at which peak strength occurs was typically delayed as the initial state was loosened.

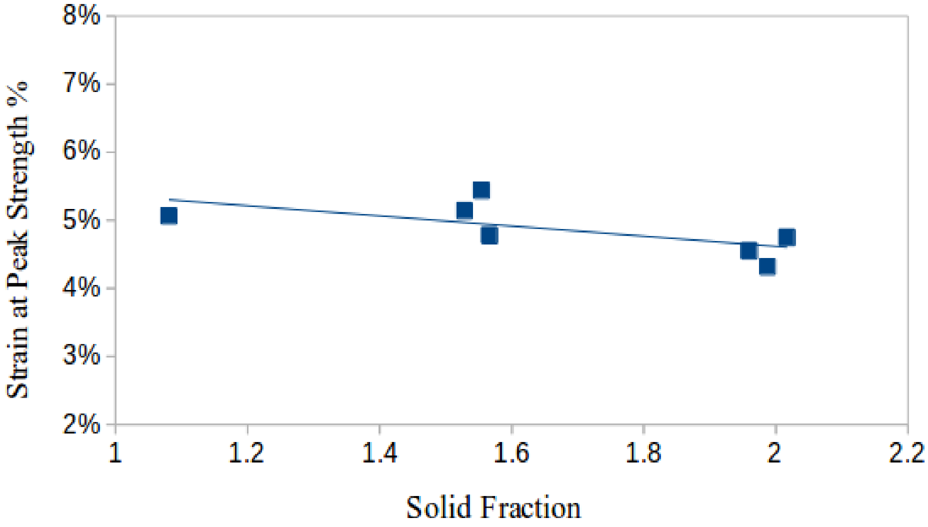

Figure 59. Relationship between strain at peak strength with initial solid fraction

Figure 60 shows an unclear relationship between minimum volumetric strain and initial solid fraction. Although a slight positive association existed, a greater association was expected because of the prevailing thought that the contractile regime in triaxial test results was accentuated as initial solid fraction decreased.

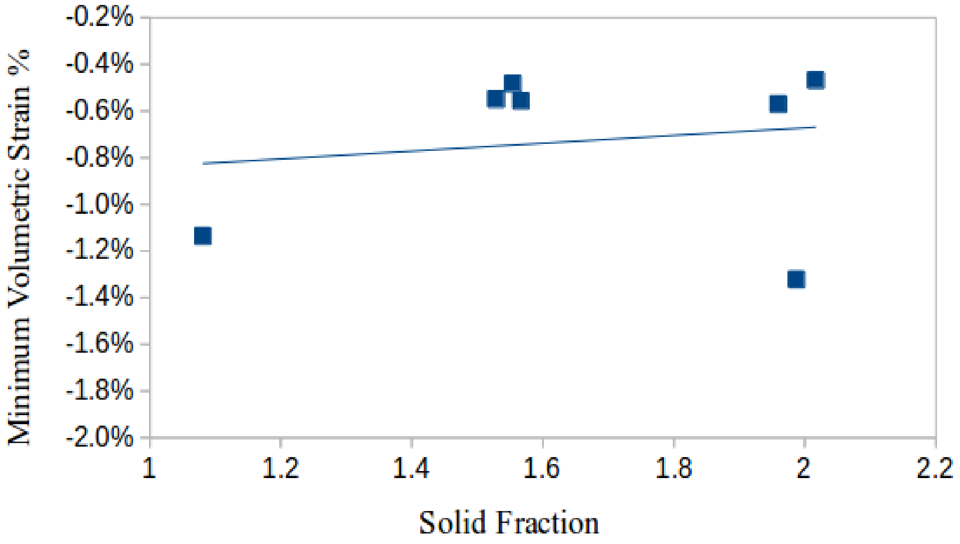

Figure 60. Unclear relationship between minimum volumetric strain and initial solid fraction

Although Figure 60 shows discouraging volume change results for calibration purposes, Figure 61 points to reasonable positive association between dilatancy angle and initial solid fraction.

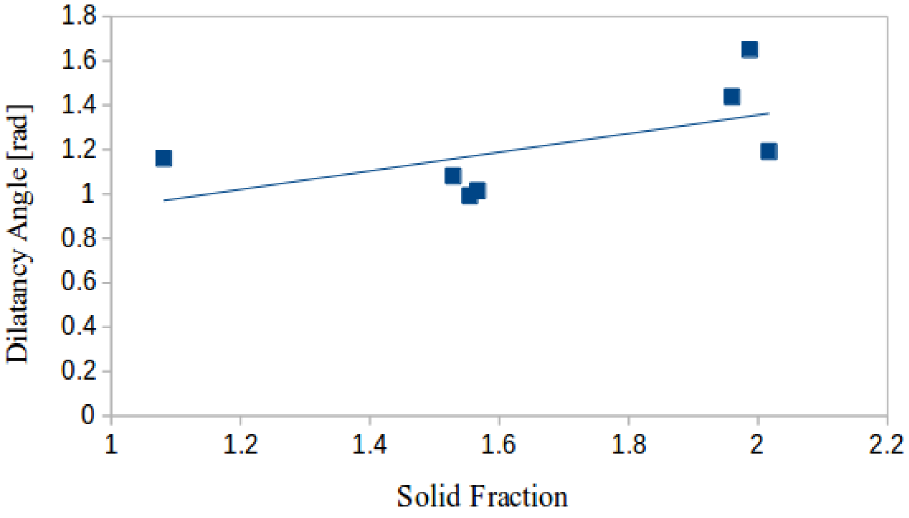

Figure 61. Relationship between maximum dilatancy angle and initial solid fraction

Finally, Figure 62 adds additional encouraging association between maximum volumetric strain and initial solid fraction.

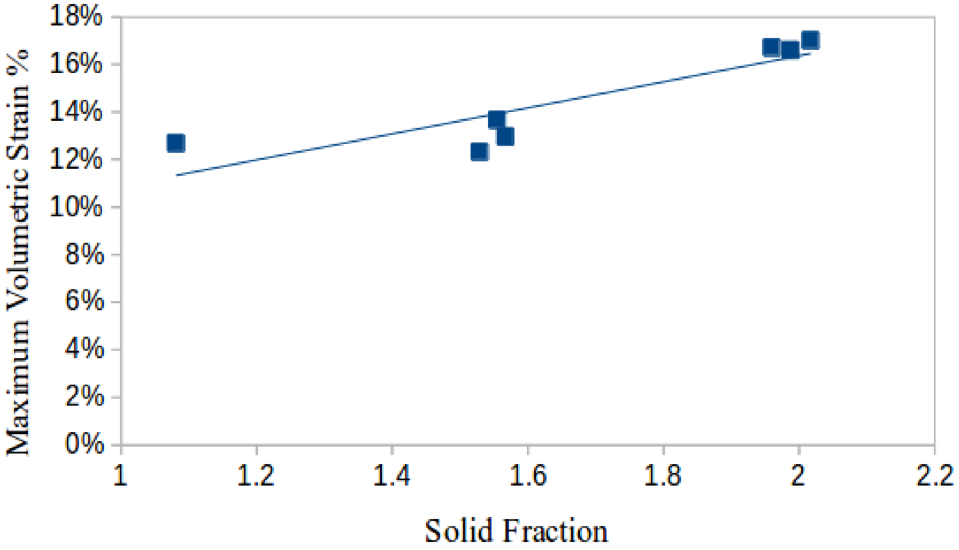

Figure 62. Correlating maximum volumetric strain with initial solid fraction

All mechanical outcomes except minimum volume strain (Figure 60) exhibited linear dependence on initial solid fraction.

Critical state strength

The exploratory data set in Table 13 was used to statistically relate sliding and rolling friction coefficients to critical state strength from virtual triaxial tests. The univariate relationships between friction coefficients and critical state strength were not adequate for DEM input parameter calibration, so combinations of sliding and rolling friction coefficient were experimented with while controlling for other input variables. The R statistical package (2013) was used to calculate regression coefficients and assess the fit of the combined friction models.

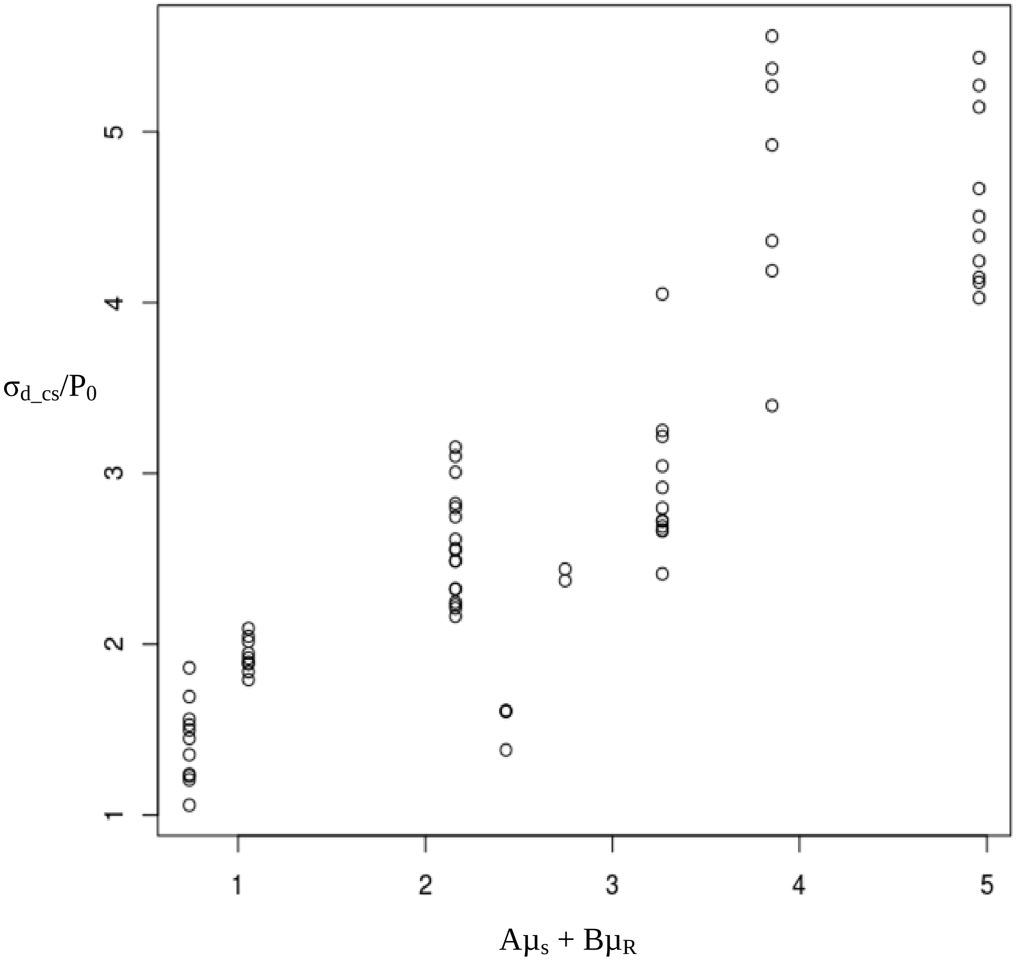

Figure 63. Linear multivariable regression model of sliding (μ_s) and rolling friction (μ_R) vs critical state strength (σ_{d_cs}/P_0), from linear regression fit, A=3.16, B=4.23, (R^2=0.94, RSE = 0.60, both terms, $p < 0.05$).

Figure 63 shows that linear combinations of sliding and rolling friction produced a statistical model with a high goodness of fit (R^2=0.94), but the model produced non-unique parameter sets for μ_s and μ_R. Adding the interaction term, $\mu_s\mu_R$ (p=0.22) did not improve the model. Non-linear combinations of μ_s and μ_R were explored as well.

Five non-linear forms of μ_s and μ_R were tested using the non-linear regression technique in the R statistical package.

Friction term 1: $10\mu_s^{\sqrt{\mu_R}}$

Friction term 2:
$$a_0(1 - \exp(-a_1 frictionterm1^{a_2}))$$
$$where\ a_0 = 5.5; a_1 = 0.334; a_2 = 1.49$$

Friction term 3: $\frac{\mu_s \mu_R}{1+\mu_R}$

Friction term 4: $\frac{\mu_s \mu_R}{1+3\mu_R}$

Friction term 5: $1 + 4(1 - \exp(-12.4 * frictionterm4)$

Each friction term was related to the non-dimensional critical state strength, σ_{d_cs}/P_0. Friction term 1 produced poor results, so it was transformed further to produce friction term 2. The results of *friction term 2* regression analysis are shown in Figure 64.

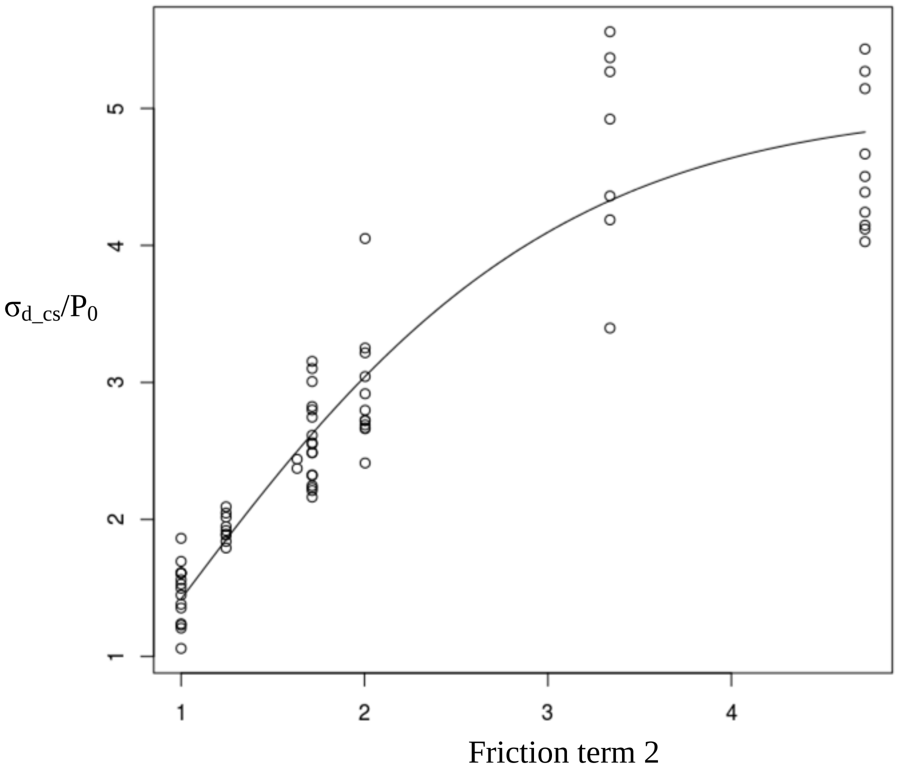

Figure 64. Friction term 2 vs non-dimensional critical state strength (R^2=0.98)

Friction term 2 in Figure 64 presented the same problem as the linear combination of friction in Figure 63 where a single friction term described a wide variety of possible

critical state strengths. In an attempt to improve the fit, friction term 3 was correlated with non-dimensional critical state strength (
Figure 65).

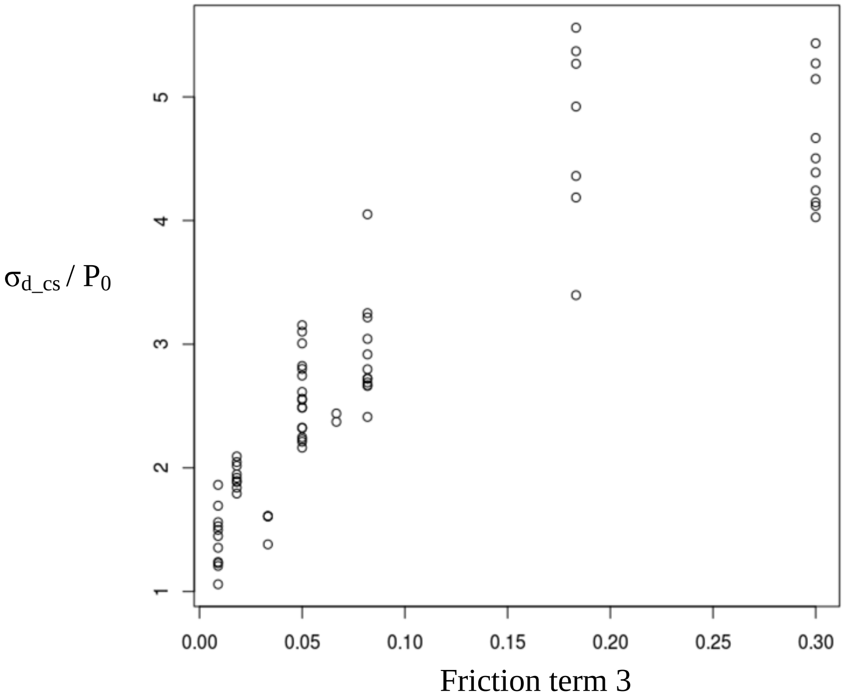

Figure 65. Friction term 3 vs non-dimensional critical state strength (R^2=0.93)

The correlation between *friction term 3* and normalized strength was significantly worse than *friction term 2*. *Friction term 4* is shown in Figure 66. *Friction term 4* exhibited considerable scatter from the simulation data, but captured the overall trend of the data. It is possible that *Friction term 4* can be further refined to account for the variance seen in Figure 66.

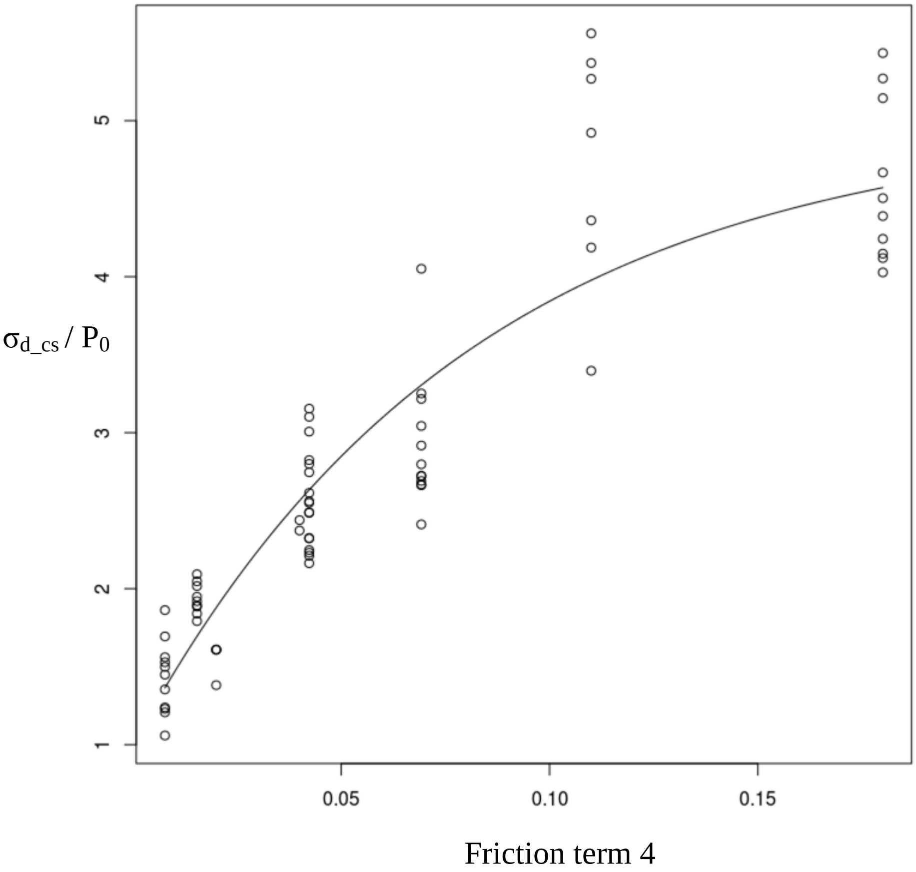

Figure 66. Friction term 4 vs non-dimensional critical state strength (R^2=0.94)

Transforming *friction term 4* and controlling for *log(E)/10*, yielded Figure 67. As previously mentioned, refining *Friction term 4* to account for particle stiffness tightened the scatter of simulation data. In addition, the transformed term produced a linear correlation with normalized granular strength.

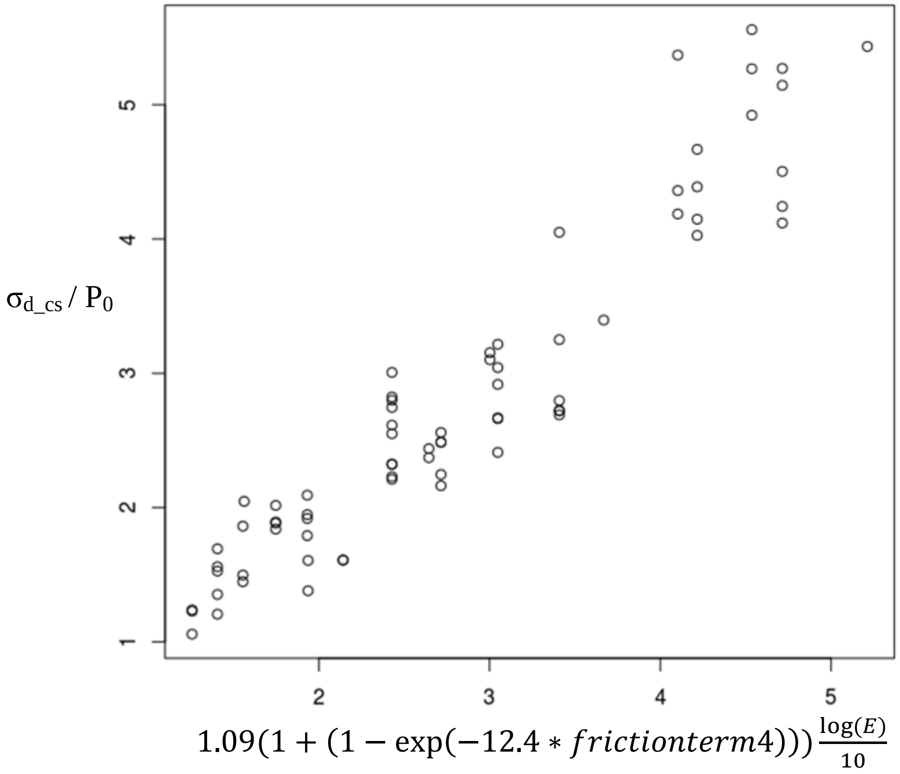

Figure 67. Friction term 5 including Young's modulus transformation (R^2=0.98, RSE=0.39)

The statistical residual plot associated with friction term 5 is shown in Figure 68.

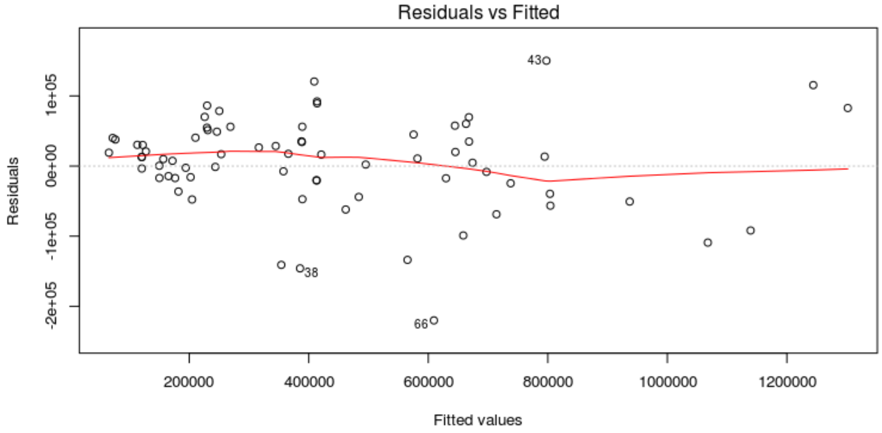

Figure 68. Residual plot of friction term 5 vs critical state strength

The residual plot in Figure 68 makes the deviation from the fit line apparent. A deviation of 100kPa is common for all values of friction term 5.

Friction term 5 is a better model than friction terms 1-4; however, it is purely empirical and not theoretically relevant. Additional work to obtain a semi-empirical correlation between friction coefficients and critical state strength is needed for more robust calibration. In addition, there is still considerable qualitative scatter in the correlation between *Friction term 5* and normalized strength. An analytical or semi-analytical solution for a correlative term will have to eliminate the non-unique solutions for normalized strength shown in Figure 67.

Final void ratio

The void ratio of virtual triaxial test specimens was analyzed at critical state, or when dilatancy angle approached zero, and was termed the *final void ratio*, e_f. The exploratory data set in Table 13 was parsed and transformed to describe e_f as a function of DEM input parameters. The combined predictive term, equation 5.1, was manually developed using the R statistical software (equation 5.1, R^2=0.988, RSE=0.0478).

$$e_f = \frac{\mathrm{A}\log(E)}{\log(P_0)} + B\mu_s + \frac{C\mu_s}{1+\mu_R^{0.25}} + 0.64 \qquad 5.1$$

Where A = 0.578, t-statistic=3.83, p=0.012;

B = 1.16, t-statistic=7.941, p=0.000051;

C = -1.40, t-statistic=-5.602, p=0.0025.

Figure 69 shows the correlation of equation 5.1 to e_f.

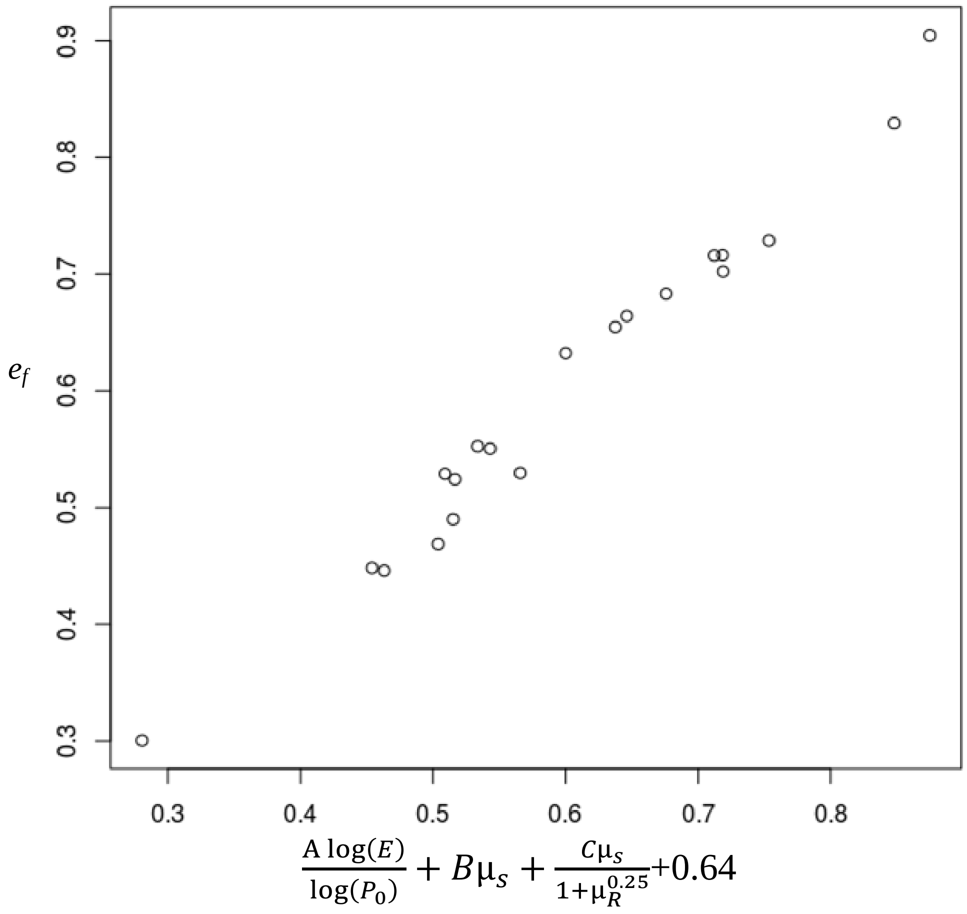

Figure 69. Correlation of predictive term to final void ratio

Figure 69 indicates that the final void ratio can be readily described by DEM parameters. The effect sizes of the linear statistical model show that the two terms which include friction coefficients (B and C) influence the model much more than the stiffness and confining pressure term (A). Indeed, friction is a dominant predictive factor as related to final void ratio.

Volumetric contraction

The contraction of overconsolidated physical triaxial test specimens is related to grain deformation rather than reconfiguration (Whitman et al., 1964). Virtual triaxial test specimens were constructed to identify the DEM input parameters which contribute the most to the contraction of overconsolidated soils. Sliding and rolling friction coefficients were held at 0.5 and 0.55 respectively. Eight triaxial test specimens were compressed deviatorically and the minimum volumetric strain was recorded. Each specimen was isotropically consolidated at a lower coefficient of sliding friction, 0.1. Confining pressure and Young’s modulus of the Hertzian particles was varied. The radius of the particles was held constant at 1.5 mm over all virtual experiments. Since the Hertzian stiffness of spherical particles is non-linear with respect to interparticle contact force, an experimental effective stiffness term that includes Young’s modulus, as well as confining pressure, was created to describe the relationship between DEM input parameters and global volumetric strain (equation 4.2).

$$k_e = \frac{\log_{10} E}{\log_{10} P_0} \qquad (4.2)$$

The effective stiffness term is related to minimum volumetric strain in Figure 70.

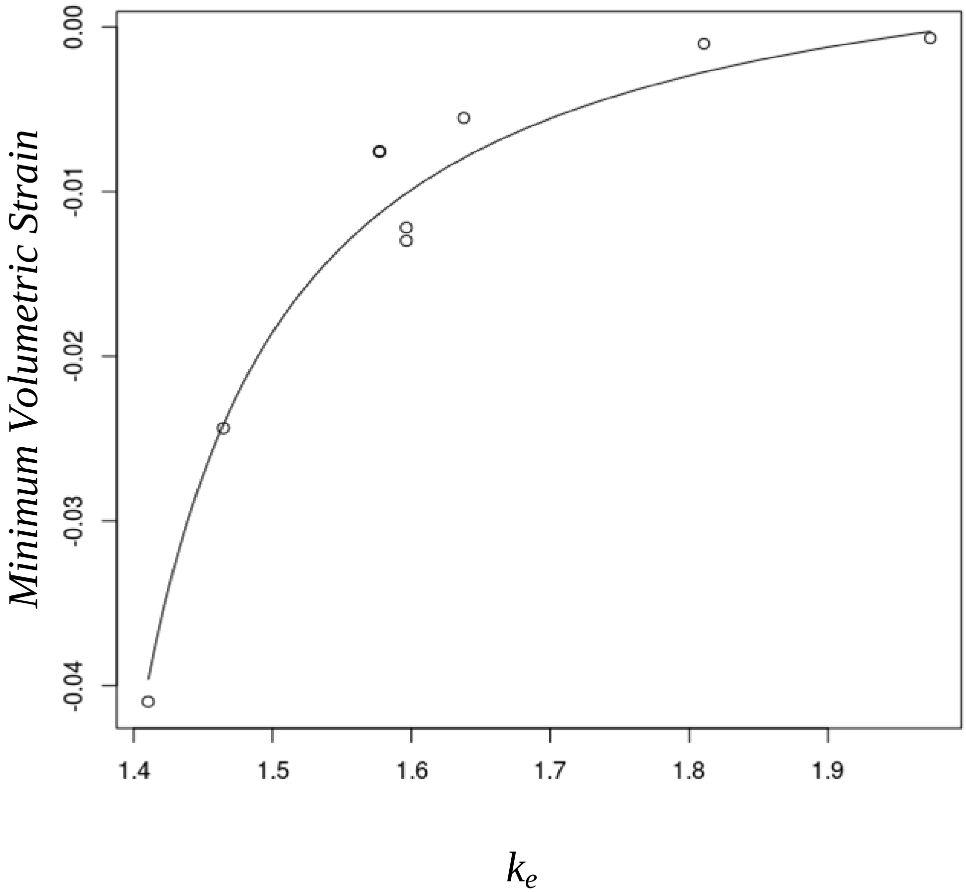

Figure 70. Experimental effective stiffness term related to minimum volumetric strain

Figure 70 includes only constant radius particles. Therefore, a complete empirical understanding of specimen contraction should include specimens composed of differing particle radii.

Dilatancy

The dilatancy angle of a virtual triaxial test specimen was measured for each simulation in the DOE. A non-dimensional parameter that describes the initial state of the virtual specimen was used as a correlative factor. The initial state is tentatively defined in equation 4.3.

$$I = \frac{log(E)}{e_0^{0.25}\log(P_0)} \tag{4.3}$$

Initial state is strongly related to dilatancy angle, as shown in Figure 71.

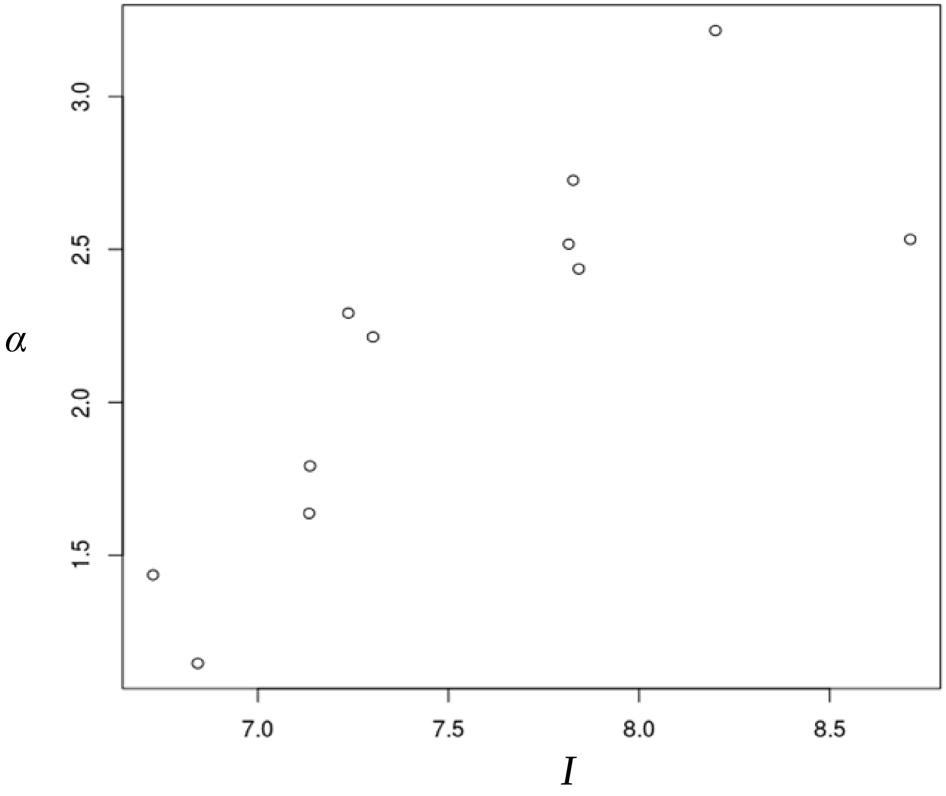

Figure 71. Dilatancy angle as related to initial state variable

Initial state accounts for considerable variation by itself, and by adding friction coefficients, as seen in Figure 72 further improved the descriptive model.

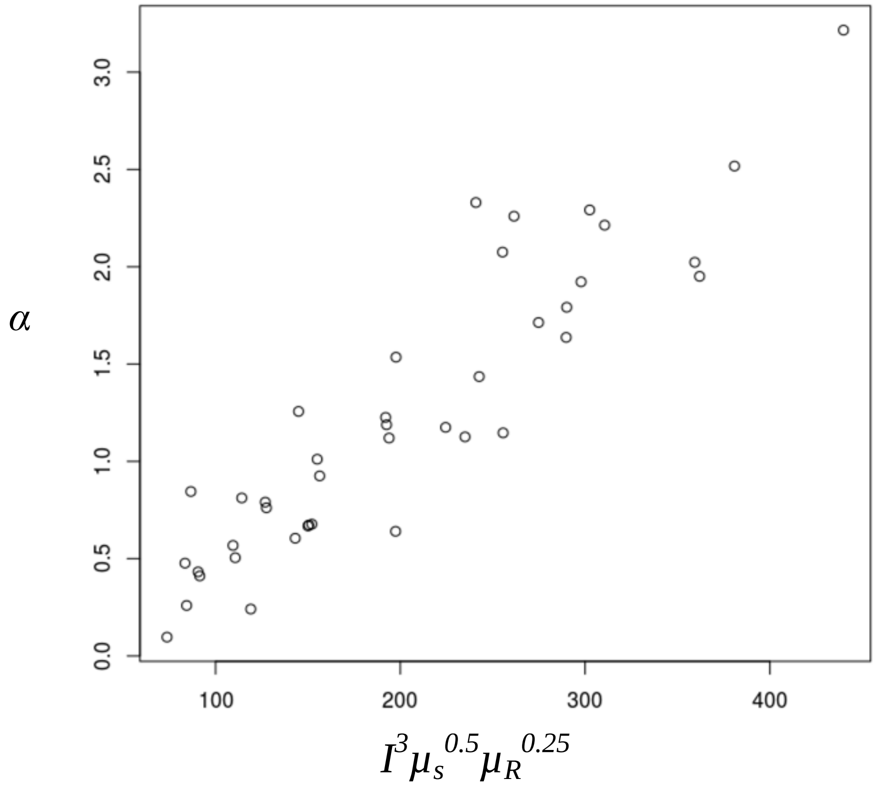

Figure 72. Dilatancy angle as related to initial state and friction

Finally, including angularity creates a term that linearly relates to dilatancy angle. Figure 73 shows that while high goodness of fit (R^2) can be attained; significant root-square error (RSE) limits the use of this statistical term in predictive DEM calibration. Analytical models that account for particle angularity are difficult to derive in three dimensions. Therefore, statistical methods need to be refined to meet the requirements of DEM parameter prediction.

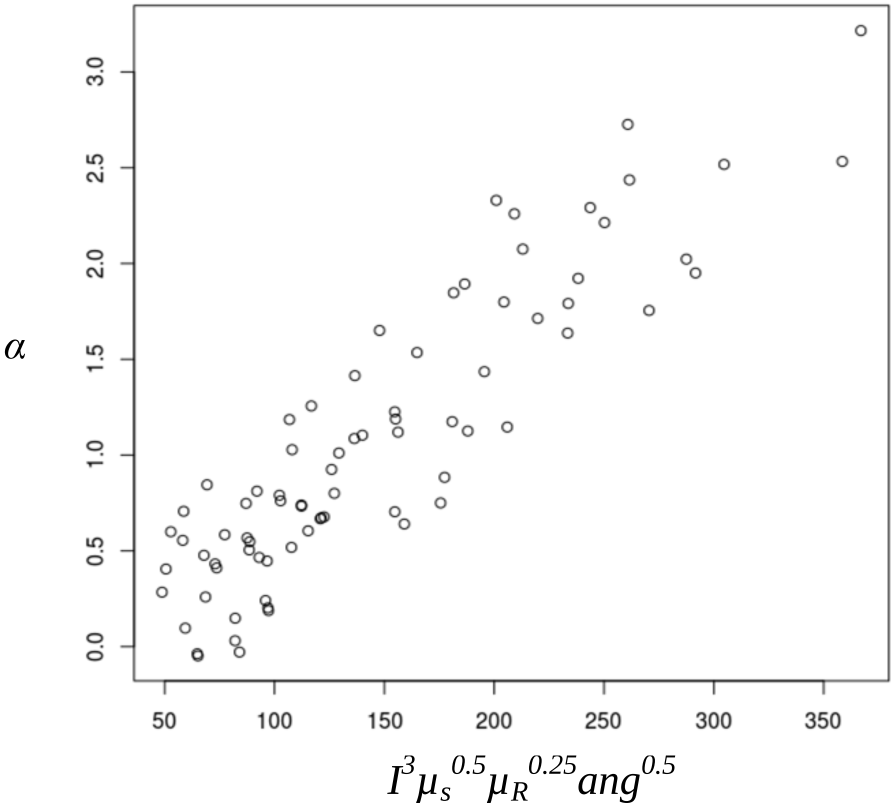

Figure 73. Dilatancy angle as related to initial state, friction, and angularity, R^2=0.93, RSE=0.34, n=77

Relative density

Salot et al. (2009) has shown the importance of relative density in relating physical density to virtual density. A method was developed to assess the maximum and minimum void ratio of a virtual granular assembly. Virtual assemblies are defined by material properties, external loads, and a structural state, and the limits of possible structural states are defined by material properties and external loads. Therefore, a virtual experiment was designed to assess the limits of structural state with respect to material properties and loads. Material properties include the following:

- Sliding friction
- Rolling friction
- Cohesion
- Particle stiffness

- Particle size and distribution
- Particle shape

The maximum void ratio was determined by lightly air-pluviating cohesionless virtual specimens into a virtual box. The external load was then applied left to equilibrate. Then the void ratio of the specimen was measured. The minimum void ratio was determined by exciting the virtual specimen with triaxial mechanical vibrations while still under external load. The minimum void ratio after an extended period of vibration was measured. In order to understand the effect of friction, the particle stiffness, size, distribution, and shape were held constant. A Hertzian formulation was used for the particles with a Young's modulus of $29x10^8$ Pa. Spherical particles of diameter 3mm with a monodisperse distribution were assembled using the default random particle insertion method in LIGGGHTS. The vertical load was also restricted to 10 kPa. The sample was confined so that lateral reaction pressure was unbounded.

Table 14. Experimental design of relative density study

Specimen #	Sliding Friction	Rolling Friction
1	0.2	0.1
2	0.3	0.1
3	0.4	0.3
4	0.5	0.4
5	0.05	0.05
6	0.05	0.03

Six simulations were run in the LIGGGHTS DEM environment. The time history evolution of void ratio is shown in Figure 74. Each void ratio time history curve is characterized by an intermediate plateau and a final asymptote. The first plateau corresponds with the maximum void ratio, and the final asymptote corresponds with the minimum void ratio.

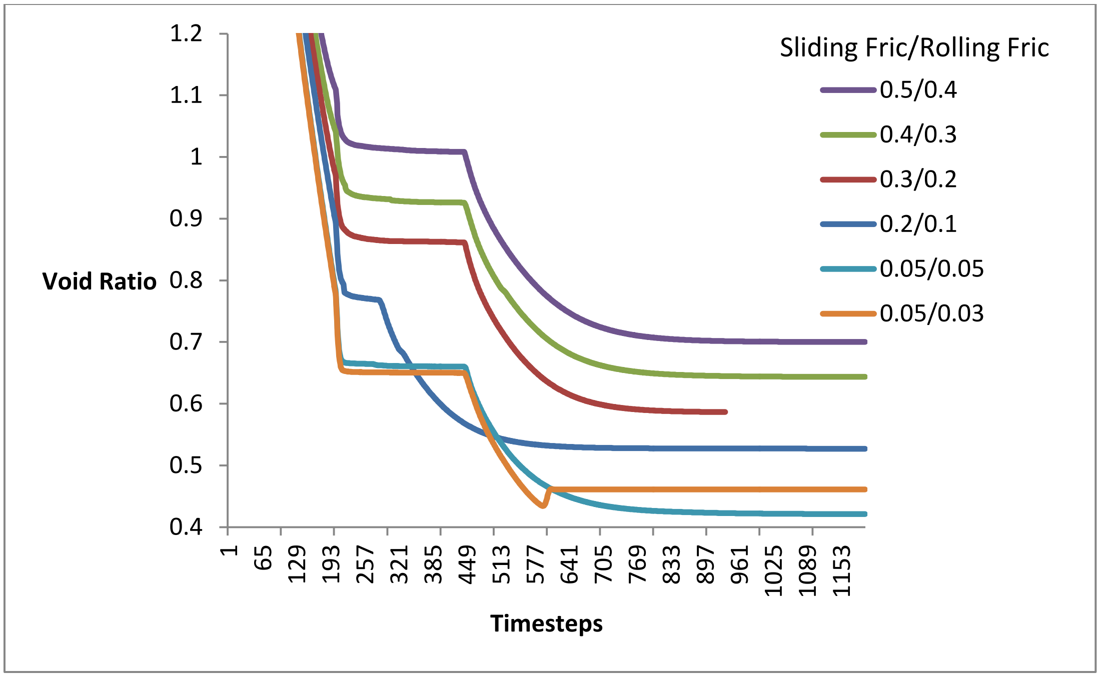

Figure 74. Time history of void ratio in relative density simulations

The maximum and minimum void ratios were extracted from the data in Figure 74 and presented in Table 15.

Table 15. Maximum and minimum void ratios of virtual granular assemblies from relative density simulations

Sliding Friction Coefficient	Rolling Friction Coefficient	Maximum Void Ratio	Minimum Void Ratio
0.05	0.03	0.65	0.46
0.05	0.05	0.66	0.42
0.2	0.1	0.77	0.53
0.3	0.2	0.86	0.59
0.4	0.3	0.93	0.64
0.5	0.4	1.01	0.70

There is an unclear relationship in the complex interaction of sliding and rolling friction which will be addressed in detail in a subsequent chapter. Without a rigorous interaction model for sliding and rolling friction coefficient, it is difficult to elegantly draw a correlation to maximum and minimum void ratios.

The data in Table 15 envelopes the final void ratios from the earlier DOE (Figure 69), The maximum void ratios from the relative density tests are consistently higher than the final void ratios from the triaxial tests. The expectation was that granular assemblies initialized at the final void ratio would not exhibit any dilatancy, and aside from contraction due to grain deformation, would exhibit a constant volume response. Although the focus of current DEM calibration efforts were focused on dry and drained unsaturated media, undrained constant-volume conditions could potentially be modeled using careful prescription of initial state.

Cohesion calibration

Common cohesion models in DEM codes have been described in Chapter 2. Several models for cohesive granular materials are available in DEM literature as well as in commercial and open-source DEM software. Water bridging models are very commonly used in geomechanical simulation, however, the phenomenological performance of water bridging models is limited. Figure 75 shows the strength of cohesive DEM assemblies subjected to direct shear. The strength of the granular assemblies does not consistently increase as user-input cohesion coefficients increase.

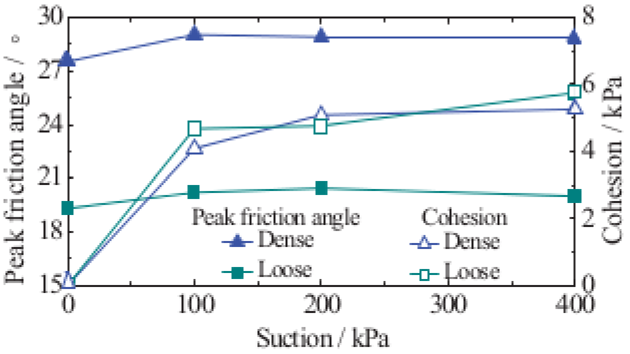

Figure 75. Typical water bridging model in DEM, assessed in virtual direct shear test (Source: Jiang and Shen, 2013)

SJKR2 calibration

The JKR model is a cohesion formulation that was described in detail in Chapter 2. The built-in water bridging formulation of cohesion (SKJR2) in LIGGGHTS was tested to see if it was suitable for modeling bulk granular assemblies. Seven direct shear tests were ran until they reached a shear displacement of 15 mm. The vertical stress was varied over two levels (60-100kPa). The cohesion energy density was varied over three levels

(100, 1000, 2000 kJ/m^3). Critical state shear strength was captured at shear displacement of 12 mm.

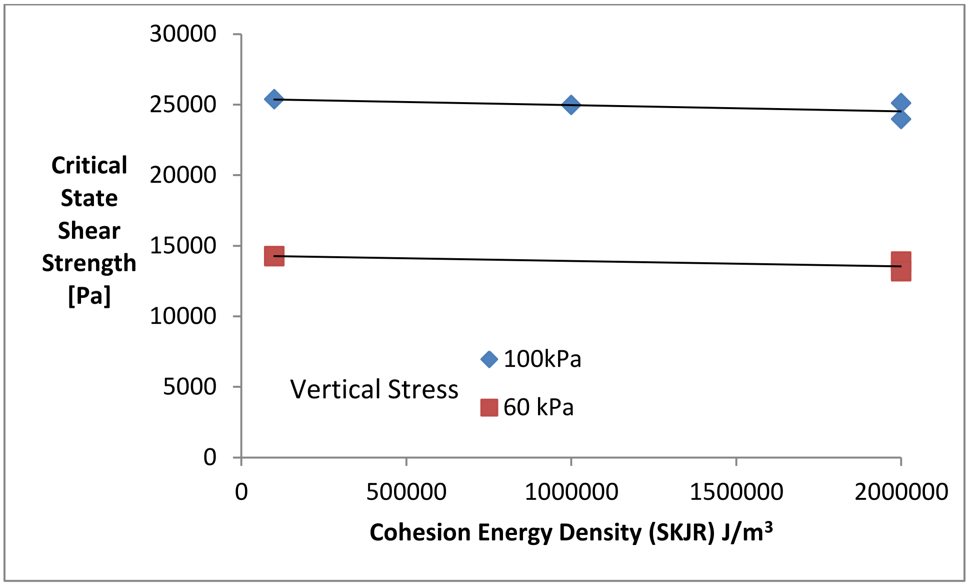

Figure 76. Evaluation of SKJR2 cohesion model in LIGGGHTS

The SKJR2 model behaved rather similarly to the water bridging model evaluated in Figure 75. As such, the usefulness of the SKJR2 model was limited. The non-responsiveness of critical state strength to increases in the user-defined cohesion energy density was problematic for modeling real soils and powders that exhibit higher cohesion than what the SKJR model delivered.

Projected area cohesion

A new cohesion model was developed to address the shortcomings of the SKJR water bridging model. Macro-scale cohesion was continuum concept. As such, micro-scale cohesion, equation 4.5, was formulated as if void space around a particle was non-existent (i.e. as part of a continuum). Each particle of diameter, *d*, was projected onto a 2D square of side length, *d*. The area of the 2d square is the area over which the micro-scale cohesion acts (equation 4.4).

$$A_{square} = d^2 \tag{4.4}$$

$$F_{cohesion} = CA_{square} \tag{4.5}$$

where A_{square} = projected area of a square.

d = diameter of particle.

$F_{cohesion}$ = micro-scale cohesive force acting between particles

C = cohesion coefficient, Pa.

A small study tested the sensitivity of the micro-scale cohesion formulation on the mechanical behavior of DEM particle assemblies subjected to triaxial compression. All virtual triaxial tests were run with the following DEM parameter set:

Sliding friction coefficient = 0.55

Rolling friction coefficient = 0.55

Young's modulus = $1\text{x}10^{10}$ Pa

Confining pressure = 200kPa

Particle diameter = 3mm

% Aspherical = 44%

Particle aspect ratio = 2

Absolute damping coefficient = 1 N-s/m

All specimens were isotropically consolidated. The micro-scale cohesion energy density was varied over a moderate range (Table 16).

Table 16. Cohesion range

Specimen	Cohesion Energy Density [J/m^3]
1	1
2	50000
3	150000
4	200000
5	300000

Initial void ratio (after isotropic consolidation) changed slightly with respect to cohesion coefficient (Figure 77).

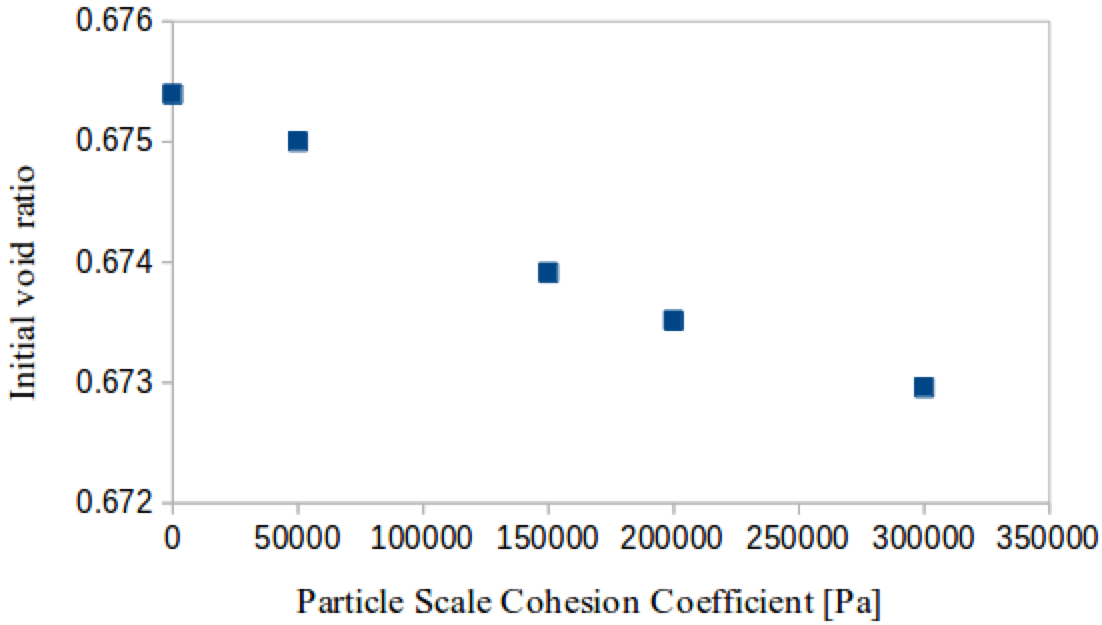

Figure 77. Covariance of micro-scale projected area cohesion coefficient and initial void ratio after isotropic consolidation

Despite the small covariance of void ratio with cohesion coefficient, significant data was gleaned from the simulations. Figure 78 shows the linearity of the global deviatoic stress with respect to cohesion coefficient over many strain levels. It was reasonable to assume that the effects of the small void ratio covariance subsided as axial strains exceeded 15%. Therefore, the behavior of the projected area cohesion model was well predicted using linear regression methods.

For the purposes of calibration, it was found that the projected area cohesion could be included in a linear statistical model for a complete Mohr Coulomb failure criteria for simulated granular materials because the covariance in Figure 77 is small enough to be neglected.

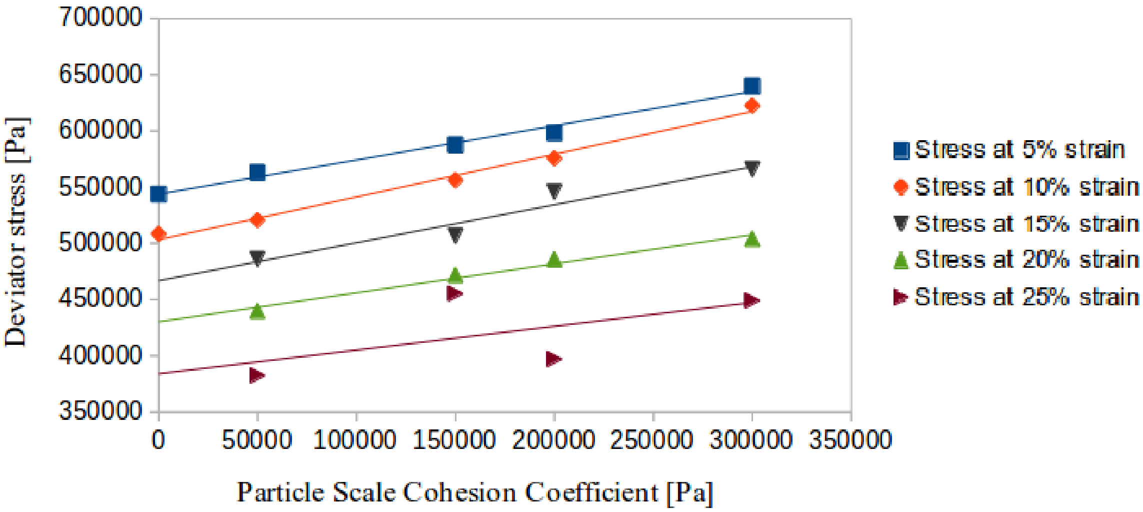

Figure 78. Deviatoric stress at various strain levels of virtual triaxial specimens using the projected area cohesion model

Summary and Conclusions

Exploratory fractional factorial design of experiment analyses were conducted on virtual test data from many DEM simulations. Statistical regression methods were used to describe and predict the complex role of friction, stiffness, and initial state on strength and volume change characteristics of loaded granular assemblies.

The repeatability of DEM simulations was assessed and was found to be good using random particle insertion built into LIGGGHTS as well as the 3D extension of Bagi (2005). The initial structural or configurational state of a virtual granular assembly was highly correlated with granular strength, dilatancy, and final volume change conditions. The sliding and rolling friction coefficients served as a baseline strength upon which the initial state was additive. Over-consolidated initial states added to the baseline strength, whereas under-consolidated initial states reduced strength from the baseline. However, the critical state strength of virtual granular assemblies was unaffected by initial state. In properly controlled statistical analysis, particle stiffness was only correlated with the contractile regime of the volume change curve, which is consistent with physical experiments by Whitman et al. (1964). Cohesion models were also explored, and it was found that the SKJR models of cohesion were not appropriate for meso-scale modeling of dense granular systems, especially those that exhibit cohesion intercepts on Mohr-Coulomb failure envelopes. On the other hand, the phenomenological behavior of projected-area cohesion scaled linearly with its user-input coefficient. Finally, relative density was examined as a function of sliding and rolling friction coefficient. It was found that sliding friction was moderated by rolling friction, which made the prediction of phenomenological behavior difficult when relying on independent sliding and rolling friction terms. Additional focus is required to discern the moderating effects of rolling friction on resistance to motion.

CHAPTER 5. VALIDATION STUDIES

Introduction

The DEM calibration methodology developed in previous chapters required testing. This chapter details three studies which investigated the strength and weakness of the DEM calibration approach. Three different studies were developed with the thought that different mechanisms of deformation of granular assemblies were explored. The first study compared physical and virtual blade mixing of sand using the new DEM calibration methods. The blade mixing study investigated quasi-static shear conditions of granular deformation. The second study described cone penetrometer experiments. The cone penetrometer was an important test because, aside from ubiquity, it introduced a mixed mode of granular deformation: combined compaction and shearing. The final validation study compared physical and virtual hopper discharge of agricultural grains. The DEM calibration methodology, when founded in appropriate theory, extended to all dry granular materials. Thus, agricultural grains were an appropriate granular medium for testing the calibration methodology. In addition, the dense particle flow behavior in the hopper discharge experiments presented yet another mode of deformation of granular assemblies.

Blade Mixing

Soil-tool interaction in DEM

Many soil-tool interaction problems were simulated using DEM including cutting, blade sweeping, and cone penetration (Shmulevich, 2010). Shmulevich et al. 2007 performed blade cutting simulations on various blade geometries using a calibrated soil model from Asaf et al. 2007. Zhang and Li (2006) consider cohesive effects of moisture when modeling soil-blade interaction in 2D using breakable bonds. Using similar methods, Sadek et al. (2011) performed soil calibration using laboratory direct shear tests over a range of moisture contents. A tool-soil problem simulated by Obermayr et al. (2011) used triaxial test data as a basis for calibration as well as the relative density model proposed by Salot et al. (2009). Correlation between experimental and nonrotational DEM model showed that the relative density method of calibration finds applications outside of standard geotechnical testing.

Methods - direct shear test

Six specimens of Michigan 2NS sand underwent direct shear testing at three normal loads. The critical state shear strength of each specimen was recorded and plotted (Figure 79) for calculation of the critical state friction angle, ϕ.

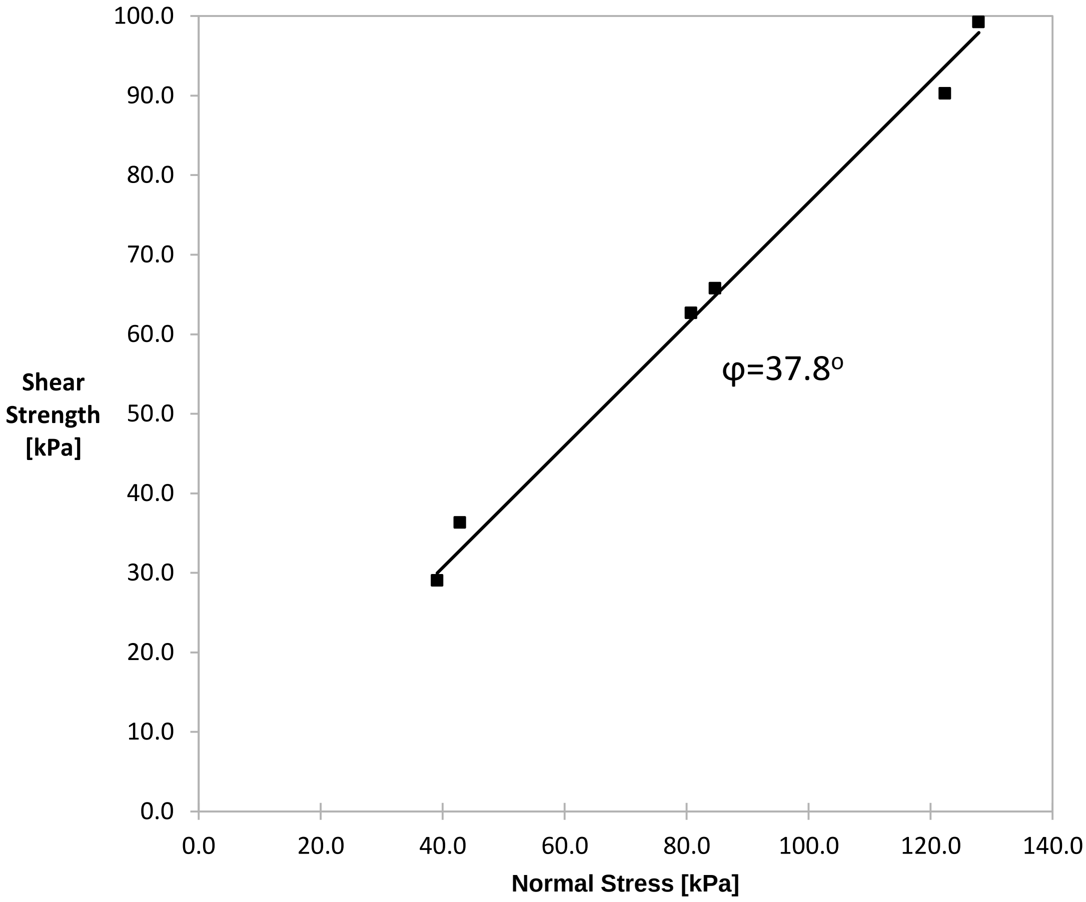

Figure 79. Mohr-Coulomb failure envelope of critical state shear strength for Michigan 2NS sand from direct shear tests

The minimum and maximum void ratios of the Michigan 2NS sand was also determined at e_{min} = 0.54 and e_{max} = 0.82 [ASTM 4253, 4254, and 854-06].

Physical blade sweep

A torsional load cell was fabricated by outfitting a hollow, square aluminum shaft with 4 strain gages in a full Wheatstone bridge configuration (Figure 40). It was calibrated by applying a known moment load to the shaft and measuring voltage drop across the Wheatstone bridge circuit.

A string potentiometer was pulley-coupled to the aluminum shaft to measure angular position. A rectangular (100 mm x 23 mm) steel mixing blade was also bolted to the shaft. The shaft-blade assembly was lowered into a bucket while a bearing constrained all movement except cylindrical rotation. The bucket was filled with 2NS sand and lightly tamped and leveled (Figure 41). The void ratio of the prepared sand specimen was 0.65 (relative density, D_r = 40%). The bulk density of the sand specimen was 1600 kg/m^3. The bulk volume of the sand was approximately 3750 cm^3.

After the sand was leveled and the data acquisition equipment was active, the blade shaft was manually rotated to sweep the blade through the sand. Shaft torque and blade angle was measured through three trials of the blade sweep (Figure 80).

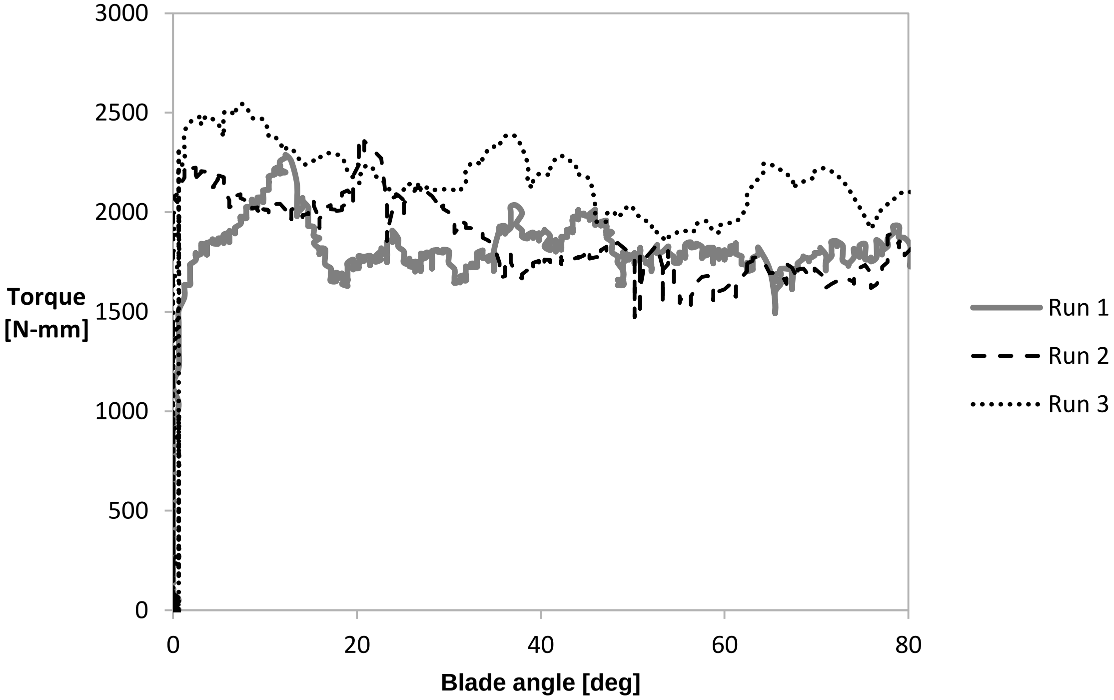

Figure 80. Blade shaft reaction torque from physical blade sweep tests

Each of the three blade-sweeps were rotated at different speeds to assess the sensitivity of shaft reaction torque on shaft velocity. The shaft velocity curves for each test are shown in Figure 81.

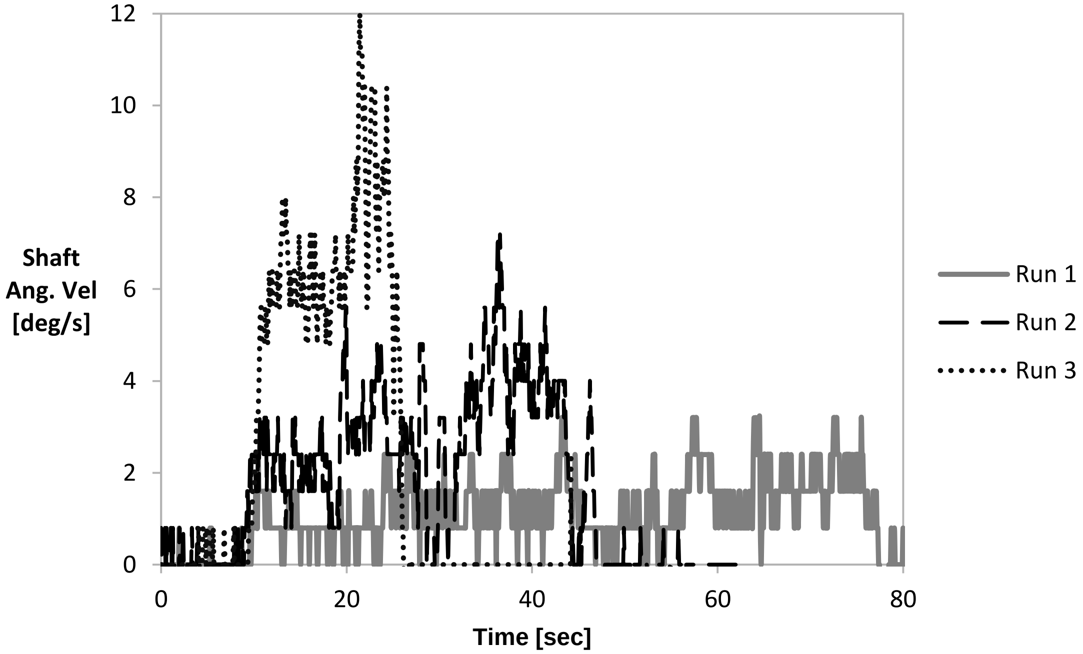

Figure 81. Shaft velocity for each run of the physical blade sweep test

From Figure 80 and Figure 81, shaft reaction torque was sensitive to shaft velocity greater than 4 deg/s. Therefore, the DEM simulation of the blade sweep system was performed at a shaft velocity of 2 deg/s.

DEM Setup

A cylindrical bin of radius of 15 cm was initialized with an elastic wall of Young’s modulus 200 GPa and Poisson’s ratio of 0.3. Bottom surface of the bin was also modeled by the same elastic wall, but the top of the bin was left open. The interaction between the walls and the particles were modeled by the Hertzian contact law. The sliding and rolling friction coefficients acting between the particles and wall were 0.3 and 0.155, respectively. The steel blade was modeled as a tri-surface mesh with Young’s modulus of 200 GPa and Poisson’s ratio of 0.3. The shaft was omitted from the simulation. However, the blade’s rotation was centered on the rotation axis of the shaft. In addition, the reaction forces acting on the blade were transformed to a reaction torque acting on the shaft axis. The blade was rotated at 2 deg/sec.

The physical sand specimen, after leveling, was approximately 70 mm deep. Therefore, the cylindrical DEM specimen was initialized at a depth of 70 mm. The bulk density of the physical sand was matched in DEM at 1.596 g/cm^3, but only after the specimen was brought to equilibrium at a desired initial state. Therefore, the particle density was highly dependent on the void ratio immediately before the simulation started.

Calibration

Calibration was carried out using the information flow chart in Figure 82.

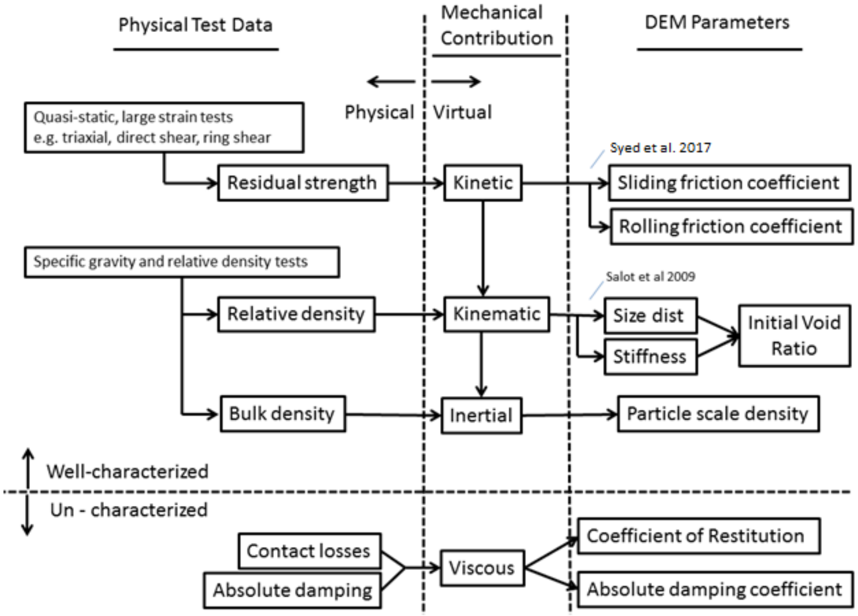

Figure 82. DEM Calibration flow chart for dry, non-cohesive granular material

The coefficients of sliding and rolling friction are identified by the effective friction angle method in Syed et al. (2017) based on the critical state strength of the 2NS sand (Figure 79). Particle-scale Young's modulus was chosen at 10^8 Pa to keep the timestep size above 10^{-6} seconds. Poisson's ratio was arbitrarily chosen to be 0.3. The particle radius was set to 2 mm so that reasonable computation times could be achieved on available computing hardware (AMD Opteron 6274, 32 cores @ 2.2 Ghz). The relative density of the physical specimen was estimated to be 40%. However, the shaft blade geometry and the irregular bin shape create some error in the determination of physical relative density. In addition, precise prescription of virtual initial state is often confounded by tool geometry; especially in cases where a blade is represented by shell surface. Regardless, the virtual relative density was approximately prescribed at 40%. The actual virtual relative density after specimen preparation was approximately 51%. Using the initial void ratio and physical bulk density, the particle scale density was prescribed at 2606 kg/m^3. The coefficient of restitution was arbitrarily set to 0.1. Absolute damping was not active in this simulation. Table 17 summarizes the calibrated DEM input parameters.

Table 17. DEM input parameters

Input Parameters	
Sliding friction, μ_S	0.3
Rolling friction, μ_R	0.155
Particle radius [mm]	2.0 mm (mono disperse)
Young's modulus [Pa]	1x10^8 Pa
Target virtual relative density, D_r [%]	Estimated 40%
Intermediate Values	
Maximum void ratio, e_{max}	0.873
Minimum void ratio, e_{min}	0.446
Initial void ratio, e_0	0.655
Actual virtual relative density	51%
Particle-scale density	2606 kg/m^3
Number of particles	87884

Results and discussion

The virtual blade reaction torque about the axis of rotation was measured and compared to the physical reaction torque acting on the shaft (Figure 83). The virtual and physical steady state reaction torque is in agreement. However, the transient response of the virtual test lags behind the physical results. It was hypothesized that the particle scale stiffness could be increased to reduce the error below 15 degrees of shaft rotation.

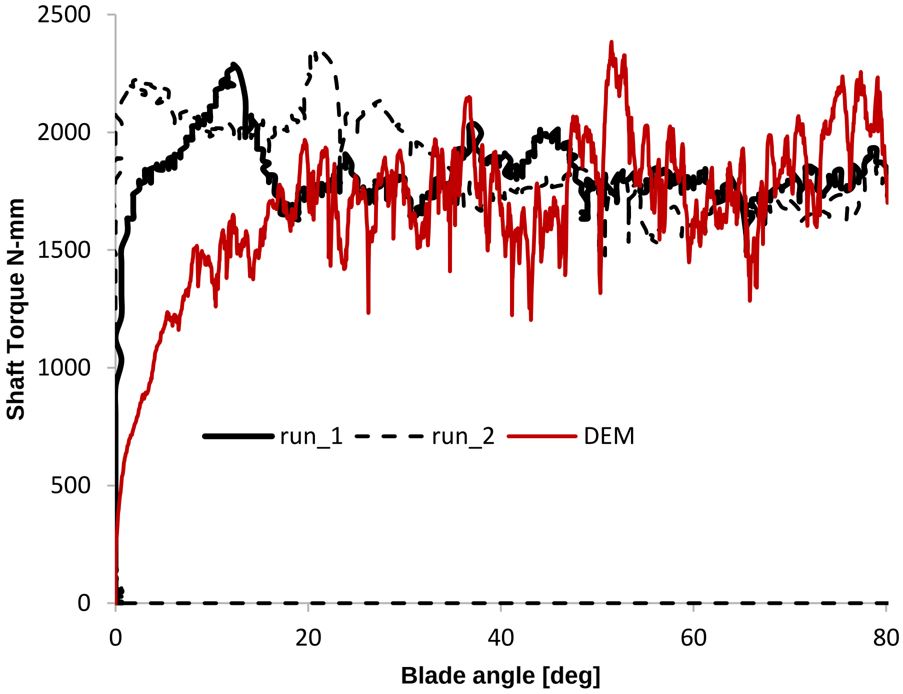

Figure 83.Virtual and physical shaft reaction torque in blade mixing. Virtual blade velocity = 2 deg/s

In addition to the lag, the simulation exhibits a noisy signal compared to the physical test results. This is attributed to the ratio of the blade characteristic length to the average particle diameter. Figure 84 shows a moving average of the shaft torque reaction from simulation compared to the average shaft torque from physical testing.

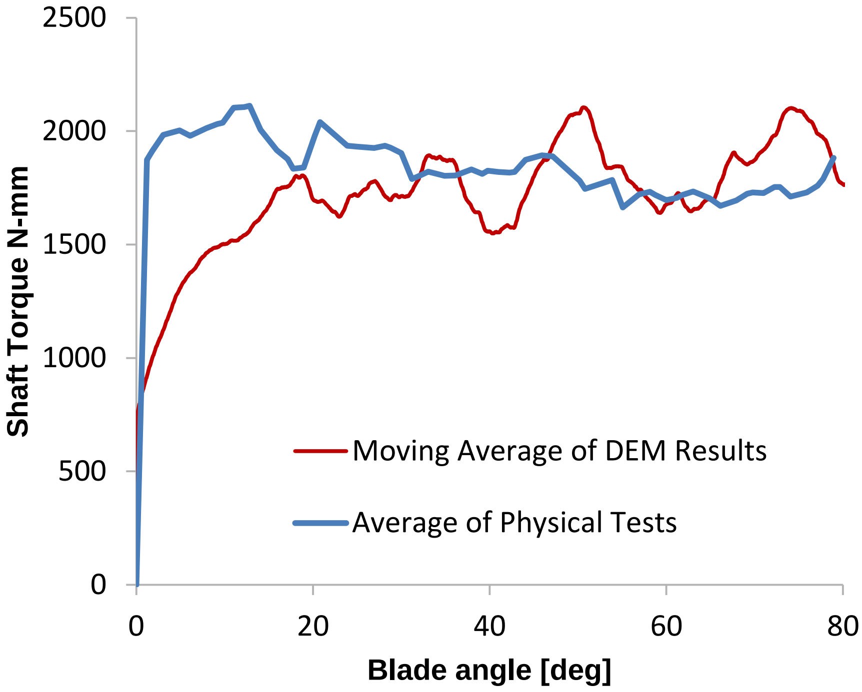

Figure 84. Average physical vs. moving average DEM blade mixing

Indeed, from Figure 84, the lagging nature of the DEM simulation compare to the physical testing is still apparent, even after smoothing and averaging operations. Additional work is necessary to explain the shortcomings of the current DEM simulation.

When the blade speed was increased to 6 deg/s, the calibrated DEM model under-predicted the shaft reaction torque. It seemed that dynamics became a significant contributor to shaft torque at 6/deg/s. It was hypothesized that the coefficient of restitution would improve the agreement between virtual and physical experiments in the dynamic case. Coefficient of restitution was uniformly varied over 5 blade mixing simulations and shaft torque was recorded as a function of blade rotation. The results of the virtual experiment are shown in Figure 85.

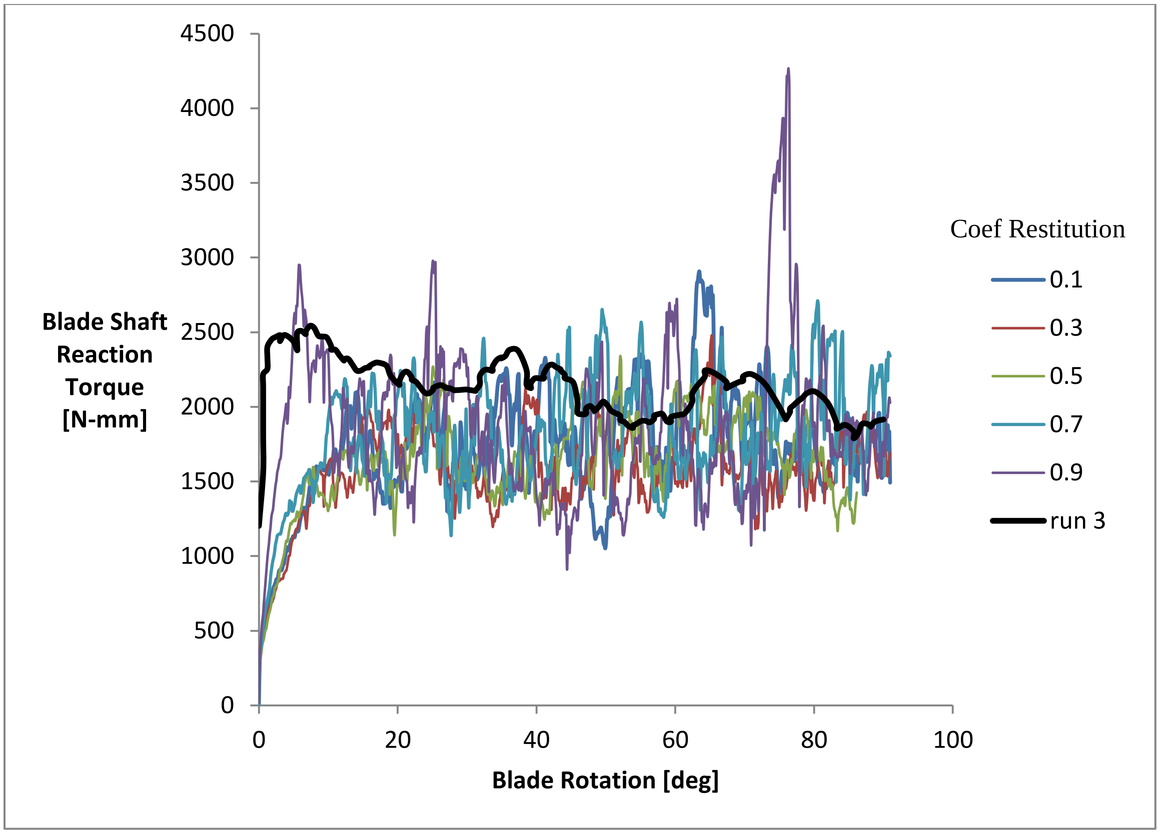

Figure 85. Blade mixing at shaft velocity 6 deg/s. Run 3 = Physical experiment. Coefficient of restitution varied from 0.1 to 0.9 in virtual experiments.

Figure 85 shows that increasing coefficient of restitution did not improve shaft reaction torque prediction. Indeed, the signal became noisier as the coefficient of restitution was increased.

Density scaling test

Thornton (2000), O'Sullivan et al. (2002), and Gong et al. (2012) used density scaling to increase the critical time step and speed up DEM simulation times in the simulation of standard, quasi-static geotechnical tests. The limits of density scaling were often described in terms of strain rate, but for tool-soil interaction problems, strain rate was difficult to know *a priori*. Practical limits of density scaling needed to be developed. Density scaling was tested on the blade sweep simulation at a blade rotation speed of 2 deg/s with monodisperse particles with radii of 2 mm. Particle density was scaled by a factor of 16 to achieve a 4x increase in the critical timestep. Figure 86 shows the difference between density-scaled and unscaled specimens. The particle interaction parameters for both samples were the same as in Table 17 and initial void ratio was e_0=0.655.

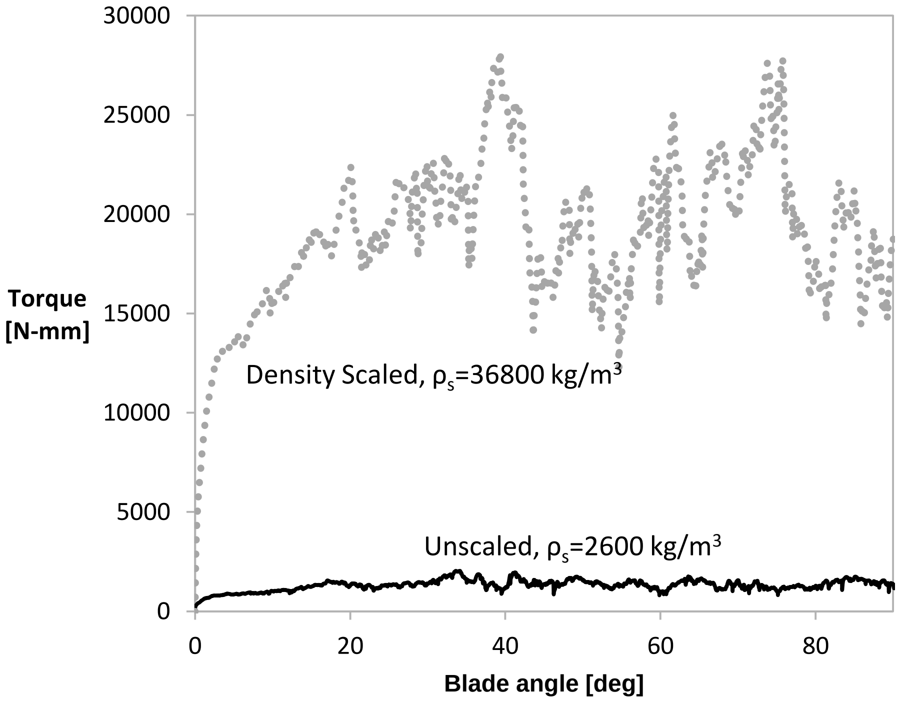

Figure 86. Comparison of density scaled and unscaled DEM blade sweep simulations, ρ_s=particle scale density

The DEM comparison in Figure 86 shows that density scaling added significant inertial effects to a 2 deg/s blade sweep and therefore was unsuitable for this speed and type of simulation.

Cone Penetrometer

Cone penetrometer testing was a simple and easy method for characterizing in-situ soil strength. Modeling soil reaction from conical tip penetration for DEM material calibration was helpful to predict dynamic soil behaviors including shear, compression and cutting (Gill and VandenBerg, 1968) simulation of tool-soil interaction problems. Asaf et al. (2007) simulated wedge sinkage on soil and performed energy analysis that showed that friction energy is the dominant source of resistance to deformation. Calibration was performed using two different wedge angles because non-unique solutions were found when minimizing error with a single wedge. Their studies showed that 20 and 30 iterations were required to minimize the objective function until matching the penetration energy into soil from a physical experiment. Ucgul et al. (2014) used angle of repose tests to calibrate a soil model for cone and disk penetration simulation. Interestingly enough, hysteretic contact models used by Ucgul et al. (2014) exhibited better correlation than Hertz-Mindlin to physical test results, but it is unclear as to whether or not hysteretic contact stiffness was *required* for such simulations. The number of DEM particles contacting the ASABE cone was also factor in the accuracy of solution. Jiang and Yu (2006) suggested that 13 DEM particles was the minimum that should contact the cone. The size of the virtual container in which the cone penetrometer test was performed had an effect on the magnitude of cone penetration resistance. Bolton and Gui (1993) showed that cone penetration resistance test was insensitive on soil container radii larger than 40 times the cone base radius. The ASABE (ASAE standards, 1999) cone base had a diameter of 12.53 mm. Following Bolton and Gui’s (1993) suggestion, a DEM virtual container with a diameter of 501.2 mm could be used for DEM cone penetrometer modeling. Preliminary DEM simulation showed that the experimental container size effects can be attenuated or amplified by DEM particle size, stiffness, and friction. Many studies used different approaches in modeling cone penetration in soil to address DEM particle scaling, contact models and boundary to median particle size (B/d50) (Table-1). Previous experimental and DEM simulation studies showed that calibration procedure of DEM material properties using simple test such as cone penetrometer required further understanding of particle size to cone penetrometer ratio, simulation versus laboratory tests geometry scaling ratio and robust DEM material properties calibration methodology.

Table 18. Review of DEM simulation formulation and parameters for virtual cone penetrometer (and similar) studies

Study	Type	Particle Size	Initial State	μ_s	μ_R	Normal Stiffness	B/d50
Alvaro and Ooi, 2016	30 deg ASABE	5mm +/-10%	Porosity = 0.53 before consolidation	0.2-0.8	0.1	Hookean-Hysteretic, 100/500-2500 kN/m	NR [b]
Arroyo et al., 2011	CPT[a]	26.5mm C_u [c] =1.31	$0.75<D_r<0.97$	0.35	0 and inf	Hookean, 300MN/m	2.7
Falagush et al., 2015	CPT	1-2mm	Porosity 0.37-0.42	0.2-1.0	prohibited	Hookean, 500 KN/m	18
Jiang et al., 2014	CPT	7.6mm C_u=1.3	2D_Void Ratio = 0.27	0-0.5	n/a	Hookean, 75MN/m	21

[a] CPT refers to Cone Penetration Test commonly used in geotechnical site characterization

[b] NR- Not Reported

[c] C_u = Coefficient of Uniformity

The objective of the study was to develop DEM calibration of sandy loam soil with different initial relative density and validate the DEM model using ASABE standard cone penetrometer testing.

Materials and methods - cone penetrometer test

A cone penetrometer device was developed with commercial-off-the-shelf components. An analog S-type load cell (500-lb capacity) was fixed to a smooth rod and ASABE cone tip (a 30-degree cone and 12.53 mm cone base diameter). The analog signal from the load cell was read using the ADC built into the Arduino which was used to transfer data back to a PC for analysis. An ultrasound range finder was used to determine depth of penetration. The cone penetrometer device was used to measure cone penetration resistances of Norfolk Sandy Loam (NSL) that has particle size distribution of 72% sand, 17% silt and 11% clay (Batchelor, 1984).

Norfolk Sandy Loam (NSL) was provided from the National Soil Dynamics Laboratory in Auburn, AL. The soil was prepared at a moisture content of 6.3% (d.b.). To simplify calibration, NSL was calibrated as cohesion-less media. Soil bulk densities of

1.71 Mg/m^3 and 1.22 Mg/m^3 (Tekeste et al., 2007) were assumed as the maximum and minimum bulk density for initial bulk density in DEM simulation.

Cone penetration resistance of NSL was measured using ASAE standard cone penetrometer (Figure 87). The soil specimens were prepared in a section of PVC pipe that was 102 mm in diameter. Specimens were pluviated and tamped periodically to attain desired bulk densities that correspond to the relative densities. The specimen height inside the PVC pipe section ranged from 200 to 230 mm. The PVC pipe section and data acquisition system is shown in Figure 87. The cone penetrometer was manually plunged into the NSL very slowly at approximate speed of 16.5 mm/sec. to maintain quasi-static conditions.

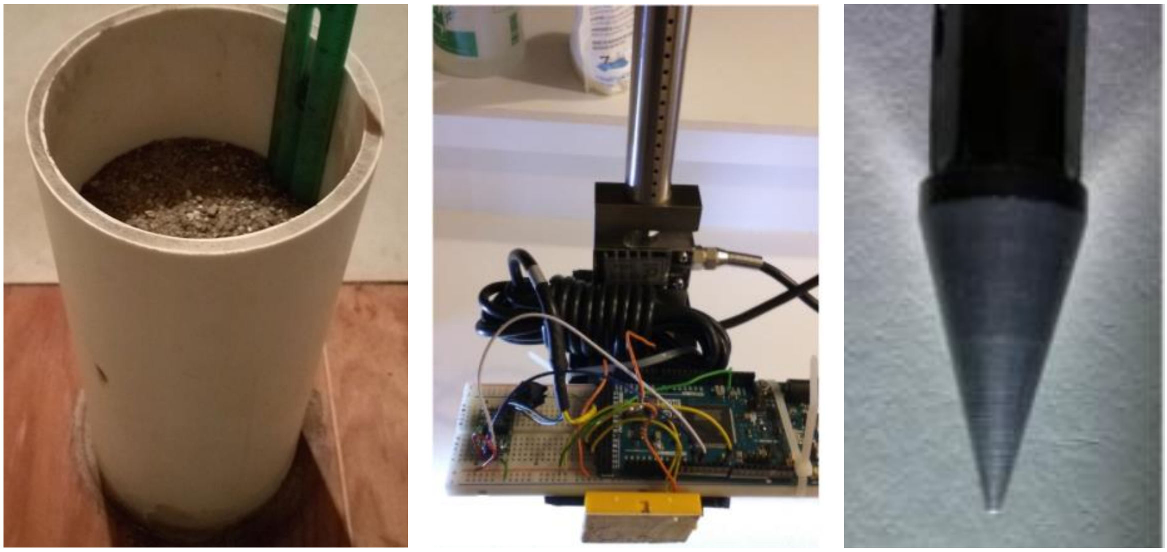

(A) (B) (C)

Figure 87. PVC pipe section filled with loose Norfolk sandy loam soil at 6.3% moisture content (A); Arduino data acquisition system ans S-beam load cell (B); and ASABE 30- deg cone (C).

DEM soil pone penetrometer and DEM model calibration

The 30 degree ASABE cone has a diameter of 12.53 mm. The diameter of the virtual container was modeled to be 500 mm. The depth of the virtual container was 300 mm.

The DEM particle radius was 2 mm. Comparing characteristic lengths of the ASABE cone to the particle provides, a cone diameter to particle diameter of three was used to ensure three particles at randomly in contact to the cone at once.

DEM material properties calibration

The DEM calibration procedure after (Syed et al., 2017) was used to determine DEM soil parameters including the initial soil assembly structural states of the virtual NSL DEM soil model. The DEM algorithm (Figure 82) comprised of the assumption that relative density and bulk density strongly influences the kinematic and inertial behaviors of particle dynamic systems; and the critical state soil strength strongly affects the kinetic particle dynamic behaviors. Assuming this cause-effect relationship of soil properties and mechanical behaviors, the DEM material properties (sliding friction coefficient, rolling friction coefficients, contact stiffness) were calibrated using automated iterative DEM simulations in LIGGGHTS (Open source DEM code) (Syed et al., 2017). The initial void ratio and particle scale density were also iteratively adjusted in relation to the DEM particle size and bulk density. Viscous damping DEM properties were assumed to have negligible influence for quasi-static tool-soil DEM simulation and were not included in the DEM calibration methodology.

Critical state internal angle of friction was estimated from quick direct shear tests at low normal stresses. Based triaxial test estimated relationship between octahedral shear stress and octahedral normal stress, a yield function with non-cohesion (Bailey and Johnson, 1989) was assumed for the DEM soil contact model selection. The estimated friction coefficient values of sliding (μ_s=0.03) and rolling (μ_R=0.025) were used for the DEM simulation. Relative densities of 5%, 30%, and 90% were used to determine the initial void ratios for DEM simulations of three density conditions. From simulations described in Salot et al. 2009, the maximum and minimum void ratios for the virtual NSL are e_{max}=0.66 and e_{min}=0.42. Therefore, three DEM cone penetrometer simulations will be performed at void ratios near e_{loose}=0.65, e_{medium}=0.61, and e_{dense}=0.44. Relative density (D_r) was characterized as $D_r = \frac{e_{max} - e}{e_{max} - e_{min}}$.

Stable DEM soil specimens

A technique was developed to create stable DEM soil assembly in the cylindrical specimens at initial states (Figure 88). DEM particles were initialized in a cylindrical container with a rigid base and a temporary lid, and were allowed to equilibrate over many DEM cycles. During this time, the reaction force on the lid of the cylinder was monitored. The reaction force decreased over the DEM calculation cycles as the specimen tended toward the minimum potential energy state. Eventually, the specimen could no longer equilibrate, at which point, the cylinder was transversely vibrated with amplitude of 0.1xParticle Radius at 30 Hz. The vibration is turned off when the lid reaction reaches zero. At this point, the sample is completely stable and the lid can be removed. Figure 89 shows the trend of lid reaction force as equilibration progresses.

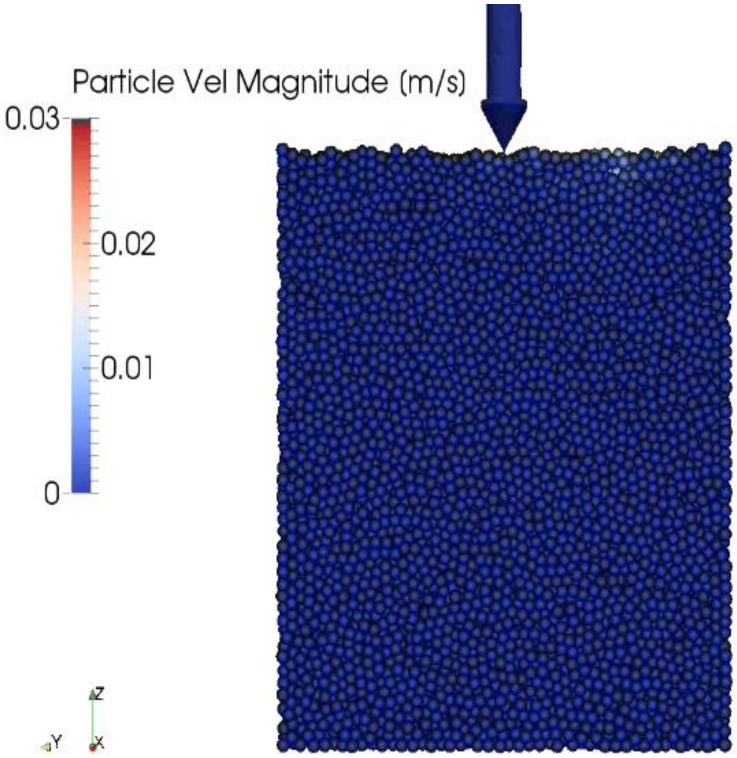

Figure 88. DEM cone penetrometer simulation side view

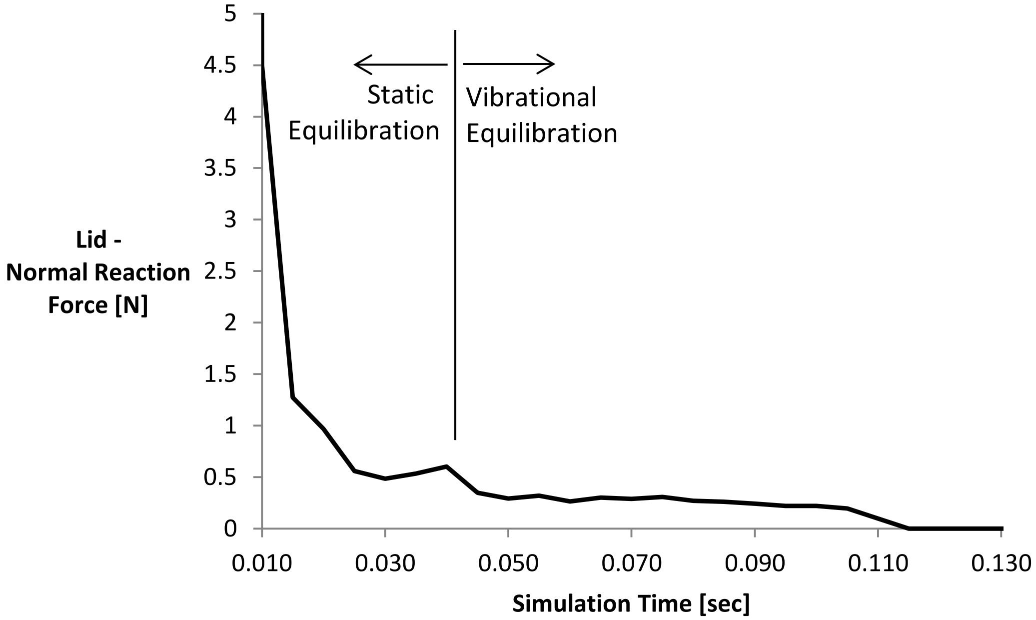

Figure 89. Lid reaction forces over time

DEM particle size sensitivity

DEM particle size was varied to assess their contribution to the reaction force of an ASABE cone penetrating a dense granular assembly at 16.5 mm/s. Effect of particle size on signal noise (Figure 90) showed smaller particles seem to reduce the noise in the cone resistance data.

Indeed, the practical requirements of particle size involve the number of contact with a tool face at any given moment during a simulation. Since the cone penetrometer device is relatively small to begin with, it demands small DEM particles in the simulation of its operation. In addition, computational demands of smaller particles very often limit particle size. The necessary balance between particle size, tool geometry, and computational demand is often upended by computational demand.

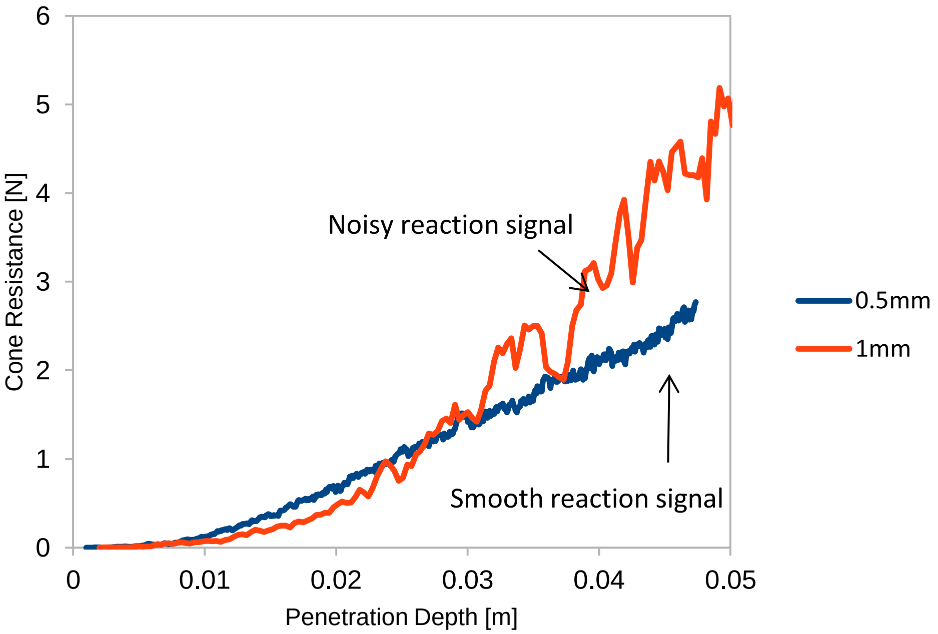

Figure 90. Effect of particle size on DEM predicted signal noise

It is computationally infeasible to run multiple iterations of the DEM simulation with DEM particle similar to the physical soil particle size distribution or at 1 mm particle diameter size. As particle size decreases, critical stable time step and particle count take computationally long simulation times. After preliminary tests, DEM particle radius of 2 mm was chosen to validate the DEM simulation of cone penetrometer at different relative density.

Results and discussion - Norfolk Sandy Loam cone penetrometer test

The results from physical cone penetrometer testing are shown in Figure 91. The soil penetration resistance exhibited softening for all initial relative density values. The loose specimens exhibited softening before 50 mm of penetration, while the densest specimen softened at around 110 mm of penetration. In a remolded uniform soil specimen without hardpan, the relatively uniform steady-state deformation after the softening could be explained by the cavity-expansion theory of soil penetration tests as noted in Yu and Mitchel (1998).

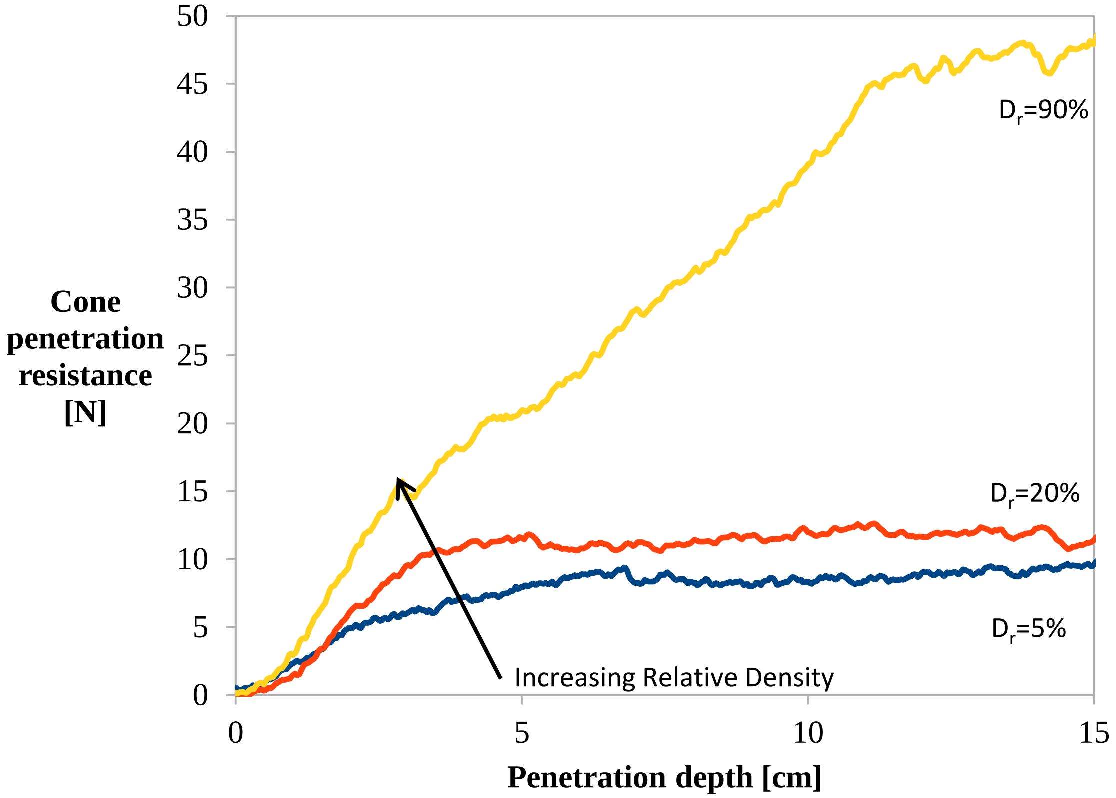

Figure 91. Cone penetration resistance measurement from Norfolk Sandy Loam soils for three Relative Density (RD) values of 5%, 20% and 90%.

NSL cone penetrometer DEM simulation

The DEM soil model for NSL was calibrated using direct shear test data. A Hertzian particle contact formulation was used with Young's modulus = 1x10^8 Pa and Poisson's ratio =0.3. The sliding and rolling friction coefficients were 0.03 and 0.025, respectively. The particle density was 2000 kg/m^3. Initial void ratios were varied to approximate the physical relative density values of NSL. The physical relative densities are estimated from average volume measurements of soil in the PVC cylinder.

Table 19 and

Table 20 show the approximate physical and DEM relative densities. The physical relative densities are estimated from average volume measurements of soil in the PVC cylinder.

Table 19. Initial states of soil used for cone penetration tests

Physical Specimen #	Condition	Physical relative soil density
1	Loose	5.0%
2	Medium	30%
3	Dense	90%

Table 20. Initial states of virtual cone penetrometer tests

Virtual Specimen #	Condition	Virtual Relative Density	DEM Initial Void Ratio
1	Loose	7%	0.641
2	Loose	22%	0.606
3	Medium	43%	0.556
4	Medium	52%	0.534

The DEM particle radius was chosen to be 2 mm for reasonable computation times, and as a result, the noisy cone resistance signal needed to be smoothed using a moving average technique which used the arithmetic mean of +/- 20 data points for each step. Figure 92 shows the moving average and raw signal of DEM simulation cone penetration resistance.

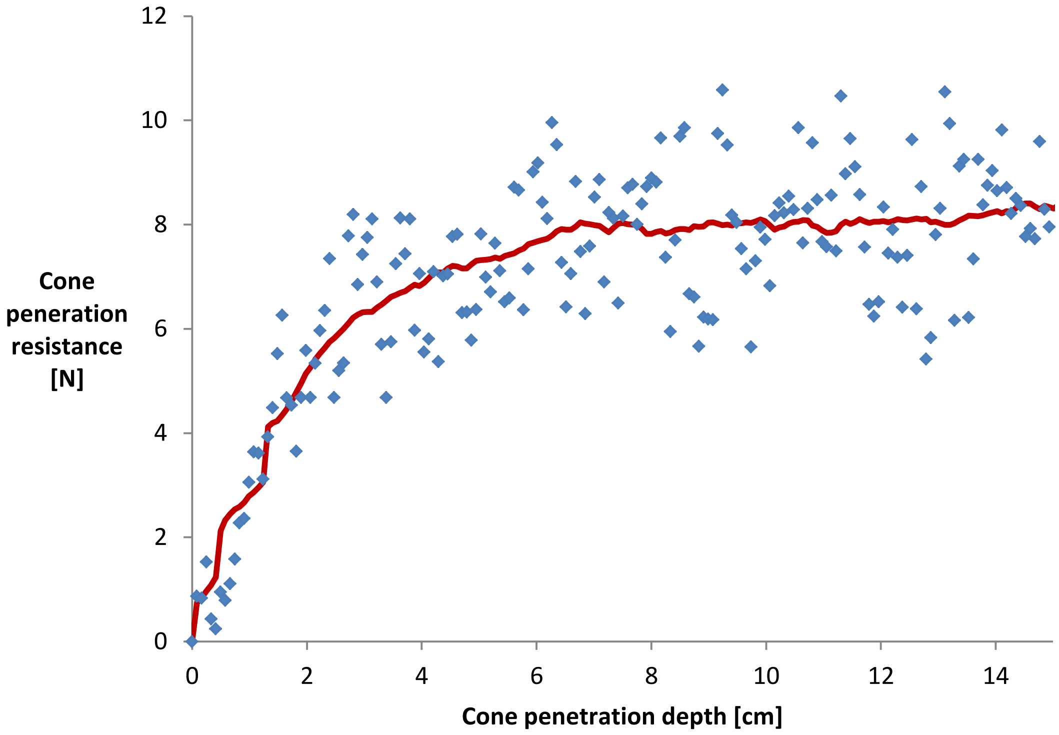

Figure 92. Comparing moving averaged to raw DEM cone penetration resistance, red line = moving average, blue points = raw DEM cone resistance.

The data points from raw DEM in Figure 92 exhibit considerable scatter because the contact between the virtual cone penetrometer and the DEM particles is intermittent. Effect of particle size on DEM predicted signal noise shows that the noise can be reduced considerably by reducing the particle size, and consequentially, increasing the tool diameter-to-particle diameter ratio.

The moving average method in Figure 92 was reliable for resolving general transient trends and steady state behavior. However, localization, shear plane prediction, and assessing the effects of small tool features will require smaller particles.

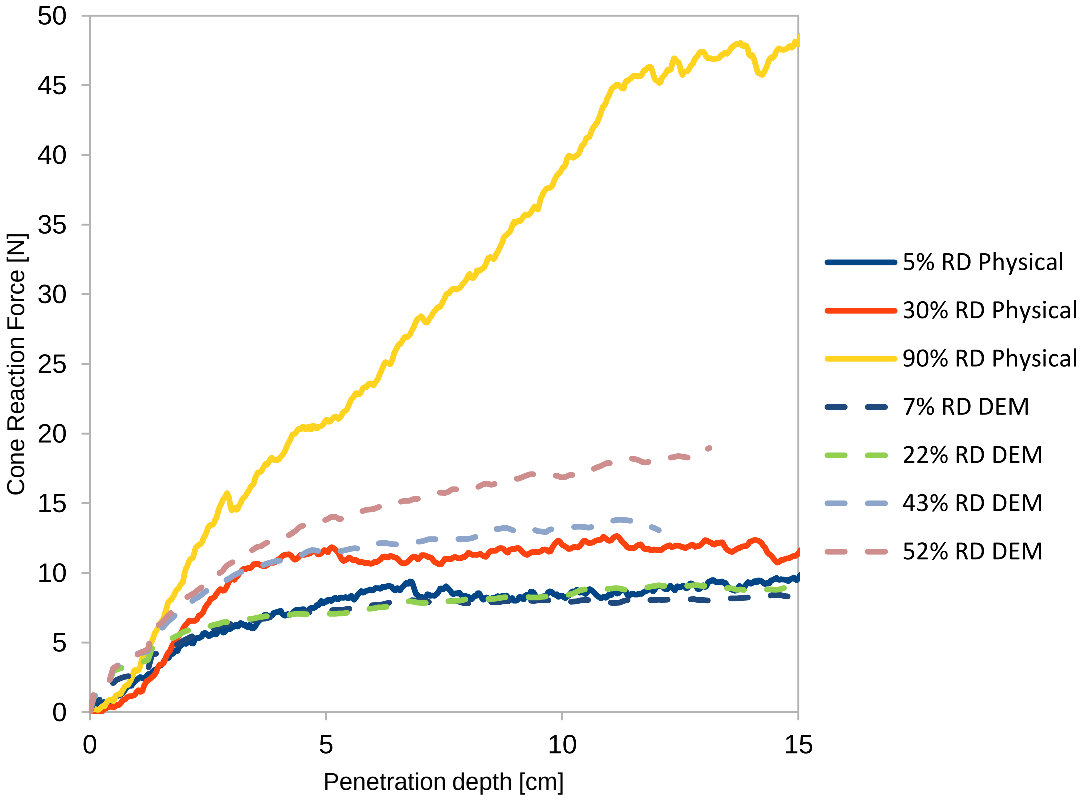

Figure 93. Comparing Comparison of physical and virtual experiments of the cone penetrometer test, RD=relative density.

The comparison between the physical tests and calibrated DEM simulations are shown in Figure 93. The trend of increasing cone resistance as initial density increases for both physical and virtual experiments (Figure 93). The cone penetration resistance for the dense state 90% RD physical was not successfully modeled in DEM. Further DEM calibration will be required for dense soil conditions. Utilizing direct shear test (less than 100 kPa consolidation stress) in the DEM calibration may also affect the robustness of the DEM calibration for reproducing the initial void ratio and optimize the DEM parameters. In predicting soil compaction behavior from wheel loading, Bailey and Johnson (1989) soil compaction model for Norfolk sandy loam was developed from triaxial test with 500 kPa confining stress. As shown in Figure 93 and a close-up comparison between the physical RD=5% and virtual RD=7% conditions in Figure 94, DEM predicted transient and steady state cone resistance force in close agreement to the physical experiment.

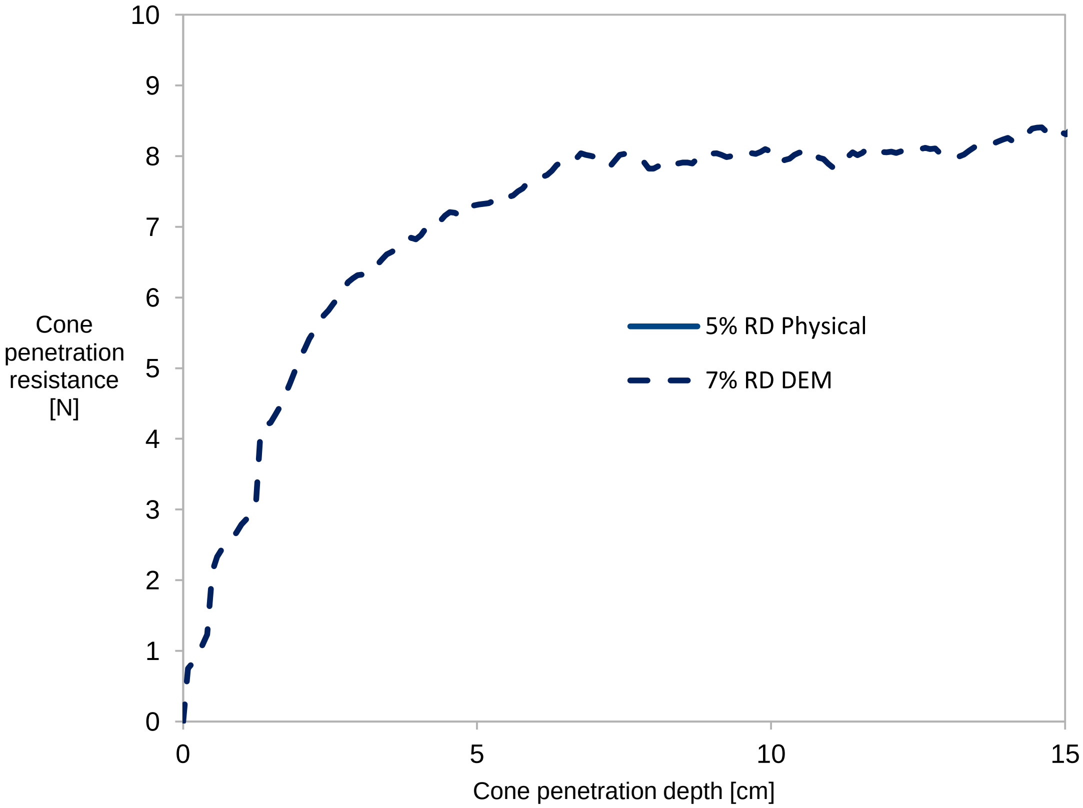

Figure 94. Comparison of virtual and physical tests at low relative density

Comparing the mean steady state or near steady state cone penetration resistance between the DEM simulation and physical experiments (Figure 95), DEM predicted steady state forces were similar to the physical data except for the 90% physical relative density .

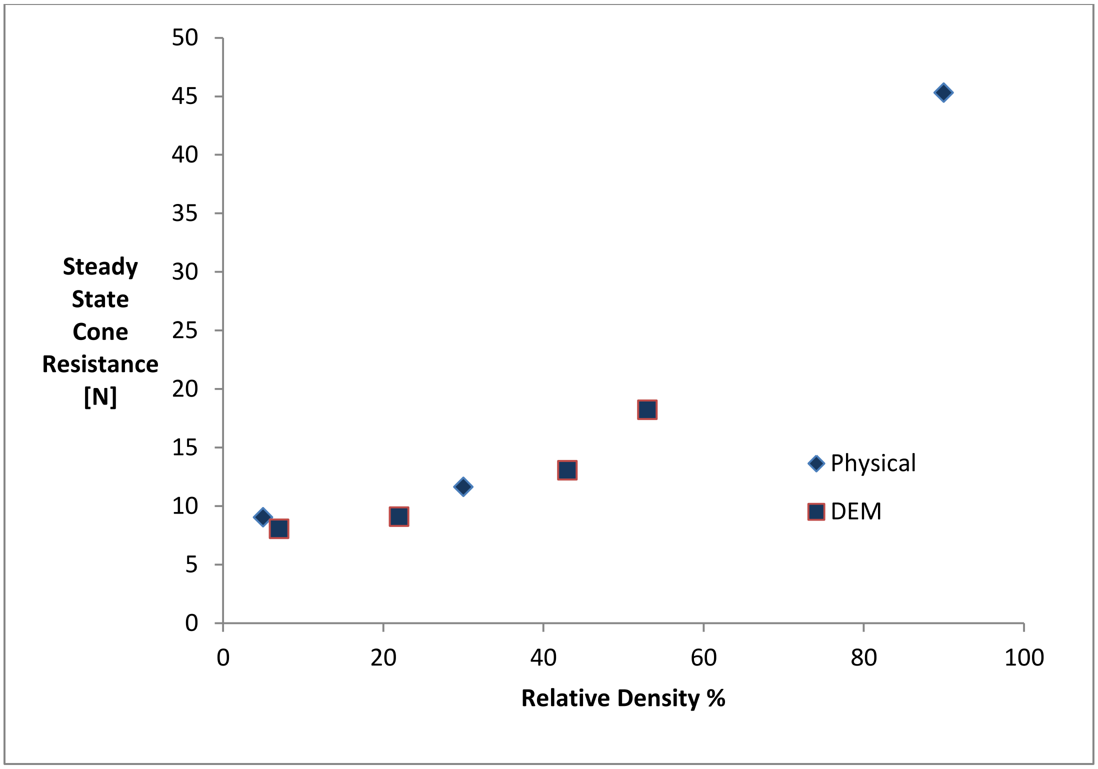

Figure 95. Comparison of physical and virtual steady state cone penetration resistance for different relative density

Figure 95 also showed the increased in cone penetration resistance with increase in relative density was captured both in DEM and physical tests. The hypothesis proposed by Salot et al. (2009) that physical relative density can be set equal to virtual relative density is supported by the data in Figure 95.

Conclusion

DEM model for Norfolk Sandy Loam (NSL) was developed using the proposed DEM calibration methodology and validated using cone penetration test. Within the range of 5 to 30% relative density, DEM model predicted the soil cone penetration resistance with reasonable minimum errors. Relative density, a critical soil property parameter, was successfully integrated into DEM calibration methodology and showed strong influence on both physical test and DEM simulation of cone resistance. The current DEM calibration methodology requires further improvement for simulation and DEM material properties calibration of higher relative density. The quasi-static calibration algorithm developed for DEM soil model uses critical state internal friction angle as an anchor and requires that engineers determine the appropriate relative density of the material without altering other DEM parameters. Future work will involve creating very dense DEM model, yet stable DEM specimens to verify whether the proposed calibration applies to high density soils subject to cone penetrometer testing.

Hopper Discharge

Many studies of granular flow have used hopper discharge to calibrate DEM parameters. Anand et al. (2008) use a pseudo-3D DEM model of hopper discharge to test various parameters in Beverloo's massflow rate equation (1961) with very close agreement. Ketterhagen et al. (2008) examined the effects of constraining particle rotation on hopper discharge and found that DEM models generally agree with Jenike theory in predicting mass-flow and funnel-flow conditions. Segregation of fines was also observed in the funnel-flow conditions. Höhner et al. (2013) uncovered an interesting limitation in that, while hexagonal particles self-align and block flow in physical discharge experiments, the polyhedral DEM model of hexagonal particles do not exhibit such alignment. However, other particle shapes (icosa-, dodeca-, octa-, and tetrahedra) exhibited reasonable discharge flow behavior. Markauskas et al. (2015) simulated hopper discharge of maize kernels using multisphere and single particle approaches using methods from Wensrich and Katterfield (2012) to approximate rolling friction coefficient. Markauskas et al. noted a significant change in hopper discharge time when moving from single sphere to multisphere methods.

The grain-grain sliding friction coefficient was difficult to measure directly (Gonzalez-Montellano et al., 2012). However, it was deduced by comparing direct shear tests to DEM simulations (Coetzee and Els 2009). Coetzee and Els (2009) modeled corn grains using two particle clumps whose parameter calibration was performed in the context of 2D direct shear and Oedometer tests. Sliding friction coefficient, μ_s=0.12, was selected for their simulations to represent bulk internal friction angle, θ=24deg. Although porosity was not considered, Coetzee and Els showed qualitative agreement comparing simulations with blade sweep experiments. González-Montellano (2012) experimentally determined many DEM parameters for maize kernels including grain-wall friction, stiffness, and coefficient of restitution. However, Coetzee (2016) founds that massflow rate from DEM hopper discharge simulations was insensitive to grain-wall friction, stiffness, and contact damping. Alternate measurements from hopper discharge were also studied, such as drag on a submerged load cell in a discharging bed (Moysey et al., 2013).

Although massflow rate and reaction forces were often used as calibration points for DEM simulations, there was little evidence that showed the effects of initial state on the volumetric change in granular flow. In this study, it was shown that the initial state of a granular assembly affected grain velocity independently of massflow rate. In addition, calibration processes accounted for the state of the physical bulk material, as well as the familiar particle scale properties. The proposed calibration process was inspired by the work of Coetzee (2016) and Wensrich and Katterfield (2012).

Physical test methodology

A small hopper was used to discharge 14 kg of gently air pluviated corn grains on to a load cell. The bulk density, ρ_b, of the corn was 800 kg/m^3. The cross section of the hopper was a square of side length 26 cm. As pluviated, the height of the corn assembly was approximately 26 cm. The cross-section of the discharge chute of the hopper was a 10 cm x 10 cm square. A 60 degree includes surface connected the main hopper body to the discharge chute. A string potentiometer was used to monitor the height of the center of the top surface of the corn grain assembly. The load cell and the string potentiometer data was collected at a sample rate of 15 Hz using an Arduino controller.

DEM methodology

A virtual hopper test was created using the open-source LIGGGHTS software. The physical hopper geometry was replicated in the virtual environment. The LVDT ball from the physical experiment was approximated using the DEM parameters shown in Table 21. Interparticle contact was simulated using the Hertz-Mindlin model with history effects. Rolling friction was simulated using the built-in EPSD model.

Calibration

When calibrating DEM spheres to aspherical kernels, it was hypothesized that the scaling needed to satisfy two inertial requirements: 1) particle-scale rotational inertia, 2) bulk inertia. The rotational inertia was enforced by equating the kernel's radius of gyration to that of the sphere (equation 5.2). The kernel was approximated by an ellipsoid with three principle semi-axes, x, y, and z.

$$\frac{I_{kernel}}{\rho_{kernel}\frac{4}{3}\pi\, x\, y\, z} = \frac{I_{sphere}}{\rho_{sphere}\frac{4}{3}\pi\, r^3} \tag{5.2}$$

The ellipsoidal kernel had three mass moments of inertia. However, for this analysis, only the maximum and minimum values of rotational inertia are considered. Algebraic manipulation revealed that rotational inertia could be enforced by setting the radius of the sphere equal to r_{ave}.

$$x^2 + y^2 = 8\, r_{\max}^2 \tag{5.3}$$

$$y^2 + z^2 = 8\, r_{\min}^2 \tag{5.4}$$

$$r_{ave} = \frac{r_{\min} + r_{\max}}{2} \tag{5.5}$$

$$\rho_{kernel} x\, y\, z = \rho_{sphere}\, r_{ave}^3 \tag{5.6}$$

From equation 5.6, r_{ave}=4mm. Finally, the bulk inertia was enforced by equating the bulk density of the physical specimen to that of the virtual specimen (equation 5.7).

$$\rho_b = \rho_{sphere}\, S \tag{5.7}$$

Where S = initial solid fraction;

ρ_b = bulk density.

Recall that solid fraction and void ratio were related by equation 5.8.

$$e = \frac{1}{S} - 1 \tag{5.8}$$

Where e = void ratio

The initial void ratio of a granular assembly was controlled by several methods. In the current study, particles' friction coefficients were manipulated as they were pluviated into the hopper. Lower friction coefficients during pluviation yielded lower void ratios, and vice versa. In addition, the hopper was vibrated to obtain slightly denser samples than was possible by pluviation alone.

Bulk and particle density

All hopper specimens were pluviated with particle density, ρ_s=1300 kg/m^3. After the particle assembly reached equilibrium, the solid fraction of the virtual assembly was measured and ρ_s was adjusted so that the virtual bulk density exactly matched the physical bulk density of the grain specimen (ρ_b=800 kg/m^3). Equation 6.7 was always enforced, regardless of the particle size or void ratio of the assembly just before before discharge.

Rolling friction

Rolling friction models added moment to spheres to mimic the effects of shape, angularity and surface roughness. In the case of corn kernels, the effects of shape on rotation behavior outweighed the effects of roughness. Therefore, the current analysis focused on using the particle geometry to develop a suitable rolling friction coefficient. The following analysis was adapted and simplified from Wensrich and Katterfield (2012). Consider the 2d projection of the rigid ellipsoid on a plane in Figure 96. External moment, M_a, was acting on the ellipsoid to rotate it 'over-center.'

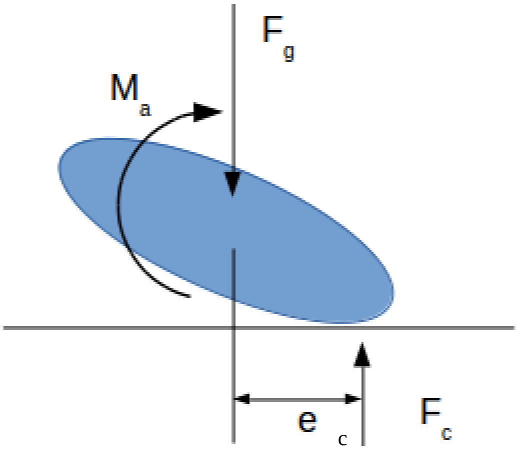

Figure 96. Free body diagram of rigid ellipsoid on a plane

To rotate the ellipse over-center, M_a must have exceeded the F_g-F_c couple.

$$M_a \geq F_c\, e_c \tag{5.9}$$

Now consider the 2d project of a rigid sphere with rolling friction, as in Figure 96, with similar moment, M_a, acting on it. In order for the sphere to have exhibited rotation, M_a must have exceed maximum rolling resistance M_R. Elastoplastic spring dashpot (EPSD) models of rolling resistance defined M_R with respect to a coefficient of rolling friction, μ_R, normal contact forces, F_c, and sphere radius, r_s. Therefore, the mobilization condition was described by equation 5.10.

$$M_a \geq M_R = \mu_R\, F_c\, r_s \tag{5.10}$$

Comparing equations 5.9 and 5.10, the sphere's rolling resistance was analogous to the ellipsoid's eccentric contact.

$$\mu_R{}' = \frac{e}{r_s} \tag{5.11}$$

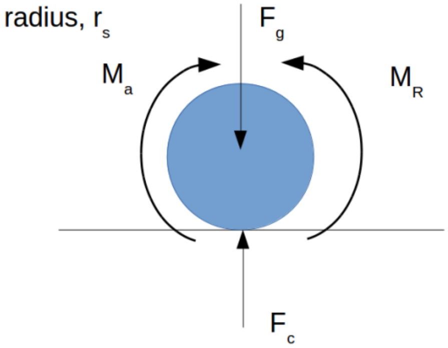

Figure 97. Free body diagram of rigid sphere on plane

Many corn kernels in the physical sample may have had an initial fabric which more closely resembles Figure 98, where the ellipsoid was already over center and required no additional moment to rotate. In this case, the rolling friction coefficient was effectively zero. For the purposes of this analysis, 50% of the corn kernels were assumed over-center (Figure 98), thus the rolling friction coefficient was approximated by equation 5.12.

$$\mu_R = \frac{\mu_R'}{2} \tag{5.12}$$

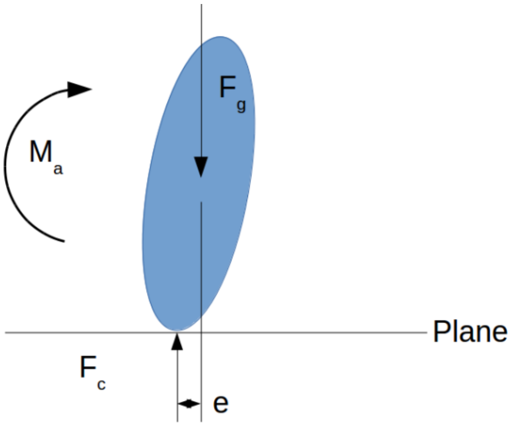

Figure 98. Free body diagram of over-center ellipsoid

The micromechanical model was used to determine the rolling friction coefficient, particle size, and particle density.

Other DEM parameters

Additional DEM parameters were taken from Gonzalez-Montellano et al. (2012), see Table 21. Although Coetzee's (2009) reported that dry corn under direct shear conditions exhibited an internal friction angle of 23 degrees and selected 0.12 as the coefficient of sliding friction. The methodology from Syed et al. (2017) predicted the effective friction coefficient to be 0.134. The difference between Coetzee and Els (2009) and Syed et al. (2017) was nearly the same considering the statistical scatter in Syed et al's direct shear model.

Table 21. DEM parameters for hopper discharge of corn grains

Parameter	Value	Source
Young's Modulus	298.1 MPa	Gonzalez-Montellano et al (2012)
Poisson's Ratio	0.3	-
Sliding friction coefficient particle-particle	0.12	Coetzee and Els 2009
Rolling friction coefficient particle-particle	0.532	Current Study
Sliding friction coefficient particle-wall	0.336	Gonzalez-Montellano et al. (2012)
Coefficient of restitution, particle-wall	~0.60	Gonzalez-Montellano et al. (2012)
Coefficient of restitution, particle-particle	~0.25	Gonzalez-Montellano et al. (2012)
Particle radius	4 mm	Current study
Particle density	1334 kg/m^3	Current study

Note that the rolling friction coefficient calculated in the previous analysis produced a rolling friction coefficient that was larger than the sliding friction coefficient. Thus, the micromechanical EPSD rolling friction model limited the rolling friction coefficient to the ceiling set by the sliding friction coefficient.

The DEM parameters in Table 21 served as an anchor for calibration efforts. The initial relative density of the corn assembly was not prescribed and required iteration to arrive at a calibrated DEM parameter set.

Calibration using simulation data

Sensitivity analyses were performed to verify DEM parameters from Table 21. In addition, sensitivity analyses were used to describe the effects of the initial configuration of the virtual corn grains.

Mass flow of grain discharge was typically used to calibrate DEM parameters to granular material flow. However, mass flow did not fully capture the bulk response of the granular material. Two hopper systems were simulated with identical bulk density, interparticle friction, and particle size. The DEM parameters from Table 21 were used except the sliding and rolling friction coefficients were set to 0.5. The initial void ratios of the systems differed (e_0=0.743 vs. 0.594). In this case, the mass flow curves of both the systems are identical (Figure 99), but the displacements of the LVDT ball were not the same (Figure 100). This observation indicates that granular calibration using hopper tests could be enhanced by capturing some feature of volume change, as the LVDT ball did.

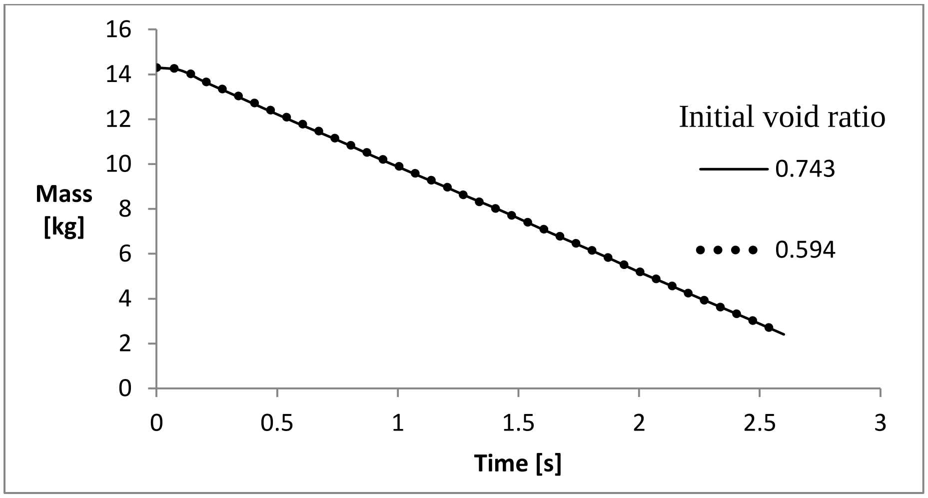

Figure 99. Remaining mass in hopper vs. time

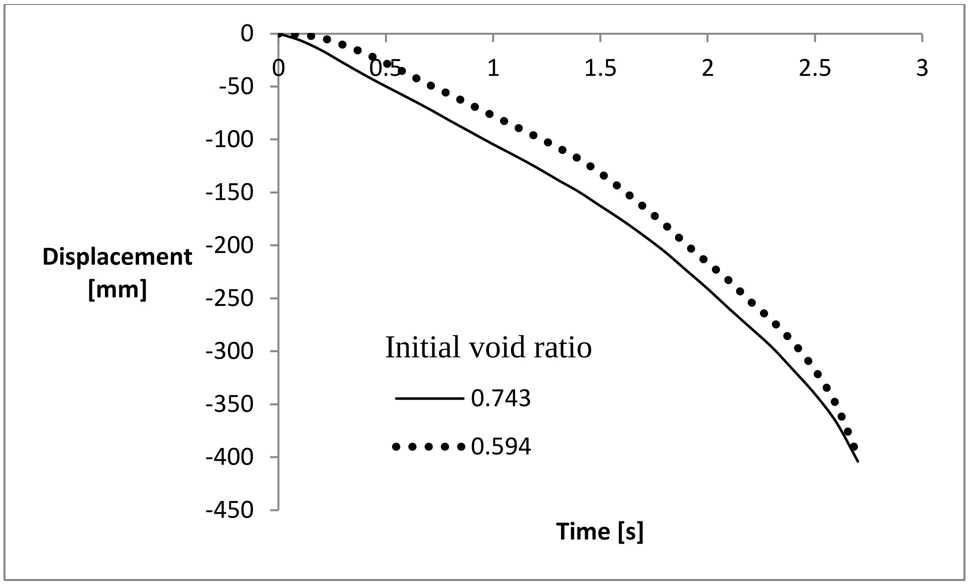

Figure 100. Displacement of the LVDT ball during grain discharge from the hopper

Five DEM hopper discharges were simulated to provide a baseline for calibration. The hopper specimens were prepared by air pluviating the grains into the hopper. The friction coefficients were not varied between pluviation and discharge. Therefore, the relative density of all simulations was that of a gently, air-pluviated specimen. As expected, the slope of the mass vs. time curves (Figure 100) decreased as the sliding friction coefficient increased. It was important to remember that as pluviation friction increased, initial void ratio also increased. However, as evident from Figure 99, the initial void ratio did not affect the mass flow of discharge as long as bulk density was held constant. Therefore, the variation in the discharge mass curves in Figure 101 was only due to the change in sliding friction coefficient.

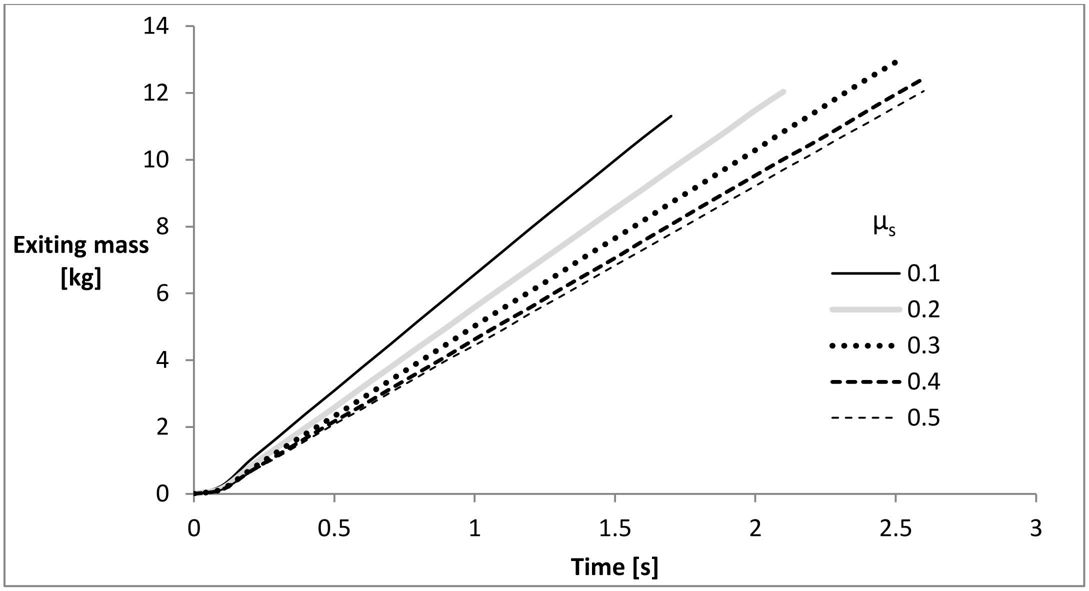

Figure 101. Mass leaving the hopper with respect to time over various DEM sliding friction coefficients

The ball displacement vs. time curves in Figure 102 showed how the center of the top surface of the granular bed changed as discharge ensued. The initial void ratio for each simulation was noted because, from Figure 100, the effects on the ball velocity were independent from friction.

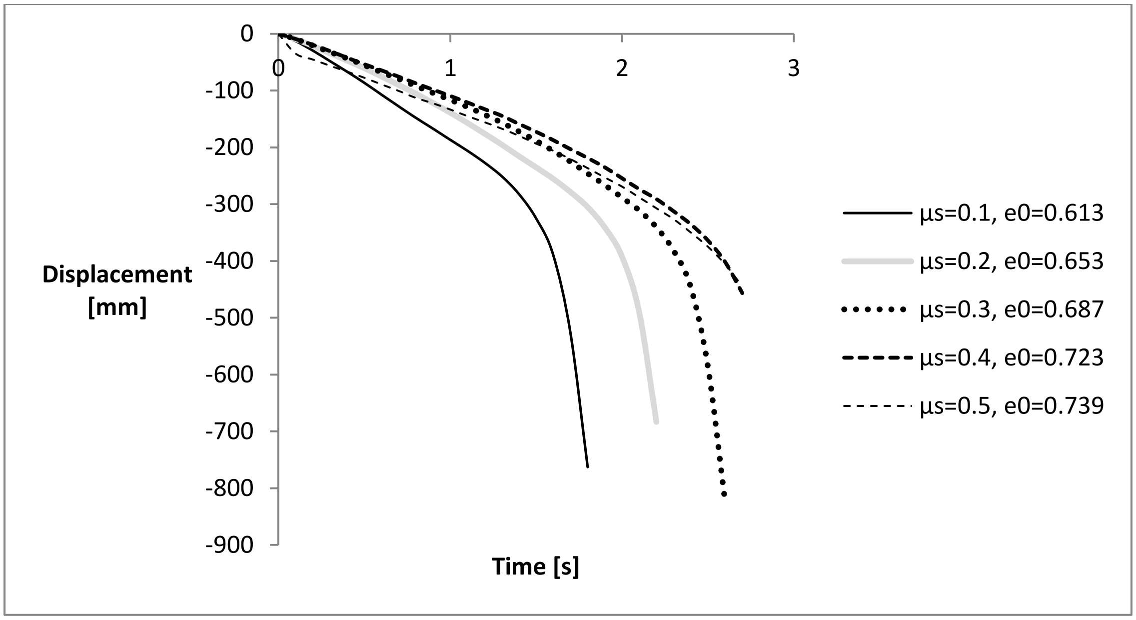

Figure 102. DEM Displacement of the LVDT ball as a function of sliding friction coefficient and initial void ratio

Figure 103 plots the DEM massflow rate with respect to sliding friction coefficient, μ_s. The experimental massflow rate was satisfied by μ_s=0.467. The DEM ball velocity was also plotted with respect to μ_s in Figure 104 and it did not converge with the experimental ball velocity. Therefore, the next course of action was to simulated hopper tests using μ_s=0.467 while varying the initial void ratio.

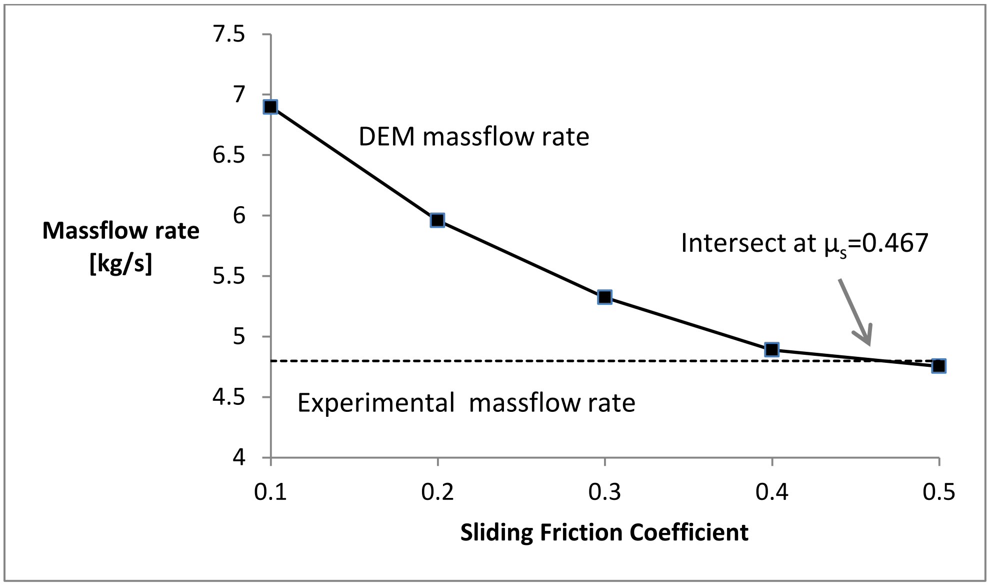

Figure 103. Massflow rate with respect to sliding friction coefficient

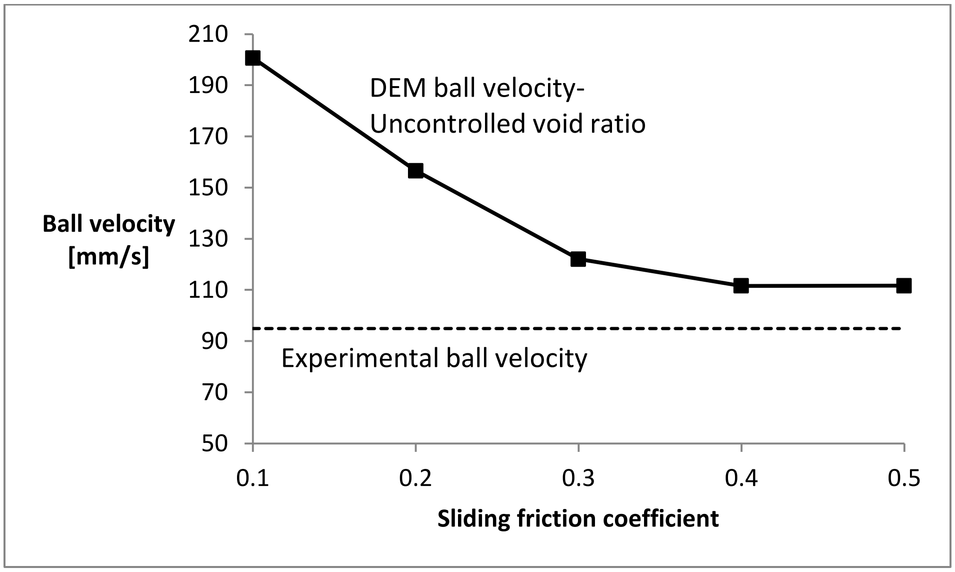

Figure 104. DEM and physical LVDT ball velocity as a function of sliding friction coefficient

Simulations varying initial void were performed by varying friction during pluviation. As pluviation friction decreased, the initial void ratio also decreased. As pluviation friction approached zero, the initial void ratio tended to the lower limit of 0.577 for random packed monodisperse spheres (Song et al., 2008). However, since flexible spheres were used (with the same elasticity as real corn kernels), additional energy was used to further densify the packing. Kinetic energy was introduced into the system by vibrating the hopper in three translational directions (Amplitude=0.1 x particle diameter, freq=100Hz) to produce slightly more compact specimens. Figure 105 shows ball velocity with respect to initial void ratio while denoting the compaction method.

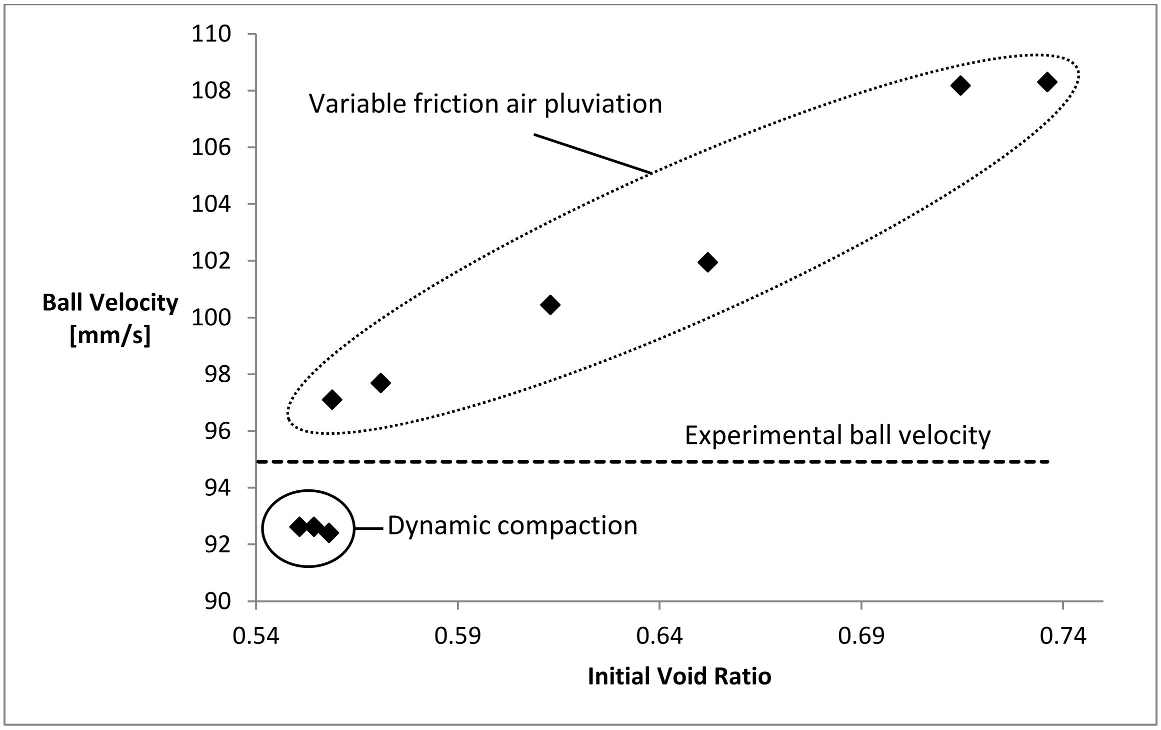

Figure 105. Ball velocity as a function of initial void ratio

Two points from Figure 105 that had nearly the same initial void ratio, but different compaction methods, exhibited vastly different steady state ball velocities. It was hypothesized that kinetic energy from dynamic compaction may have changed the fabric of contact between the specimens, which resulted in different bulk volume change behavior. It would be interesting for further studies to investigate the effects of initial fabric on bulk volumetric flow behavior.

Calibration result

The calibration of DEM spheres to physical kernels and hopper test results showed good agreement in both discharge mass (Figure 106) and ball velocity (Figure 107). The initial void ratio was 0.551.

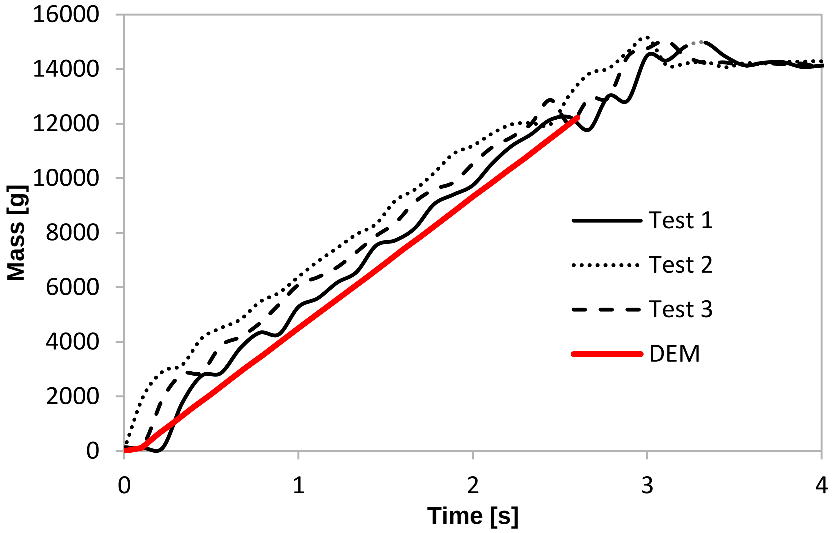

Figure 106. Comparison of physical and DEM experiments of corn mass discharging from hopper

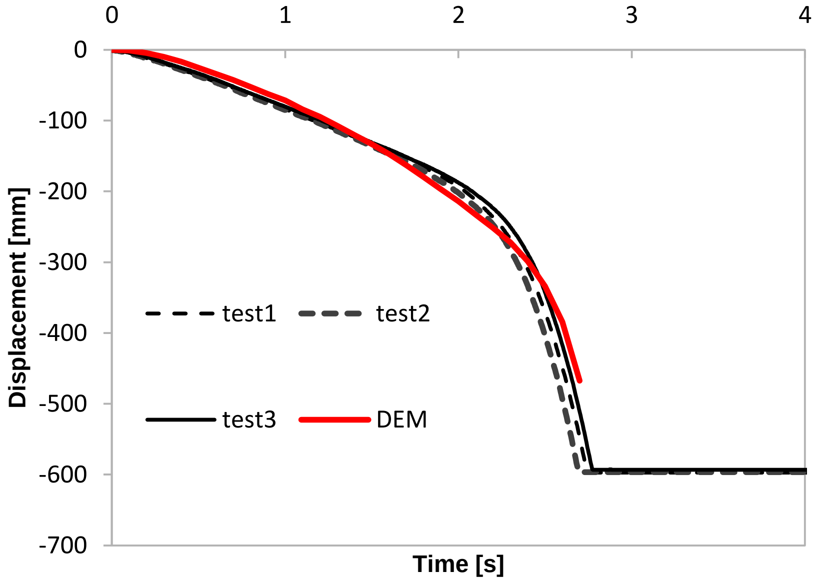

Figure 107. Comparison of physical and calibrated DEM model of LVDT ball displacement over time

Images of the physical hopper test (Test 1) were compared with the virtual hopper discharge simulation in Figure 108.

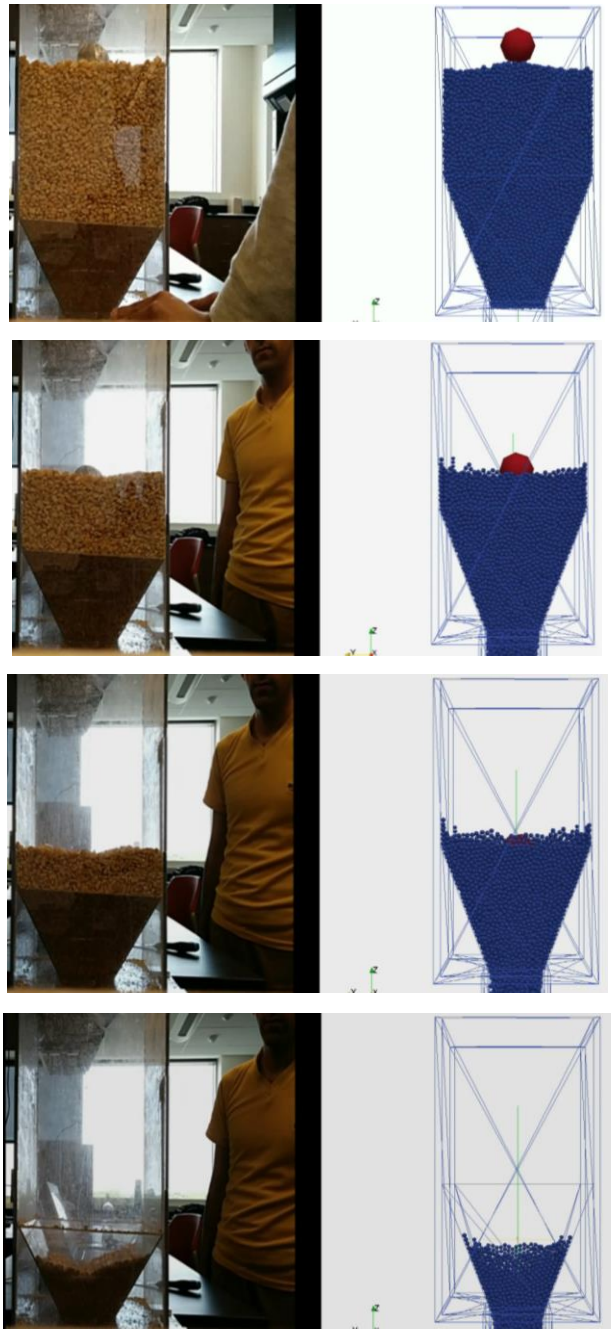

Figure 108. Images of physical (left) and virtual (right) hopper discharge test (Test 1)

Indeed, close scrutiny of Figure 108 showed that the sinkage of the LVDT ball in both physical and virtual tests was highly correlated. However, the shape of the upper surface of the grain assembly differed from physical to virtual. The virtual test showed that particles created stacks in the corners of the hopper where the physical test showed no such thing. In addition, the discharge rate between physical and virtual was slightly asynchronous, which was also apparent in Figure 107. Improved calibration is possible with a larger hopper and granular specimen because fully developed flow during discharge around the LVDT ball only exists for a very short period of time and calibration to this small timeframe was difficult.

Conclusions and future work

Conclusions from the hopper discharge experiments are listed here.

- Increased sliding friction resulted in decreased massflow rate and ball velocity.
- Massflow rate was unaffected by initial void ratio as long as bulk density was held constant
- Initial void ratio uniquely affected ball velocity
- Massflow rate and volumetric flow rate were decoupled (within limits)
- Calibration of granular flow considered initial void ratio after sliding friction coefficient was calibrated.

Future work should explore the role of the initial state of polydisperse and multisphere particles on volumetric flow rate. Also, the fabric of specimens may influence the volumetric flow. To enhance the accuracy of calibration, larger hopper tests (25 kg+) should be correlated with DEM because the steady state velocity of the ball existed for less than 2 seconds using a 14 kg specimen of corn kernels. In addition, a methodical procedure for bringing DEM specimens to a target void ratio should be developed and standardized.

CHAPTER 6: CONCLUSIONS AND FUTURE WORK

This chapter presents an overview of the technical merit and scientific value gained from the study and an overview of the lessons learned. The conclusions are grouped into four categories (e.g., conclusions about statistical calibration, friction, relative density, and structured calibration) and associated with outcomes, benefits, and applications. The conclusions also associated with the goal of the research. Finally, future work in DEM modeling of soils and granular material is recommended, starting with refined particle interactions to practical handling of large scale simulations.

Statistical Calibration

Statistical methods for calibrating DEM input parameters to mechanical behavior of dense granular materials were limited by assumptions about non-linearity and statistical interactions. Therefore, a more theoretically driven approach should be used to develop DEM calibration models. Sliding and rolling friction coefficients were particularly difficult to calibrate using statistical methods because the nature of their statistical interaction was unknown *a priori*. Therefore, the quality of a statistical interaction model was highly dependent on the form of the assumed interaction term. A theoretical structure for the interaction of sliding and rolling behavior, such as effective friction, enhanced the modeling capability.

On the other hand, statistical calibration of DEM relative density and effective friction coefficient was useful because their relationship to strength and dilatancy was linear in practical ranges for common geomaterials. In addition, some granular systems were difficult to calibrate with a theoretical guide. Calibration of granular flow through a hopper was successfully calibrated using purely empirical methods.

Statistical methods in calibration of DEM input parameters was an invaluable tool when theoretical methods fell short of predicting phenomenological outcomes of DEM simulations; however, the use of statistical methods should be preceded by exhaustive theoretical calibration.

Friction

A theoretical accounting for total friction acting between two DEM particles was very important in understanding the non-linear and interactive contribution that sliding and rolling friction coefficients had on internal friction angle of dense granular materials. A combined friction coefficient, termed *effective friction coefficient* resolved the interaction between micromechanical sliding and rolling resistance, and thus, was used in a statistical calibration of DEM inputs to mechanical behavior of dense granular materials. Micro-scale effective friction uniquely correlated with critical state strength of granular materials. Particle stiffness, size, and structural state had no effect on critical state internal friction angle. Therefore, DEM friction coefficients were calibrated before any other parameters are considered. Pre-calibrating the friction coefficients simplified DEM parameter calibration greatly because the design space of calibration was reduced by two variables. In addition, the effects of friction on latent concepts, like relative density, were controlled because pre-calibrated friction coefficients did not change throughout calibration of the remaining DEM parameters.

Relative Density

The initial structural or configurational state of dense DEM particle assemblies was a latent input variable in DEM simulations that simplified calibration. The initial state was measured using common geotechnical and granular mechanics concepts such as void ratio, porosity, and solid fraction. As in traditional drained granular mechanics, the relative density of a DEM assembly was strongly associated with peak strength and dilatancy. In addition, the relative density had no effect on the critical state strength of a granular assembly. The latent nature of relative density confounded its ability to be modeled using generic statistical methods. The friction coefficients chosen to calibrate critical state strength altered the maximum and minimum possible void ratios associated with a virtual granular assembly. Thus, the initial void ratio that corresponded with a particular initial relative density was determined *after* friction coefficients were calibrated. The relative density was a powerful link between physical and virtual specimens because when the physical and virtual relative densities were equated, the degree of impending dilation or contraction was approximately accounted for. A calibration method that calibrated DEM friction coefficients and relative density sequentially was robust enough to capture peak and critical state friction angles, as well as dilatancy. Furthermore, absolute volumetric strain was also captured by relative density. Indeed, equating physical and virtual relative density captured substantially more key features of soil and grain mechanical behavior than other methods available today.

Structured Calibration

A structured, closed-loop calibration model was developed after exhaustive theoretical and empirical studies. The calibration model began with an anchoring step. The critical state strength of drained granular material was measured using triaxial or direct shear laboratory tests. Using semi-empirical methods proposed in the current study, sliding and rolling friction coefficients were prescribed. Subsequently, friction coefficients, along with stiffness, particle size distribution, and cohesion, defined a material without an initial state. The possible initial states of a virtual material were determined numerically in any DEM code. Likewise, the possible initial states of physical granular material were determined by air-pluviation or vibratory compaction. Equating relative density between physical and virtual systems created a prescription of initial void ratio for virtual specimens. Attaining a specific initial void ratio in DEM simulations was difficult. Additional work should focus on fast DEM techniques to minimize system energy in desired structural states.

The proposed structured calibration did not require open ended iteration for soil and grain problems such as blade mixing, cone penetration, and hopper discharge. A single pass through the calibration algorithm created viable DEM parameter sets suitable for simulation of complex cutting and compaction soil and other granular material.

Summary of Conclusions

The goal of the study was to develop a clear methodology to calibrate DEM parameters to mechanical behavior from laboratory tests of drained soil and other granular materials. The calibration algorithm presented in this study was an intelligent, structured, and closed loop method which relates simple geotechnical laboratory tests to DEM parameters without open ended iteration. Validation studies showed that the presented method was robust with respect to cutting and compaction behavior in the context of cone penetrometer and blade mixing simulations. In addition, bulk granular flow of corn grains from a hopper was also modeled successfully. Properly calibrated models of granular material have helped develop insights into the mechanisms of bulk material handling and soil deformation as a result of soil-tool interaction.

Future Work

The studies performed and insights gained have paved a path forward to guide future research in DEM calibration methodology. For the advancement of the current DEM methodology, further research will be needed in the following areas.

Cohesion models

Additional work is needed to refine cohesion models that scale realistically with normal stresses. The current cohesion models, like JKR, add attractive forces between particles, but do not mechanistically increase net attractive forces as a particle assembly becomes denser. Future algorithms to model cohesion need to consider detection of a local coordination number to adjust attractive forces accordingly.

Initial state algorithms

In the Methods Chapter, a particle generation algorithm was described in detail. The reality is that 3D particle packing algorithms are very limited. One problem with particle generation is that for each particle that is inserted, the optimal position of the new particle is unknown; and the optimal position of the new particle remains unknown until a great deal of particle assembly volume has already been generated. Therefore, smart heuristics which can guide an algorithms' placement of particles need to be developed so that generation can be fast and linear. Heuristics also need to point to a desired and stable void ratio so that many DEM computation cycles are not wasted on achieving a particular structural or configurational state.

Dynamics

This study focused on DEM parameters without inertial or velocity sensitivity. Indeed, real particle systems are often most accurately modeled dynamically and further research is required to adapt DEM parameters that influence dynamic behavior.

Absolute viscous damping

From early results presented in the Methods chapter on absolute viscous damping, it is reasonable to hypothesize that absolute viscous damping could be a critical parameter in modeling saturated drained soil responses.

Contact damping – coefficient of restitution

Results from the blade mixing study presented in the Validation Studies chapter showed that the contact damping (coefficient of restitution) has an unclear influence on the mechanical response of soil under dynamic mixing (blade shaft velocity = 6 deg/sec). Theoretical reasoning suggests that an increase in coefficient of restitution should increase the resistance on the mixing blade, but simulation results do not show expected trends. Further work is needed to refine the understanding of contact damping on phenomenological behavior.

DEM computational efficiency for large scale simulations

Finally, the practical aspects of granular simulation have to be addressed rigorously. Work by Thornton (2000) showed that the critical timestep size could be increased by altering particle density and slowing Rayleigh wave propagation through a particle. This “density scaling” was a first attempt at managing the computational demands of dense DEM simulation. During the course of this study, an interesting hypothesis was developed to limit the Rayleigh wave propagation speed numerically (without altering particle density). A velocity filter could be added to the integration of DEM particle position which would cut off velocities higher than a critical user-defined value. This “Rayleigh bypass” integration method could be used for pseudo-static and slow dynamic systems. Thorough investigation is required to document the benefits and limitations of a Rayleigh bypass integrator.

CHAPTER 7. WORKS CITED

Abo-Elnor, Mootaz, R Hamilton, and JT Boyle. 2003. "3D Dynamic analysis of soil–tool interaction using the finite element method." *Journal of Terramechanics* 40 (1):51-62.

Ai, Jun, Jian-Fei Chen, J Michael Rotter, and Jin Y Ooi. 2011. "Assessment of rolling resistance models in discrete element simulations." *Powder Technology* 206 (3):269-282.

Alder, Berni J, and TE Wainwright. 1959. "Studies in molecular dynamics. I. General method." *The Journal of Chemical Physics* 31 (2):459-466.

Anand, Anshu, Jennifer S. Curtis, Carl R. Wassgren, Bruno C. Hancock, and William R. Ketterhagen. 2008. "Predicting discharge dynamics from a rectangular hopper using the discrete element method (DEM)." *Chemical Engineering Science* 63 (24):5821-5830.

Andrade, José E, Qiushi Chen, Phong H Le, Carlos F Avila, and T Matthew Evans. 2012. "On the rheology of dilative granular media: Bridging solid-and fluid-like behavior." *Journal of the Mechanics and Physics of Solids* 60 (6):1122-1136.

Andrade, José E., and Carlos F. Avila. 2012. "Granular element method (GEM): linking inter-particle forces with macroscopic loading." *Granular Matter* 14 (1):51-61.

Arroyo, M., Joanna Butlanska, A. Gens, Francesco Calvetti, and Michael Jamiolkowski. 2011. "Cone penetration tests in a virtual calibration chamber." *Géotechnique* 61 (6):525-531.

ASAE. 1999. "EP542 Procedures for using and reporting data obtained with the soil cone penetrometer." *St. Joseph, MI*.

Asaf, Z., D. Rubinstein, and I. Shmulevich. 2007. "Determination of discrete element model parameters required for soil tillage." *Soil and Tillage Research* 92 (1):227-242.

ASTM. 1994. "D3080-90: Standard test method for direct shear test of soils under consolidated drained conditions." *Annual Book of ASTM Standards* 4:290-5.

ASTM. 2007a. D2850 Test Method for Unconsolidated-Undrained Triaxial Compression Test on Cohesive Soils. www.astm.org.

ASTM. 2007b. D4767 Test Method for Consolidated Undrained Triaxial Compression Test for Cohesive Soils. www.astm.org.

ASTM. 2013. ASTM D7181-11 Method for Consolidated Drained Triaxial Compression Test for Soils. www.astm.org.

ASTM, D. "854-06 (2006).“." *Standard test method for specific gravity of soil solids by*.

ASTM, D. "4253.(2006).“." *Standard Test Methods for Maximum Index Density and Unit Weight of Soils Using a Vibratory Table*.

ASTM, D. "4254." *Standard Test Methods for Minimum Index Density and Unit Weight of Soils and Calculation of Relative Density (Unified Soil Classification System). ASTM International, West Conshohocken, PA*.

Avci, B, and P Wriggers. 2012. "A dem-fem coupling approach for the direct numerical simulation of 3d particulate flows." *Journal of Applied Mechanics* 79 (1):010901.

Bagi, K. 1999. "Microstructural stress tensor of granular assemblies with volume forces." *Journal of applied mechanics* 66 (4):934-936.

Bagi, Katalin. 2005. "An algorithm to generate random dense arrangements for discrete element simulations of granular assemblies." *Granular matter* 7 (1):31-43.

Bailey, Alvin C., and Clarence E. Johnson. 1989. "A soil compaction model for cylindrical stress states." *Transactions of the ASAE* 32 (3):822-825.

Balevičius, R, I Sielamowicz, Z Mróz, and R Kačianauskas. 2012. "Effect of rolling friction on wall pressure, discharge velocity and outflow of granular material from a flat-bottomed bin." *Particuology* 10 (6):672-682.

Bardet, Jean-Pierre, and J. Proubet. 1991. "Numerical investigation of the structure of persistent shear bands in granular media." *Geotechnique* 41 (4):599-613.

Batchelor, J. A. 1984. "Properties of bin soils." *Auburn, Ala.: USDA-ARS National Tillage Machinery Laboratory*.

Belheine, N, J-P Plassiard, F-V Donzé, F Darve, and A Seridi. 2009. "Numerical simulation of drained triaxial test using 3D discrete element modeling." *Computers and Geotechnics* 36 (1):320-331.

Benvenuti, L., C. Kloss, and S. Pirker. 2016. "Identification of DEM simulation parameters by Artificial Neural Networks and bulk experiments." *Powder Technology* 291:456-465.

Bernhardt, M. L., C. O'Sullivan, and G. Biscontin. 2012. "Macro-and micro-scale effects of pluviation based sample preparation in DEM." In *GeoCongress 2012: State of the Art and Practice in Geotechnical Engineering*, 2392-2401.

Bernhardt, ML, C O'Sullivan, and G Biscontin. 2014. "Macro-and Micro-Scale Effects of Pluviation Based Sample Preparation in DEM." *Bridges* 10:9780784412121.245.

Beverloo, W. A., H. A. Leniger, and J. Van de Velde. 1961. "The flow of granular solids through orifices." *Chemical engineering science* 15 (3-4):260-269.

Bhandari, Anil, and Jie Han. 2010. "Investigation of geotextile–soil interaction under a cyclic vertical load using the discrete element method." *Geotextiles and Geomembranes* 28 (1):33-43.

Bishop, Alan W. 1957. "AMICE and DJ Henkel, B." *Sc.(Eng.), AMICE,"The Measurement of Soil Properties in The Triaxial Test" AW Bishop and DF Henkel*.

Bolton, M. D., and M. W. Gui. 1993. *The study of relative density and boundary effects for cone penetration tests in centrifuge*: University of Cambridge, Department of Engineering.

Bolton, M. D., Y. Nakata, and Y. P. Cheng. 2008. "Micro-and macro-mechanical behaviour of DEM crushable materials." *Géotechnique* 58 (6):471-480.

Bono, J. P., and G. R. McDowell. 2014. "Discrete element modelling of one-dimensional compression of cemented sand." *Granular Matter* 16 (1):79-90. doi: 10.1007/s10035-013-0466-0.

Bourrier, Franck, François Kneib, Bruno Chareyre, and Thierry Fourcaud. 2013. "Discrete modeling of granular soils reinforcement by plant roots." *Ecological Engineering* 61, Part C (0):646-657. doi: http://dx.doi.org/10.1016/j.ecoleng.2013.05.002.

Butcher, Mike. 1998. "Determining gyratory compaction characteristics using servopac gyratory compactor." *Transportation Research Record: Journal of the Transportation Research Board* 1630 (1):89-97.

Calvetti, F. 2003. "Limitations and perspectives of the micromechanical modelling of granular materials." *Mathematical and computer modelling* 37 (5):485-495.

Calvetti, F., and R. Nova. 2005. "Micro-macro relationships from DEM simulated element and in-situ tests." 2005.

Carrillo, Alex R, David A Horner, John F Peters, and John E West. 1996. "Design of a large scale discrete element soil model for high performance computing systems." Proceedings of the 1996 ACM/IEEE conference on Supercomputing (CDROM).

Chandratilleke, G. R., A. B. Yu, and J. Bridgwater. 2012. "A DEM study of the mixing of particles induced by a flat blade." *Chemical engineering science* 79:54-74.

Chazallon, Cyrille, Georg Koval, and Saida Mouhoubi. 2012. "A two-mechanism elastoplastic model for shakedown of unbound granular materials and DEM simulations." *International Journal for Numerical and Analytical Methods in Geomechanics* 36 (17):1847-1868.

Chen, Cheng. 2013. "Discrete element modelling of geogrid-reinforced railway ballast and track transition zones." University of Nottingham.

Chen, Jiun-Shyan, Chunhui Pan, Cheng-Tang Wu, and Wing Kam Liu. 1996. "Reproducing kernel particle methods for large deformation analysis of non-linear structures." *Computer Methods in Applied Mechanics and Engineering* 139 (1):195-227.

Chen, Yaochung, and Hsiuyen Hung. 1991. "Evolution of shear modulus and fabric during shear deformation." *Soils and Foundations* 31 (4):148-160.

Chen, Ying, Lars J. Munkholm, and Tavs Nyord. 2013. "A discrete element model for soil–sweep interaction in three different soils." *Soil and Tillage Research* 126 (0):34-41. doi: http://dx.doi.org/10.1016/j.still.2012.08.008.

Cheng, Y. P., M. D. Bolton, and Y. Nakata. 2004. "Crushing and plastic deformation of soils simulated using DEM." *Geotechnique* 54 (2):131-142.

Cheng, Y. P., M. D. Bolton, and Y. Nakata. 2005. "Grain crushing and critical states observed in DEM simulations." *P&G05* 2:1393-1397.

Cheng, Y. P., Y. Nakata, and M. D. Bolton. 2003. "Discrete element simulation of crushable soil." *Geotechnique* 53 (7):633-642.

Cheung, Geraldine, and Catherine O'Sullivan. 2008. "Effective simulation of flexible lateral boundaries in two-and three-dimensional DEM simulations." *Particuology* 6 (6):483-500.

Chorney, Drew, Piyush Jain, Melanie Grob, and Mirko van der Baan. 2012. "Geomechanical modeling of rock fracturing and associated microseismicity." *The Leading Edge* 31 (11):1348-1354.

Chung, Y. C., and J. Y. Ooi. 2006. "Confined compression and rod penetration of a dense granular medium: discrete element modelling and validation." In *Modern Trends in Geomechanics*, 223-239. Springer.

Coetzee, C. J. 2016. "Calibration of the discrete element method and the effect of particle shape." *Powder Technology* 297:50-70.

Coetzee, C. J., and D. N. J. Els. 2009a. "Calibration of granular material parameters for DEM modelling and numerical verification by blade–granular material interaction." *Journal of Terramechanics* 46 (1):15-26.

Coetzee, CJ, and DNJ Els. 2009b. "Calibration of discrete element parameters and the modelling of silo discharge and bucket filling." *Computers and electronics in agriculture* 65 (2):198-212.

Cui, L., and C. O'Sullivan. 2006. "Exploring the macro-and micro-scale response of an idealised granular material in the direct shear apparatus." *Geotechnique* 56 (7):455-468.

Cui, L., C. O'Sullivan, and S. O'Neill. 2007. "An analysis of the triaxial apparatus using a mixed boundary three-dimensional discrete element model." *Geotechnique* 57 (10):831-844.

Cui, Liang, and Catherine O’Sullivan. 2003. "Analysis of a triangulation based approach for specimen generation for discrete element simulations." *Granular Matter* 5 (3):135-145.

Cui, Liang, and Catherine O’Sullivan. 2005. "Development of a mixed boundary environment for axi-symmetric DEM analyses." *Powders and Grains*:301-305.

Cundall, P. A. 1987. "Distinct element models of rock and soil structure." *Analytical and computational methods in engineering rock mechanics* 4:129-163.

Cundall, Peter A, and Otto DL Strack. 1979. "A discrete numerical model for granular assemblies." *Geotechnique* 29 (1):47-65.

D1587M-15, ASTM D1587 /. 2015. Standard Practice for Thin-Walled Tube Sampling of Fine-Grained Soils for Geotechnical Purposes, ,. ASTM International, West Conshohocken, PA: www.astm.org.

DCS Computing, Gmbh. 2015. "LIGGGHTS 3.X Manual." accessed April. http://www.cfdem.com/media/DEM/docu/Manual.html.

de Bono, JP, and GR McDowell. 2014. "Discrete element modelling of one-dimensional compression of cemented sand." *Granular Matter* 16 (1):79-90.

Delaney, Gary W., Shio Inagaki, and Tomaso Aste. 2007. "Fine tuning DEM simulations to perform virtual experiments with three-dimensional granular packings." *Granular and Complex Materials. Edited by ASTE TOMASO ET AL. Published by World Scientific Publishing Co. Pte. Ltd., 2007. ISBN# 9789812771995, pp. 169-185*:169-185.

Delenne, Jean-Yves, Moulay Saïd El Youssoufi, and Jean-Claude Bénet. 2005. "Approach of Mechanical Behaviour and Rupture of Cohesive Granular Media. Validation on a Model Medium." In *Mechanical Modelling and Computational Issues in Civil Engineering*, 103-112. Springer.

Devillers, Olivier, Sylvain Pion, and Monique Teillaud. 2002. "Walking in a triangulation." *International Journal of Foundations of Computer Science* 13 (02):181-199.

Donzé, Frédéric V, Vincent Richefeu, and Sophie-Adélaïde Magnier. 2009. "Advances in discrete element method applied to soil, rock and concrete mechanics." *Electron J Geotech Eng* 8:1-44.

Duncan, James Michael, Kai S Wong, and Phillip Mabry. 1980. "Strength, stress-strain and bulk modulus parameters for finite element analyses of stresses and movements in soil masses." In *Geotechnical engineering*. University of California.

El Shamy, Usama, and Natasha Zamani. 2012. "Discrete element method simulations of the seismic response of shallow foundations including soil-foundation-structure interaction." *International Journal for Numerical and Analytical Methods in Geomechanics* 36 (10):1303-1329.

Falagush, O., G. R. McDowell, and Hai-Sui Yu. 2015. "Discrete element modeling of cone penetration tests incorporating particle shape and crushing." *International Journal of Geomechanics* 15 (6):04015003.

Fang, X, and J Tang. 2007. "A direct simulation Monte Carlo approach for the analysis of granular damping." *Journal of computational and nonlinear dynamics* 2 (2):180-189.

Feng, Y. T., K. Han, and D. R. J. Owen. 2003. "Filling domains with disks: an advancing front approach." *International Journal for Numerical Methods in Engineering* 56 (5):699-713.

Ferellec, J. F., and G. R. McDowell. 2008. "A simple method to create complex particle shapes for DEM." *Geomechanics and Geoengineering: An International Journal* 3 (3):211-216.

Ferrez, Jean-Albert. 2001. "Dynamic triangulations for efficient 3D simulation of granular materials."

Frenning, Göran. 2010. "Compression mechanics of granule beds: A combined finite/discrete element study." *Chemical Engineering Science* 65 (8):2464-2471.

Frenning, Göran. 2013. "Towards a mechanistic model for the interaction between plastically deforming particles under confined conditions: A numerical and analytical analysis." *Materials letters (General ed.)* 92:365-368.

Frost, JD, TM Evans, Y Lu, and X Zhao. 2012. "Selected Observations from 3-D Experimental and Numerical Studies of Shear Banding in Biaxial Shear Tests." *Bridges* 10:9780784412121.115.

Fu, Pengcheng, and Yannis F Dafalias. 2011a. "Fabric evolution within shear bands of granular materials and its relation to critical state theory." *International Journal for Numerical and Analytical Methods in Geomechanics* 35 (18):1918-1948.

Fu, Pengcheng, and Yannis F Dafalias. 2011b. "Study of anisotropic shear strength of granular materials using DEM simulation." *International Journal for Numerical and Analytical Methods in Geomechanics* 35 (10):1098-1126.

Fu, Pengcheng, and Yannis F Dafalias. 2012. "Quantification of large and localized deformation in granular materials." *International Journal of Solids and Structures* 49 (13):1741-1752.

Gill, W., and G. VandenBerg. 1968. "Agriculture handbook no. 316." *Agricultural Research Service US Department of Agriculture*.

Gong, Guobin, Colin Thornton, and Andrew HC Chan. 2011. "DEM Simulations of Undrained Triaxial Behavior of Granular Material." *Journal of Engineering Mechanics* 138 (6):560-566.

Gong, Guobin, Xiaoxiong Zha, and Jun Wei. 2012. "Comparison of granular material behaviour under drained triaxial and plane strain conditions using 3D DEM simulations." *Acta Mechanica Solida Sinica* 25 (2):186-196.

Goniva, Christoph, Christoph Kloss, Niels G. Deen, Johannes A. M. Kuipers, and Stefan Pirker. 2012. "Influence of rolling friction on single spout fluidized bed simulation." *Particuology* 10 (5):582-591. doi: http://dx.doi.org/10.1016/j.partic.2012.05.002.

González-Montellano, C., J. M. Fuentes, E. Ayuga-Téllez, and F. Ayuga. 2012. "Determination of the mechanical properties of maize grains and olives required for use in DEM simulations." *Journal of Food Engineering* 111 (4):553-562.

Graziani, Alessandro, Claudio Rossini, and Tatiana Rotonda. 2012. "Characterization and DEM Modeling of Shear Zones at a Large Dam Foundation." *International Journal of Geomechanics* 12 (6):648-664.

Grima, Andrew P, and Peter W Wypych. 2011. "Investigation into calibration of discrete element model parameters for scale-up and validation of particle–structure interactions under impact conditions." *Powder Technology* 212 (1):198-209.

Grisso, R.D. 1985. *Compaction of agricultural soil by continuous deviatoric stress*. PhD diss. Auburn, Ala.: Auburn University, Department of Agricultural Engineering.

Gu, Yile, Ali Ozel, and Sankaran Sundaresan. 2016. "A modified cohesion model for CFD–DEM simulations of fluidization." *Powder Technology* 296:17-28.

Gui, M. W., M. D. Bolton, J. Garnier, J. F. Corte, G. Bagge, J. Laue, and R. Renzi. "Guidelines for cone penetration tests in sand." 1998.

Gui, M. W., M. D. Bolton, J. Garnier, J. F. Corte, G. Bagge, J. Laue, and R. Renzi. 1998. "Guidelines for cone penetration tests in sand." 1998.

Guler, Murat, Hussain U Bahia, Peter J Bosscher, and Michael E Plesha. 2000. "Device for measuring shear resistance of hot-mix asphalt in gyratory compactor." *Transportation Research Record: Journal of the Transportation Research Board* 1723 (1):116-124.

Guo, Ning, and Jidong Zhao. 2013. "The signature of shear-induced anisotropy in granular media." *Computers and Geotechnics* 47:1-15.

Hambleton, JP, and A Drescher. 2008. "Modeling wheel-induced rutting in soils: Indentation." *Journal of Terramechanics* 45 (6):201-211.

Hancock, B. 2004. "Ordered packing induced by simultaneous shear and compaction." Tailings and Mine Waste'04: Proceedings of the Eleventh Tailings and Mine Waste Conference, 10-13 October 2004, Vail, Colorado, USA.

Hanley, Kevin J, Xin Huang, Catherine O'Sullivan, and Fiona Kwok. 2013. "Challenges of simulating undrained tests using the constant volume method in DEM." POWDERS AND GRAINS 2013: Proceedings of the 7th International Conference on Micromechanics of Granular Media.

Harthong, B, J-F Jérier, P Dorémus, D Imbault, and F-V Donzé. 2009. "Modeling of high-density compaction of granular materials by the discrete element method." *International Journal of Solids and Structures* 46 (18):3357-3364.

Hierrezuelo, J, and C Carnero. 1995. "Sliding and rolling: the physics of a rolling ball." *Physics Education* 30 (3):177.

Holt, RM, J Kjølaas, I Larsen, L Li, A Gotusso Pillitteri, and EF Sønstebø. 2005. "Comparison between controlled laboratory experiments and discrete particle simulations of the mechanical behaviour of rock." *International Journal of Rock Mechanics and Mining Sciences* 42 (7):985-995.

Holt, RM, L Li, and JF Stenebraten. 2007. "Compaction Behavior of Unbonded Granular Media: Discrete Particle Vs. Experimental Vs. Analytical Modeling." 1st Canada-US Rock Mechanics Symposium.

Hotta, Kazuyuki, Kazuo Takeda, and Koichi Iinoya. 1974. "The capillary binding force of a liquid bridge." *Powder Technology* 10 (4-5):231-242.

Huang, Hai, and Steven Chrismer. 2013. "Discrete element modeling of ballast settlement under trains moving at "Critical Speeds"." *Construction and Building Materials* 38 (0):994-1000. doi: http://dx.doi.org/10.1016/j.conbuildmat.2012.09.007.

Huang, J, M Vicente da Silva, and K Krabbenhoft. 2013. "Three-dimensional granular contact dynamics with rolling resistance." *Computers and Geotechnics* 49:289-298.

Huang, Xin, Kevin J Hanley, Catherine O'Sullivan, and Chung Yee Kwok. 2014. "Exploring the influence of interparticle friction on critical state behaviour using DEM." *International Journal for Numerical and Analytical Methods in Geomechanics* 38 (12):1276-1297.

Höhner, D., S. Wirtz, and V. Scherer. 2013. "Experimental and numerical investigation on the influence of particle shape and shape approximation on hopper discharge using the discrete element method." *Powder technology* 235:614-627.

Ismail, R, M Tauviqirrahman, Jamari, and D Schipper. 2009. "Finite Element Modeling of Static Contact between Ellipsoid Bodies." *International Journal of Science Engineering and Technology* 2 (3):71-75.

Iwashita, Kazuyoshi, and Masanobu Oda. 1998. "Rolling resistance at contacts in simulation of shear band development by DEM." *Journal of engineering mechanics* 124 (3):285-292.

Iwashita, Kazuyoshi, and Masanobu Oda. 2000. "Micro-deformation mechanism of shear banding process based on modified distinct element method." *Powder Technology* 109 (1):192-205.

Janda, Alvaro, and Jin Y. Ooi. 2016. "DEM modeling of cone penetration and unconfined compression in cohesive solids." *Powder Technology* 293:60-68.

Jensen, Richard P, Peter J Bosscher, Michael E Plesha, and Tuncer B Edil. 1999. "DEM simulation of granular media—structure interface: effects of surface roughness and particle shape." *International Journal for Numerical and Analytical Methods in Geomechanics* 23 (6):531-547.

Jiang, M. J., H-S Yu, and D. Harris. 2006. "Discrete element modelling of deep penetration in granular soils." *International Journal for Numerical and Analytical Methods in Geomechanics* 30 (4):335-361.

Jiang, M. J., H. H. Zhu, and D. Harris. 2008. "Classical and non-classical kinematic fields of two-dimensional penetration tests on granular ground by discrete element method analyses." *Granular Matter* 10 (6):439-455.

Jiang, Mingjing, Yongsheng Dai, Liang Cui, Zhifu Shen, and Xinxin Wang. 2014. "Investigating mechanism of inclined CPT in granular ground using DEM." *Granular Matter* 16 (5):785-796.

Jiang, Mingjing, Fang Liu, Huaning Wang, and Xinxin Wang. 2015. "Investigation of the effect of different gravity conditions on penetration mechanisms by the Distinct Element Method." *Engineering Computations* 32 (7):2067-2099.

Jiang, Mingjing, and Zhifu Shen. 2013. "Strength and fabric evolution of unsaturated granular materials by 3D DEM analyses." POWDERS AND GRAINS 2013: Proceedings of the 7th International Conference on Micromechanics of Granular Media.

Jiang, MJ, JM Konrad, and S Leroueil. 2003. "An efficient technique for generating homogeneous specimens for DEM studies." *Computers and geotechnics* 30 (7):579-597.

Jianhua, Xu Zhonghua Wang. 2005. "Advances in finite element analysis of soil cutting [J]." *Transactions of The Chinese Society of Agricultural Machinery* 1.

Jie, Zhou. 2015. "Macro-Micro Research on the Influence of Model Dimension to Soil Behaviors in DEM Tests." *Chinese Journal of Underground Space and Engineering* 1:013.

Ketterhagen, William R., Mary T. am Ende, and Bruno C. Hancock. 2009. "Process modeling in the pharmaceutical industry using the discrete element method." *Journal of pharmaceutical sciences* 98 (2):442-470.

Ketterhagen, William R., Jennifer S. Curtis, and Carl R. Wassgren. 2005. "Stress results from two-dimensional granular shear flow simulations using various collision models." *Physical Review E* 71 (6):061307.

Ketterhagen, William R., Jennifer S. Curtis, Carl R. Wassgren, and Bruno C. Hancock. 2008. "Modeling granular segregation in flow from quasi-three-dimensional, wedge-shaped hoppers." *Powder Technology* 179 (3):126-143.

Kloss, Christoph, Christoph Goniva, Alice Hager, Stefan Amberger, and Stefan Pirker. 2012. "Models, algorithms and validation for opensource DEM and CFD–DEM." *Progress in Computational Fluid Dynamics, an International Journal* 12 (2-3):140-152.

Kozicki, J, J Tejchman, and Z Mróz. 2012. "Effect of grain roughness on strength, volume changes, elastic and dissipated energies during quasi-static homogeneous triaxial compression using DEM." *Granular Matter* 14 (4):457-468.

Krabbenhoft, K, AV Lyamin, J Huang, and M Vicente da Silva. 2012. "Granular contact dynamics using mathematical programming methods." *Computers and Geotechnics* 43:165-176.

Kruyt, N. P., and L. Rothenburg. 2005. "Strength, dilatancy, energy and dissipation in quasi-static deformation of granular materials." *Powders and Grains*:251.

Kuhn, Matthew R. 1999. "Structured deformation in granular materials." *Mechanics of materials* 31 (6):407-429.

Kuhn, Matthew R. 2003. "Heterogeneity and patterning in the quasi-static behavior of granular materials." *Granular Matter* 4 (4):155-166.

Kushwaha, R. L., and J. Shen. 1995. "Finite element analysis of the dynamic interaction between soil and tillage tool." *Transactions of the ASAE-American Society of Agricultural Engineers* 38 (5):1315-1320.

Lamei, Mahan, and Ali Asghar Mirghasemi. 2011. "A discrete element model for simulating saturated granular soil." *Particuology* 9 (6):650-658.

Lanaro, F., L. Jing, O. Stephansson, and G. Barla. 1997. "DEM modelling of laboratory tests of block toppling." *International Journal of Rock Mechanics and Mining Sciences* 34 (3-4):173-e1.

Langston, Paul, Jun Ai, and Hai-Sui Yu. 2013. "Simple shear in 3D DEM polyhedral particles and in a simplified 2D continuum model." *Granular Matter* 15 (5):595-606.

Lawton, P. J., and J. A. Marchant. 1980. "Direct shear testing of seeds in bulk." *Journal of Agricultural Engineering Research* 25 (2):189-201.

Lee, Seung Jae, Youssef M. A. Hashash, and Erfan G. Nezami. 2012. "Simulation of triaxial compression tests with polyhedral discrete elements." *Computers and Geotechnics* 43:92-100.

Li, J., C. Webb, S. S. Pandiella, and Grant M. Campbell. 2003. "Discrete particle motion on sieves—a numerical study using the DEM simulation." *Powder Technology* 133 (1):190-202.

Li, Xia, Hai-Sui Yu, and Xiang-Song Li. 2013. "A virtual experiment technique on the elementary behaviour of granular materials with discrete element method." *International Journal for Numerical and Analytical Methods in Geomechanics* 37 (1):75-96.

Li, Xikui, Xianhong Han, and M Pastor. 2003. "An iterative stabilized fractional step algorithm for finite element analysis in saturated soil dynamics." *Computer Methods in Applied Mechanics and Engineering* 192 (35):3845-3859.

Lim, Wee Loon. 2004. "Mechanics of railway ballast behaviour." University of Nottingham.

Liu, L, and Y Yuan. 2000. "Dynamic simulation of powder compact by random packing of monosized and polydisperse particles." *Journal of Materials Science Letters* 19 (10):841-843.

Liu, SH, De'an Sun, and Hajime Matsuoka. 2005. "On the interface friction in direct shear test." *Computers and Geotechnics* 32 (5):317-325.

Logan, Daryl. 2002. "First Course In Finite Element Analysis." *Brooks/Cole*.

Lok, TMH, D Wang, and YD Xie. 2013. "Boundary effects on DEM simulation of installation and lateral movement of piles."

Lu, Ye, and David Frost. 2010. "Three-dimensional DEM modeling of triaxial compression of sands." In *Soil Behavior and Geo-Micromechanics*, 220-226.

Mahmud Sazzad, Md, Kiichi Suzuki, and A Modaressi-Farahmand-Razavi. 2012. "Macro-micro responses of granular materials under different b values using DEM." *International Journal of Geomechanics* 12 (3):220-228.

Malone, Kevin Francis, and Bao Hua Xu. 2008. "Determination of contact parameters for discrete element method simulations of granular systems." *Particuology* 6 (6):521-528.

Markauskas, Darius, Álvaro Ramírez-Gómez, Rimantas Kačianauskas, and Evaldas Zdancevičius. 2015. "Maize grain shape approaches for DEM modelling." *Computers and Electronics in Agriculture* 118:247-258.

Masad, Eyad, B Muhunthan, Naga Shashidhar, and Thomas Harman. 1999. "Quantifying laboratory compaction effects on the internal structure of asphalt concrete." *Transportation Research Record: Journal of the Transportation Research Board* 1681 (1):179-185.

Mason, G, and WC Clark. 1965. "Liquid bridges between spheres." *Chemical Engineering Science* 20 (10):859-866.

Masson, S., and J. Martinez. 2001. "Micromechanical analysis of the shear behavior of a granular material." *Journal of Engineering Mechanics* 127 (10):1007-1016.

Matsumoto, Makoto, and Takuji Nishimura. 1998. "Mersenne twister: a 623-dimensionally equidistributed uniform pseudo-random number generator." *ACM Trans. Model. Comput. Simul.* 8 (1):3-30. doi: 10.1145/272991.272995.

Medina-Cetina, Z, and HDV Khoa. 2009. "Probabilistic calibration of discrete particle models for geomaterials." ISSMFE conference, Alexandria, Egypt.

Mesri, Gholamreza, and Barames Vardhanabhuti. 2009. "Compression of granular materials." *Canadian Geotechnical Journal* 46 (4):369-392.

Mindlin, R.D. 1949. "Compliance
of elastic bodies in contact." *J. Appl. Mech* 16:259-268.

Mitchell, James Kenneth, and Kenichi Soga. 2005. "Fundamentals of soil behavior."

Molenda, Marek, and Jozef Horabik. 2004. "On applicability of a direct shear test for strength estimation of cereal grain." *Particle and Particle Systems Characterization* 21 (4):310-315.

Mollanouri Shamsi, M. M., and A. A. Mirghasemi. 2012. "Numerical simulation of 3D semi-real-shaped granular particle assembly." *Powder Technology* 221:431-446. doi: 10.1016/j.powtec.2012.01.042.

Montes, JM, FG Cuevas, and J Cintas. 2006. "A new expression for the effective pressure on powders under compression." *Computational materials science* 36 (3):329-337.

Mouazen, Abdul Mounem, and Miklós Neményi. 1999. "Finite element analysis of subsoiler cutting in non-homogeneous sandy loam soil." *Soil and Tillage Research* 51 (1):1-15.

Moysey, Paul A., Nadella V. Rama Rao, and Malcolm H. I. Baird. 2013. "Dynamic coefficient of friction and granular drag force in dense particle flows: Experiments and DEM simulations." *Powder technology* 248:54-67.

Nakashima, H, H Fujii, A Oida, M Momozu, Y Kawase, H Kanamori, S Aoki, and T Yokoyama. 2007. "Parametric analysis of lugged wheel performance for a lunar microrover by means of DEM." *Journal of Terramechanics* 44 (2):153-162.

Nakashima, Hiroshi, Yasuyuki Shioji, Taizo Kobayashi, Shigeru Aoki, Hiroshi Shimizu, Juro Miyasaka, and Katsuaki Ohdoi. 2011. "Determining the angle of repose of sand under low-gravity conditions using discrete element method." *Journal of Terramechanics* 48 (1):17-26.

Ng, Tang-Tat. 2004. "Macro-and micro-behaviors of granular materials under different sample preparation methods and stress paths." *International Journal of Solids and Structures* 41 (21):5871-5884.

Ng, Tang-Tat. 2006. "Input parameters of discrete element methods." *Journal of Engineering Mechanics* 132 (7):723-729.

Nguyen, Trung, Gaël Combe, Denis Caillerie, and Jacques Desrues. 2014. "FEM× DEM modelling of cohesive granular materials: numerical homogenisation and multi-scale simulations." *Acta Geophysica* 62 (5):1109-1126.

Ning, Z, and TM Evans. 2013. "Discrete Element Method Study of Shear Wave Propagation in Granular Soil." *Proc. of the 18th ICSMGE, Paris*.

Nitka, Michał, Gaël Combe, Cristian Dascalu, and Jacques Desrues. 2011. "Two-scale modeling of granular materials: a DEM-FEM approach." *Granular Matter* 13 (3):277-281.

Nouguier-Lehon, C., and E. Frossard. 2005. "Influence of particle shape on rotaions and rolling movements in granular media." *Powders and Grains*:1339-1343.

O'Sullivan, C., J. D. Bray, and M. F. Riemer. 2002a. "3-D DEM validation using steel balls with regular packing arrangements." In *Discrete Element Methods: Numerical Modeling of Discontinua*, 217-221.

O'Sullivan, Catherine. 2011. *Particulate discrete element modelling*: Taylor & Francis.

O'Sullivan, Catherine, Jonathan D Bray, and Michael F Riemer. 2002b. "Influence of particle shape and surface friction variability on response of rod-shaped particulate media." *Journal of Engineering Mechanics* 128 (11):1182-1192.

O'Sullivan, Catherine, Liang Cui, and Stuart C. O'Neill. 2008. "Discrete element analysis of the response of granular materials during cyclic loading." *Soils and foundations* 48 (4):511-530.

Obermayr, Martin, Klaus Dressler, Christos Vrettos, and Peter Eberhard. 2011. "Prediction of draft forces in cohesionless soil with the Discrete Element Method." *Journal of Terramechanics* 48 (5):347-358.

Obermayr, Martin, Klaus Dressler, Christos Vrettos, and Peter Eberhard. 2013. "A bonded-particle model for cemented sand." *Computers and Geotechnics* 49:299-313.

Obermayr, Martin, Christos Vrettos, Jan Kleinert, and Peter Eberhard. 2013. "A Discrete Element Method for as-sessing reaction forces in excavation tools." *Keywords: discrete element method, rolling resistance, cohesionless soil, draft force (17 pages*.

Oda, M., and H. Kazama. 1998. "Microstructure of shear bands and its relation to the mechanisms of dilatancy and failure of dense granular soils." *Geotechnique* 48 (4):465-481.

Oda, M., S. Nemat-Nasser, and Morteza M. Mehrabadi. 1982. "A statistical study of fabric in a random assembly of spherical granules." *International Journal for Numerical and analytical methods in Geomechanics* 6 (1):77-94.

Onate, E, and J Rojek. 2004. "Combination of discrete element and finite element methods for dynamic analysis of geomechanics problems." *Computer methods in applied mechanics and engineering* 193 (27):3087-3128.

O'Donovan, J, C O'Sullivan, and G Marketos. 2012. "Two-dimensional discrete element modelling of bender element tests on an idealised granular material." *Granular Matter* 14 (6):733-747.

O'Sullivan, C., and J. D. Bray. 2001. "A comparative evaluation of two approaches to discrete element modeling of particulate media." 2001.

O'Sullivan, Catherine. 2011. "Particle-based discrete element modeling: geomechanics perspective." *International Journal of Geomechanics* 11 (6):449-464.

O'Sullivan, Catherine, Jonathan D. Bray, and Michael Riemer. 2004. "Examination of the response of regularly packed specimens of spherical particles using physical tests and discrete element simulations." *Journal of engineering mechanics* 130 (10):1140-1150.

Powrie, W., Q. Ni, R. M. Harkness, and X. Zhang. 2005. "Numerical modelling of plane strain tests on sands using a particulate approach." *Géotechnique* 55 (4):297-306.

Rabinovich, Yakov I, Madhavan S Esayanur, and Brij M Moudgil. 2005. "Capillary forces between two spheres with a fixed volume liquid bridge: theory and experiment." *Langmuir* 21 (24):10992-10997.

Richefeu, V, MS El Youssoufi, R Peyroux, and C Bohatier. 2005. "Frictional contact and cohesion laws for Casagrande's shear test on granular materials by 3D DEM–comparison with experiments." *Powders and Grains*:509-512.

Rokonuzzaman, Md, and Toshinori Sakai. 2010. "Calibration of the parameters for a hardening–softening constitutive model using genetic algorithms." *Computers and Geotechnics* 37 (4):573-579.

Rosa, U. A., and D. Wulfsohn. 2002. "Application of the finite element method in agricultural soil mechanics." In *Advances in Soil Dynamics Volume 2*, 117. American Society of Agricultural and Biological Engineers.

Roux, Jean-Noël, and François Chevoir. 2005. "Discrete numerical simulations and mechanical behaviour of granular materials." *Bulletin des laboratoires des ponts et chaussées* 254:109-138.

Sadek, Mohammad A., Ying Chen, and Jude Liu. 2011. "Simulating shear behavior of a sandy soil under different soil conditions." *Journal of Terramechanics* 48 (6):451-458.

Salazar, Antonio, Esteban Sáez, and Gislaine Pardo. 2015. "Modeling the direct shear test of a coarse sand using the 3D Discrete Element Method with a rolling friction model." *Computers and Geotechnics* 67 (0):83-93. doi: http://dx.doi.org/10.1016/j.compgeo.2015.02.017.

Salot, Christophe, Philippe Gotteland, and Pascal Villard. 2009. "Influence of relative density on granular materials behavior: DEM simulations of triaxial tests." *Granular matter* 11 (4):221-236.

Sanchez-Castillo, Francisco X, Jamshed Anwar, and David M Heyes. 2003. "Molecular dynamics simulations of granular compaction: The single granule case." *The Journal of chemical physics* 118 (10):4636-4648.

Sandbaekken, G., T. Berre, and S. Lacasse. 1986. "Oedometer testing at the Norwegian Geotechnical Institute." In *Consolidation of soils: Testing and evaluation*. ASTM International.

Sarkar, Avik, and Carl R. Wassgren. 2012. "Comparison of flow microdynamics for a continuous granular mixer with predictions from periodic slice DEM simulations." *Powder technology* 221:325-336.

Sayeed, Md Abu, Md Mahmud Sazzad, and Kiichi Suzuki. 2014. "Mechanical Behavior of Granular Materials Considering Confining Pressure Dependency." *Bridges* 10:9780784412121.225.

Scheibel, H. G., and J. Porstendo. 1983. "Generation of monodisperse Ag-and NaCl-aerosols with particle diameters between 2 and 300 nm." *Journal of Aerosol Science* 14 (2):113-126.

Schmertmann, John H. 1975. "Measurement of insitu shear strength: Proc Conference on In-situ Measurement of Soil Properties, Raleigh, NC, 1–4 June 1975, V2, P57–138, disc P139–179."

Scholtès, L, B Chareyre, F Nicot, and F Darve. 2009. "Micromechanics of granular materials with capillary effects." *International journal of engineering science* 47 (1):64-75.

Shamsi, MM Mollanouri, and AA Mirghasemi. 2012. "Numerical simulation of 3D semi-real-shaped granular particle assembly." *Powder Technology* 221:431-446.

Sheng, Y, CJ Lawrence, BJ Briscoe, and C Thornton. 2004. "Numerical studies of uniaxial powder compaction process by 3D DEM." *Engineering Computations* 21 (2/3/4):304-317.

Shewchuk, Johnathan Richard. 1996a. "Robust adaptive floating-point geometric predicates." Proceedings of the twelfth annual symposium on Computational geometry.

Shewchuk, Jonathan. 1996b. "Triangle: Engineering a 2D quality mesh generator and Delaunay triangulator." *Applied computational geometry towards geometric engineering*:203-222.

Shmulevich, I. 2010. "State of the art modeling of soil–tillage interaction using discrete element method." *Soil and Tillage Research* 111 (1):41-53.

Shmulevich, I., Z. Asaf, and D. Rubinstein. 2007. "Interaction between soil and a wide cutting blade using the discrete element method." *Soil and Tillage Research* 97 (1):37-50.

Sima, Jun, Mingjing Jiang, and Chuangbing Zhou. 2014. "Numerical simulation of desiccation cracking in a thin clay layer using 3D discrete element modeling." *Computers and Geotechnics* 56:168-180.

Sitharam, T. G., J. S. Vinod, and L. Rothenburg. 2005. "Shear behavior of glass beads using DEM." *Powders and Grains* 5:257-260.

Sitharam, TG, and JS Vinod. 2010. "Evaluation of shear modulus and damping ratio of granular materials using discrete element approach." *Geotechnical and Geological Engineering* 28 (5):591-601.

Smith, William, and Huei Peng. 2013. "Modeling of wheel–soil interaction over rough terrain using the discrete element method." *Journal of Terramechanics* 50 (5–6):277-287. doi: http://dx.doi.org/10.1016/j.jterra.2013.09.002.

Song, Chaoming, Ping Wang, and Hernán A. Makse. 2008. "A phase diagram for jammed matter." *Nature* 453 (7195):629-632.

Soulie, Fabien, Fabien Cherblanc, Moulay Saïd El Youssoufi, and C Saix. 2006. "Influence of liquid bridges on the mechanical behaviour of polydisperse granular materials." *International journal for numerical and analytical methods in geomechanics* 30 (3):213-228.

Standard, Asae. 2000. "ASAE S313. 3." *Soil Cone Penetrometer. ASAE, St. Joseph, MI, USA.*

Syed, Zamir, Mehari Tekeste, and David White. 2017. "A coupled sliding and rolling friction model for DEM calibration." *Journal of Terramechanics* 72:9-20.

Taibi, Said, A. Alem, and Jean-Marie Fleureau. "Influence of capillary forces on the flow of granular materials; experimental study and DEM modelling." 2005.

Takahara, T., Kikumoto, A., Yamakami, T. 2005. "A study on the simple expression method for generating excess pore pressure in DEM." Powders and Grains, Stuttgart, Germany.

Tamás, Kornél, István J. Jóri, and Abdul M. Mouazen. 2013. "Modelling soil–sweep interaction with discrete element method." *Soil and Tillage Research* 134:223-231.

Tang, Chunan, and Hongyuan Liu. 2007. "Numerical investigation of particle breakage as applied to mechanical crushing." *Handbook of Powder Technology* 12:661-739.

Team, R. Core. 2013. "R foundation for statistical computing." *Vienna, Austria* 3 (0).

Tekeste, M. Z., E. W. Tollner, R. L. Raper, T. R. Way, and C. E. Johnson. 2009. "Non-linear finite element analysis of cone penetration in layered sandy loam soil–Considering precompression stress state." *Journal of Terramechanics* 46 (5):229-239.

Tekeste, Mehari Z., Randy L. Raper, Ernest W. Tollner, and T. R. Way. 2007. "Finite element analysis of cone penetration in soil for prediction of hardpan location." *Trans. ASABE* 50 (1):23-31.

Thornton, C, and SJ Antony. 2000. "Quasi-static shear deformation of a soft particle system." *Powder Technology* 109 (1):179-191.

Thornton, Colin. 2000. "Numerical simulations of discrete particle systems." *Powder Technology* 109 (1-3):1-298.

Ting, John M, Brent T Corkum, Claudia R Kauffman, and Carlo Greco. 1989. "Discrete numerical model for soil mechanics." *Journal of Geotechnical Engineering* 115 (3):379-398.

Tordesillas, Antoinette, and Maya Muthuswamy. 2009. "On the modeling of confined buckling of force chains." *Journal of the Mechanics and Physics of Solids* 57 (4):706-727.

Tran, Quoc Anh, Bastien Chevalier, and Pierre Breul. 2016. "Discrete modeling of penetration tests in constant velocity and impact conditions." *Computers and Geotechnics* 71:12-18.

Tran, VDH, MA Meguid, and LE Chouinard. 2013. "A finite–discrete element framework for the 3D modeling of geogrid–soil interaction under pullout loading conditions." *Geotextiles and Geomembranes* 37:1-9.

Tsuji, T, Y Nakagawa, N Matsumoto, Y Kadono, T Takayama, and T Tanaka. 2012. "3-D DEM simulation of cohesive soil-pushing behavior by bulldozer blade." *Journal of Terramechanics* 49 (1):37-47.

Tsunazawa, Yuki, Daiki Fujihashi, Sho Fukui, Mikio Sakai, and Chiharu Tokoro. 2016. "Contact force model including the liquid-bridge force for wet-particle simulation using the discrete element method." *Advanced Powder Technology* 27 (2):652-660.

Ucgul, Mustafa, John M. Fielke, and Chris Saunders. 2014. "3D DEM tillage simulation: Validation of a hysteretic spring (plastic) contact model for a sweep tool operating in a cohesionless soil." *Soil and Tillage Research* 144:220-227.

Ucgul, Mustafa, John M. Fielke, and Chris Saunders. 2015. "Three-dimensional discrete element modelling (DEM) of tillage: Accounting for soil cohesion and adhesion." *Biosystems Engineering* 129:298-306.

Utili, S, and R Nova. 2008. "DEM analysis of bonded granular geomaterials." *International journal for numerical and analytical methods in geomechanics* 32 (17):1997-2031.

Vardoulakis, I. 1989. "Shear-banding and liquefaction in granular materials on the basis of a Cosserat continuum theory." *Ingenieur-Archiv* 59 (2):106-113.

Vavourakis, Vasileios, Dimitrios Loukidis, Dimos C Charmpis, and Panos Papanastasiou. 2013. "Assessment of remeshing and remapping strategies for large deformation elastoplastic Finite Element analysis." *Computers & Structures* 114:133-146.

Villard, P, B Chevalier, B Le Hello, and G Combe. 2009. "Coupling between finite and discrete element methods for the modelling of earth structures reinforced by geosynthetic." *Computers and Geotechnics* 36 (5):709-717.

Von Karman, T. H. 1911. "Strength tests with triaxial compression." *Z. Ver. dt. Ing* 55:1749-1757.

Vu-Quoc, Loc, Xiang Zhang, and Lee Lesburg. 2001. "Normal and tangential force–displacement relations for frictional elasto-plastic contact of spheres." *International journal of solids and structures* 38 (36):6455-6489.

Wang, Jianfeng, and Haibin Yan. 2011. "On the role of particle breakage in the shear failure behavior of granular soils by DEM." *International Journal for Numerical and Analytical Methods in Geomechanics*.

Wang, Yuannian, and Fulvio Tonon. 2010. "Calibration of a discrete element model for intact rock up to its peak strength." *International journal for numerical and analytical methods in geomechanics* 34 (5):447-469.

Wang, Zhengxing, Linchang Miao, and Fei Wang. 2012. "Theoretical and Numerical Analysis of Jacked Pile in Sand." In *GeoCongress 2012: State of the Art and Practice in Geotechnical Engineering*, 245-254.

Washino, K, HS Tan, MJ Hounslow, and AD Salman. 2013. "A new capillary force model implemented in micro-scale CFD–DEM coupling for wet granulation." *Chemical Engineering Science* 93:197-205.

Wensrich, CM, and A Katterfeld. 2012. "Rolling friction as a technique for modelling particle shape in DEM." *Powder Technology* 217:409-417.

Wensrich, CM, and RE Stratton. 2011. "Shock waves in granular materials: Discrete and continuum comparisons." *Powder technology* 210 (3):288-292.

Whitman, Robert V, Edmond T Miller, and Peter J Moore. 1964. "Yielding and locking of confined sand." *Journal of Soil Mechanics & Foundations Div* 90 (Proc. Paper 3966).

Widuliński, Łukasz, Jan Kozicki, and Jacek Tejchman. 2009. "Numerical simulations of triaxial test with sand using DEM." *Archives of Hydro–Engineering and Environmental Mechanics* 56 (3-4):149-172.

Xianguo, Chen, and Gao Bo. 2002. "2D FEM NUMERICAL SIMULATION FOR CLOSELY-SPACED PARALLEL TUNNELS IN METRO [J]." *Chinese Journal of Rock Mechanics and Engineering* 9:1330-1334.

Xie, Yu-ming, Qi-xiang Qing, and Qin-qing Tang. 2013. "Dynamically behavioral research of lunar soil drilling and sampling by DEM." *Chinese Journal of Engineering Design* 6:007.

Xu, Bin, Wei Luo, De Gao Zou, Xian Jing Kong, and Yang Zhou. "The Numerical Simulation of the Triaxial Test of Cemented Coarse-Grained Soils." 2011.

Yoon, Jeoungseok. 2007. "Application of experimental design and optimization to PFC model calibration in uniaxial compression simulation." *International Journal of Rock Mechanics and Mining Sciences* 44 (6):871-889.

Yoon, JS, S Jeon, A Zang, and O Stephansson. 2011. "Bonded particle model simulation of laboratory rock tests for granite using particle clumping and contact unbonding." Proceedings of the 2nd International FLAC/DEM Symposium, Continuum and Distinct Element Numerical Modeling in Geomechanics, Melbourne, Australia.

Yu, H. S., and J. K. Mitchell. 1998. "Analysis of cone resistance: review of methods." *Journal of Geotechnical and Geoenvironmental Engineering* 124 (2):140-149.

Zhang, Jie, Trush Majmudar, and Robert Behringer. 2008. "Force chains in a two-dimensional granular pure shear experiment." *Chaos* 18 (4):41107.

Zhang, L., and C. Thornton. 2005. "Characteristics of granular media at the critical state." *Powders and Grains 2005*:267-270.

Zhang, Rui, and Jianqiao Li. 2006. "Simulation on mechanical behavior of cohesive soil by Distinct Element Method." *Journal of Terramechanics* 43 (3):303-316.

Zhang, YB, Z Medina-Cedina, and HDV Khoa. 2011. "Probabilistic Calibration of a Discrete Particle Model for Geomaterials." Geo-Frontiers 2011@ sAdvances in Geotechnical Engineering.

Zhao, Hong-hua, Long-tan Shao, and Shun-ying Ji. 2011. "Numerical Simulation of Triaxial Test on the Dense Sand by DEM." Instrumentation, Testing, and Modeling of Soil and Rock Behavior.

Zhao, Jidong, and Tong Shan. 2013. "Coupled CFD–DEM simulation of fluid–particle interaction in geomechanics." *Powder Technology* (239):248-258.

Zhu, H. P., Z. Y. Zhou, R. Y. Yang, and A. B. Yu. 2007. "Discrete particle simulation of particulate systems: theoretical developments." *Chemical Engineering Science* 62 (13):3378-3396.